UNIVERSITY OF COPENHAGEN
FACULTY OF SCIENCE

This thesis has been submitted to the PhD School of the Faculty of Science, University of Copenhagen

Ph.D. Thesis

Magnetic proximity effects in heterostructures designed for quantum computing devices

Kamaldeep Dalal

Supervisors:

Dr. Nina-Juliane Steinke, Institut Laue-Langevin

Dr. Thomas Saerbeck, Institut Laue-Langevin

Prof. Dr. Kim Lefmann, Niels Bohr Institute

Prof. Dr. Peter Krogstrup, Niels Bohr Institute

December 2024

Abstract

This thesis investigates two interrelated topics: magnetic proximity effects (MPEs) in heterostructures involving europium sulfide (EuS), lead (Pb), and indium arsenide (InAs), and the intrinsic magnetic behavior of EuS thin films above and below their Curie temperature (T_C). A primary goal is to enhance comprehension of the magnetic and structural interactions at interfaces within these systems, helping optimize device structure design for quantum computing.

The first part of the study focuses on the heterostructures that are designed to explore the MPEs at the EuS/Pb interfaces, featuring the InAs/Pb/EuS/Pb/cap configuration. These heterostructures were characterized using techniques such as X-ray diffraction (XRD), transmission electron microscopy (TEM), SQUID magnetometry, polarized neutron reflectometry (PNR), and X-ray reflectometry (XRR). The results show that thin films of Pb (200 and 400 Å) behave unexpectedly as a type II superconductor, with a consistent transition to the normal state around 7 K. EuS in thin films ($10\ \text{Å} \leq d_{EuS} \leq 40\ \text{Å}$) exhibits ferromagnetic behavior consistent with theory. An antiparallel arrangement of magnetic moments, consistent with MPEs, was detected that extends up to 30 Å in Pb layers near the EuS/Pb interfaces. Moreover, the magnetic signal is found to be more pronounced at one EuS/Pb interface than at the other. These findings highlight the critical role of EuS layer thickness in achieving robust MPEs at interfaces for heterostructures intended for topological quantum devices.

The second part of the study examines the intrinsic magnetic properties of EuS thin films with thicknesses ranging from 15 to 100 Å, grown on InAs substrates (111 B). The ferromagnetic transition of EuS in the samples behaved as expected for the thin EuS layers. Surprisingly, significant magnetic signals were observed in EuS films well above (T_C), up to 300 K, under applied magnetic fields. PNR measurements revealed that this magnetic signal is uniformly distributed throughout the EuS layer, rather than being confined to the interface. The magnetic signal above T_C in EuS thin

films depends on the magnetic field and temperature, suggesting a polarization effect of magnetic moments rather than spontaneous magnetic ordering. These results provide a foundation for further exploration of high-temperature magnetic behavior in EuS thin films and its implications for quantum computing and spintronic devices.

This work demonstrates the potential of EuS-based heterostructures for the realization of MPEs and explores the intriguing high-temperature magnetism of EuS thin films. Together, these findings contribute to the development of scalable quantum and spintronic devices that take advantage of the magnetic properties of EuS.

Resume

Denne afhandling undersøger to indbyrdes relaterede emner: magnetiske proximity-effekter (MPE'er) i heterostrukturer, der involverer europiumsulfid (EuS), bly (Pb) og indiumarsenid (InAs), samt den iboende magnetiske adfærd af EuS-tyndfilm over og under deres Curie-temperatur (T_C). Et primært mål er at forbedre forståelsen af de magnetiske og strukturelle interaktioner ved grænseflader i disse systemer og dermed optimere designet af enhedsstrukturer til kvanteberegning.

Den første del af studiet fokuserer på heterostrukturer med InAs/Pb/EuS/Pb/cap-konfigurationen, designet til at undersøge MPE'er ved EuS/Pb-grænsefladerne. Disse heterostrukturer blev karakteriseret ved hjælp af teknikker som røntgendiffraktion (XRD), transmissionselektronmikroskopi (TEM), SQUID-magnetometri, polariseret neutronreflektometri (PNR) og røntgenreflektometri (XRR). Resultaterne viser, at tynde Pb-film (200 og 400 Å) opfører sig uventet som en type II superleder med en konstant overgang til den normale tilstand omkring 7 K, mens EuS i tynde film (10 Å $\leq d_{EuS} \leq$ 40 Å) udviser ferromagnetisk adfærd i overensstemmelse med teorien. En antiparallel ordning af magnetiske momenter, konsistent med MPE'er, blev detekteret, som strækker sig op til 30 Å i Pb-lag nær EuS/Pb-grænsefladerne. Desuden blev det magnetiske signal fundet at være mere udtalt ved den ene grænseflade end ved den anden. Disse resultater understreger den afgørende betydning af EuS-lagets tykkelse for at opnå stærke MPE'er i heterostrukturer, der er tiltænkt topologiske kvanteenheder.

Den anden del af studiet undersøger de iboende magnetiske egenskaber af EuS-tyndfilm med tykkelser fra 15 til 100 Å, der er vokset på InAs-substrater (111 B). Den ferromagnetiske overgang af EuS i prøverne opførte sig som forventet for de tynde EuS-lag. Overraskende blev der observeret betydelige magnetiske signaler i EuS-film langt over (T_C), op til 300 K, under påførte magnetiske felter. PNR-målinger afslørede, at dette magnetiske signal er jævnt fordelt gennem EuS-laget og ikke begrænset til grænsefladen. Det magnetiske signal over T_C i EuS-tyndfilm afhænger af magnetfel-

tet og temperaturen, hvilket antyder en polariseringseffekt af magnetiske momenter frem for spontan magnetisk orden. Disse resultater skaber grundlag for yderligere udforskning af højtemperatur magnetisk adfærd i EuS-tyndfilm og dets implikationer for kvanteberegning og spintroniske enheder.

Dette arbejde demonstrerer potentialet i EuS-baserede heterostrukturer til at realisere magnetiske proximity-effekter og udforsker den spændende højtemperatur magnetisme i EuS-tyndfilm. Samlet bidrager disse resultater til udviklingen af skalerbare kvante- og spintroniske enheder, der udnytter de magnetiske egenskaber ved EuS.

Acknowledgements

The journey of completing my Ph.D. has been a great learning experience filled with personal and professional growth. This achievement would not have occurred without the support, guidance, and encouragement of many individuals, to whom I extend my sincere thanks.

First, I would like to express my profound gratitude to my advisors, **Dr. Nina-Juliane Steinke**, **Dr. Thomas Saerbeck**, **Prof. Dr. Kim Lefmann** for their continuous guidance and mentorship throughout the course of my research. They provided key theoretical insights and assisted in learning experimental techniques, data collection, and analysis. I express my sincere gratitude to them for their help and guidance during the long neutron and X-ray beamtimes.

I am also thankful to **Prof. Dr. Peter Krogstrup** for valuable discussions during the initial phase of my Ph.D. and **Dr. Yu Liu** and **Dr. Malvika Tripathi** for their help with sample fabrication and insightful discussions. I am especially grateful to **Dr. Peter Mills** for helping me with GenX software during the initial phase of my Ph.D. My sincere thanks also go to **Dr. Christy Kinane** and **Dr. Andrew J. Caruana** for their help and discussions during the ISIS neutron beamtime, particularly for their support with Refl1D software. In addition, I would like to acknowledge **Dr. Fabrice Wilhelm** for his support during the ESRF beam time.

I am deeply grateful to my family for their unconditional love, encouragement, and belief in me throughout this process. I am truly grateful to Sabhyata for sticking by my side during the challenging times of my thesis, as well as for her invaluable help in proofreading. To all my friends at ILL, especially **Chakib**, **Beatrice**, **Riccardo**, **Illaria**, **Tong**, **Brigida**, **Matteo**, thank you for always being there to listen, encourage, and the long coffee breaks. To all my friends outside of ILL, especially **Tejas** and **Jahnavi**, thank you for making Grenoble feel like home and for reminding me of the importance of balance in life.

I am grateful to **Jothishwaran** for guiding and encouraging me to take the first step towards this PhD journey. I also thank the **neutron research group** at NBI, whose warmth and hospitality during my secondments in Copenhagen made my time there both productive and enjoyable. I am also thankful to the **ILL PhD community** and **LSS group** for providing me with such a friendly and stimulating working environment.

Kamaldeep Dalal
December 2024

Statement of Involvement

This thesis acknowledges the participation of external collaborators in providing data and discussions. Dr. Yu Liu and Dr. Malvika Tripathi (currently at Fermi National Accelerator Laboratory, USA) fabricated the samples at the Niels Bohr Institute, University of Copenhagen. Dr. Sara Mart-Sánchez and Dr. Christian Koch, affiliated with the Catalan Institute of Nanoscience and Nanotechnology (ICN2) in Barcelona, provided the analyzed scanning transmission electron microscopy (STEM) data for the samples QD1 and QD2, as presented in Chapter 5. Furthermore, the SQUID magnetometry data presented in Chapter 5 for all samples was recorded by Dr. Shengqiang Zhou, Dr. Mohd Saif Shaikh, Dr. Zichao Li and Dr. Marc Uhlarz of Helmholtz-Zentrum Dresden-Rossendorf, Germany.

With the guidance and help of my supervisors, I recorded X-ray diffraction (XRD) and X-ray reflectometry (XRR) data for the samples. In addition, I collected the SQUID data for the substrate and samples in Chapter 6. Together with my supervisors and collaborators (Dr. Yu Liu and Dr. Malvika Tripathi), I participated in planning and executing the neutron and X-ray beamtimes to record the data for samples using polarized neutron reflectometry (PNR) and X-ray absorption spectroscopy (XAS).

I conducted a detailed analysis of the raw data from techniques that includes XRD, SQUID magnetometry, XAS, PNR, and XRR, interpreting the results/analysis in the broader context of the study. The conclusions and interpretations presented in the thesis are based on my analysis and discussions with my supervisors.

Kamaldeep Dalal
Niels Bohr Institute (NBI)
University of Copenhagen
December 2024

Contents

Chapter 1

Introduction

Recent advancements in quantum computing have introduced various platforms based on different systems for quantum information processing, such as trapped ions, neutral atoms, superconducting loops, photonics, etc. ([1, 2, 3, 4]). However, these systems face challenges, mainly in scalability and decoherence [5]. Scalability involves maintaining a large number of high-quality quantum bits (qubits) with reliable connectivity and low error rates, whereas decoherence is the loss of quantum information with time caused by interactions with the environment, such as stray fields and subatomic particles, thermal energy, etc. These interactions limit the practical use of quantum systems. To address these issues, advancements in qubit fidelity, error correction protocols, and hardware design are crucial. Strategies such as cryogenic cooling, quantum error correction, and dynamical decoupling can mitigate decoherence, but come with implementation challenges and scalability limitations. As a result, efforts have been focused on improving systems and developing new quantum computing technologies to overcome these barriers [5].

A promising approach to overcome the limitations of current quantum computing technologies is the development of topological quantum computers, which utilize topological qubits based on exotic quasiparticles called anyons [6]. Proposed by Alexei Kitaev in 1997, these qubits are inherently robust against decoherence due to their topological properties, making them less sensitive to local perturbations [7]. An ideal candidate for topological qubits is Majorana fermions (MFs), predicted by Ettore Majorana in 1937 [8]. MFs are particles that are identical to their antiparticles and emerge as quasiparticles under specific conditions, typically appearing in pairs [9]. Kitaev's model demonstrated how these MFs could be spatially separated [10]. Various condensed matter systems and device structures have been proposed to experimentally explore MFs and their potential in quantum computing.

Systems combining superconductor (SU), and semiconductor (SE) materials have the potential to host Majorana bound states (MBSs), which are Majorana fermions localized at boundaries and can be used for information storage [11, 12, 13, 14]. MBSs belong to the class of non-Abelian anyons, which makes them valuable for exploring topological quantum computation [15]. The concept of MBSs-based topological qubits was first proposed in the early 2000s [6, 16], and significant experimental efforts are ongoing to improve device structures and observe MBSs. MBSs are expected to emerge at the ends of one-dimensional SE nanowires coupled to SU and subjected to a strong Zeeman field.

Superconductors are essential for studying MBSs due to their particle-hole symmetry, which enables the formation of essential quasiparticles for MBSs [17, 18]. The superconducting proximity effect induces a superconducting state in the semiconductor, and for MBSs to emerge, strong spin-orbit coupling and a Zeeman field are required to split the SE bands. Typically, Zeeman energy is provided by an external magnetic field that is applied along the axis of the nanowire. However, challenges arise in the scalability of the system, as the external magnetic field deteriorates the superconducting properties [19] and enforces strict limits on the device's geometry since the external field must align parallel to the wire axis. An alternative is to integrate a ferromagnetic insulator (FM) into the system, which generates the necessary exchange interactions for Zeeman splitting, eliminating the need for an external field, and offers a promising route for intrinsically topological structures [20]. The initial challenge to develop an intrinsically topological trilayer structure is to choose a suitable FM material and then ensure the appropriate strength of magnetic proximity effects (MPEs) at the interfaces of FM with SU and SE materials[21]. In altered device configurations incorporating FM, MPEs facilitate the transition to a topological state, potentially leading to the emergence of MBSs.

In SU/FM systems, the proximity effects result from the interplay between magnetism and superconductivity at the interface. These effects include spin-transfer, charge-transfer, dipolar interactions, and interdiffusion of ions or molecules. Spin transfer at the SU/FM interface occurs as a result of the exchange of angular momentum between spin-polarized electrons in the FM and Cooper pairs in the SU. Spin polarization from the ferromagnet can extend into the superconductor, affecting the singlet pairing in SU [22, 23, 24]. Charge transfer, driven by processes such as Andreev reflection and tunneling, reveals the spin-dependent nature of electron transport across the SU/FM interface [25]. Dipolar interactions at the SU/FM interfaces arise from the interplay between the stray magnetic fields of the ferromagnet and the magnetic response of the superconductor [26]. These interactions can induce vortices and suppress the superconducting gap. SU can introduce the superconducting order parameter in FM that can suppress the magnetic moments in FM, leading to a dead magnetic region in FM near the interface. Furthermore, proximity to FM can also induce weak magnetization or spin polarization within the SU near the interface, altering its magnetic state [27, 28, 29].

The aim of this Ph.D. project was to observe and quantify MPEs at the SU/FM interfaces in the heterostructures. To observe and quantify MPEs at the SU/FM interfaces, polarized neutron reflectometry (PNR) was used. MPEs at the interfaces are crucial for entering the topological phase. PNR is a useful technique to study buried interfaces that are not accessible by other techniques and has been a technique of choice for studying buried magnetic interfaces in the past [27, 30, 31, 32, 33, 34, 35, 36, 37]. This study evaluates the magnetic proximity observed in Pb/EuS/Pb type systems, aiding in the optimization and experimental development of quantum computing devices.

Chapter 2 provides an introduction to the materials chosen for this study, focusing on their intrinsic properties. In Chapter 3, a concise account of the underlying principles of the experimental techniques utilized in this study to investigate the structural and magnetic properties of heterostructures is presented. In Chapter 4, a comprehensive examination of the analysis of the reflectometry data is presented, elaborating on the methodologies employed and the software utilized in this study. Chapter 5 provides an in-depth investigation of MPEs in InAs(sub.)/Pb/EuS/Pb type heterostructures. Chapter 6 investigates the magnetism in the EuS thin films on the InAs substrate below and above the Curie temperature (T_C). Conclusions and outlook are presented in Chapter 7.

Chapter 2

Materials and fabrication methods

2.1 Choice of materials

The primary motivation behind the choice of materials lies in the development of the structure of the quantum computing device that can be adapted to encode information based on the existence of MBS. To experimentally detect magnetic proximity effects, superior quality of interfaces is necessary. The set of materials chosen for the study involve lead (superconductor), indium arsenide (semiconductor), and europium sulfide (ferromagnetic insulator).

2.1.1 Lead (Pb)

The crystal structure of Pb is face-centered cubic (lattice parameters in Table 2.1). The atomic number of Pb is 82 with electronic configuration [Xe] $4f^{14}$ $6s^2$ $5d^{10}$ $6p^2$. In atomic form, Pb possesses two electrons in its outer shell (6p), and in its stable ground-state configuration, these electrons are paired, leading to a diamagnetic state. Pb is a conventional s-wave superconductor described by the BCS theory [38], meaning that conduction electrons form Cooper pairs. Pb exhibits a transition temperature (T_{SU}) of approximately 7.18 K [39]. Pb is relatively inert to oxidation, and its experimentally accessible transition temperature makes it useful for the study of magnetic proximity effects. The critical magnetic field H_c for elemental Pb (bulk, type I) in its superconducting state is around 0.8 T close to zero kelvin [40]. However, there is a dirty thickness limit that is a function of London penetration depth (λ_L), thickness of the layer (d_{Pb}), and the coherence length of Pb (ξ_{Pb}) [41]. If the mean free path of the cooper pairs is less than the coherence length of the superconductor, then, the superconductor is in the dirty limit. As a consequence, Pb changes its behavior from type I to type II superconductor when the thickness is below the dirty limit [42]. The coherence length of Pb (ξ_{Pb}) in bulk form is approximately 800 Å [43]. The thickness of Pb thin films in the present study is less than 800 Å, which is below the dirty limit for Pb. Thus, Pb is expected to exhibit type II superconducting behavior in the samples.

2.1.2 Indium arsenide (InAs)

A suitable semiconductor material should have strong spin-orbit band splitting, high electron mobility, large g factor, and low effective mass [20]. These requirements are met by InAs and indium antimonide (InSb) [44]; however, the lattice constant of InAs aligns more closely with that of EuS than InSb. InAs is a compound with a narrow direct band gap of 0.35 eV [45], an electron mobility of 20000 cm^2 V^{-1} s^{-1} at RT [46] and a cubic crystal structure [47]. In the InAs compound, In and As are present in the oxidation states + 3 and − 3, respectively. The lattice mismatch of InAs with EuS is less than 1%, which facilitates the production of superior-quality thin films of EuS on InAs substrates.

2.1.3 Europium sulfide (EuS)

The reasons for using EuS as a ferromagnetic material are the high magnetic moment and semiconducting properties. EuS is a binary compound with Eu (+2) and S (−2) in the divalent state. The unit cell of EuS is face-centered cubic (FCC), where the atoms of Eu and S have a coordination number of six [48]. Eu has an atomic number of 63 with electronic configuration [Xe] $4f^7$ $6s^2$. There are 7 unpaired electrons in the 4f shell (half filled) of the Eu^{2+} ion, and these electrons are well shielded. Thus, the localized f-electron spins do not engage in direct exchange interactions with the spins of other Eu ions. The exchange interactions in EuS material are mediated by S atoms and Eu 5d orbitals [49].

EuS thin film has an in-plane magnetic anisotropy, with electron spins aligning ferromagnetically below the Curie temperature (T$_C$) of around 16.5 K [50, 51]. Eu has a large magnetic moment per ion, that is, around 6.9 μ_B/ion. Moreover, EuS is one of the known pure Heisenberg ferromagnets with large exchange coupling constants, that is, $J_1 \approx 0.221$ k_b K and $J_2 \approx$ - 0.100 k_b K [52, 53]. Here, k_b is the Boltzmann constant [54]. EuS was preferred over EuO (T$_C \sim 69$ K) because it is easier to handle for evaporation and stable in air compared to EuO [55].

Table 2.1 lists some of the properties of the materials. The lattice mismatch between the crystal structure of the EuS ($a \approx 5.969$ Å) and InAs ($a \approx 6.048$ Å) crystal structure

Table 2.1: Properties of the materials. The data is taken from refs. [47, 48, 56, 57]

Parameter	**Pb**	**InAs**	**EuS**
Crystal lattice (type)	Cubic (FCC)	Cubic (FCC)	Cubic (FCC)
Cell parameter (Å)	4.950	6.048	5.969
Scattering lengths (fm)	9.405	10.65 - 0.05j	10.04 - 1.26j
Number density (Å^{-3})	0.033	0.018	0.019
Mass density (g cm^{-3})	11.35	5.67	5.75
Molar mass (g mol^{-1})	207.19	189.74	184.02

is only $\sim$ 1 %, and for EuS/Pb (or InAs/Pb) it is around 20 %. These materials are toxic and harmful if inhaled, and can cause skin/eye irritation, therefore, require careful handling. The stringent requirements make the choice of materials very limited, and this particular material combination is one of the sets of materials that is being studied to build the topological quantum computation platform. In addition, atomic-level precision is required during the fabrication process for the optimization and reproducibility of the target device structure.

Table 2.2 lists the properties and stability of some of the compounds of europium with oxygen and sulfur.

Table 2.2: Europium compounds with sulfur and oxygen.

Compound	**Eu valency**	**Magnetic state**	**T$_C$**	**Stability in air**	**NSLD**
			(K)		**($\times 10^{-6}$ Å^{-2})**
EuS	+2	ferromagnetic	16.5 [50]	metastable	1.89
EuO	+2	ferromagnetic	69.2 [58]	metastable	3.82
Eu_2S_3	+3	paramagnetic	-	stable	2.22
Eu_2O_3	+3	paramagnetic	-	stable	3.99
Eu_2O_2S	+3	paramagnetic	-	stable	2.50
$Eu_2(SO_4)_3$	+3	paramagnetic	-	stable	4.04
Eu_3S_4	(+2, +3)	paramagnetic	-	least stable	2.13

2.2 Sample growth techniques

The aim was to grow epitaxial layers of Pb, EuS, InAs, and the capping layer (Al_2O_3) by using electron beam deposition and molecular beam epitaxy (MBE).

2.2.1 Moleculer beam epitaxy (MBE)

Molecular beam epitaxy (MBE) is a widely used technique to fabricate uniform and superior quality epitaxial layers, offering consistent control over the thickness and composition of the film. In MBE, the target material within the crucible is heated to the point of evaporation. The crucibles are covered with computer-controlled shutters to select the target and control the thicknesses of the layers to atomic precision. The evaporated molecules are then deposited on the substrate that is placed at a calibrated distance from the target. The word beam in the technique's name indicates that the evaporated atoms or molecules travel without interacting with each other or with any gases within the vacuum chamber until they reach the surface of the substrate.

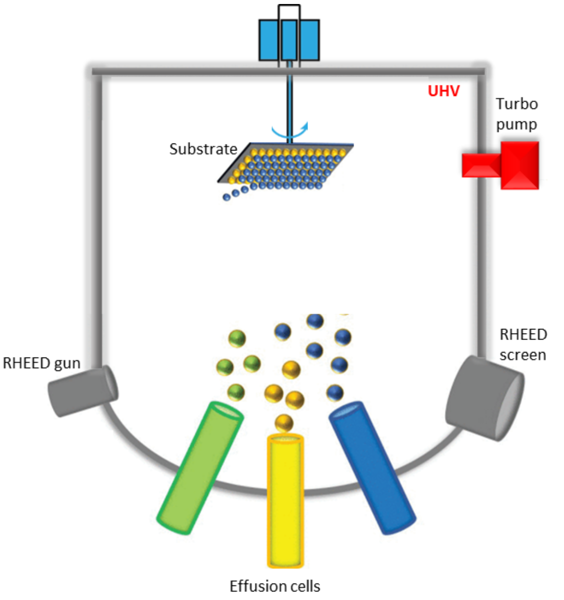

Figure 2.1: The image showing the typical MBE instrument set up. This image is adapted from the image in this reference article [59]

A heater is connected to the substrate to maintain an optimum temperature. There is a possibility to rotate the substrate or keep it at an angle during deposition to ensure the uniform deposition. An in situ reflection high-energy electron diffraction (RHEED) gun is used to keep track of the growth rate and to check the quality of the thin films. A turbo pump is attached to the deposition chamber to maintain the required ultra-high vacuum conditions [Figure 2.1].

Upon contact with the substrate surface, a molecule can undergo physisorption, chemisorption, or lateral movement. Physisorption involves weak physical interactions with the substrate such as van der Waals forces, while chemisorption involves electron exchange and chemical bonding with the surface. For the formation of thin crystallographically oriented layers, a molecule must reach epitaxial sites and form chemical bonds [60].

There are several parameters that can be adjusted to control and optimize the growth of thin films in the MBE method. These parameters include the flux rate, distance between the source and the substrate, substrate temperature, and growth time. Generally, a higher substrate temperature provides more thermal energy for the arriving molecules to adjust and move on the surface, resulting in ordered materials, but it can promote diffusion in multilayer systems. More abrupt and often higher quality interfaces are generated by having a lower substrate temperature. In contrast, there are chances of creating point defects in thin layers because of reduced mobility of molecules on the surface. Therefore, all parameters need to be optimized for each material. A solid source Varian GEN-II MBE was used for the growth of a 500 Å thick InAs buffer layer. Before InAs growth, the substrate was baked at approximately 800 K for two hours in an arsenic atmosphere to remove the oxidized layers from the top. The InAs was then deposited at a substrate temperature of 775 K using separate sources of indium and arsenide. For deposition of the rest of the layers, the sample is moved carefully without breaking the vacuum conditions to the electron beam deposition chamber.

2.2.2 Electron beam deposition (EBD)

Electron beam deposition is a type of physical vapor deposition (PVD) that utilizes an energetic electron beam to evaporate the material from the target anode. This method is used for the deposition of high-purity multicomponent films, facilitated by the precise control of the electron beam by applying a magnetic field [61]. This technique offers a higher material utilization efficiency in comparison to other deposition methods. The focused and high-energy electron beam has the capability of evaporating materials with high melting points that cannot be evaporated by conventional deposition techniques. In addition, the use of confined electron beam helps in reducing the contamination from the crucible as it only heats the target material. The deposition occurs at ultra-high vacuum conditions to avoid interaction of the electron beam and evaporated material with impurities. The tungsten filament, an electron source, is kept out of line-of-sight to avoid melting due to the evaporated material [Figure 2.2]. A disadvantage of EBD is the deterioration of the filament in the electron gun, leading to non-uniform evaporation rates of the target material [62].

The process involves scanning the electron beam on the surface of the target to facilitate a uniform distribution of heat. The static magnetic field is used to control and direct the beam onto the target. The kinetic energy of the electrons is transferred as thermal energy to the target material increasing the surface temperature to help it evaporate and deposited as a thin layer on the substrate. The substrate is maintained at a predetermined temperature according to the material being deposited. The thermal energy resulting from the substrate temperature helps molecules move and settle on the surface of the substrate. Thus, it facilitates the formation of thin crystalline layers on the substrate.

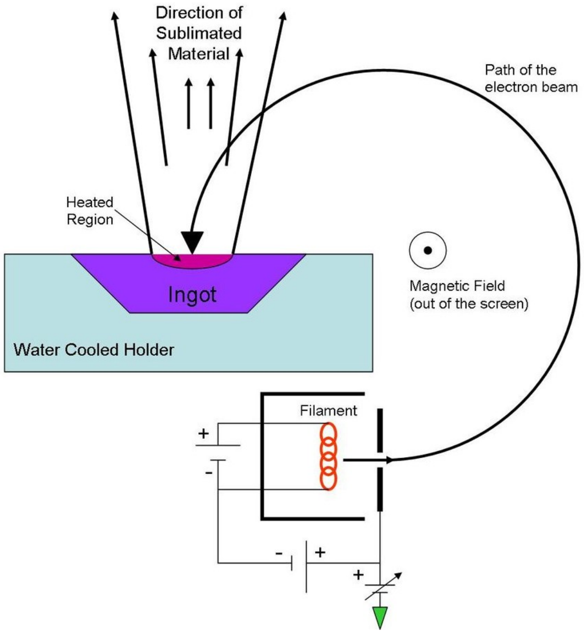

Figure 2.2: Schematic of the experimental set-up for the electron beam evaporation technique. This image is taken from ref. [63].

The thickness of the layer can be monitored using an in-site quartz crystal monitor. To deposit multiple layers, it is possible to switch among different targets and apply uniquely optimized deposition settings for each specific material. The deposition rate depends on the power of the electron beam and the target material. The deposition rate ranges from a fraction of an angstrom to a few millimeters per second [64].

Thin films of EuS and Pb were deposited using the electron beam deposition method at substrate temperatures of approximately 450 K and 428 K, respectively. The substrate was placed at a 45° angle to the normal to promote uniform layer growth. The deposition rate for Pb and EuS was 2.4 Å/s and 0.1 Å/s, respectively. To protect the surface from oxidation, an amorphous capping layer of aluminum oxide (Al_2O_3) with thicknesses of approximately 20 to 60 Å was deposited on each sample. The sample growth was carried out in the dedicated facility available at the Niels Bohr Institute (NBI) of the University of Copenhagen [Figure 2.3]. The MBE and e-beam deposition chambers are connected and remain under the same ultra-high vacuum conditions. The sample was moved from one chamber to the other without breaking the vacuum conditions in the chambers. The deposition was performed on 2 inch InAs (111 B) wafers. Figure [2.4] shows the pictures of the sample during growth.

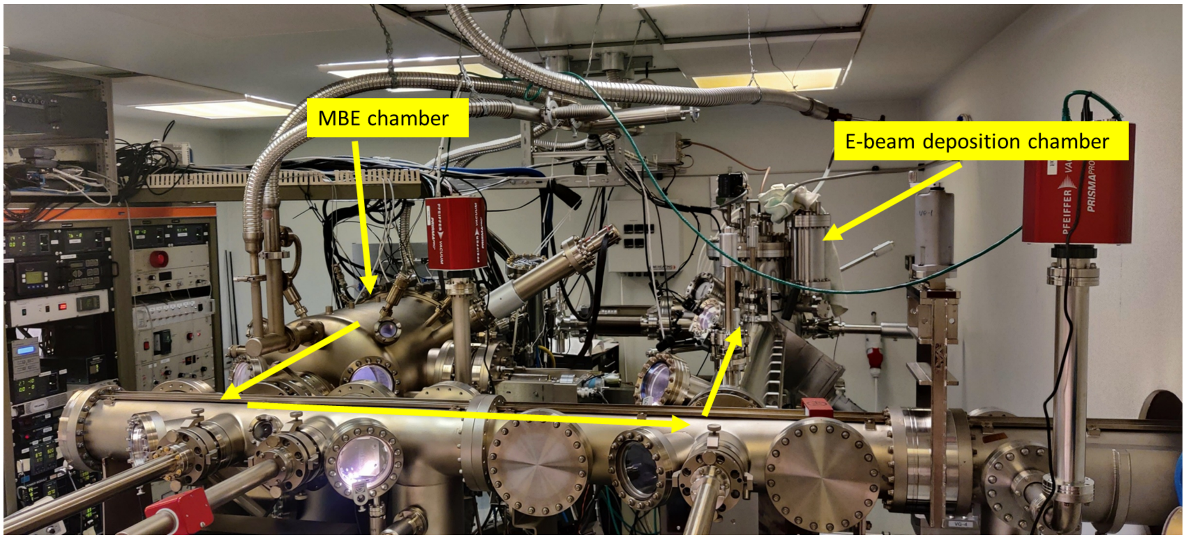

Figure 2.3: Sample deposition facility present at NBI.

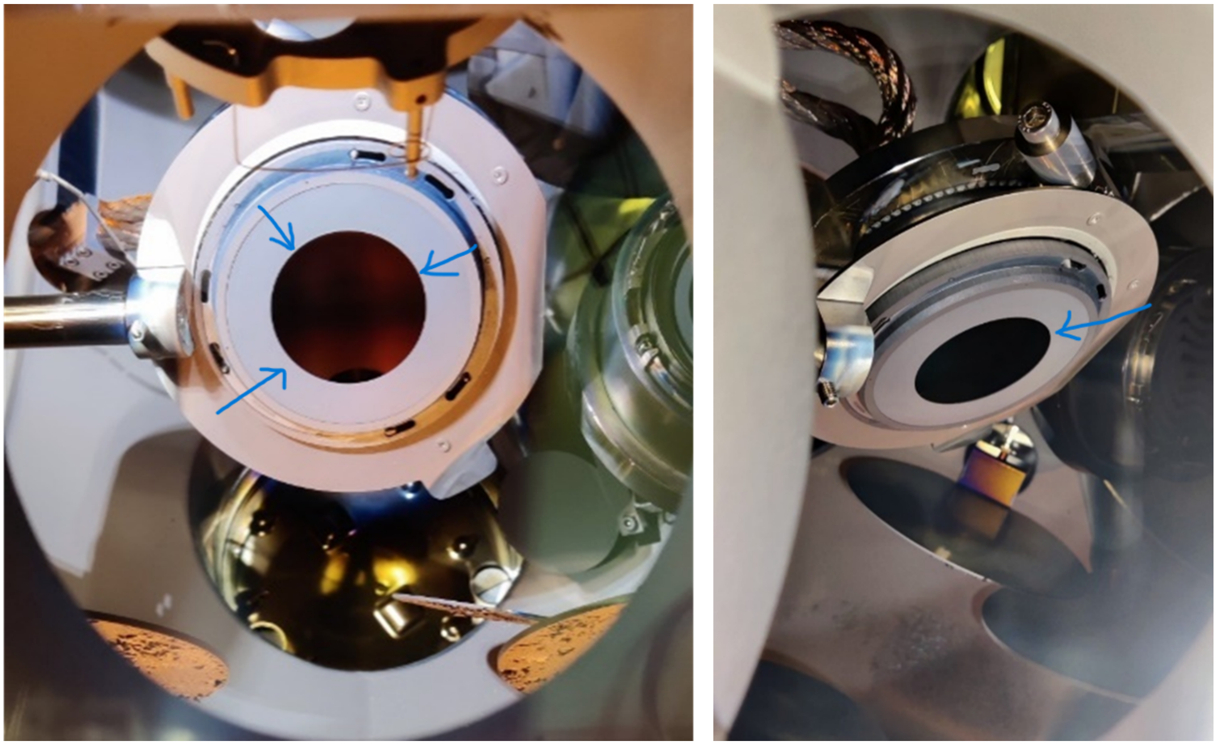

Figure 2.4: Samples inside the electron beam deposition chamber during the fabrication.

Table 2.3: A list of the samples and their fabrication dates.

Sample	**Date**
QD1	22/07/2021
QD2	21/06/2021
QD3	21/05/2022
QD4	23/03/2022
QD5	31/08/2023
QEu1	11/08/2023
QEu2	09/11/2023
QEu3	28/11/2023
QEu4	29/11/2023

Chapter 3

Experimental techniques

This chapter provides an overview of the characterization techniques employed in the thesis. It begins with an introduction to the basic properties of neutrons, their interaction with matter and proceeds to derive the expression for the reflectivity of neutrons from the surface and interfaces in multilayer samples. The subsequent sections briefly describe the theory behind the working of complementary techniques and how these techniques were employed to acquire information.

3.1 Neutron reflectometry (NR)

Neutron possesses a magnetic moment and undergoes dipole-dipole interactions with the magnetic moments of the atoms in the sample. Consequently, neutrons can provide insight into the magnetic properties of samples [65]. These capabilities make neutrons a versatile tool for investigating atomic and magnetic structures, together with the dynamics of materials, in the field of hard condensed matter physics [66]. Neutrons have no electrical charge; thus, they can penetrate deeper into the samples. Neutrons engage in nuclear and magnetic interactions with the sample. Nuclear interactions occur between the nucleus of an atom and the neutron because of strong nuclear forces, which are short-ranged in nature. This makes neutrons sensitive to atomic positions and dynamics. Table 3.1 lists some of the basic properties of the neutron, with μ_B and h ($\hbar = h/2\pi$) being the Bohr magneton and Planck's constant, respectively.

In neutron scattering experiments, a beam of neutrons interacts with a sample, providing detailed information about its internal structure. A specialized form of neutron scattering is neutron reflectometry, which is used to study surfaces and interfaces at the nanoscale [69]. There is no exchange of energy between the incident wave and the sample, and reflectometry falls under the elastic scattering regime.

Table 3.1: Basic properties of the neutron. The information is taken from this ref. [67]

Parameter	**Value**
Mass (kg)	1.67×10^{-27}
Spin	$-\hbar/2$
Magnetic moment (μ_B)	-0.001 [68]
Mean lifetime (s)	885.9 ± 0.9

The term reflectivity (R) is described as the ratio between the reflected intensity and the incident intensity of the neutron beam. R is just a number and does not have a unit. By directing a collimated neutron beam at a sample surface and measuring the intensity of the reflected neutrons as a function of incident angle or neutron wavelength, information about the sample depth profile, including layer thicknesses, densities, and interfacial roughness, is obtained.

Similarly to other subatomic particles, neutrons also have a dual nature. The wave-particle duality concept was first introduced by Louis de Broglie [70] and later confirmed by several experiments. Broglie presented a relation between the momentum (p) and wavelength (λ) of the matter wave associated with the particle of mass "m_n", moving with a velocity "v".

$$|\vec{p}| = m_n \cdot v = \frac{h}{\lambda} = \hbar \cdot |\vec{k}| \tag{3.1}$$

where h is the Planck constant with value $6.626\text{x}\times10^{-34}$ Js, and wave vector $|\vec{k}|=\frac{2\pi}{\lambda}$. Thus, in its most fundamental representation, a neutron can be modeled as a plane wave characterized by the wavevector $\vec{k}$. A more accurate depiction of a neutron will be a wave packet formed by a coherent superposition of multiple plane waves, with a range of distinct wave vectors. However, for the problem at hand, a single-plane wave representation of neutrons is significantly accurate [71]. The Schrödinger equation that describes the dynamics of neutrons is similar to the wave equation for light and results in neutrons that exhibit characteristic optical behaviors such as total reflection and refraction [72]. In the present thesis, the focus is on elastic scattering measurements in which a neutron does not lose or gain energy when interacting with the sample. Consequently, the neutron wave function and the time-independent Schrödinger equation of motion do not show an explicit time dependence [71], expressed as follows

$$\frac{\hbar^2}{2m_n} \cdot \Delta^2\psi(\vec{k},\vec{r}) + V_N(\vec{r}) \cdot \psi(\vec{k},\vec{r}) = E_{med} \cdot \psi(\vec{k},\vec{r}) \tag{3.2}$$

Here, $\psi(\vec{k},\vec{r})$ is the time-independent wave function for a neutron wave, $V_N(\vec{r})$ is a potential step presented by the medium at the interface, and E_{med} is the total energy of the neutron in the medium. The time independent wave function $\psi(\vec{k},\vec{r})$ for a neutron wave in three dimensions can be represented as follows:

$$\psi(\vec{k},\vec{r}) = \psi_o \cdot e^{i(\vec{k}\cdot\vec{r})} \tag{3.3}$$

Here, ψ_o is the amplitude of the wavefunction. The probability of finding the neutron at a given time and specific spatial position is expressed by the square of the modulus of the wavefunction, denoted ψ_o^2. The neutrons used in the condensed matter studies are non-relativistic in nature and the potential energy term $V_N(\vec{r})$=0 for vacuum. Thus, a neutron in vacuum with wavevector $\vec{k_i}$ has a total energy (E_{vac}) equal to their kinetic energy.

$$E_{vac} = \frac{\hbar^2|\vec{k_i}|^2}{2m_n} \tag{3.4}$$

Here, k_i is the wave vector in vacuum and m_n is the mass of a neutron. When a neutron passes through a medium, it experiences a potential step, $V_N(\vec{r})$, which represents the cumulative impact of interactions between the neutron and the medium's scatterers.

$$V_N(\vec{r}) = \frac{2\pi\hbar^2\rho_n}{m_n} \tag{3.5}$$

Here, ρ_n is the scattering length density (SLD) of the material for neutrons (NSLD). SLD (ρ_n) is a product of the number density (N) and the scattering length (b) of the material.

$$\rho_n = N \cdot b \tag{3.6}$$

Here, the number density (N) is the number of scattering units per unit volume. Scattering length (b) is the unique property of the nucleus that describes the strength of the interaction [67]. Moreover, b is a complex quantity, $b = b_o + b' - ib''$, where b_o is the bound coherent scattering length, b' is the bound incoherent scattering length, and the imaginary part (b'') accounts for the absorption of neutrons. b_o is responsible for the interference effects which depends on the position of the scatterers, while b' results in random scattering which is uniform in all directions leading to diffuse background intensity and finally, b'' accounts for the absorption of neutrons by materials. However, for the materials under investigation in this thesis, b' is negligible and therefore $b \simeq b_o - ib''$.

The total energy of neutron is conserved during the interactions. As a neutron wave penetrates a medium, its kinetic energy is altered. The total neutron energy in the medium E_{med}, with modified wavevector $\vec{k_m}$, given by

$$E_{med} = \frac{\hbar^2|\vec{k_m}|^2}{2m_n} + \frac{2\pi\hbar^2\rho_n}{m_n} \tag{3.7}$$

Equating the relations for the initial (equation 3.4) and final energy (equation 3.7) of the neutron, a relation is obtained between the wave vector within the medium ($\vec{k}_m$) and the vacuum ($\vec{k}_i$), expressed in equation 3.8. The magnitude of the final wavevector $\vec{k_m}$ depends on the magnitude of $\vec{k}_i$ and SLD of the medium.

$$|\vec{k_m}|^2 = |\vec{k_i}|^2 - 4\pi\rho_n \tag{3.8}$$

For the ideal case, it is assumed that $\rho_n = \rho_n(z)$ depends solely on z and remains constant laterally, meaning $\delta\rho/\delta x$ and $\delta\rho/\delta y$ are zero. The layers are perfectly smooth and homogeneous with infinite lateral extent. Consequently, the wave vectors in the x and y directions are conserved. Thus, in a layer with uniform in-plane density, reflection is specular, with neutrons reflecting at the same angle as the incident angle relative to the surface. This means wavevector changes only perpendicular to the sample surface. Hence, the neutron wave equation simplifies to one dimension, z. The one dimensional neutron wave function $\psi(k_z, z)$ and the time-independent Schrödinger equation are then given by

$$\left(\frac{\hbar^2}{2m_n} \cdot \frac{\delta^2}{\delta z^2} + V_N(z)\right) \cdot \psi(k_z, z) = E_{med} \cdot \psi(k_z, z) \tag{3.9}$$

A refractive index (η) of a medium for neutrons is defined which depends on the number of scatterers in the medium and the degree to which they scatter. η is a ratio of the magnitude of the component of wave vector in the medium (equation 3.8) and the wave vector in the vacuum along z direction ($\vec{k}_{iz}$), analogous to wave optics. Using the magnitude of $k_{iz}=\frac{2\pi}{\lambda}$, η is expressed as

$$\eta = \frac{k_{mz}}{k_{iz}} = \frac{\sqrt{{k_{iz}}^2 - 4\pi\rho_n}}{k_{iz}} = \sqrt{1 - \frac{4\pi{\rho_n}^2}{k_{iz}}} = \sqrt{1 - \frac{\lambda^2}{\pi}N \cdot b} \approx \left(1 - \frac{\lambda^2}{2\pi}N \cdot b\right) \tag{3.10}$$

The second term is very small in the square root, thus, the Taylor expansion is used and the higher-order terms are neglected as the product $(N \cdot b)^S$ is very small compared to '1' for $S > 1$.

Figure 3.1 shows an example of a sample with one layer on a substrate. The incident and reflected neutron waves are depicted in the image. The refractive indices for

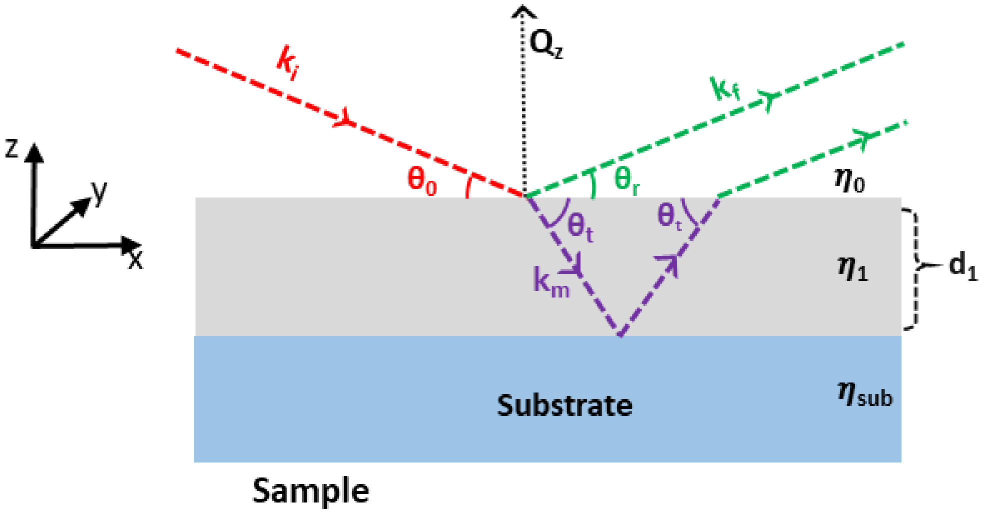

Figure 3.1: An incident neutron wave at an angle of θ_o with the sample surface is shown. Incident, reflected, and transmitted waves are marked on the image along with momentum transfer Q_z in the normal direction.

the media are η_o, η_1, and η_{sub}. The incident wave vector and the wave vector in the medium are represented by $\vec{k_i}$ and $\vec{k_m}$, respectively. The constructive and destructive interference of the reflected waves from the surface and the interface forms an interference fringe pattern on the detector, called a Kiessig fringe pattern [73]. Similar to wave optics, Snell-Descartes law applies to neutron waves as it ensures the phase continuity and momentum at boundaries of two media, The relationship between the refractive indices, angles of incidence (θ_o) and refraction (θ_t) for a neutron wave passing through a boundary between two different media (Figure 3.1) can be described by the Snell-Descartes law. Here, the angles are defined with respect to the sample surface, Figure 3.1.

$$\eta_o \cdot \cos(\theta_o) = \eta_1 \cdot \cos(\theta_t) \tag{3.11}$$

A critical angle (θ_c) is defined as the angle below which the neutrons incident on the surface are completely reflected externally ($\theta_t = 0$). The critical angle can be calculated for the boundary between the two mediums given in Figure 3.1 as follows.

$$\eta_o \cdot \cos(\theta_c) = \eta_1 \tag{3.12}$$

Using the small angle approximation, $cos(\theta_c)$ can be expanded in terms of θ_c (neglecting the higher order terms).

$$\cos(\theta_c) \approx 1 - \frac{\theta_c^2}{2} = \frac{\eta_1}{\eta_o} \tag{3.13}$$

After re-arranging the terms, we get a relationship between the critical angle and the refractive indices of the media concerned.

$$\frac{\theta_c^2}{2} = 1 - \frac{\eta_1}{\eta_o} \tag{3.14}$$

η_o=1 (for vacuum) and using equation 3.10, the critical angle in terms of scattering length comes out to be

$$\theta_c \approx \sqrt{\frac{\lambda^2}{\pi} N \cdot b} \tag{3.15}$$

The vector $\vec{Q_z}$ that accounts for the momentum transferred in the direction normal to the surface of the sample is calculated by measuring the change in initial wave vector, $\vec{k_i}$. Since $|\vec{k_r}| = |\vec{k_i}| = \frac{2\pi}{\lambda}$, expression for momentum transfer is given by

$$|\vec{Q_z}| = |\vec{k_r} - \vec{k_i}| = 2k_i \cdot \sin(\theta_0) = 4\pi \cdot \frac{sin(\theta_0)}{\lambda} \tag{3.16}$$

Using equation 3.15 and small angle approximation for $\sin\theta$, we can calculate the magnitude of the critical momentum transfer vector $\vec{Q_c}$ as follows

$$|\vec{Q_c}| = 4\pi \cdot \frac{\sin(\theta_c)}{\lambda} \approx 4\pi \cdot \frac{\theta_c}{\lambda} = \sqrt{16\pi N \cdot b} \tag{3.17}$$

Above the critical angle, one always observes that a fraction of the wave is transmitted into the medium. The Fresnel reflectance coefficient (r), similar to wave optics, for the neutron wave at the interface between vacuum and the layer can be calculated [74]. Expression for r, equation 3.18, is obtained by solving the Schrödinger equation and applying the boundary conditions to ensure the continuity of both the wave function and its derivative across the interface. Continuity of the wave function prevents sudden variations in neutron probability density across the boundary. Moreover, the continuity of the wavefunction's first derivative guarantees the continuity of the quantum mechanical probability current, describing neutron flow across the boundary between two media.

$$r = \frac{k_{iz} - k_{mz}}{k_{iz} + k_{mz}} \tag{3.18}$$

In reflectometry experiments, the intensity of the reflected neutron waves gets measured but not their phases. Intensity is the product of the amplitude of the quantum mechanical probability (r) and its complex conjugate (r^*). The reflectivity (R) for the interface, shown in Figure 3.1, is then defined as

$$R = \frac{I_{reflected}}{I_{incident}} = r \cdot r^* = \left(\frac{k_{iz} - k_{mz}}{k_{iz} + k_{mz}}\right)^2 \tag{3.19}$$

In practice, the boundary between two layers is never perfect, leading to a gradual change in the SLD rather than a sharp transition between the materials. The interface between two layers has a roughness, interdiffusion of atoms or both from one layer to the other. However, with specular reflectivity measurements, these differences cannot be distinguished because the lateral average of the scatterer density in the sample remains the same, resulting in identical effects on the reflectivity profile [75]. These non-perfect interfaces are modeled as a roughness profile using an error function transition from one layer to the other, the approach developed by Nevot Croce [76]. The error function enables a smooth transition of SLD between layers, similar to the gradual changes seen in physical roughness. To accommodate this, the coefficient (r) for the neutron wave at the interface between the layer and substrate is modified as

$$r = \frac{k_{iz} - k_{mz}}{k_{iz} + k_{mz}} \cdot \exp\left(-2k_{iz}k_{mz}\sigma^2\right) \tag{3.20}$$

Here, σ is the root mean square (RMS) roughness of the interface between the layer and substrate.

For a multilayer sample, like the one shown in Figure 3.2, the Fresnel coefficient (r) can also be calculated by modifying the expression in equation 3.19. In order to calculate $r_{m,m+1}$ for the interface between layer m and $m+1$, an amplitude factor that takes into account the path length of the neutron wave inside layer m must be included in the equation. For an in-depth explanation of the reflectivity calculations for both single- and multilayer samples using Parrat's formalism, the readers should consult these references [77, 71]. Here is the modified expression for the reflectance coefficient ($r_{m,m+1}$) and reflectivity ($R_{m,m+1}$) for an interface between the layer m and $(m+1)$ in the multilayer sample.

$$r_{m,m+1} = \frac{k_{mz} - k_{(m+1)z}}{k_{mz} + k_{(m+1)z}} \cdot \exp\left(-2k_{mz}k_{(m+1)z}\sigma^2_{m,m+1}\right) \tag{3.21}$$

$$R_{m,m+1} = r_{m,m+1} \cdot r^*_{m,m+1} \tag{3.22}$$

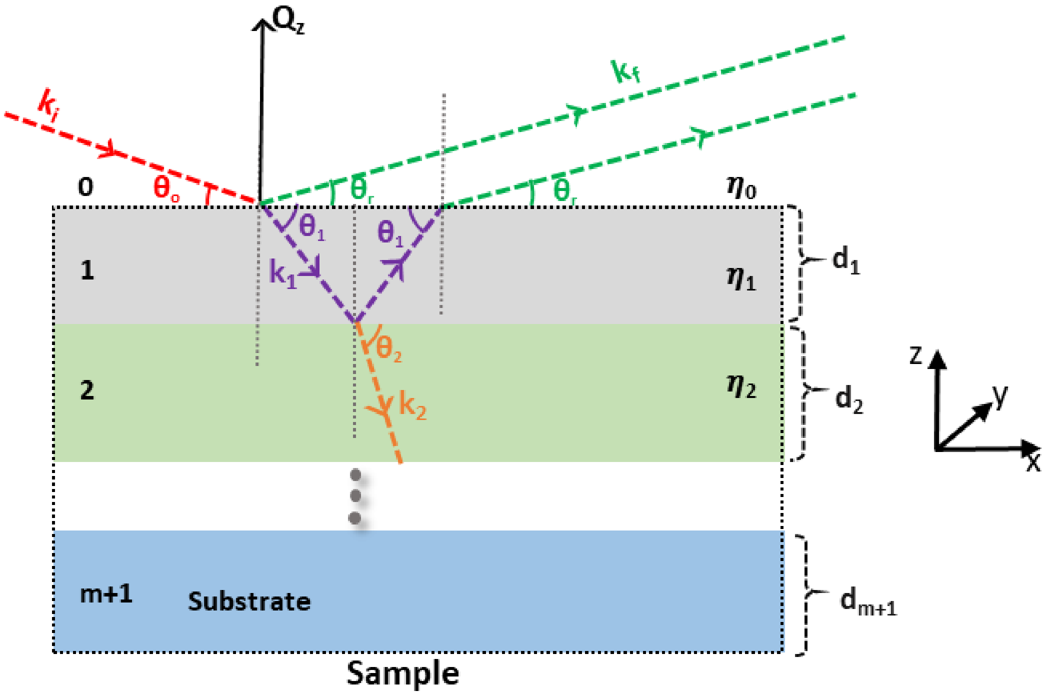

Figure 3.2: Interaction of waves at the surface and interfaces inside the multilayer sample with layers named from 0 to $m + 1$. The reflected and transmitted waves for two of the interfaces are marked on the diagram. The layers are marked with their refractive indices (η) and thicknesses (d_m).

However, the Nevot-Croce approach to simulate roughness at the interface between two layers is not flawless and may occasionally fail. Sometimes, it can produce nonphysical features in the SLD profile of the sample. For example, if the interfacial roughness exceeds half the thickness of the layer, consecutive error functions overlap, resulting in an unrealistic SLD profile. Therefore, to tackle such situations, the layers are treated as a combination of thin sliced layers (such as 1 Å thick), with constant SLD, without any interfacial roughness between them.

For the case of microslicing, it becomes computationally challenging to calculate the reflectivity of individual thin sliced layers using Parrat's formalism. Therefore, the transfer matrix method, similar to optics, is preferred to tackle these kinds of equation [78, 79]. This method is a matrix-based computational approach to solve problems related to the propagation of waves and their scattering. This matrix method is applied to calculate the reflectivity from the thin sliced layers, without the interfacial roughness between them. The reflection and transmission of a neutron wave, as it passes through layers in a multilayer sample, can be represented as a matrix multiplication for each individual layer. A matrix G_m is calculated individually for each layer using the Fresnel coefficients from equation 3.20, such as the one shown below for the layer m

$$G_m = \begin{pmatrix} \exp(ik_{mz}d_m) & r_{m,m+1}\exp(ik_{mz}d_m) \\ r_{m,m+1}\exp(-ik_{mz}d_m) & \exp(-ik_{mz}d_m) \end{pmatrix} \tag{3.23}$$

where k_{mz} $(= \sqrt{(k_{(m-1)z})^2 - 4\pi(\rho_{n,m} - \rho_{n,(m-1)})}$) is the wave vector of the neutron beam in the layer m, d_m is the thickness of the layer m and i is the imaginary number ($i^2 = -1$). These characteristic matrices for the individual layers are then multiplied to obtain a final 2×2 matrix:

$$G^* = G_0 \cdot G_1 \cdot G_2 \cdot \ldots \cdot G_m = \begin{pmatrix} G^*_{11} & G^*_{12} \\ G^*_{21} & G^*_{22} \end{pmatrix} \tag{3.24}$$

By multiplying the matrices for each layer and interface, the matrix method accounts for the complex interactions of neutron waves with the multilayer structure, allowing for the calculation of the reflectivity profile. The neutron reflectivity (R) is then calculated using the total transfer matrix (G^*) for the multilayer system, given by

$$R = \left| \frac{G^*_{21}}{G^*_{11}} \right|^2 \tag{3.25}$$

3.1.1 Polarized neutron reflectometry (PNR)

Neutrons are polarized using a supermirror that selectively reflects one spin state, while transmitting or absorbing the other. A uniform guiding magnetic field is then applied to maintain polarization as they travel toward the sample. With the sample environment in place at the sample position, an external in-plane magnetic field is applied to align the moments within the sample, creating a well-defined magnetization vector $\vec{\mathrm{M}}$. The spin states of neutrons are defined relative to this magnetization. Specifically, the spin-up state corresponds to the spin of the neutron being parallel to $\vec{\mathrm{M}}$ and the spin-down state corresponds to the spin of the neutron being antiparallel to $\vec{\mathrm{M}}$.

For magnetic samples, neutrons interact with atomic nuclei and unpaired electrons (source of magnetism). Thus, there is an extra term in the expression for the potential, which takes into account the dipole-dipole interaction of the neutron with the magnetic sample. The magnetic field induction comprises two parts: the externally applied magnetic field ($\mu_o\vec{\mathrm{H}}$) and the magnetization vector $\vec{\mathrm{M}}$ of the layer. The corresponding magnetic potential (V_M) for the interaction between neutron and the magnetic induction is given by

$$V_M = -\vec{\mu} \cdot (\mu_o \vec{\mathrm{H}} + \mu_o \vec{\mathrm{M}}) \tag{3.26}$$

Here, $\vec{\mu}$ is the magnetic moment of neutron. $\mu_o \vec{\mathrm{H}}$ is homogeneous inside and outside the sample, therefore, does not contribute to the magnetic contrast. However, in case of superconductors exhibiting Meissner state, field expulsion due to $\vec{\mathrm{H}}$ can lead to a magnetic contrast and therefore, it should be included for those cases. For the general case,

$$V_M = -\vec{\mu} \cdot (\mu_o \vec{\mathrm{H}} + \mu_o \vec{\mathrm{M}}) = -|\vec{\mu}|(\mu_o \mathrm{H}) - |\vec{\mu}|(\mu_o \mathrm{M}_\perp) = \frac{2\pi\hbar^2}{m_n} N \cdot b_m \tag{3.27}$$

Here, $\mathrm{M}_\perp$ is the component of magnetization perpendicular to vector $\vec{Q_z}$ and b_m is the magnetic scattering length. b_m is analogous to neutron scattering length but accounts for the magnetic contributions and its magnitude is proportional to the net magnetic moment per ion of the magnetic layer. Magnetic scattering length density (MSLD, ρ_M) is defined as a product of N and b_m.

$$\rho_M = N \cdot b_m \tag{3.28}$$

$$N \cdot b_m = 2.316 \times 10^{-6} \text{Å}^{-2}\mathrm{T}^{-1} \times \mu_o \ \mathrm{H[T]} + 2.911 \times 10^{-12} \text{Å}^{-2}\mathrm{mA}^{-1} \times \mathrm{M}_\perp[\mathrm{Am}^{-1}] \tag{3.29}$$

The magnitude of neutrons spin magnetic moment is taken from Table 3.1. The potential ($V_\pm$) of a magnetic layer for two spin states (spin up and spin down) of neutron is then given by

$$V_\pm = V_N \pm V_M = \frac{2\pi\hbar^2}{m_n} N \cdot (b \pm b_m) \tag{3.30}$$

As a consequence, the refractive index of the magnetic layer for neutrons has an extra term that accounts for magnetism. The refractive index and the wave vector in medium ($k_{mz}^\pm$) is modified as

$$\eta^\pm = \sqrt{1 - \frac{\lambda^2}{\pi} N \cdot (b \pm b_m)} \tag{3.31}$$

$$k_{mz}^\pm = k_{iz} \cdot \eta^\pm \tag{3.32}$$

Consequently, magnetism within the layer influences the critical momentum transfer for total external reflection across both neutron polarization states.The modified critical momentum transfer in the direction normal to the surface is given by

$$Q_c^\pm = \sqrt{16\pi N \cdot (b \pm b_m)}. \tag{3.33}$$

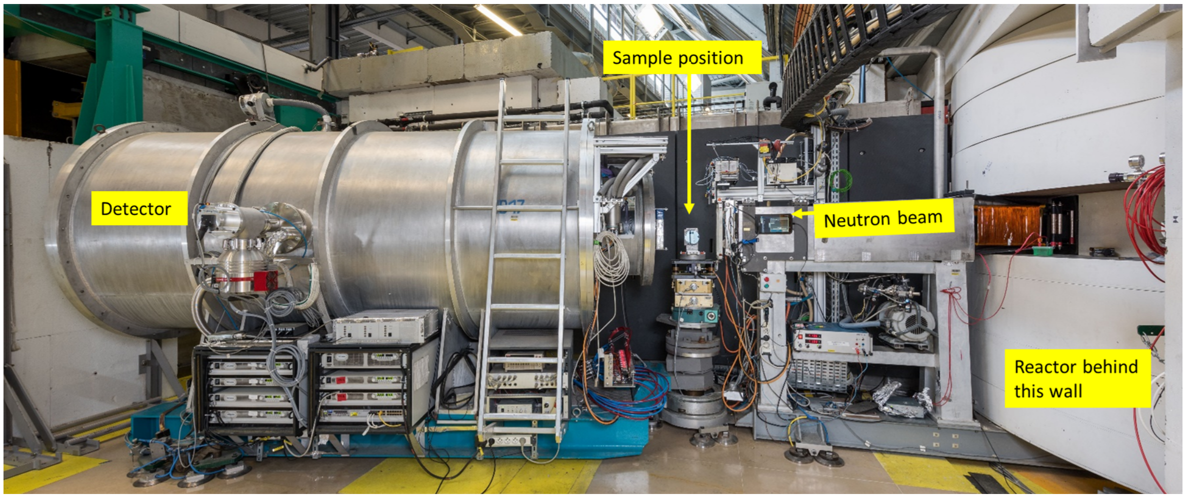

Figure 3.3: An image of the experimental setup of a polarized neutron reflectometer (D17 instrument) available at ILL [80], France.

Similarly, the Fresnel coefficients gets modified, and then, the final matrices for each layer gets modified.

$$r^{\pm} = \frac{k_{iz} - k_{mz}^{\pm}}{k_{iz} + k_{mz}^{\pm}} \cdot \exp\left(-2k_{iz}k_{mz}^{\pm}\sigma_m^2\right) \tag{3.34}$$

Spin-flip scattering occurs when the in-plane magnetization of the sample is not collinear with the neutron spin state. In this case, the spin state of the neutron is flipped after interaction with the sample. However, this is not the case for the present thesis; therefore, the discussion is limited to non-spin flip scattering where the spin state remains before and after the interaction with the sample. PNR measures the intensity of the polarized neutrons reflected from the sample as a function of the neutron spin state and the transfer of momentum normal to the surface.

The specular PNR measurement can be recorded in two ways, (i) by varying the angle of incidence while keeping the wavelength constant (monochromatic mode) and (ii) by using a range of wavelengths at a fixed angle (time of flight mode). For time of flight mode, the measurements are usually performed at more than one fixed angle to cover the wider q-range for the data that contain useful features.

PNR measurements were performed on the D17 instrument in ILL and on the POLREF instrument in ISIS. Data were recorded in time-of-flight mode. The measurements were recorded at three fixed angles. Figure 3.4 shows the samples attached to the sample holder, featuring four positions to swap samples within the cryostat without removal at D17 instrument. Due to depth sensitivity, PNR effectively differentiates the magnetic signal from the ferromagnetic layer and induced magnetization in adjacent non-magnetic layers, making it suitable for this study.

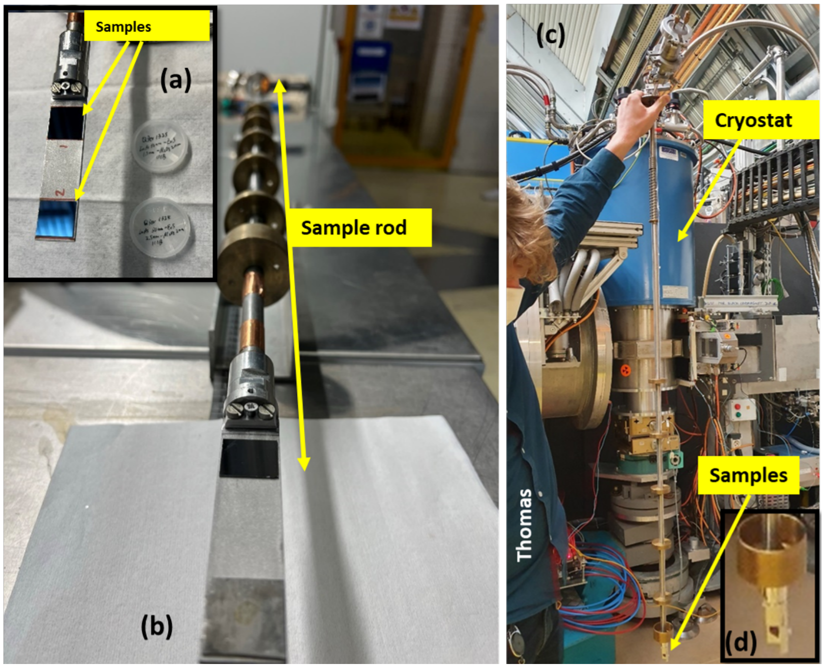

Figure 3.4: (a) Two 20 mm x 20 mm samples pasted to the sample holder with four sample holding capacity. (b) A cryostat sample rod with a 20 mm x 20 mm sample attached to it (c) An image showing the size of the sample rod with cryostat at the sample position in the background. (d) A zoomed image showing the sample attached at end of the rod.

3.2 Complementary techniques

Analyzing neutron and X-Ray reflectivity data is challenging, as discussed in previous sections. To approximate a unique physical solution, the boundaries for the parameters must be constrained with the help of the information obtained from other complementary techniques. This section summarizes how complementary techniques were used in the present thesis to estimate the boundary values of the parameters that help with the fitting of the PNR data.

3.2.1 X-Ray reflectometry

X-ray reflectometry provides a different contrast between materials due to the differences in the interaction of neutrons and X-rays with matter. It acts as a complementary technique to polarized neutron reflectometry, also providing structural information with depth. Moreover, X-ray scattering theory is analogous to neutron scattering theory, with the difference that X-rays interact with the electron cloud of atoms [81]. The interaction of X-rays with the electron cloud is significant and leads to their lower penetration depths inside the samples. Similarly to neutrons, a general form of the refractive index (η_X) of the layers for X-rays can be written as

$$\eta_x = \sqrt{1 - \frac{\lambda^2}{\pi}\rho_x} = \sqrt{1 - \frac{\lambda^2}{\pi}N \cdot r_e f} \approx \left(1 - \frac{\lambda^2}{2\pi}N \cdot r_e f)\right) \tag{3.35}$$

$$\rho_x = N \cdot r_e f \tag{3.36}$$

where, ρ_x is the SLD for X-rays (XSLD), r_e is the classical electron radius with value 2.818×10^{-5} Å, N is the number density, and f is the scattering length for X-rays. Similarly to b, f is also a complex quantity, $f = f_o + f' - if''$. f_o represents the atomic scattering coefficient for X-ray scattering, while $f^{'}$ is the dispersion correction to f_o, considering X-ray interactions near an absorption edge with bound electrons. f'' is the anomalous dispersion factor that accounts for the absorption of X-rays in the material. The absorption of X-rays by the studied materials is higher than the absorption of neutrons, for instance, the absorption scattering length density for X-rays ($=N \cdot r_e f''$) for Pb is approximately 5.654×10^{-6} Å^{-2} and for neutrons ($=N \cdot b''$) is around 0.

Similarly to neutron reflectometry, the critical angle for total external reflection of X-rays from the surface of a medium can be calculated as

$$\theta_c = \sqrt{\frac{\lambda^2}{\pi}N \cdot r_e f} \tag{3.37}$$

Then, the critical momentum transfer, Q_c, for X-rays is expressed as

$$Q_c = \sqrt{16\pi N \cdot r_e f} \tag{3.38}$$

The equations for calculating the reflectivity follow a matrix formalism similar to the neutron reflectivity, described by the equation 3.23. Fresnel coefficients and matrices [82] for the individual layer in the sample can be defined similarly to neutrons by using information from equation 3.35. XRR measurements were performed using a Rigaku SmartLab instrument ([83]) within the material characterization laboratory at the ISIS facility in the United Kingdom and an Empyrean X-ray bench from PANalytical available at ILL. Figure 3.5 shows the images of the mounted sample in the Rigaku SmartLab instrument.

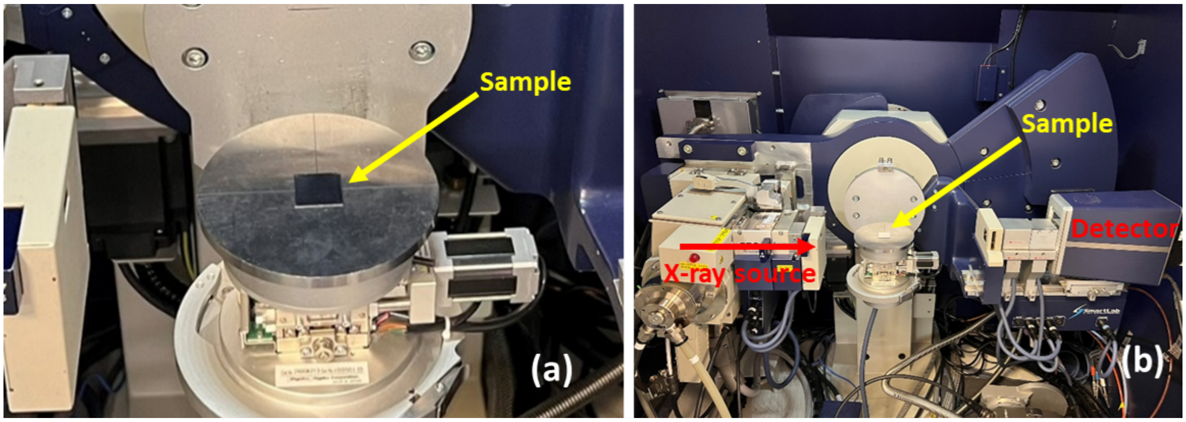

Figure 3.5: (a) Image of the 400 mm^2 sample placed on the sample holder for Rigaku SmartLab instrument at ISIS (b) Image showing the X-ray source, detector and sample.

Since the SLDs are different for X-rays and neutrons, therefore, we get a different SLD contrast between materials with both PNR and XRR techniques. For the present study, the SLD contrast between the Pb layer and capping layer is higher for X-rays than the neutrons; thus XRR helps in determining the thickness of both layers with more confidence.

3.2.2 X-Ray diffraction (XRD)

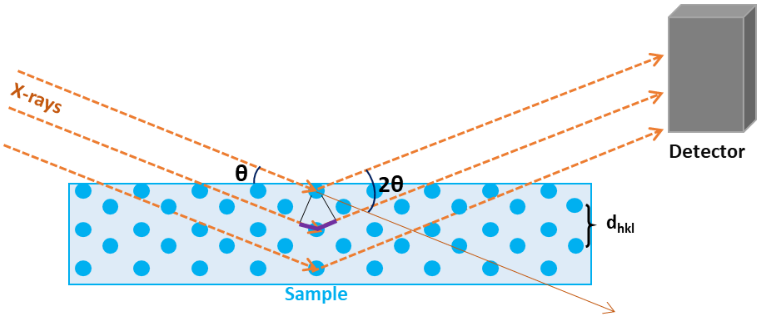

Figure 3.6: General schematic for the XRD measurements showing the incoming and diffracted X-ray beams from the sample. The lines in violet show the extra path covered by the X-rays in the sample compared to the rays that are getting diffracted from the top surface, and the black lines are normal to this path. This diagram is adopted from p.94 in ref. [84]

XRD is a structural characterization technique that is used to gain an understanding of the crystalline structure of materials. William Bragg and his son Lawrence Bragg shared the Nobel Prize in 1915 for the development of this technique [85]. The general measurement schematic for the instrument is shown in Figure 3.6. X-ray diffraction (XRD) technique is used to determine the unit cell parameters and detect the orientation of the crystalline phases in the samples. More information on the technique can be found, for example, in the book on *Elements of X-Ray diffraction* by B. D. Cullity [84] and *Thin film analysis by X-ray scattering* by Birkholz [86].

The underlying principle behind the working of this technique is the interference of waves scattered by periodic atomic planes within the sample. X-rays are made to incident on the sample and get diffracted from the atomic planes in the sample. These diffracted waves interfere constructively and destructively to produce an interference pattern at the detector. For constructive interference, the scattered waves must be in phase, and the path difference between waves must be equal to an integer number of wavelengths. The equation that governs the working principle is called the Bragg equation, and a mathematical expression is given in equation 3.39. Here θ is the angle between the exposed lattice planes and the incident X-ray beam of wavelength λ. d_{hkl} is the distance between the lattice planes with miller indices (hkl) and n is the order of the diffraction maxima (an integer number) [84].

$$2d_{hkl} \cdot \sin(\theta) = n\lambda \tag{3.39}$$

The interference pattern, characteristic of the lattice, has high-intensity peaks at specific 2θ positions, an angle between incident beam and detector (illustrated in Figure 3.6). The distance between the two lattice planes can be calculated for each material using the 2θ value of the corresponding peak in the XRD pattern. To calculate the lattice parameters for the samples, a $\lambda \approx 1.5418 \pm 0.0001$ Å was used for the monochromatic copper source.

To record XRD measurements, the angles between the source and the sample (θ), and the angle between the incident beam and the detector (2θ) are changed with the help of a goniometer (part of the diffractometer). The instrument used for this study has a fixed sample holder, so the source tube and detector were moved to perform the measurements. Measurements were performed in θ - 2θ scanning mode where the detector was moved simultaneously by always keeping it at twice the incident angle (θ). There are other modes of measurement, such as mode 2θ - ω where an offset (ϕ) is maintained between the angles between the source and the sample $(\omega = \theta \pm \phi)$, and the angle between the incident beam and the detector (2θ). Detailed information on the other modes of XRD measurements is given in ref. [87].

The intensity of the diffraction peaks in the XRD pattern is a function of the structure factor F_{hkl}, which depends on the atomic arrangement in the unit cell and the Miller indices (hkl) of the exposed lattice planes [84]. When the magnitude of the structure factor for a particular set of Miller indices (hkl) and the crystal lattice are zero, no diffraction peak is observed. Therefore, selection rules are defined based on the calculation of this structure factor that decides when certain planes are allowed or forbidden to diffract X-rays. For example, the selection rules for body-centered cubic lattices require that the sum of the Miller indices $(h+k+l)$ be even for observing XRD peaks. In contrast, for face-centered cubic lattices, the selection rules require that (hkl) be all even or all odd. In the present study, the materials (Pb, EuS, and InAs) used form a face-centered cubic lattice. For a cubic lattice, d_{hkl} can be expressed in terms of the crystal lattice parameter (a) and the miller indices of the exposed plane (hkl), as shown in equation 3.40. The lattice parameters are calculated using equations 3.39 and 3.40.

$$d_{hkl} = \frac{a}{\sqrt{h^2 + k^2 + l^2}} \tag{3.40}$$

XRD data were recorded in the 2θ range from 10° to 90°. The measurements were performed on a Rigaku SmartLab instrument available at the ISIS facility and an Empyrean X-ray bench from PANalytical available at ILL.

XRD results show Laue oscillations near peaks, arising from interference caused by coherently scattered X-rays [88]. The periodicity of these oscillations is inversely related to the coherence length (X_L), which is a measure of the distance over which the same crystallite extends without dislocations. The coherence lengths can be calculated using the equation 3.41 where δQ is the difference in the scattering vector ($Q = \frac{4\pi sin(\theta)}{\lambda}$) between successive peaks in the interference pattern around the XRD peaks.

$$X_L = \frac{2\pi}{\delta Q} \tag{3.41}$$

3.2.3 Scanning transmission electron microscopy (STEM)

STEM is a microscopy technique that is being used in the field of materials science and biology to acquire information on structural and compositional aspects on the atomic scale [89, 90]. The roots of this technique go long back to Louis de Broglie's proposition of dual nature, suggesting that electrons also possess wave-like characteristics in addition to having particle nature, with a wavelength far shorter than visible light. The use of electrons to study samples was started after the realization of the resolution limit imposed by the wavelength of visible light [91]. Electron microscopy has since transformed our understanding of materials and offers detailed structural data at the atomic level.

Currently, high-resolution transmission electron microscopy is capable of distinguishing individual columns of atoms within samples. The electrons interact with the electron cloud and the nucleus of an atom. The primary aim is to detect the transmitted electrons that have deviated from their original direction. These electrons provide information on the internal structure and arrangement of atoms. A focused electron beam with spot size ranging from 1-10 nm is scanned across the sample, and the transmitted electrons are detected. The key signals collected using designated detectors [illustrated in Figure 3.7] include high-angle annular dark field (HAADF), annular dark field (ADF) and bright field (BF) imaging. These detectors capture electrons that deviate from their trajectory, for instance, the HAADF detector captures electrons that scatter at high angles. HAADF detector signal primarily consists of incoherently (Rutherford) scattered electrons owing to interactions between incoming electrons and atomic nuclei [92]. As a result, the contrast in HAADF images is influenced by the atomic number, which allows atomic-resolution images to be obtained. For the present study, TEM measurements were performed with the HAADF imaging mode to investigate the quality of the interfaces and deposited layers. By carefully examining the contrasts between the layers in the high-resolution TEM images, information about the atomic arrangement near the interfaces, such as interdiffusion of atoms between layers and defects

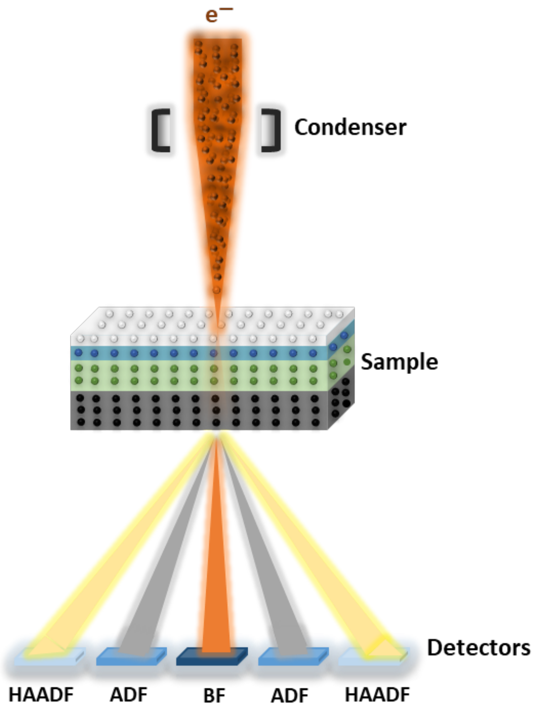

Figure 3.7: Schematic of the STEM instrument. The diagram shows the propagation and detection of a focused electron beam after interaction with the sample. This diagram is adopted from the original diagram on page 359 in ref. [91].

in the layers, was obtained. Using the length scale given on the STEM images, the thicknesses and roughnesses of the layers were approximated. In addition, information on the preferred orientation of the crystal lattice directions in layers was obtained. The extracted information on the structural parameters is used to define the parameter boundaries and build initial models for the fitting of the reflectometry data. The data for the STEM measurements were recorded and analyzed by our collaborators.

3.2.4 Superconducting quantum interference device (SQUID) magnetometry

SQUID magnetometery is a magnetic characterization technique to measure the bulk magnetic properties of the sample [93]. Its sensitivity to small magnetization, i.e. down to 10^{-8} emu at low fields, makes it useful for the present study of magnetic thin films. For this study, a Quantum Design (model MPMS3) SQUID magnetometer was used [94].

Figure 3.8 shows the schematic of the experimental setup for the SQUID magnetometer. The sample area is surrounded by a ring that is a pair of Josephson junctions consisting of two superconductors joined by a thin insulating material. A zero voltage current, with a constant phase difference, flows through the circuit because of the tunneling of cooper pairs through the thin barrier joining the two pieces of superconductor. The phase difference between the current in two arms of the ring changes with the change in magnetic flux. Thus, the unknown magnetization is measured indirectly by measuring the current flowing or the voltage difference through these junctions. The output electric signal is then converted into electromagnetic units (emu) that describe the magnetic response of the sample [95, 96]. The superconducting

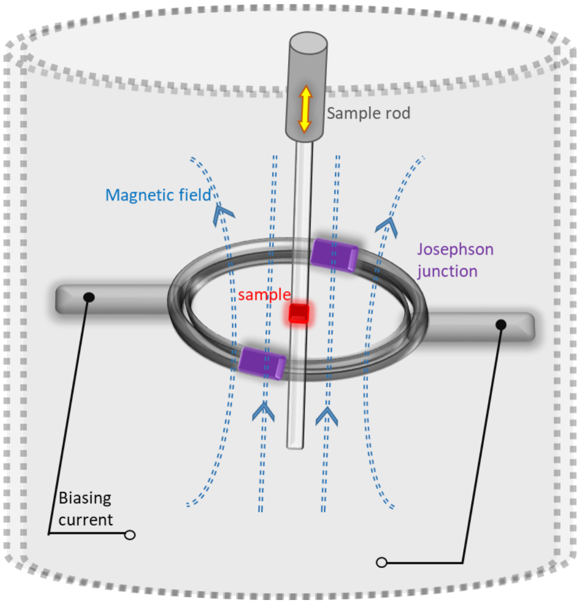

Figure 3.8: An experimental SQUID magnetometer setup with a sample (in red) attached to the sample rod. The Josephson junctions are shown in violet color.

magnet and a cryostat play a pivotal role in providing the necessary magnetic-field and temperature environment for the measurements, respectively.

SQUID can operate in two modes: VSM (vibrating sample magnetometer) and DC mode. In DC mode, the magnetic moments are measured directly by detecting the change in magnetic flux when the sample is moved slowly or kept static. However, in VSM mode, the sample vibrates sinusoidally at a defined frequency through the cross section of superconducting rings, and the change in magnetic flux is detected. SQUID VSM mode was used to track changes in magnetization of the samples with temperature and magnetic field. Information about superconducting and ferromagnetic transition temperatures was obtained by analyzing the magnetization (M) versus temperature (T) data in the presence of a constant applied magnetic field.

Figure 3.9 (a) shows an example of magnetization versus temperature plotted together with its non-linear fit using a function F^n, expressed in equation 3.42.

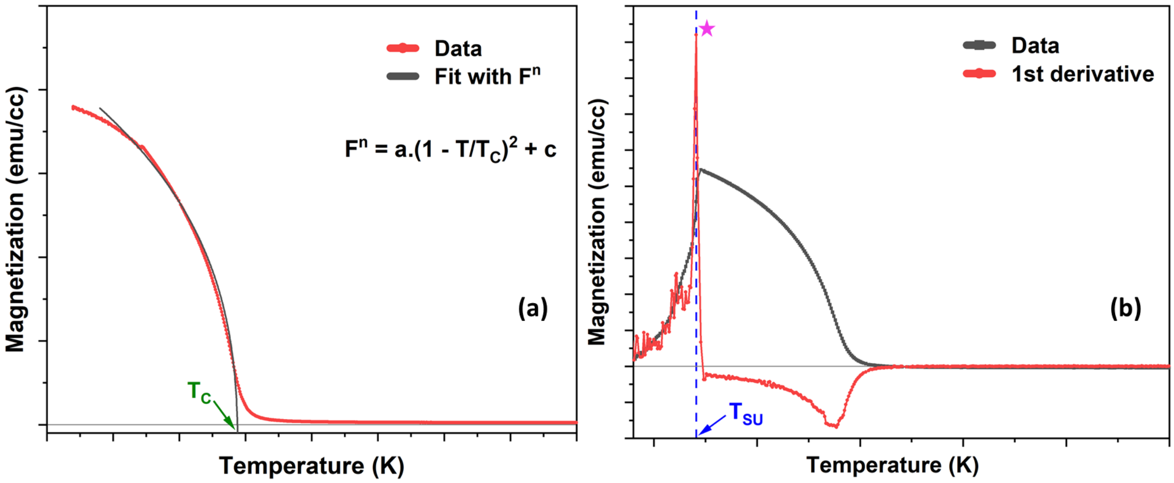

Figure 3.9: (a) Magnetization versus temperature data and its non-linear fit with a F^n are plotted together. The fit gives the value of T_C and β. (b) Magnetization versus temperature data with its first derivative. The point of inflection or the peak, marked by a red star, is used to determine the superconducting transition temperature (T_{SU}).

$$F^n = a \cdot \left(1 - \frac{T}{T_C}\right)^{\beta} + c \tag{3.42}$$

Here, a is the scaling factor, c is the magnetization offset, and β_1 is the critical exponent. β_1 describes the behavior of magnetization near T_C. Two temperature ranges were used for the fit, then the averages for T_C and β_1 were taken, with errors calculated for these averages. Figure 3.9 (b) shows an example of magnetization versus temperature data which were recorded after the sample was cooled in the zero field. The first derivative of the data is also plotted. The superconducting transition temperature (T_{SU}) is read from the value on the x-axis corresponding to the point of inflection (peak), marked with a pink star on the red curve in Figure 3.9 (b). The T_{SU} value error is determined by the smallest difference between two adjacent values.

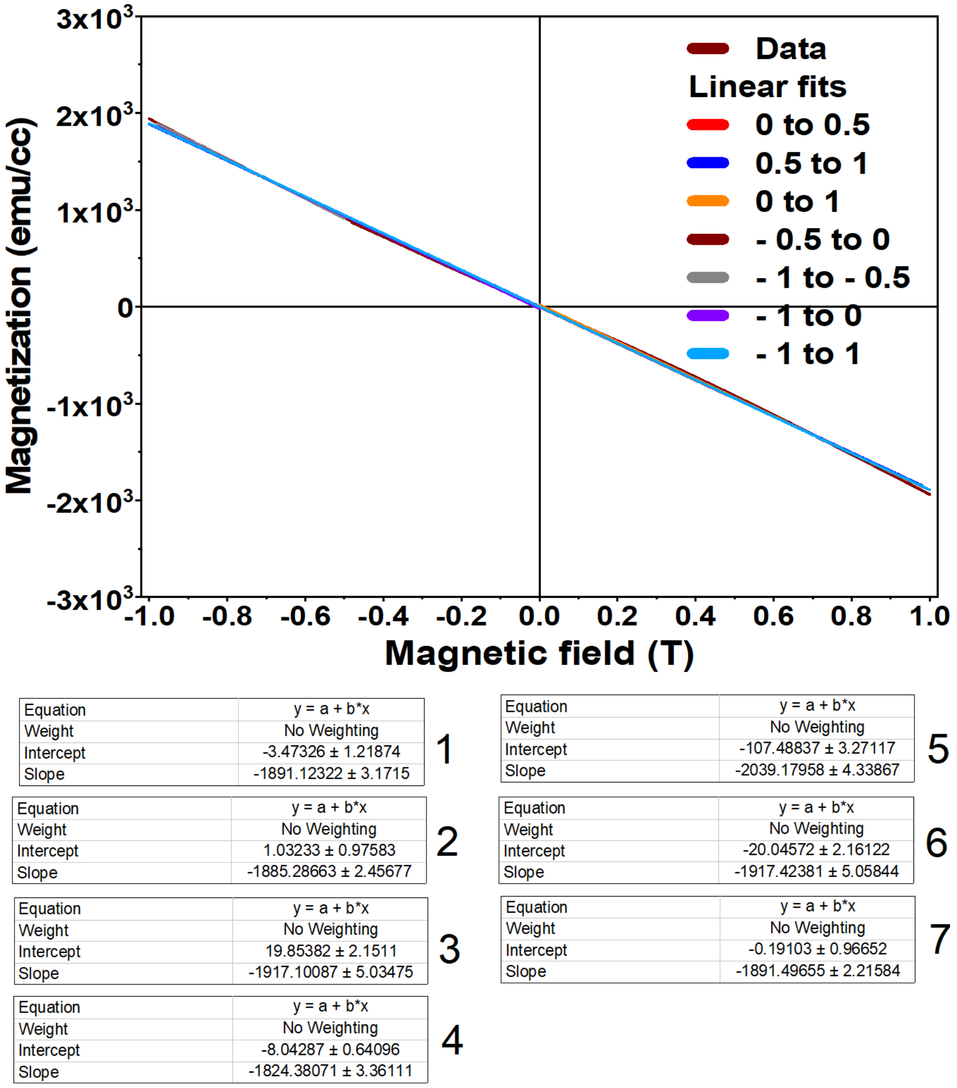

1

Equation	y = a + b*x
Weight	No Weighting
Intercept	-3.47326 ± 1.21874
Slope	-1891.12322 ± 3.1715

2

Equation	y = a + b*x
Weight	No Weighting
Intercept	1.03233 ± 0.97583
Slope	-1885.28663 ± 2.45677

3

Equation	y = a + b*x
Weight	No Weighting
Intercept	19.85382 ± 2.1511
Slope	-1917.10087 ± 5.03475

4

Equation	y = a + b*x
Weight	No Weighting
Intercept	-8.04287 ± 0.64096
Slope	-1824.38071 ± 3.36111

5

Equation	y = a + b*x
Weight	No Weighting
Intercept	-107.48837 ± 3.27117
Slope	-2039.17958 ± 4.33867

6

Equation	y = a + b*x
Weight	No Weighting
Intercept	-20.04572 ± 2.16122
Slope	-1917.42381 ± 5.05844

7

Equation	y = a + b*x
Weight	No Weighting
Intercept	-0.19103 ± 0.96652
Slope	-1891.49655 ± 2.21584

Figure 3.10: An example of hysteresis loop at a temperature higher than T_C along with the linear fits. The data was fitted in 7 ranges of magnetic fields. Tables show the equation, intercept and slope of the linear fits corresponding to each fit.

In addition, the magnetic response of the sample as a function of the magnetic field strength (hysteresis loops) was measured at constant temperatures. In Figure 3.10, a hysteresis loop recorded above T$_C$ is depicted with seven individual linear fits. The x-axis was divided into seven segments, each fitted separately. The average slope was calculated from these fits, considering the errors of each slope for error estimation. This slope served to correct for the slope of the remaining data set for the diamagnetic contribution.

$$Average\_slope = \frac{1}{7} \cdot \sum (slope)_i \tag{3.43}$$

$$Error = \frac{1}{7} \cdot \sqrt{\Sigma (slope)_i} \tag{3.44}$$

$$M = M_{raw\_data} + (Average\_slope) \cdot \mathrm{H}_{ext}\ (\mathrm{T}) \tag{3.45}$$

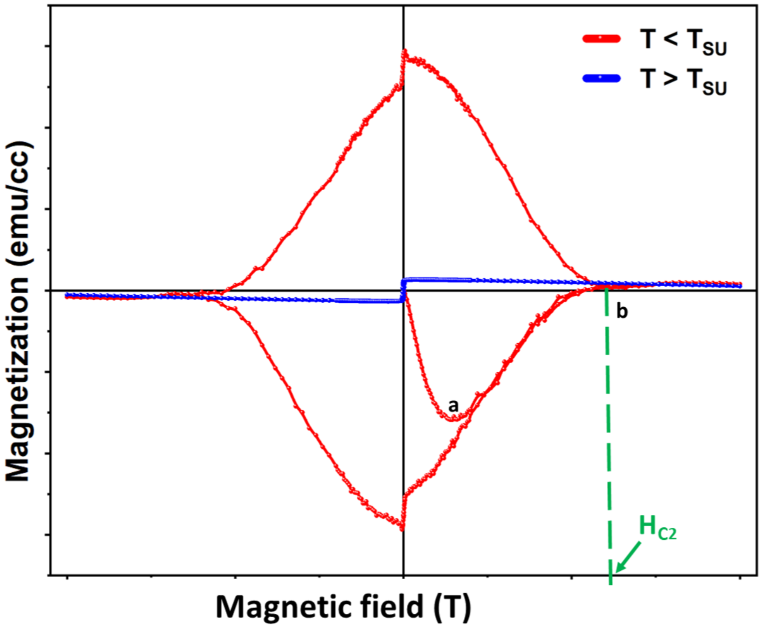

Figure 3.11: Magnetization versus magnetic field data for two temperatures both below T$_C$ but one below T$_{SU}$ (red) and one above T$_{SU}$ (blue). The point at which the red curves merge (marked by b on plots) is the upper critical magnetic field point for the superconductor.

The shape of hysteresis loops was inspected to gather information about the critical magnetic field for the superconductor at the measurement temperatures. Figure 3.11 presents an example of the hysteresis curves for a sample measured below and above T$_{SU}$, but still below T$_C$. When the temperature is below T$_{SU}$, the sample exhibits a strong magnetic response with contributions from both superconducting Pb and ferromagnetic EuS. The point labeled "b" on this curve represents the upper critical field (H_{C2}) for the superconductor is the field at which the superconducting state is completely suppressed and the material transitions to a normal, non-superconducting state. Beyond this point, the superconducting contribution to the magnetization diminishes. The value of H_{C2} is read from the x-axis value corresponding to point "b".

Note that the SQUID magnetometer captures the average magnetic signal from the whole sample. Therefore, the diamagnetic signal of the substrate and capping layer was subtracted by measuring their diamagnetic response alone without the magnetic layers (EuS and Pb). For comparison across samples, the magnetic response on the y axis is normalized to the volume of the EuS layer in each sample. To determine the volume, the thickness of the EuS layer is obtained from the PNR results. The area of the sample was calculated after measuring the length and width using a standard length measurement ruler, the error of which is ± 0.5 mm. It is important to account for propagation of the errors in measuring the volume of EuS layer. The error was calculated using equation 3.47. Here, V is the volume, L is the length, W is the width, and D is the thickness of the EuS layer. The errors in the estimation of L, W, and D are σ_L, σ_W and σ_D, respectively. σ_{LW}, σ_{LD}, and σ_{WD} is the covariance between the variables. L, W, and D are not correlated, therefore, the covariance terms are zero. Finally, σ_V is the error in volume estimation. Volume is calculated in cubic centimeters (cc), and normalized magnetization is shown in units emu/cc.

$$V = L \cdot W \cdot D \tag{3.46}$$

$$\sigma_V \approx |V| \cdot \sqrt{\left(\frac{\sigma_L}{L}\right)^2 + \left(\frac{\sigma_W}{W}\right)^2 + \left(\frac{\sigma_D}{D}\right)^2 + 2\frac{\sigma_{LW}}{L \cdot W} + 2\frac{\sigma_{LD}}{L \cdot D} + 2\frac{\sigma_{WD}}{W \cdot D}} \tag{3.47}$$

The information about transition temperatures and critical field is useful because the PNR measurements were recorded as a function of temperature and magnetic field to see their effect on the magnetic proximity effects in the samples. SQUID measurements for the data presented in Chapter 5 were gathered by our collaborators, whereas those for Chapter 6 were collected by myself.

3.2.5 X-ray absorption spectroscopy (XAS)

X-ray absorption spectroscopy is used to acquire information about the local structure and magnetism of the samples [97]. Because electron energy levels are unique to atoms, the X-ray energy can be adjusted for element-specific spectroscopic measurements. With this technique, the absorption of X-ray photons by the core electrons is studied, i.e. the absorption spectrum, which exhibits the characteristic absorption edges of elements present in the sample. There are two detection methods for studying the X-ray absorption: fluorescense yield and electron yield. The fluorescence yield method records the X-ray fluorescence emitted by the atoms as they de-excite after X-ray absorption, offering bulk-sensitive information. However, the electron-yield mode detects the electrons emitted from the surface of the sample because of the X-ray absorption, making it more surface-sensitive. For this thesis, the data were recorded in the fluorescense detection mode. The core electrons undergo transitions to unfilled valence band states and these transitions are governed by the selection rules [98]. All transitions follow Fermi's golden rule:

$$W_{fi} = \frac{2\pi}{\hbar} |\langle \Psi_f | \hat{H} | \Psi_i \rangle|^2 \rho(E_f) \tag{3.48}$$

where $|\Psi_i\rangle$ and $|\Psi_f\rangle$ describe the initial and final states, W_{fi} is the transition rate from $|\Psi_i\rangle$ to the $|\Psi_f\rangle$ state, $\rho(E_f)$ is the density of states, and $\hat{H}$ is the Hamiltonian. The selection rules are $\triangle L = \pm 1$, $\triangle m = 0, \pm 1$, and $\triangle S = 0$ [98]. The Hamiltonian for the system can be written as:

$$\hat{H} = \hat{H}_o + \hat{H}_{\text{int}}, \tag{3.49}$$

where $\hat{H}_o$ represents the Hamiltonian for the free electrons and the electromagnetic field due to X-rays [99]. The interaction between X-ray radiation and electrons is characterized by Hamiltonian ($\hat{H}_{\text{int}}$). Taking into account a minimal coupling, $\hat{H}_{\text{int}}$ can be expressed in the following form:

$$\hat{H}_{\text{int}} = -\frac{e}{m_e} \sum_i \hat{\mathbf{A}}(\mathbf{r}_i) \cdot \hat{\mathbf{p}}_i + \frac{e^2}{2m_e} \sum_i \hat{\mathbf{A}}(\mathbf{r}_i) \cdot \hat{\mathbf{A}}(\mathbf{r}_i), \tag{3.50}$$

where e is the electron charge, m_e is the mass of electron, $\hat{\mathbf{A}}(\mathbf{r}_i)$ is the vector potential of the electromagnetic field at the position of the i^{th} electron and $\hat{\mathbf{p}}_i$ is the momentum operator for the ith electron.

X-ray absorption near edge spectroscopy (XANES)

A sharp rise in the absorption of X-rays is observed when the energy of the X-rays is close to the energy required to excite a core electron in an atom. This sharp rise in instrument terms is known as an "edge", hence the technique's name. It is also known as the near-edge X-ray absorption fine structure (NEXAFS). XANES can determine local electronic and structural properties of matter, such as the valence states of elements and the crystal field around the atom that allows for precise fingerprinting [100, 101]. The XANES signal is obtained by taking an average of the absorption spectra from both left- and right-circularly polarized X-ray measurements, since polarized X-rays were used for XMCD measurements (discussed in the following section), but it can be performed without the need for polarized X-rays.

X-ray magnetic circular dichroism (XMCD)

The use of polarized X-rays enables the acquisition of element-specific magnetic contributions in the sample. The X-ray magnetic circular dichroism spectrum is characterized as the difference between the absorption of right- and left-circularly polarized X-rays [97]. The inner shell of the atoms is probed to acquire information about the spin and orbital moments of the ion [98]. Figure 3.12 shows an example of a magnetic sample in which the core 2p electrons are resonantly excited by polarized X-rays. Due to spin orbit coupling, the 2p level splits into two levels with the $2p_{1/2}$ level being more bound.

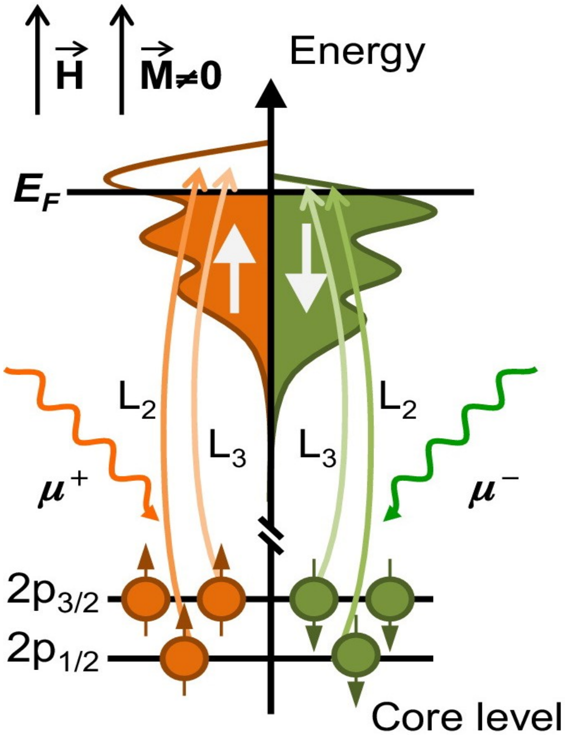

Figure 3.12: Schematic of the XMCD technique showing the absorption of left (μ^-) and right (μ^+) circularly polarized X-Rays by electrons bound in the states within 2p subshell. $\vec{H}$ and $\vec{M}$ are applied magnetic field and sample magnetization, respectively. L_2 and L_3 are the edges of the material. The picture is taken from ref. [97].

The right and left circularly polarized X-rays interact differently with spin-up and spin-down core electrons. The probability of excitation of the spin up and spin down electrons varies for each polarization state of X-rays, such as 62.5 % of spin up electrons are excited by right circular and 37.5 % of spin up electrons are excited by left circularly polarized X-rays. The excited electrons occupy empty states in the valence band, which results in an absorption difference if the valence band electrons are spin polarized. This difference in absorption is directly related to the magnetic signal.

XMCD signal was recorded as a function of energy for the samples, which reveal the contribution of each of the valence states to the ferromagnetism observed in the samples. In addition, the XMCD signal as a function of the temperature and the external magnetic field was measured by fixing the energy of the X-rays at a value that corresponds to the intense peak in XMCD versus energy results for the samples. The samples were field-cooled (FC) and the measurements were taken after stabilizing at each temperature or magnetic field step.

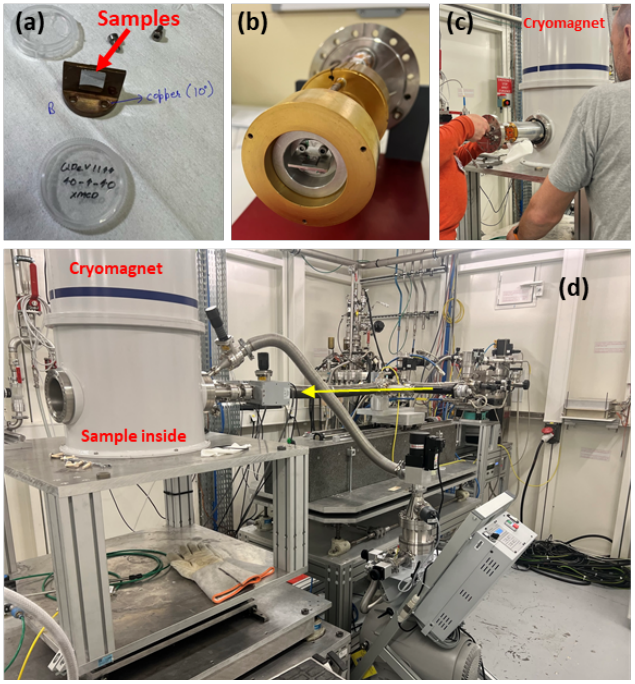

Figure 3.13: (a) Sample mounted on a copper sample holder with 10° angle with the horizontal plane (b) Sample holder attached to the cryomagnet rod (c) Sample inserted in the cryomagnet for the experiment (d) Experimental setup of the ID12 beamline.

X-ray absorption spectroscopic measurements were performed at the ID12 beamline of the European Synchrotron Radiation Facility [102]. The absorption of circularly polarized X-rays at the europium L_3-edge was studied under different temperatures and magnetic field environments. The Eu L_3-edge that exhibits a $2p_{3/2}$ to 5d dipolar transition in empty 5d orbitals was studied [103]. The d orbital of the europium atom was examined to gain insight into its valence state as well as to extract the associated magnetic signal. The XANES results for each sample provided information on the relative abundance of the oxidation states. The experimental setup and samples mounted during the measurements are shown in Figure 3.13.

The samples were cooled in a zero magnetic field to 3K, and then a horizontal in-plane magnetic field was applied to record the data. The absorption spectrum was recorded at the Eu L_3-edge for four samples in the energy range of 6955 to 7025 eV. This energy range was divided into 240 energy intervals, and the absorption of X-rays was measured at each step, resulting in 241 data points in the energy range. The data were normalized by the difference in the XANES signal observed at both ends of the energy range, as shown below.

$$(XANES)_{nx} = \frac{XANES - XANES(scan_1)}{XANES(scan_{240}) - XANES(scan_1)} \tag{3.51}$$

$$(XMCD)_{ne} = \frac{XMCD}{XANES(scan_{240}) - XANES(scan_1)} \tag{3.52}$$

Here, $(XANES)_{nx}$ and $(XMCD)_{ne}$ are the normalized XANES and XMCD signal. However, the normalization factor is different for the XMCD data that were recorded at fixed energy of X-rays, as the data set corresponds to a specific X-ray energy, i.e. 6975.72 eV. This different normalization concerns the XMCD signal recorded as a function of temperature and external magnetic field strength. Equations 3.53 and 3.55 show the normalization of XMCD.

$$(XMCD)_1 = \frac{XMCD_p - XMCD_m}{XMCD_p + XMCD_m} \tag{3.53}$$

$$Fact = \frac{(XMCD)_{ne,peak}}{(XMCD)_{\mathrm{3T,3K}}} \tag{3.54}$$

$$(XMCD)_n = (XMCD)_1 \cdot Fact \tag{3.55}$$

Here, $XMCD_p$ and $XMCD_m$ are the signals corresponding to right and left circular polarized X-rays, respectively. $(XMCD)_{ne,peak}$ is the normalized XMCD signal corresponding to the intense peak of XMCD versus the energy data for each sample. $(XMCD)_{\mathrm{3T,3K}}$ is the XMCD signal corresponding to 3 K (in 3 T) taken from the raw XMCD data versus external magnetic field data for each sample. Then $Fact$ is the scaling factor used to obtain the normalized signal $(XMCD)_n$.

To obtain further insights into the magnetic proximity effects, we have tried to record the data for XANES and XMCD at the Pb edge. However, the substantial background signal from the substrate (Arsenic, K-edge) lies close to the Pb M_5-edge, which precluded any observable effects at the Pb edge. Furthermore, the volume fraction of Pb was considerably less than that of As (substrate), leading to a significantly diminished signal. Thus, it was concluded that the sample structure was not ideal for studying the Pb edge for magnetic proximity effects.

To determine the error bars on the data, the data set was smoothed to identify the overall trend. Subsequently, the deviations of the raw data from this smoothed version were computed, followed by the calculation of the standard deviation of these deviations. This standard deviation served as an estimate of the errors associated with the data points.

Chapter 4

Data analysis

This chapter describes the basic functioning of the GenX and RefL1D software and how they are used for the analysis of the reflectometry data. The approach to data analysis and the choice of the best models for the data is shared in detail in the following sections. In addition, the correlation and uncertainty analysis performed using Refl1D software is explained in the last section of this chapter.

4.1 GenX software

GenX is a Python scripted versatile tool that was employed for the analysis of polarized neutron reflectometry (PNR) and X-ray reflectometry (XRR) data. This software allows for the fitting of experimental data to theoretical models, providing detailed insight into the structural and magnetic properties of thin films and multilayer samples [104]. The detailed information on software and its installation is given in refs. [105, 106].

4.1.1 Interface

GenX interface includes menus and options to load data, configure models, and run simulations as shown in Figure 4.1. The experimental data sets can be imported on the basis of the format of the reduced data (number of columns in the dataset). The type of data loader could be different for different instrument's data. For example, the D17 instrument data have four columns that contain information about the resolution information in the fourth column, whereas POLREF instrument data have only three columns. For the present thesis, PNR measurements were performed on both D17 (ILL) and POLREF (ISIS), therefore, it is necessary to choose a different data loader option from the list for corresponding datasets. One can choose to fit more than one data set

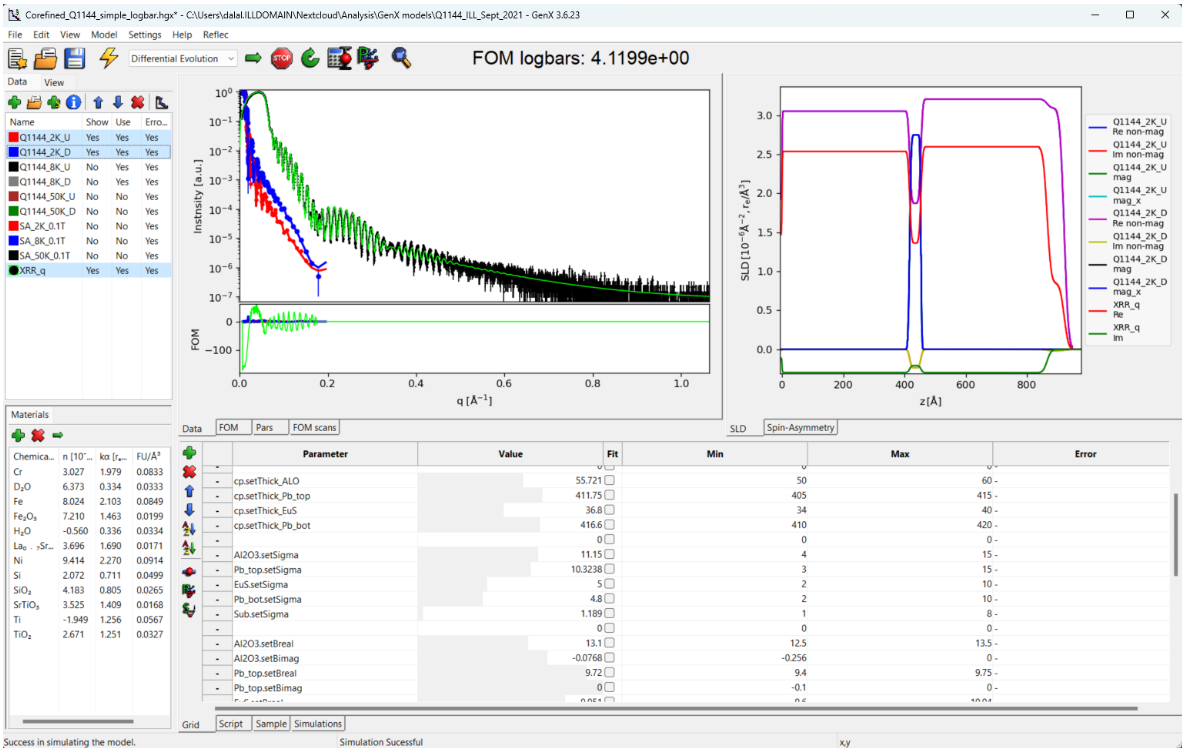

Name	Show	Use	Erro...
🟥 Q1144_2K_U	Yes	Yes	Yes
🟦 Q1144_2K_D	Yes	Yes	Yes
⬛ Q1144_8K_U	No	Yes	Yes
⬛ Q1144_8K_D	No	Yes	Yes
🟫 Q1144_50K_U	No	No	Yes
🟩 Q1144_50K_D	No	No	Yes
🟥 SA_2K_0.1T	No	No	Yes
🟦 SA_8K_0.1T	No	No	Yes
⬛ SA_50K_0.1T	No	No	Yes
● XRR_q	Yes	Yes	Yes

Chemica...	n [10⁻...	kα [rₑ...	FU/Å³
Cr	3.027	1.979	0.0833
D_2O	6.373	0.334	0.0333
Fe	8.024	2.103	0.0849
Fe_2O_3	7.210	1.463	0.0199
H_2O	-0.560	0.336	0.0334
$La_{0.7}Sr$...	3.696	1.690	0.0171
Ni	9.414	2.270	0.0914
Si	2.072	0.711	0.0499
SiO_2	4.183	0.805	0.0265
$SrTiO_3$	3.525	1.409	0.0168
Ti	-1.949	1.256	0.0567
TiO_2	2.671	1.251	0.0327

	Parameter	Value	Fit	Min	Max	Error
-	cp.setThick_ALO	55.721	☐	50	60	-
-	cp.setThick_Pb_top	411.75	☐	405	415	-
-	cp.setThick_EuS	36.8	☐	34	40	-
-	cp.setThick_Pb_bot	416.6	☐	410	420	-
-		0	☐	0	0	-
-	Al2O3.setSigma	11.15	☐	4	15	-
-	Pb_top.setSigma	10.3238	☐	3	15	-
-	EuS.setSigma	5	☐	2	10	-
-	Pb_bot.setSigma	4.8	☐	2	10	-
-	Sub.setSigma	1.189	☐	1	8	-
-		0	☐	0	0	-
-	Al2O3.setBreal	13.1	☐	12.5	13.5	-
-	Al2O3.setBimag	-0.0768	☐	-0.256	0	-
-	Pb_top.setBreal	9.72	☐	9.4	9.75	-
-	Pb_top.setBimag	0	☐	-0.1	0	-

Success in simulating the model.

Simulation Sucessful

Figure 4.1: An image of the user interface of GenX software. Top left: Menu with options for loading data, models, and performing simulations. The list of different datasets is displayed. Top center: Reflectivity versus momentum transfer (q) along with the figure of merit of the model. Top right: The scattering length density versus depth profiles are shown. Bottom left: A table containing structural properties for materials. Bottom right: List of parameters with their values and boundaries defined for its variation.

together, and it is useful for co-refining the models to fit the data from the PNR and XRR techniques. GenX includes visualization tools that allow users to plot experimental and fitted reflectivity curves, inspect residuals, and monitor the convergence of the fitting process [Figure 4.1]. These visualizations provide feedback on the quality of the fit, highlighting areas where the model may need refinement. A detailed description of the interface and the options provided with the software is provided in [106].

4.1.2 Algorithm and optimizer settings

For the present thesis, a slower but more robust differential evolution algorithm (DE) was chosen from a list of algorithms that GenX provides to perform the fitting analysis. The algorithms available within this software include differential evolution (DE), Levenberg-Marquardt, Remote DiffEv, etc. The DE algorithm excels at finding the best fit between experimental data and theoretical models by efficiently exploring the parameter space. The DE algorithm operates by evolving a population of potential solutions over successive generations [107]. Each solution is represented by a vector of parameters. For the initiation, each parameter is assigned a value within the defined boundary limits for that parameter. The algorithm iteratively improves these solutions through mutation, crossover, and selection processes, guided by a fitness function that measures how well each solution fits the experimental data. This approach continues until it converges to what the algorithm deems optimal.

The quality of the fit process in GenX is evaluated using a figure of merit (FOM), which quantifies the agreement between the experimental data and the theoretical model. With GenX, one has the option to choose from a list of FOMs that are shown in Figure 4.2. Commonly used FOMs include *chi2bars* (χ^2_{bar}), *logbars* and *chibar* (χ_{bar}). These FOMs take error bars in the reflectivity measurement into account while analyzing the fit. The expressions for FOMs are described as follows:

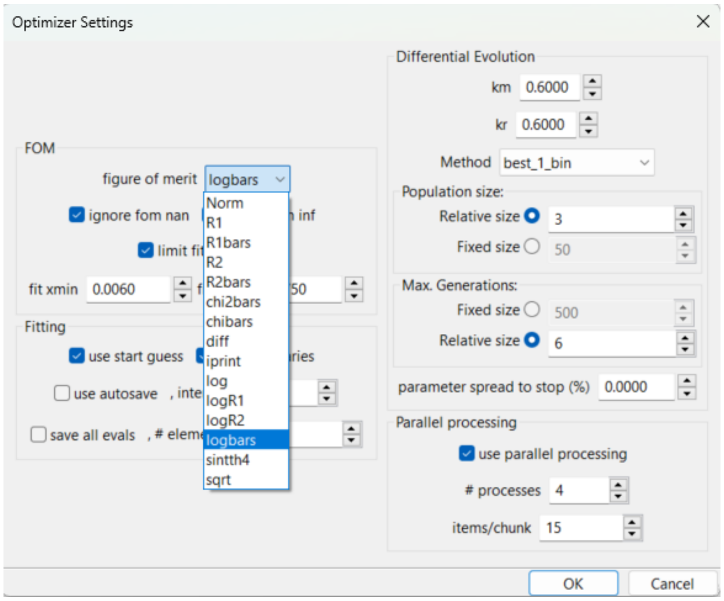

Optimizer Settings

FOM

figure of merit logbars

☑ ignore fom nan

inf

☑ limit fi

fit xmin 0.0060

50

Fitting

☑ use start guess

ries

☐ use autosave , inte

☐ save all evals , # eleme

Differential Evolution

km 0.6000

kr 0.6000

Method best_1_bin

Population size:

Relative size ● 3

Fixed size ○ 50

Max. Generations:

Fixed size ○ 500

Relative size ● 6

parameter spread to stop (%) 0.0000

Parallel processing

☑ use parallel processing

processes 4

items/chunk 15

Figure 4.2: List of parameters that can be manipulated to optimize the fitting process.

$$\chi^2_{bar} = \frac{1}{N_{data} - N_p} \sum_{i=1}^{N_{data}} \left(\frac{R_{exp,i} - R_{model,i}}{E_i} \right)^2 \tag{4.1}$$

$$\chi_{bar} = \frac{1}{N_{data} - N_p} \sum_{i=1}^{N_{data}} \left(\frac{R_{exp,i} - R_{model,i}}{E_i} \right) \tag{4.2}$$

$$logbars = \frac{1}{N_{data} - N_p} \sum_{i=1}^{N_{data}} \left(\frac{log_{10}(R_{exp,i}) - log_{10}(R_{model,i})}{E_i . log_{10}(R_{exp,i})} \right)^2 \tag{4.3}$$

Here, N_{data} is the number of data points, N_p is the number of free parameters used to fit the data, $R_{exp,i}$ is the experimental reflectivity, $R_{model,i}$ is the corresponding simulation and E_i is the error associated with $R_{exp,i}$. Since the error bars are small in the low Q_z range, a small difference between $R_{exp,i}$ and $R_{model,i}$ is more pronounced in the case of χ^2_{bar}. Thus, χ^2_{bar} is often used as an FOM to fit the reflectometry data.

Optimizer settings such as population size, maximum generations and mutation factors (km and kr) are tuned to control exploration of the parameter space and the speed of simulations [Figure 4.2] to avoid the risk of rapid misconvergence of the fit [107].

4.1.3 Reflectivity calculation

There are two theoretical frameworks for calculating the reflectivity of the models used by the GenX software, the Parratt formalism [77] and the Abeles matrix formalism [78]. These methods help to model the reflectivity of multilayered structures. Both methods involve a recursive calculation of the reflectivity considering the surface and interfaces between layers in the sample. The details of the procedure are shared in the chapter on methods.

4.1.4 *spec_adaptive* model

GenX has options for selecting the reflectivity model that has parameters to define the layers in the sample definition and simulate the reflectivity [104]. The available options include *spec_nx*, *spec_inhom*, *spec_adaptive*, *interdiff*, etc. The *spec_adaptive* model is chosen from the library of models because it most effectively describes the magnetism and elemental composition of complex structures, similar to those analyzed in this study, and employs adaptive layer segmentation. Magnetic roughness, which is different from nuclear structural roughness, can be defined separately using the *spec_adaptive* model (not possible with the often used *spec_nx* model). The adaptive layer segmentation facilitates the computation of the SLD for a given layer by partitioning it into thin slices that can have a thickness of a fraction of Å. Figure 4.3 shows an example of an SLD profile plotted against depth for a given sample, with colored horizontal dotted lines serving as guides to read the NSLD and MSLD values for the layers from the y-axis. The NSLD value for a layer can be determined from the flat segment of the SLD profile, or from a peak if the layer's thickness does not produce a flat segment (as observed for layer 1 in Figure 4.3). Layer thicknesses can be approximated by examining the x-axis values at the midpoint of the roughness profiles between the layer in question

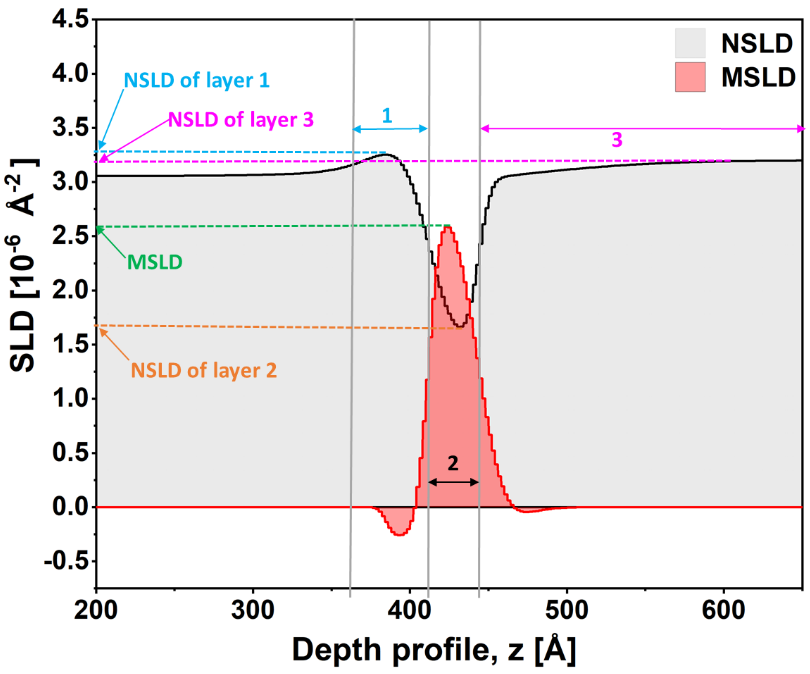

Figure 4.3: A guide to read the values of NSLD, MSLD and thickness of any layer in the sample from its SLD profile.

and its neighboring layers. An example of estimating the thickness of layers is shown in Figure 4.3 with solid gray lines passing through the midpoint of the roughness profiles of the layers in question. Selecting the *spec_adaptive* model is essential for our study of magnetic proximity effects at interfaces, as it allows us to detect the diffusion of the magnetic signal into nearby layers.

4.1.5 Process of fitting data with GenX

The objective of the data fitting process is generally to develop a physical model that accurately represents the structural and magnetic characteristics of the sample. For each sample, the approach was to create **three types of models**: simple model, modified structural interface model, and modified structural and magnetic interface model. **1. Simple model** - With this model approach, the reflectometry data were fitted with the number of original layers present in the sample and their related parameters. For this approach, only the roughness profiles of the layers were manipulated to fit the data. The fit parameters include the thickness, roughness, SLD, and MSLD (only for the EuS layer) of the layers. This approach is illustrated with an example shown in Figure 4.4 (a), the sample with its original layers.

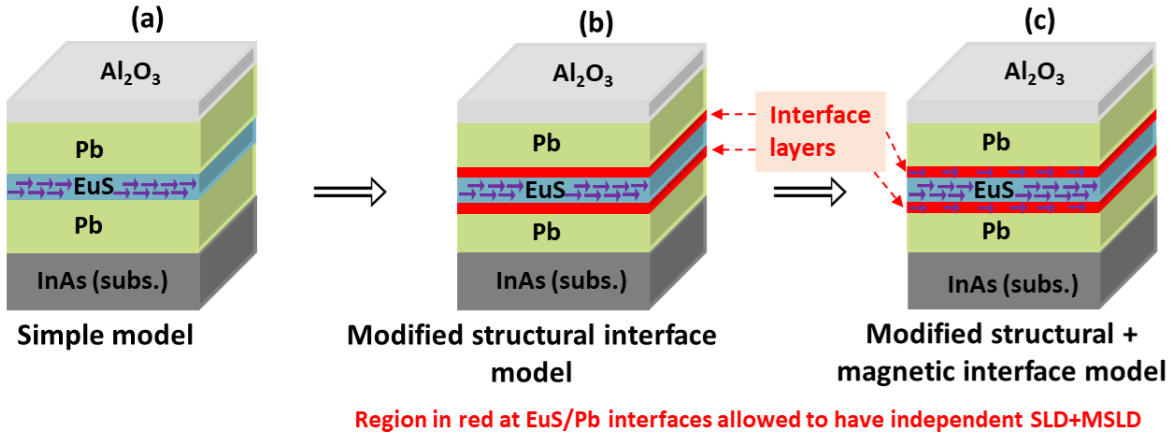

Figure 4.4: Pictorial representation of the data analysis approach using an example of sample. (a) simple model, (b) modified structural interface model, and (c) modified structural and magnetic interface model. The layers shown in red at the interfaces of the EuS and Pb layers are called interfacial layers [relevant for (b) and (c)]. The horizontal arrows represents magnetism.

2. Modified structural interface model - If changing the roughness profile of the layers does not improve the fits, then the second approach was to take a part of the Pb layer close to the interface with the EuS layer and allow it to have an SLD different from that of the original Pb layer. This divides the Pb layer into two layers, bulk and interfacial. These interfacial layers corresponding to two Pb layers in the sample are shown with the red region around the EuS layer in Figure 4.4 (b). These layers were part of the Pb layers, so the combined thickness of the interface layer and Pb layer was kept constant at a value taken from the simple model fits.

3. Modified structural and magnetic interface model - This model is a step ahead of model "2" where the magnetic parameters were allowed to have a non-zero value for the interfacial layer while fitting the data. This approach is depicted by adding horizontal arrows that represent magnetism in the interfacial layers in Figure 4.4 (c). For this model, the structural parameters of all layers were kept the same as in Model 2. This model was explored to see if setting the interfacial layer's magnetic parameter free really improves the fit or not.

The different deposition temperatures for materials, lattice mismatching, defects, or properties of the material can result in increased roughness or interdiffusion. Therefore, the interfaces change and can occasionally have effects on the reflectivity similar to that

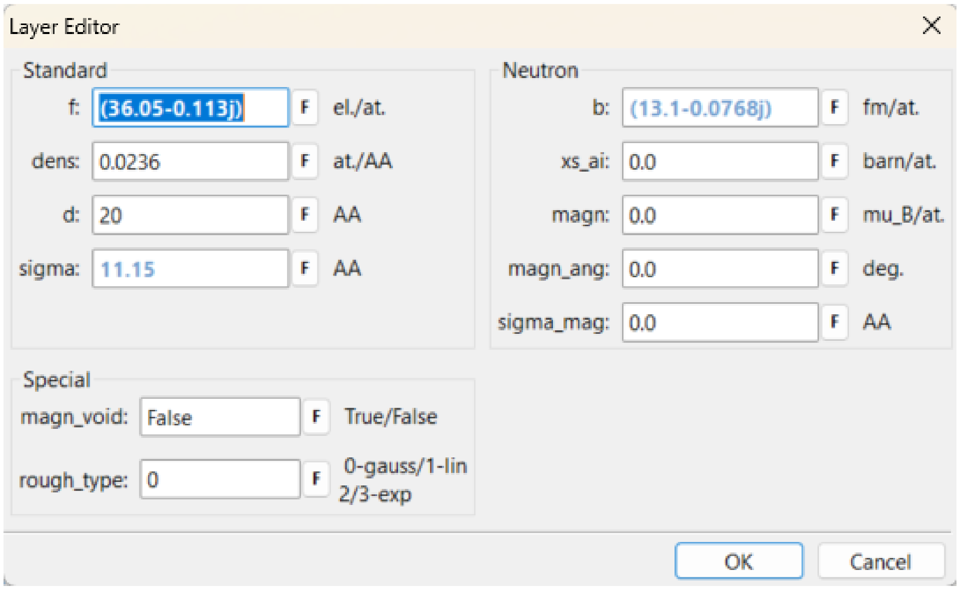

f: (36.05-0.113j) el./at.
dens: 0.0236 at./AA
d: 20 AA
sigma: 11.15 AA
b: (13.1-0.0768j) fm/at.
xs_ai: 0.0 barn/at.
magn: 0.0 mu_B/at.
magn_ang: 0.0 deg.
sigma_mag: 0.0 AA
magn_void: False True/False
rough_type: 0 0-gauss/1-lin 2/3-exp

Figure 4.5: Structural and magnetic parameters for each layer with spec-adaptive model option.

of layers with different compositions. When measured, these interfaces may exhibit distinct SLDs compared to the original layers. More importantly, for observing and quantifying the extent of the magnetic proximity effects in neighboring layers, these modified interface models are crucial, as separate magnetic parameters are needed for its investigation.

Steps for analyzing the reflectivity data from neutrons and X-rays

1. The first step involves loading the data sets into the software. The “default” data loader is selected from the settings before loading the experimental data sets, since it reads the four-column data from the D17 instrument.

2. The next step is to build a model with the definition and arrangement of the layers in the sample. This information comes from the fabrication process and structural characterizations, such as TEM (Section 3.2.3). Figure 4.5 shows the different structural and magnetic parameters that can be defined for each layer with the *spec_adaptive* model. The parameters include thickness (“d”), number density “N” (denoted here as “dens”), root mean square roughness “σ” (denoted here as “sigma”), sum of the incoherent scattering and absorption cross-section (“xs_ai”), magnetic moment per unit volume (“magn”), magnetic roughness (“*sigma_mag*”), and angle of the magnetic moments in the layer with respect to the neutron spin (“*magn_ang*”). The options “f” and “b” are the scattering lengths for X-rays and neutrons, respectively. The

software calculates the scattering length densities (SLDs) corresponding to neutrons ($\rho_n = N.b$) and X-rays ($\rho_x = N.f$) to display them as a function of depth inside the sample. The imaginary part of the scattering length is responsible for absorption and can be added with the real part by multiplying it by "-j". There is an option to select the type of roughness profile, such as Gaussian/linear/exponential decay profile, with "*rough_type*". The structural and magnetic parameters can be given a fixed value or selected to fit with an initial starting value.

3. The technique (PNR or XRR) can be defined uniquely within the instrument editor, and the parameters related to it can be modified there, as shown in Figure 4.6. The instrument parameters include the type of probe used ("probe") with/without polarization ("pol") at incident angle ("incangle"), the background intensity ("Ibkg"), the intensity scaling factor ("I0"), the type ("restype") and the value ("res") of the resolution function along with the number of points ("respoints") and the number of standard deviations ("resintrange") used for its calculation. The footprint correction can also be added if it is relevant with the option to choose the type ("footype") and size of the beam ("beamw") and the sample ("samplelen"). It is possible that the resolution settings could be different for different PNR/XRR techniques.

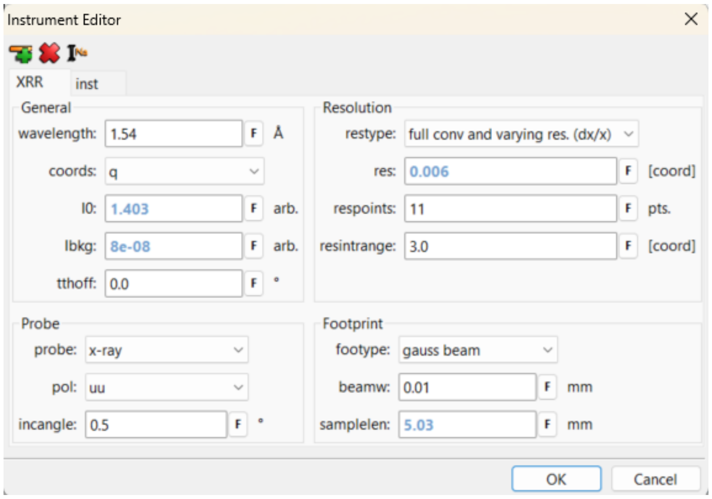

wavelength: 1.54 Å
coords: q
I0: 1.403 arb.
Ibkg: 8e-08 arb.
tthoff: 0.0 °
restype: full conv and varying res. (dx/x)
res: 0.006 [coord]
respoints: 11 pts.
resintrange: 3.0 [coord]
probe: x-ray
pol: uu
incangle: 0.5 °
footype: gauss beam
beamw: 0.01 mm
samplelen: 5.03 mm

Figure 4.6: The list of parameters that can be used to define the instrument. There is an option to apply the footprint correction in the bottom right.

4. Then, the optimization settings (Figure 4.2) such as the choice of FOM and the selection of the data range can be configured for an effective fit process.

5. After defining the sample and instrument, the next step is to start fitting the data. A PNR measurement recorded at high temperature, well above both T_{FM} and T_{SU} transitions, is used to cofit with XRR data (taken at RT). The structural parameters that are fitted include the thickness, roughness, and the scattering length ("*b*") for each layer. The SLD for any layer can be fitted by changing either the scattering length or

the number density. However, in the present study, the scattering length was changed while keeping the number density fixed during the analysis. Unexpectedly, EuS layer in two samples has shown mixed Eu valence states (Eu^{2+} and Eu^{3+}) in XAS measurements (Section 5.4.3), it is possible that the Pb layer on top of EuS could have been contaminated with PbS or PbO. Table 4.1 lists the scattering lengths corresponding to neutrons and X-rays for Pb, O, and S. When an atom of Pb is substituted with either O or S, the variation in SLD detected by X-rays is notably greater than that observed by neutrons. The sole parameter linking SLD in both methods is the number density (N). Consequently, to maintain consistency in the SLD characteristics across both techniques, the number density (N) remains constant throughout the analysis.

Table 4.1: Scattering lengths corresponding to neutrons and X-rays for Pb, O, and S.

	Scattering length	
Material	**neutrons (“b”)**	**X-rays (“f”)**
Lead (Pb)	9.41	78.13 - 8.94j
Oxygen (O)	5.80	8.05 - 0.04j
Sulfur (S)	2.85	16.33 - 0.55j

6. A convergence criterion is set before starting the fit, such as the fit being considered converged if the change in the FOM value is below a certain value over a range of iterations. Once this criterion is met, the magnetism parameters are fitted for the PNR datasets to match the splitting in spin-up and spin-down neutron measurements. The fitted magnetic parameters include the magnetization and magnetic roughness of both the EuS layer and the modified interface layers. As discussed previously, the *spec_adaptive* model provides an option to specify magnetic roughness, which helps disentangling the structural and magnetic profile of the sample.

To further check the quality of the fit, it is advantageous to perturb the fit from its minimum by changing any parameter’s value and see if it converges back to the same optimal point. For an in-depth analysis of the confidence in each parameter value and the model, the Refl1D software was used which is explained in the following section.

4.2 Refl1D software

The Refl1D program is used to analyze the converged fits from GenX software and to assess the reliability of the fitted models [108]. This software was used in the present study for uncertainty analysis and to find the correlation between pair of parameters for

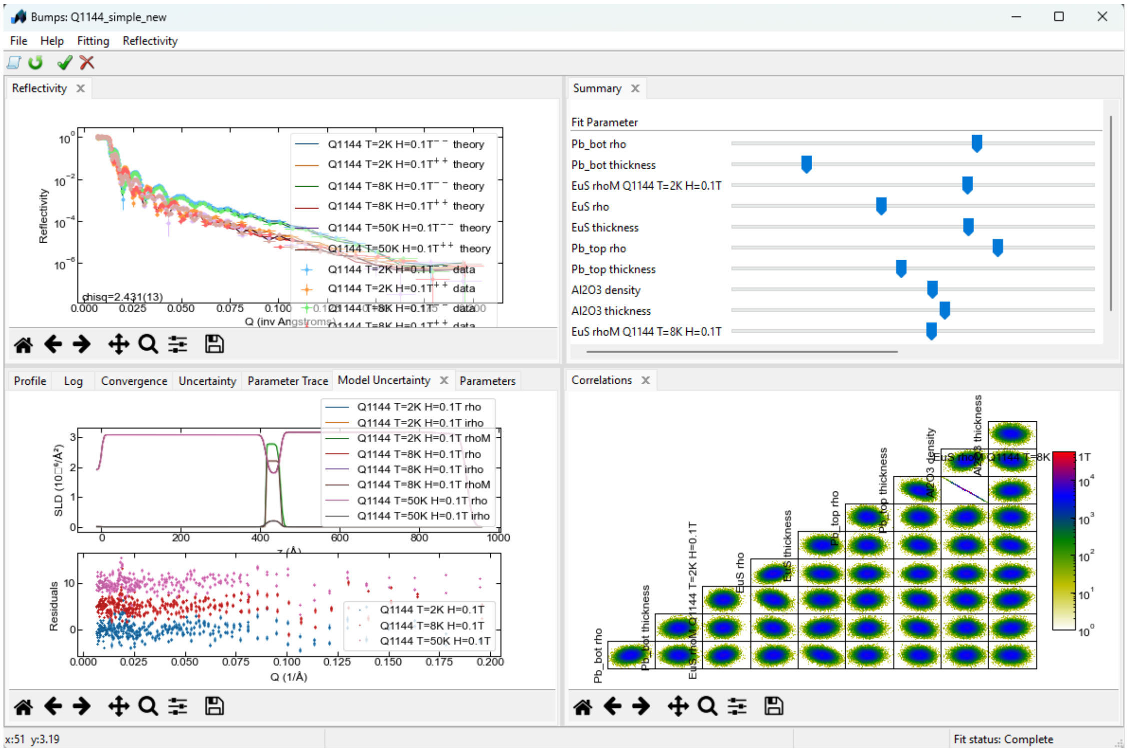

Figure 4.7: An image of the Refl1D user interface with defined sections. Top left: Reflectivity versus momentum transfer data and simulations for a set of datasets. Top right: Summary showing the present value of the parameters along with an option to change these values using the slider. Bottom left: SLD versus depth profile of the sample. Bottom right: Correlation chart for the set of parameters selected for fitting the data.

the complex models. The parameter initial values and their small boundaries (centered around the initial value) were determined using the data fitting results from the GenX software reflectometry analysis. The optimizer settings in Refl1D software were selected to explore the area surrounding the initial value of each parameter within the defined limits.

The fitting in Refl1D is based on a program called Bumps [109]. Bumps consists of a collection of routines designed for curve fitting and performing uncertainty analysis using Bayesian methods. The Bumps library has been used to analyze data in the areas of reflectometry [108, 33] and small-angle scattering [110].

4.2.1 Interface

The optimizer and its settings can be selected using the fitting option, more details in section (4.2.3). The window allows multiple sections to be viewed simultaneously. For example, Figure 4.7 demonstrates four panels displaying fit results, uncertainty in the model, correlation analysis, and a summary of the parameters. After the completion of the fit, uncertainty analysis information is extracted by selecting the "Export results" option in the "File" menu.

4.2.2 Bayesian analysis

Bayesian analysis is a statistical inference technique that applies Baye's theorem to determine the likelihood of a hypothesis based on the available evidence or information. The general equation is as follows.

$$P(H \mid E) = \frac{P(E \mid H).P(H)}{P(E)} \tag{4.4}$$

where, $P(H \mid E)$: Probability of hypothesis being true given the evidence (posterior)

$P(H)$: Probability of hypothesis being true (priors) before observation of evidence

$P(E \mid H)$: Probability of evidence given the hypothesis (likelihood)

$P(E)$: Probability of seeing the evidence

The posterior term, $P(H \mid E)$, helps in obtaining information on the mean value and uncertainties in the value of a parameter. The practical form of this equation that is useful for the fitting analysis is outlined below.

$$P(par_i \mid E, M) = \frac{P(par_i \mid M).P(E \mid par_i, M)}{P(E \mid M)} \tag{4.5}$$

Here, evidence is the data (E) and the hypothesis is a set of parameters (par_i) for a specific model (M). The parameters could be thickness, roughness, magnetization, etc. The term $P(E \mid par_i,M)$ evaluates how well the reflectivity curve matches the experimental data. The numerator in equation 4.5 must be computed for every potential set of parameters within the prior distribution $[P(par_i|M)]$.

4.2.3 Algorithm and optimizer settings

Bumps provides the option to choose from a list of algorithms to perform the fitting analysis. The algorithms available within this software include DiffeRential Evolution Adaptive Metropolis (DREAM), Nelder-Mead Simplex, Quasi-Newton BFGS, Levenberg-

Marquardt, Differential Evolution, etc. The faster algorithms such as Levenberg-Marquardt and Quasi-Newton BFGS tend to reach local minima rather than global fit minima. Thus, a slower but more robust algorithm (DREAM) was chosen that is more likely to reach global optima [111].

The DREAM algorithm is a population algorithm, especially suited to fitting and performing uncertainty analysis [112]. DREAM is an advanced Markov chain Monte Carlo (MCMC) method used for sampling from complex probability distributions, especially in Bayesian inference. The process begins with the initialization of a random population distributed using a uniform distribution across the parameter space. The candidate solutions are then updated using the Differential Evolution algorithm (Section 4.1.2) based on existing ones. The new candidate is then accepted or rejected based on the Metropolis criterion [113]. Over time, the distribution is adapted using the covariance matrix of the accepted samples to improve sampling efficiency, which is a technique called adaptive Metropolis. Multiple chains are run in parallel, and information is shared between them to enhance exploration of the parameter space avoiding any local optima.

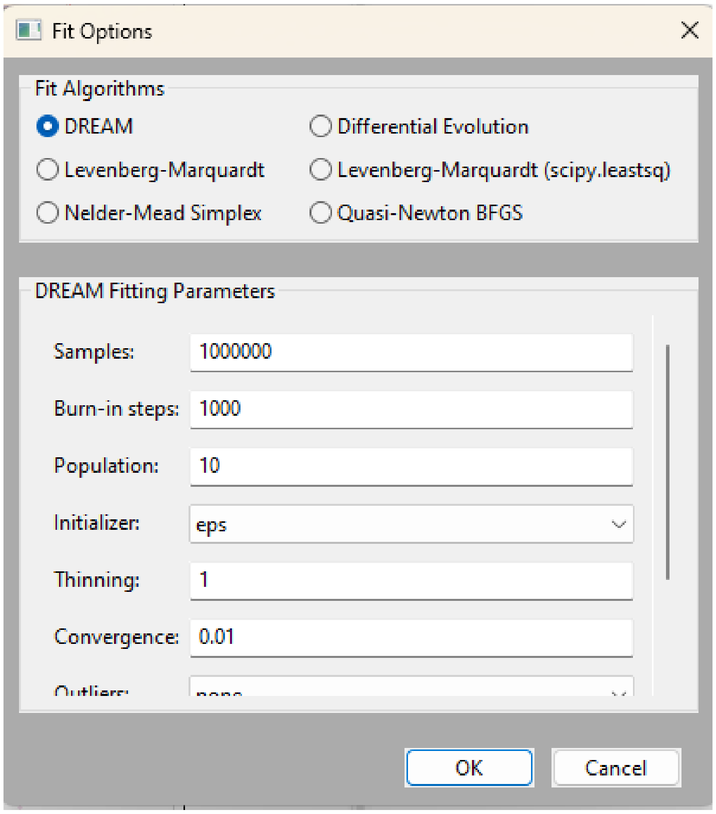

Fit Algorithms

● DREAM ○ Differential Evolution
○ Levenberg-Marquardt ○ Levenberg-Marquardt (scipy.leastsq)
○ Nelder-Mead Simplex ○ Quasi-Newton BFGS

DREAM Fitting Parameters

Samples: 1000000
Burn-in steps: 1000
Population: 10
Initializer: eps
Thinning: 1
Convergence: 0.01
Outliers: none

Figure 4.8: Fit options gives an option to choose between different algorithms. The optimization options with the DREAM algorithm are shown.

The convergence of the fit is monitored to assess when the chains have explored the target distribution sufficiently, ending in a stable population. Figure 4.8 shows the list of options that we can manipulate to perform an uncertainty analysis using DREAM. To determine the 95% confidence interval with two decimal places of precision, a minimum

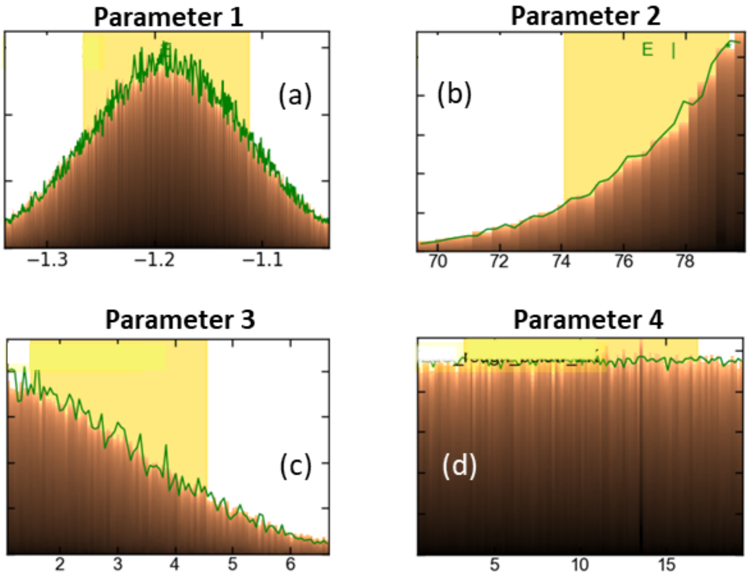

Figure 4.9: The probability distribution as a function of the parameter value on x-axis for the parameters, with each parameter's name labeled in the top of every inset image. (a) The mean value of the parameter 1 can be read from the center of the yellow region. (b) and (c) Skewed Gaussian distribution of the probability. (d) Uniform distribution for parameter 4.

of 10^7 samples is required.

4.2.4 Uncertainty and correlation analysis

Once a fit has converged (satisfied the convergence criterion), it is important to determine the uncertainty in the value of the estimated parameters and the cross-correlations between the pair of parameters. Repeating the fitting process multiple times can yield a slightly different optimal value for the parameter. Considering the measurement uncertainties and sample imperfections, a distribution of parameter values is obtained that fits the experimental data. In this study, correlation analysis was performed to assess whether the data contain sufficient information to conclusively identify the additional interfacial magnetic parameters or whether these parameters lead to greater uncertainties in other parameter values by promoting their cross-correlations. Figure 4.9 represents the posterior probability distribution for the parameters. Here, the y-axis denotes the probability (likelihood of observing a specific value), while the x-axis indicates the interval around the mean value explored to obtain the probability distribution. Furthermore, the mean value of the parameter for a Gaussian distribution [like the one shown in Figure 4.9 (a)] can be read from the center of the yellow region, and the uncertainty with a 95% credible interval for each parameter value is read from the range on the x-axis. A 95% credible interval indicates that there is a 95% chance that the actual parameter value falls within this interval. The x-axis of the probability distribution shows a segment of the specified boundary for the parameter value and captures 95% of the distribution's values within this range when the distribution shape is close to a peaked Gaussian. These values are obtained for each parameter after multiple fitting iterations. The central yellow region in each of the inset images represents the uncertainty in the mean value up to the confidence interval 68% and the error reported in the value of the parameter. The curve (in green line on top of each curve) shows the highest probability observed (best likelihood for the bin), since the parameter value is restricted to that bin. Moreover, if the maximum likelihood green line does not align with the overall pattern of the histogram for the parameter, it indicates that the region around the best value of the parameter is not adequately explored.

The selection of the prior distributions for the parameters can greatly affect the shape of the resulting probability distributions [114]. In reflectometry, it is common to choose uniform priors when there is a limited prior knowledge on parameter values, which may lead to a probability distribution that is non-Gaussian. In the current study, since the initial parameter values were extracted from the GenX fitting analysis (Section 4.1), Gaussian priors were selected for both the uncertainty and correlation analysis, which are expected to produce a Gaussian probability distribution. However, sometimes, due to the strong correlation between parameters or the physical constraints, the shape of the distribution can be non-Gaussian. Figures 4.9 (b) and (c) depict a skewed distribution for a parameter limited by boundaries, where constraints might be physical, such as non-negative roughness or thickness. Hence, a skewed or truncated probability distribution remains inevitable. A uniform distribution is shown in Figure 4.9 (d) for parameter 4, indicating equal likelihood in the range and insensitivity of the fit to the parameter value.

In addition to the uncertainties in the parameter values, the software gives a chart of correlations between the pair of parameters that were selected to fit the data. The correlation determines whether the value of a specific parameter can be estimated independently relative to other parameters of the model. Figure 4.10 shows an example of the correlations for a pair of parameters with a guide to interpret the axis for the curves. The boundaries/scale of the y and x axes for each of these boxes is the same

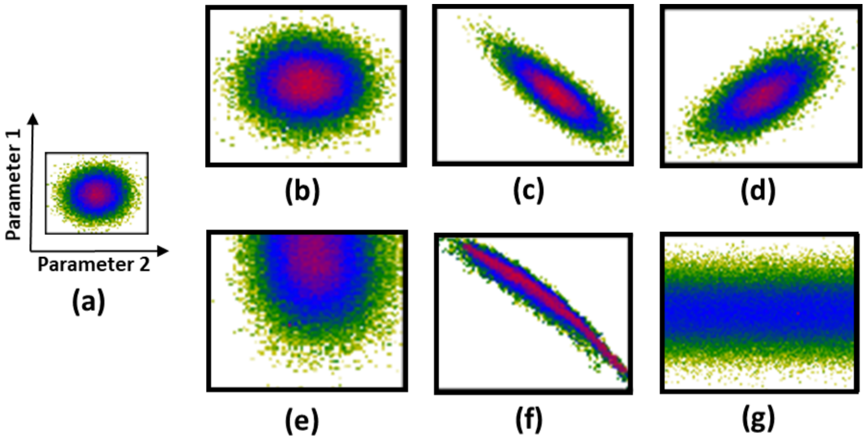

Figure 4.10: Examples of parameter cross-correlations: (a) Axis guide. (b) A near-circular shape indicates weak or no correlation (c) Positive correlation (d) Negative correlation (or anticorrelation). (e) Truncated correlation plot. (f) Strong positive correlation (g) Uniformly distributed correlation plot.

as the scale on the uncertainty plots for each parameter. A close to circular shape (shown in Figure 4.10 (b)) represents a weak or no correlation that means the values for the parameters can be uniquely determined from the fit. Figure 4.10 (c) and (d) show an ellipsoidal shape for the positive and negative correlation plots, respectively. The positive (negative) correlation in this context indicates that when one parameter experiences positive fluctuations, it is associated with positive (negative) fluctuations in the corresponding parameter of the pair [114]. There is a correlation between parameters, but the distribution is still peaking inside the box, so, their values can be estimated with some uncertainty. Figure 4.10 (e) shows the correlation plot that is cut at the one end since the value of parameter 1 is restricted by the defined boundaries due to physical limitations on the value of parameter.

An example of a strong correlation between parameters is shared in Figure 4.10 (f). A strong correlation means that the parameter values cannot be determined uniquely from the fits. The parameters try to compensate for each other during the fitting process, and there exist many combinations of their values that can fit the data in the same way. Thus, there is not enough information in the data to uniquely determine them. For example, it is difficult to determine the thickness of two neighboring layers if the SLD contrast is low for these materials for a technique. For the present study, the difference in SLD for Pb and the capping layer is around $\Delta SLD \approx 0.17\text{x}10^{-6}$ Å^{-2} for neutrons. Thus, it is hard to determine the thickness of these layers with PNR alone. Therefore, XRR is helpful as a complementary technique that provides a higher SLD contrast between layers. Figure 4.10 (g) illustrates a distribution curve that is uniformly spread in one direction, which means that the fits lack enough information to determine the correlation between the parameters.

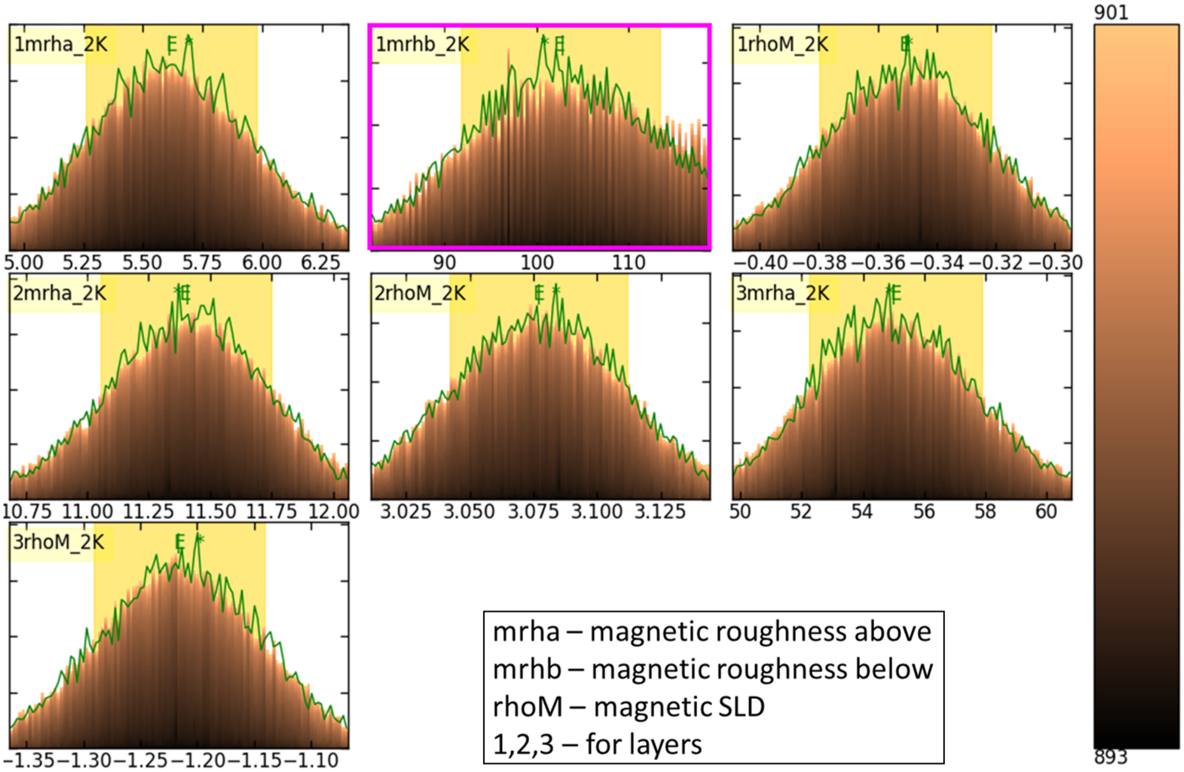

Figure 4.11: The probability distribution function for the group of parameters, with each parameter's name labeled in the top left corner of every inset image. The pink box shows that the full Gaussian distribution is lacking, as the value of the parameter is restricted by the boundaries.

An example of the actual uncertainty and correlation plots for a set of parameters is shared in Figures 4.11 and 4.12. The plots show a guide to read the names of the parameters. These plots are for the sample with three magnetic layers, and the layers are marked with a number from 1 to 3 (bottom to top). The analysis was performed only for the parameters that defined the magnetic profile of the sample. The parameters include magnetism in the layer (rhoM), magnetic roughness towards the surface (mrha), and bottom (mrhb) at a temperature of 2 K. The colored boxes are examples of plots discussed earlier in the section.

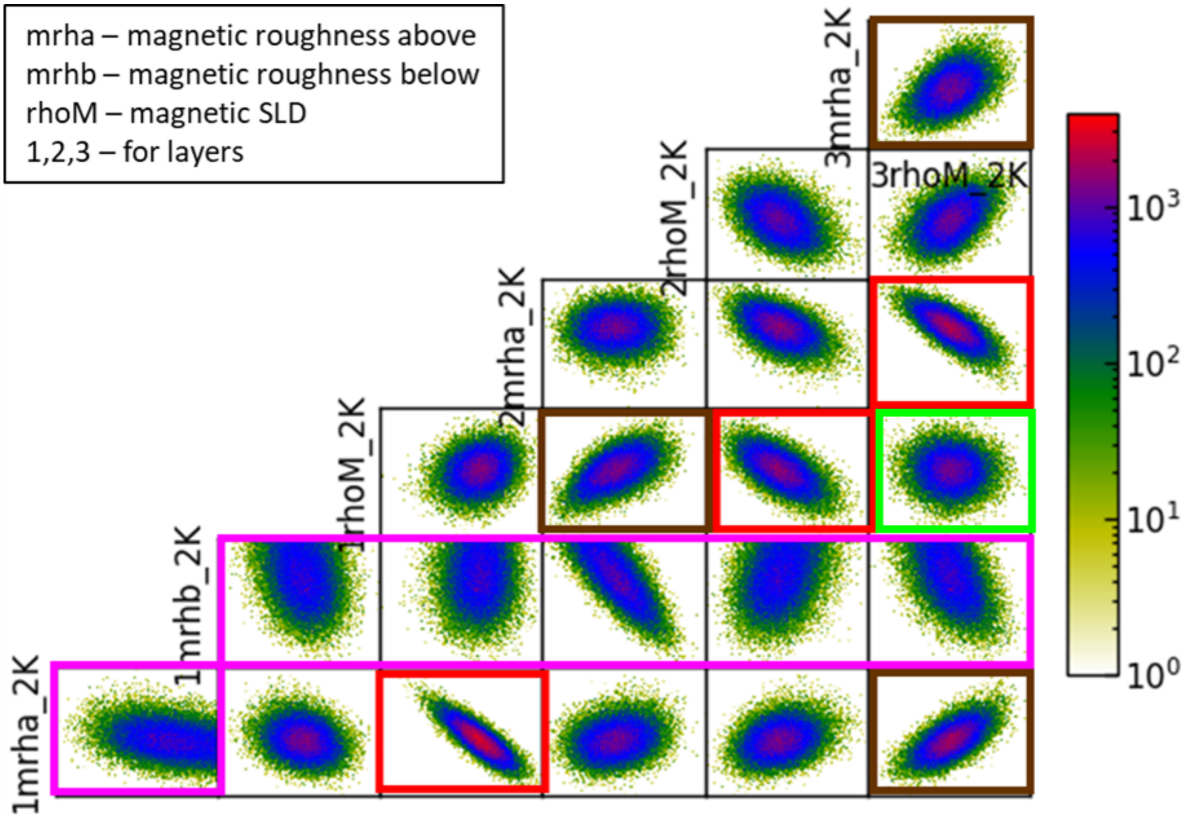

Figure 4.12: A chart of cross-correlations between parameters. Bright green box: weak correlation. Brown box: positive correlation. Red box: anti-correlation. Pink box: truncated correlation plots.

Chapter 5

Magnetic proximity effects study

5.1 Motivation

Topological states, potentially leading to the formation of Majorana bound states (MBSs), have been predicted to emerge in device systems consisting of a conventional superconductor (SU) and a semiconductor (SE) in close proximity to each other [115, 116]. SE material must have large spin-orbit split bands. One of the proposed device structures is a nanowire geometry with the SE nanowire in close proximity to the SU. To facilitate the emergence of MBSs within the system, it is essential to introduce the Zeeman energy. This is achieved by applying an external magnetic field aligned with the axis of the nanowire structure, which lifts the spin degeneracy. As the magnetic field strength increases, the system undergoes a topological phase transition and the MBSs appear in the system. However, applying a magnetic field from outside is not a good choice, as it is detrimental to the superconductivity, restricts the operations, and complicates the scaling of this technology.

One of the methods to overcome the challenges is to incorporate a ferromagnetic insulator material (FM) into the device structure that can meet the requirement of an external magnetic field through magnetic proximity effects (MPEs) at the interfaces [20]. A theoretical study by Liu *et al.* [21], on a nanowire geometry shown in Figure 5.1, to study the extension of electronic wave function across the interfaces concluded that MPEs at both EuS interfaces are needed to put the system in topological state. Therefore, the initial step towards the development of an intrinsically topological trilayer structure is to ensure adequate strength of magnetic proximity effects (MPEs) at the interfaces.

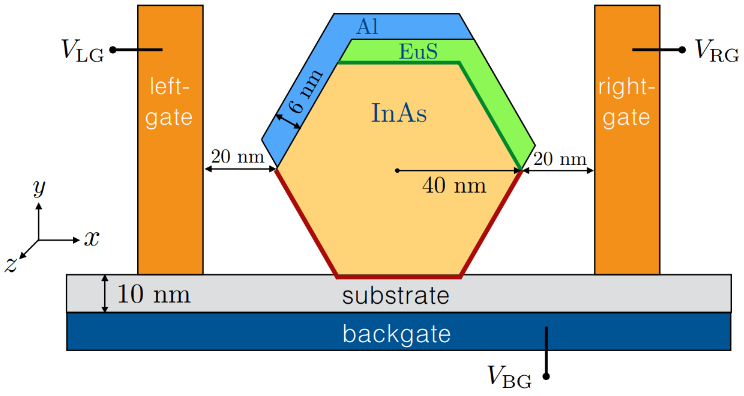

Figure 5.1: A cross-section of a hexagonal nanowire made of a semiconductor (InAs) in close proximity to a superconductor (Al) and a ferromagnetic insulator (EuS). This image is taken from ref. [21]

In a theoretical investigation conducted by Bergeret *et al.* [117] concerning SU/FM structures, it was determined that a ferromagnetic material has the potential to affect the electronic and magnetic characteristics of an adjoining nonmagnetic or superconducting material. This influence occurs without the necessity for a direct exchange of charge carriers. This contributes to the conjecture that the necessary Zeeman energy for breaking spin degeneracy within the nanowire may be supplied through the exchange interaction with the ferromagnetic (FM) layer.

Recent experiments have shown evidence of finite exchange fields in SE nanowire coupled with FM, as observed through transport measurements and tunnel spectroscopy measurements [19]. In addition, Escribano *et al.* [118] introduced a planar SM/FM/SU heterostructure, using FM as a spin-polarizing barrier, investigated the thickness of the FM layer to achieve the topological regime, and compared it with the initial nanowire configuration. The study on the nanowire and planar geometry of SU/FM/SE materials is still in progress, focusing on assessing the interplay between different materials along with the manifestation of MPEs. The ultimate goal is to eliminate the need for an external magnetic field and establish the optimal environment necessary for the detection of MBSs.

5.2 Aim

The primary aim of this investigation was to examine the presence of MPEs in systems consisting of layers of FM, SU, and SE. This study aimed to determine whether these effects existed and, if so, to explore the extent and variability of these effects with

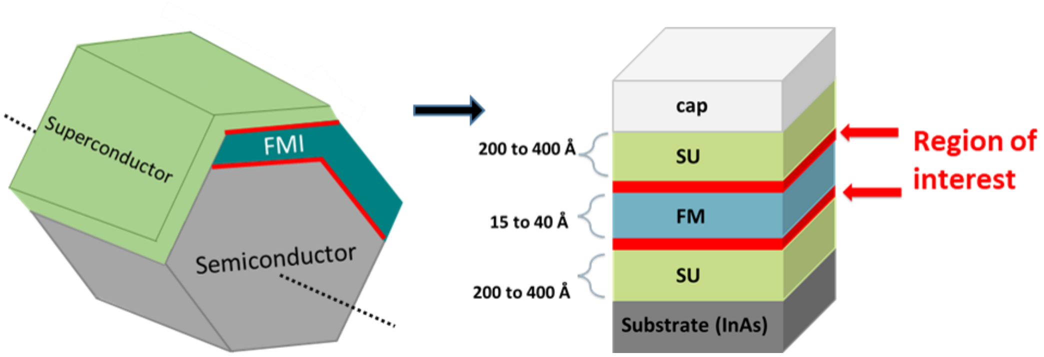

Figure 5.2: (a) Cross-sectional view of a schematic of a hexagonal SE nanowire in close proximity to a SU and FM. The red strips displays the interfaces SE/FM and SU/FM. (b) A schematic of the planar geometry (heterostructure). The range of thicknesses is mentioned besides each layer. The region of interest for the present study is marked with red color on the schematic.

changes in temperature and external magnetic fields. Furthermore, the objective was to investigate how superconductivity influences MPEs. A comprehensive understanding of the magnetic interactions at the SU/FM interface is anticipated to contribute significantly to the optimization of the final structure of the quantum device.

5.3 Approach

A planar arrangement of the materials was selected to investigate MPEs at the SU/FM interface because this configuration provides a higher interface contact between FM and SU materials than a nanowire geometry, which facilitates the induction of MPEs. Furthermore, the planar geometry simplifies the experimental exploration and examination of MPEs. Therefore, a comprehensive study of the structure and magnetism was conducted using heterostructures consisting of lead (Pb) and europium sulfide (EuS) layers that were grown on an indium arsenide substrate (InAs). The choice of materials is discussed in the chapter on materials and fabrication (Chapter 2). For this investigation, four heterostructures featuring the InAs/Pb/EuS/Pb configuration were fabricated, with thicknesses ranging from 200 to 400 Å for Pb and 15 to 40 Å for EuS, as illustrated in Figure 5.3. For three samples, the thickness of the EuS layer was changed from 4 to 1.5 nm, keeping the Pb thickness the same. However, for one of the samples, the Pb thicknesses were changed to 40 nm. The motive behind the change of thickness was to see which minimum thicknesses of EuS and Pb are enough to observe the MPEs in heterostructures, keeping in mind the originally proposed device structure. An aluminum oxide layer was deposited as a capping layer to protect the surface of the sample from contamination, oxidation, or surface reactions. The details of the fabrication of these samples can be found in the chapter on materials and fabrication (Chapter 2).

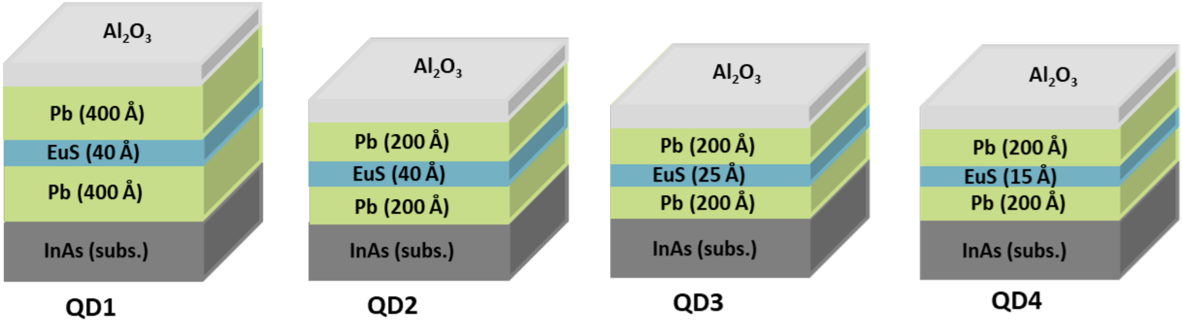

Figure 5.3: Schematic of the samples used in the study, illustrating the intended thicknesses and stacking sequence. The term QD refers to Quantum Device.

X-ray diffraction (XRD) and transmission electron microscopy (TEM) techniques were used to acquire information on the crystalline structure of the thin films and the quality of the interfaces between layers. The originally proposed device structure requires Pb to be in the superconducting state and EuS to be in the ferromagnetic state for the MBSs to emerge in the system. It was important to know the Curie temperature (T_C) of EuS, the superconducting transition (T_{SU}) of the Pb layers and how they vary with the temperature and applied magnetic fields. Therefore, SQUID magnetometry was performed to obtain information about transition temperatures and their variations. X-ray absorption spectroscopy measurements provide information on the elemental contribution to the magnetism observed in the samples. The polarized neutron reflectometry (PNR) technique was used to acquire information on the structure and magnetism with depth. PNR has been a technique of choice for studying magnetic proximity effects [27, 31, 33, 34, 36, 37]. X-ray reflectometry (XRR) was used to have a different SLD contrast between the layers to complement information on the structure with depth. PNR and XRR will help to locate MPEs in the samples if present.

5.4 Results and discussion

5.4.1 Characterization of crystalline structure

The XRD patterns presented in Figure 5.4 show the observed peaks associated with the crystallographic orientation of the layers within the samples. Measurements were

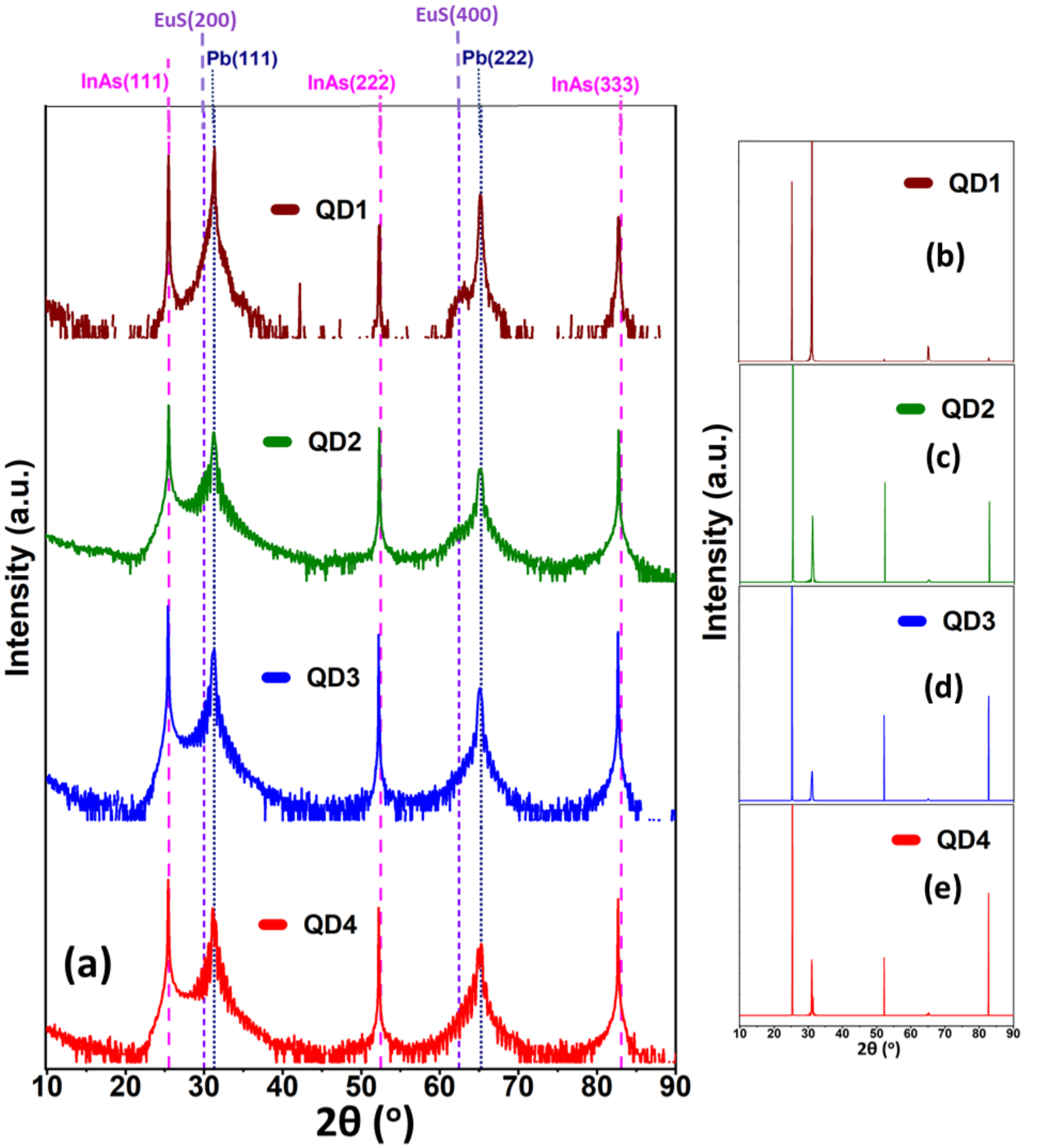

Figure 5.4: XRD results along with the reference peaks of InAs (pink), EuS (violet) and Pb (royal blue). (a) The XRD data is shown in logarithmic scale and shifted along the y-axis to enhance visibility. (b)-(e) The inset images shows the full XRD pattern on linear scale.

performed in θ - 2θ scanning mode; therefore, the lattice planes parallel to the surface of the sample were probed. The indexing of the reference peaks was performed by comparing the crystallographic powder data for the materials InAs [119], Pb [120] and EuS [121]. Table 2.1 provides details on the type of crystal structure and lattice parameters for the InAs, Pb, and EuS materials. In particular, pronounced XRD peaks appear at angles of 2θ of approximately 25.49°, 31.31°, 52.32°, 65.12°, and 82.74°. XRD peaks at 25.49°, 52.32°, and 82.74° are identified as substrate peaks corresponding to reflection planes InAs(111), InAs(222), and InAs(333), respectively. XRD peaks at 31.31° and 65.12° correspond to reflection planes Pb(111) and Pb(222). There are no strong and distinct peaks in the XRD results that could be attributed to the EuS. However, a shoulder/asymmetry is observed in Pb(222) peak at the expected EuS(400) peak for the QD1 and QD2 samples. Table 5.1 lists the calculated lattice parameters for the unit cell of Pb and InAs. To calculate these parameters, equations 3.39 and 3.40 were used (Section 3.2.2). The 2θ values were read from the peaks for Pb and InAs corresponding to each sample.

Table 5.1: Calculated unit cell parameters using the 2θ values.

	Lattice parameter "a" (Å)	
Sample	**Pb**	**InAs**
QD1	4.96 (± 0.01)	6.05 (± 0.01)
QD2	4.96 (± 0.01)	6.05 (± 0.01)
QD3	4.96 (± 0.01)	6.07 (± 0.01)
QD4	4.96 (± 0.01)	6.06 (± 0.01)

Figures 5.5 (a) and (b) show enlarged views of the XRD peaks at 31.31° and 65.12°, respectively. Interference fringes are present in the vicinity of the peaks in all samples, except that the fringes are smeared for the QD1 sample peak at 65.12°. The intensity of the fringes drops as we move away from the central intense fringe. In particular, for the QD1 sample, the difference between the 2θ values corresponding to the fringe peaks is comparatively lower, while this discrepancy is nearly uniform among the remaining samples. The interference fringes around the peaks in Figure 5.5 are identified as Laue oscillations, which occur as a result of coherent scattering of X-rays from atoms within a crystalline domain. For the QD4 sample, two peaks are observed at the center of these oscillations, while only one peak was observed for the other samples. Table 5.2

lists the calculated coherence lengths, which are estimates of the distance over which the exact same crystallite extends without dislocation or grain boundary. To calculate these lengths, equation 3.41 is used (Section 3.2.2).

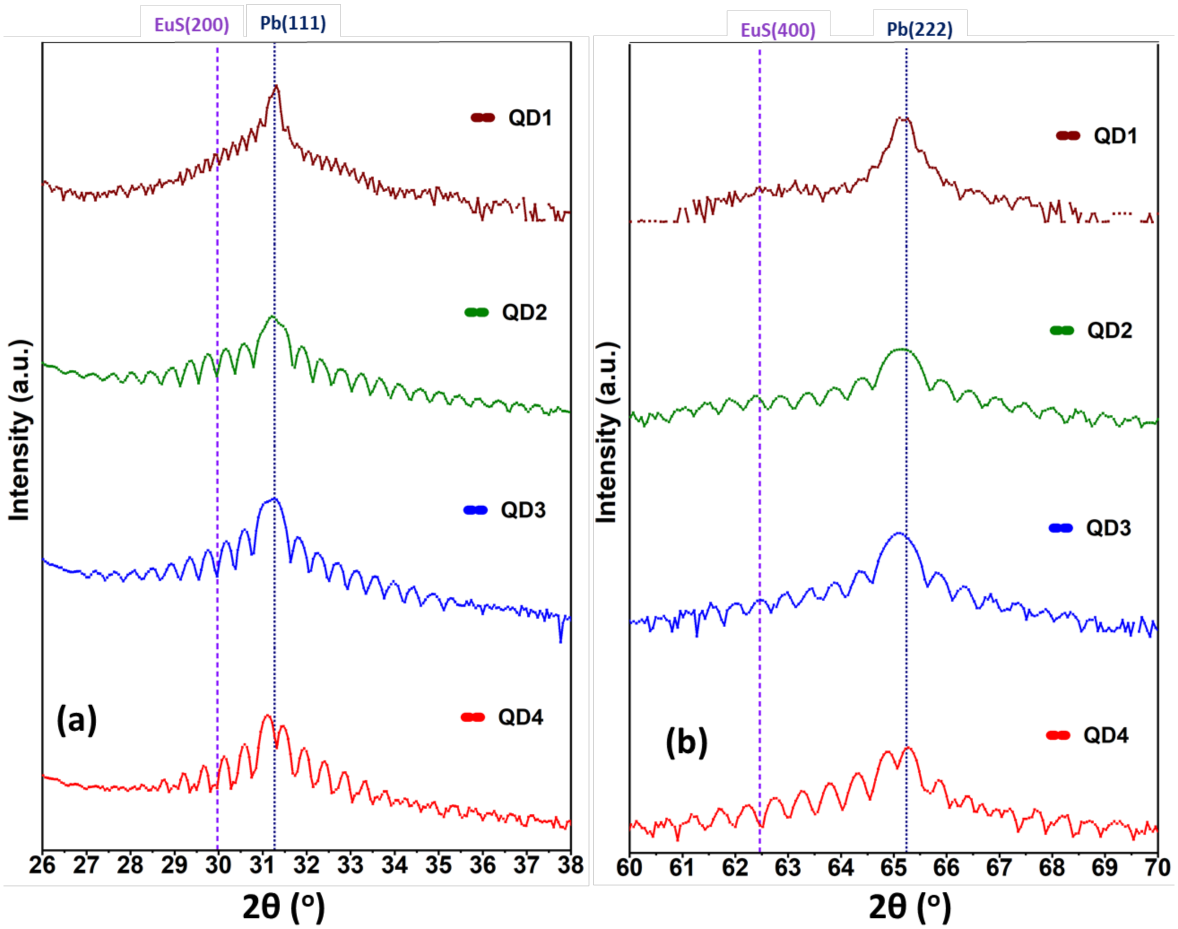

Figure 5.5: A magnified view of the XRD results around the peaks observed near (a) 31.31° (b) 65.12°.

Figure 5.6 shows TEM results of the cross section of the QD1 sample with varying resolution, respectively. The direction of the crystal orientations is marked with arrows on the layers Pb (green), EuS (red), and InAs (light gray) in Figure 5.6 (a). Insets (b) and (c) in Figure 5.6 show the magnified images of the EuS/Pb and Pb/InAs interfaces, revealing the well-ordered interfaces between the materials. The number of formula units can be counted in the enlarged TEM image [Figure 5.6 (c)], resulting in approximately 26.5 InAs and 33 Pb formula units. This gives a ratio of about 0.81, indicating a difference of roughly 20 %. Figure 5.6 (d) highlights the crystalline quality of the EuS layer and its interfaces with the Pb layers. Insets (e), (f) and (g) in Figure 5.6 show zoomed regions in the EuS layer and their crystal orientations. Figure 5.7 shows the TEM results for the sample QD2. For the QD2 sample [Figure 5.7 (c)], the number of formula units for InAs and Pb is approximately 15.5 and 19, resulting in a difference of approximately 20 % (similar to the QD1 sample).

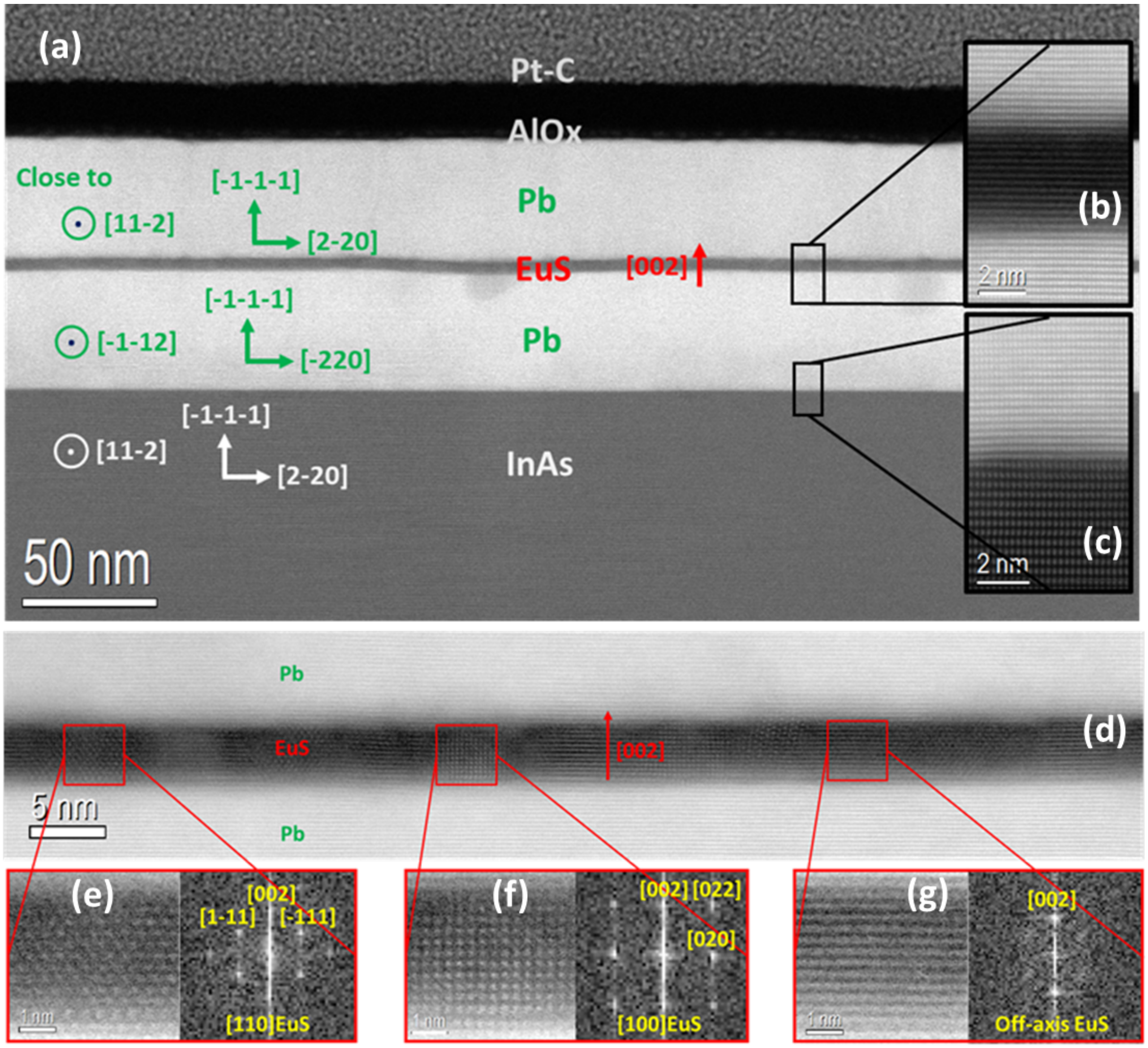

Figure 5.6: TEM images for the sample QD1 show layers with varying resolution. (a) 50 nm scale micrograph of the sample. The direction of the crystal orientations are marked using different colored arrows on the layers. Micrographs at 2 nm scale for the zoomed-in regions of the (b) EuS/Pb interfaces and (c) Pb/InAs interface. (d) 5 nm scale micrograph shows the EuS layer and its interfaces with Pb layers. Figs. (e), (f), and (g) depict various crystal orientations in the zoomed-in regions at 1 nm scale.

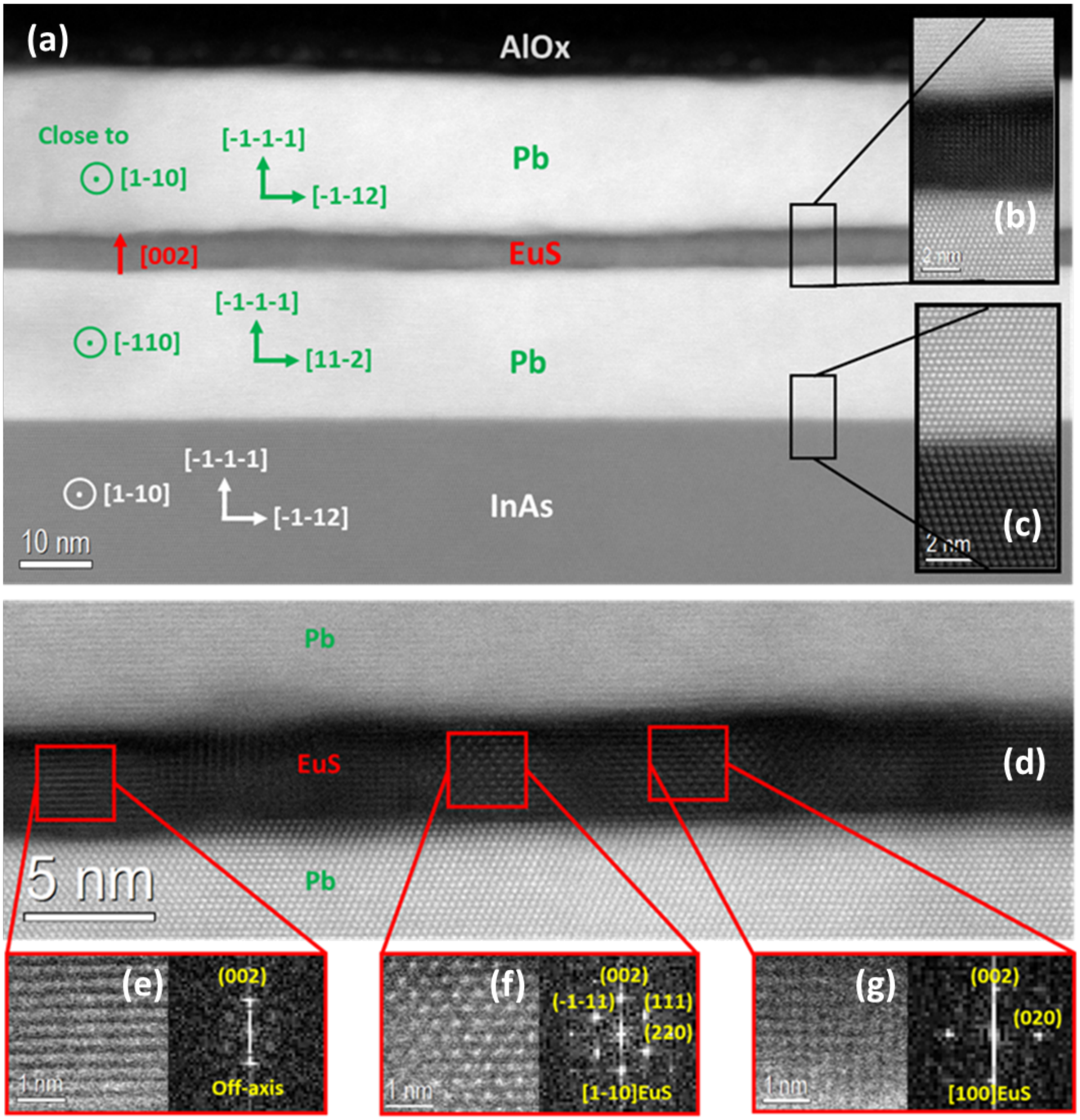

Figure 5.7: TEM images for the sample QD2 show layers with varying resolution. (a) 10 nm scale micrograph of the sample. The direction of the crystal orientations are marked using different colored arrows on the layers. Micrographs at 2 nm scale for the zoomed-in regions of the (b) EuS/Pb interfaces and (c) Pb/InAs interface. (d) 5 nm scale micrograph shows the EuS layer and its interfaces with Pb layers. Figs. (e), (f), and (g) depict various crystal orientations in the zoomed-in regions at 1 nm scale.

In summary, XRD and TEM results provide crystalline structural characterization of the samples. XRD analysis identified distinct peaks for InAs and Pb, while EuS lacks clear peaks. The determined lattice constant for Pb is approximately 4.97 Å, which closely matches the value reported in the literature [56]. In addition, the inset images (c) of Figs. 5.6 and 5.7 show that Pb is fully strain relaxed on InAs and shows a single-crystalline oriented growth. Both TEM and XRD confirmed that the crystal growth of both Pb films, grown on InAs and EuS, is along the same crystal lattice direction as that of the crystalline substrate InAs, indicating epitaxial growth of the Pb layers. It is surprising that any single-crystalline growth would develop in both Pb layers, despite the 20 % lattice mismatch of Pb with InAs and EuS. Furthermore, the observation of Laue oscillations close to the XRD peaks of Pb indicates well-defined crystal planes that are highly uniform and coherent. The coherence lengths calculated from the Laue oscillations [Table 5.2] are close to the thicknesses of the Pb layers in the samples. It is an indicator of the high crystalline quality of the Pb layers.

Table 5.2: Calculated coherence length (X_L) using the difference in the 2θ values between the two fringe peaks in Figure 5.5.

	Coherence length (Å)	
Sample	**XRD peak at 31.31°**	**XRD peak at 65.12°**
QD1	440 (± 160)	-
QD2	220 (± 39)	200 (± 29)
QD3	200 (± 39)	223 (± 35)
QD4	196 (± 31)	197 (± 28)

Furthermore, there are no peaks in the XRD results that could be attributed to EuS. Due to the low thicknesses ($\leq$ 35 Å), a very small volume contributes to its observable XRD peaks. In addition, TEM results for both QD1 [Figure 5.6 (e) to (g)] and QD2 [Figure 5.7 (e) to (g)] samples show that the crystal grains in the EuS layer are randomly aligned in the in-plane direction, but consistently exhibit the same out-of-plane orientation (002). This indicates the textured growth of the EuS layer in the samples. According to the Scherrer equation [122], the width of the XRD peak is inversely proportional to the size of the crystallite. Therefore, the expected XRD peaks may be broadened or concealed by the more prominent XRD signals originating from the substrate and Pb layers. Moreover, due to the amorphous nature of the aluminum oxide capping layer, its characteristic peaks are expected to be broad and diffuse, as it lacks a long-range atomic order [87].

5.4.2 Volume magnetometry

Magnetization as a function of temperature was recorded in the range 2 to 50 K for the samples. The data were recorded in both the zero-field-cooled warming (ZFCW) and field-cooled cooling (FCC) states of the samples in the presence of an applied magnetic field in the plane ($H_{ext,//}$). The Curie transition for EuS and superconducting transition for Pb are expected to occur around 16.5 K and 7.2 K, respectively. The normalization process of the data and the estimation of transition temperatures are discussed in Chapter 2 (Section 3.2.4). The arm of the data that is not marked, yet falls within the same field, is recorded while operating in FCC mode.

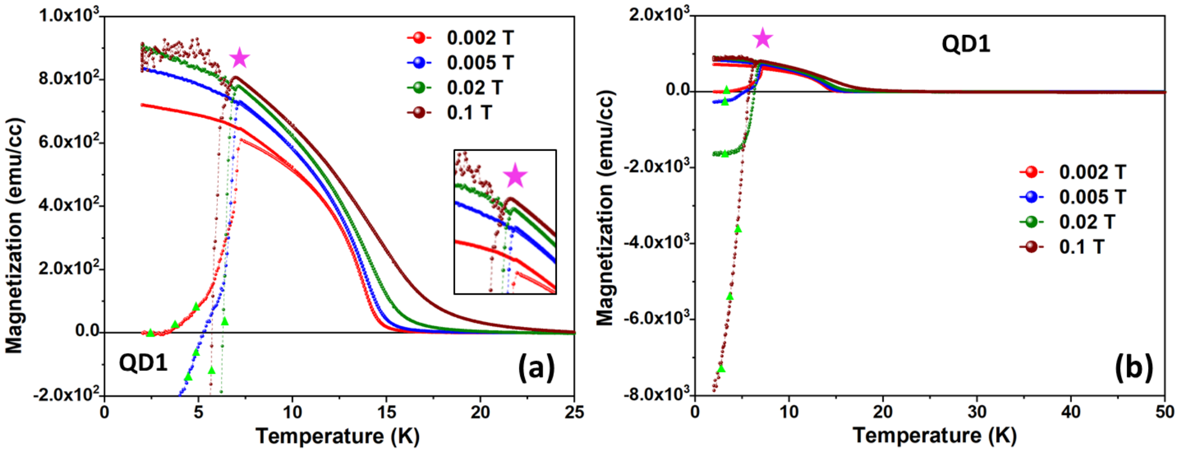

Figure 5.8: Magnetization as a function of temperature for the QD1 sample in presence of 0.002, 0.005, 0.02, and 0.1 T are shown. The triangles (in bright green) on the curve indicates the ZFCW data for each field. (a) Magnified view of the low temperature behavior. Inset shows the enlarged view of the data near the pink star. (b) Full temperature and magnetization range. The dotted lines serve as a guide to the eye.

Figure 5.8 shows the magnetization versus temperature data for QD1, with panel (a) showing a magnified view of the low temperature behavior and panel (b) showing the full range for both axes. A splitting between the ZFCW and FCC mode data is observed around 7 K for all the magnetic fields. This splitting at low temperatures increases with an increase in magnetic field strength. For the ZFCW data, a decrease in magnetization is observed with a decrease in temperature below 7 K. Moreover, a notable decrease in FCC mode data is detected at approximately 7 K, as shown in the inset image of Figure 5.8 (a). This dip is more pronounced in the data recorded in a magnetic field of 0.1 T. Moreover, within the temperature interval spanning from 14 K to 20 K, there is an observed significant drop in magnetization for all fields that ultimately reach a zero value.

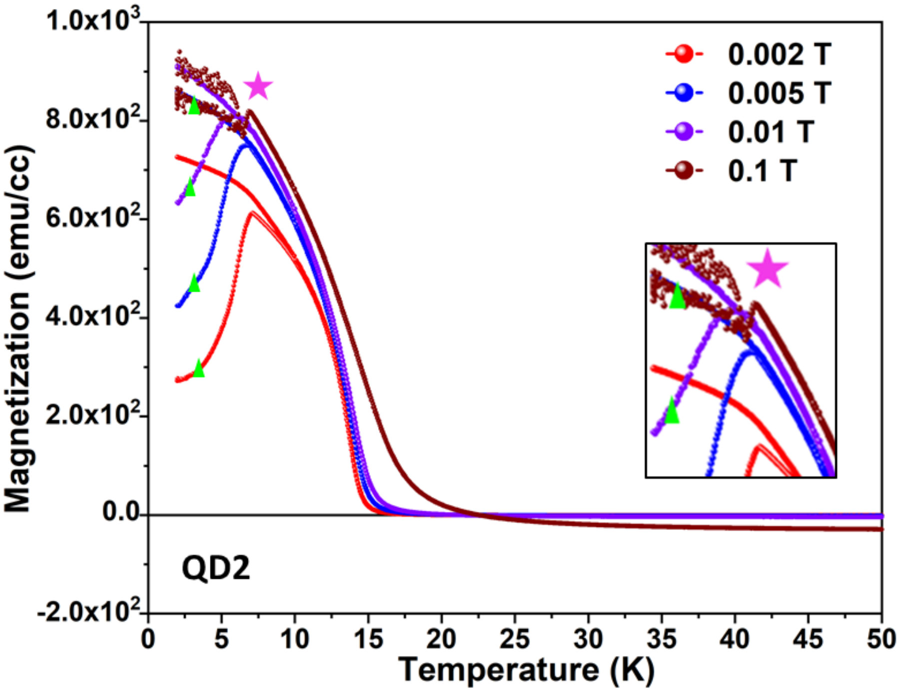

Figure 5.9: Magnetization as a function of temperature for the QD2 sample in presence of 0.002, 0.005, 0.01, and 0.1 T are shown. Inset shows the enlarged view of the data near the pink star. The dotted lines serve as a guide to the eye.

Figure 5.9 shows the magnetization versus temperature data for QD2. Similarly to QD1, a splitting between the ZFCW and FCC mode data is observed around 7 K for all the magnetic fields. In contrast to the QD1 sample, the splitting tends to decrease with an increase in magnetic field strength. Moreover, similar to QD1, a notable decrease in the FCC mode data in 0.1 T is detected at approximately 7 K, as shown in the inset image of Figure 5.9.

Figure 5.10 shows the magnetization versus temperature data for the sample QD3. Similarly to QD1 and QD2, a splitting between the ZFCW and FCC mode data is observed around 7 K for all the magnetic fields. In contrast to the data in 0.002 and 0.1 T, the ZFCW data in 0.01 T initially show a decrease with decrease in temperature, followed by a transition to an almost linear behavior, and then exhibit another decline as the temperature approaches 2 K. Furthermore, a notable decrease in the FCC mode data for 0.01 and 0.1 T is detected at approximately 7 K, higher in 0.1 T than in 0.01 T as shown in the inset image (c) of Figure 5.10.

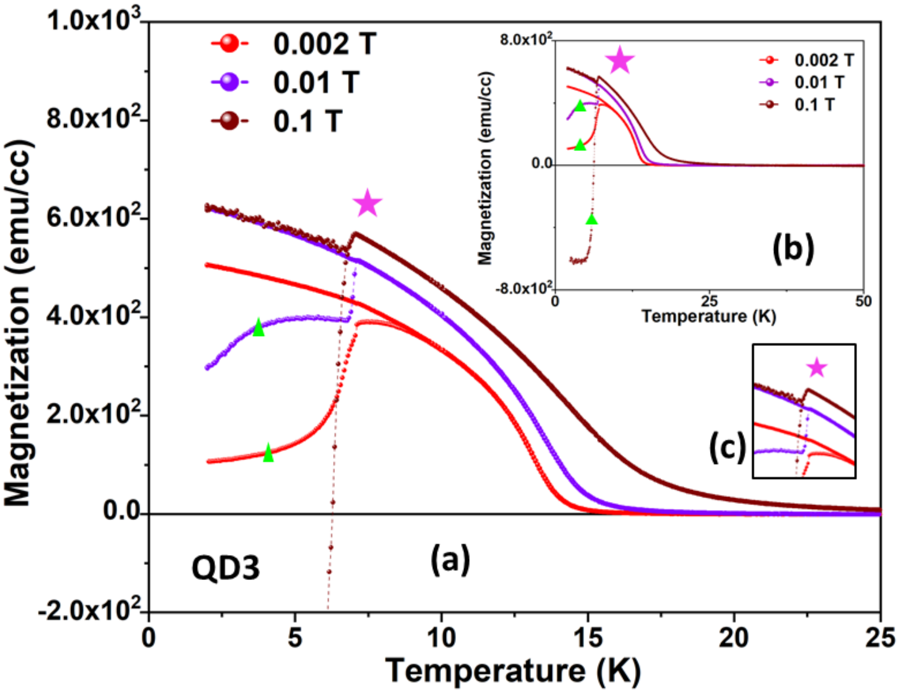

Figure 5.10: (a) Magnetization as a function of temperature for QD3 sample in presence of 0.002, 0.01, and 0.1 T are shown. The triangles (in bright green) on the curve indicates the ZFCW data for each field. (b) M versus T data in full temperature and magnetization range. (c) The enlarged view of the data near the pink star. The dotted lines serve as a guide to the eye.

Figure 5.11 shows the magnetization versus temperature data for QD4. Similarly to the other samples, a splitting between the ZFCW and FCC mode data is observed around 7 K for all the magnetic fields. Similarly to the ZFCW data in 0.01 T for the QD3 sample (Figure 5.10), the ZFC data in 0.002 and 0.005 T initially show a decrease, followed by an increase in magnetization and then exhibit another decline as the temperature approaches 2 K. Furthermore, a notable decrease in FCC mode data is detected for all fields at approximately 7 K, highest at 0.1 T, as shown in Figure 5.11.

The approach to determine T_C and T_{SU} is explained in the chapter on methods (Section 3.2.4). Table 5.3 list the values of T_C for the samples for the measurements in Figures 5.8 to 5.11, respectively. T_C is found to be the lowest in the case of the QD4 sample and is followed by T_C of the QD3 sample. Meanwhile, T_C for QD1 and QD2 are approximately the same under all magnetic field conditions examined.

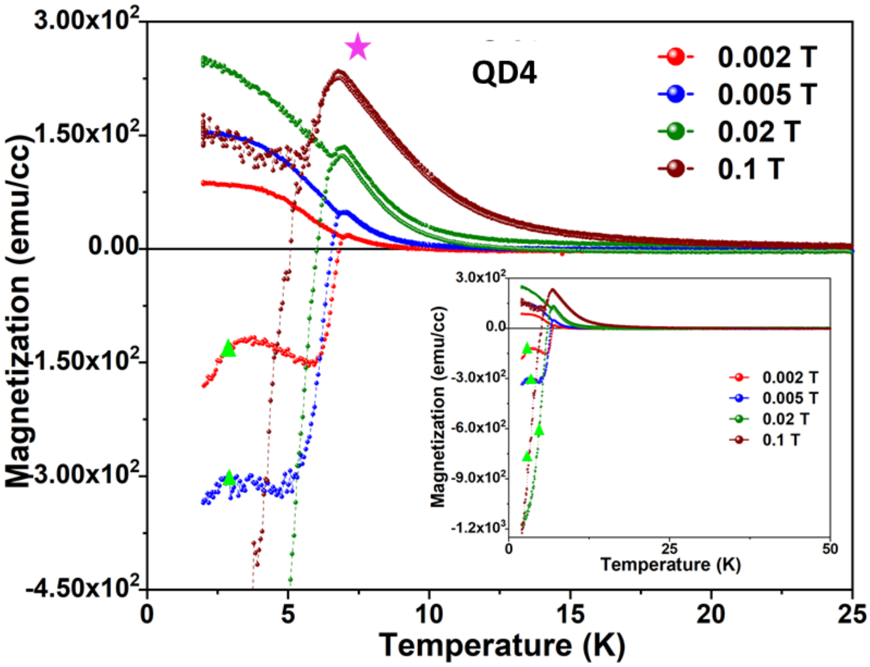

Figure 5.11: Magnetization as a function of temperature for QD4 in presence of 0.002, 0.005, 0.02, and 0.1 T are shown. The triangles (in bright green) on the curve indicates the ZFCW data for each field. Inset show the data in full temperature and magnetization range. The dotted lines serve as a guide to the eye.

Table 5.3: Curie transition temperature (T_C) for the samples. Missing values are due to lack of measurements at these fields.

$H_{ext,//}$ =	**0.002 T**	**0.005 T**	**0.01 T**	**0.02 T**	**0.1 T**
Sample	**Curie temperature (T_C, K)**				
QD1	14.28 (± 0.03)	14.53 (± 0.03)	-	15.26 (± 0.04)	16.96 (± 0.07)
QD2	14.05 (± 0.02)	14.51 (± 0.03)	14.89 (± 0.04)	-	16.46 (± 0.05)
QD3	13.83 (± 0.03)	-	14.39 (± 0.04)	-	15.72 (± 0.04)
QD4	7.3 (± 0.1)	8.3 (± 0.1)	-	8.9 (± 0.2)	11.1 (± 0.4)

Figure 5.12 shows the variation of T_C as a function of the magnetic field for the samples. T_C for the bulk EuS (16.5 K) is marked as a reference in the figure, providing a baseline for comparison. For all samples, T_C is observed to increase with increasing

magnetic field. For the samples QD1 and QD2, T_C in 0.1 T is slightly higher than the bulk EuS T_C.

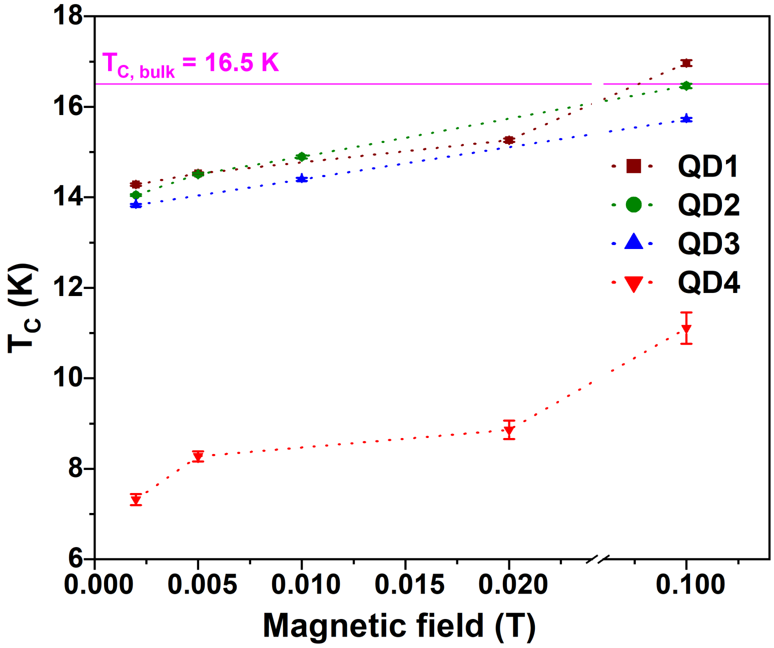

Figure 5.12: Curie temperature (T_C) as a function of magnetic field for sample. The horizontal line in pink at T = 16.5 K is the T_C for the bulk EuS. The dotted lines serve as a guide to the eye.

Table 5.4: Superconducting transition temperature (T_{SU}) for the samples. Missing values are due to lack of measurements at these fields.

$H_{ext,//}$ =	**0.002 T**	**0.005 T**	**0.01 T**	**0.02 T**	**0.1 T**
Sample	**Superconducting transition temperature (T_{SU}, K)**				
QD1	7.3 (± 0.2)	7.15 (± 0.06)	-	7.09 (± 0.06)	6.96 (± 0.06)
QD2	7.11 (± 0.06)	6.93 (± 0.09)	6.6 (± 0.4)	-	6.8 (± 0.1)
QD3	7.12 (± 0.06)	-	7.09 (± 0.06)	-	6.98 (± 0.07)
QD4	6.99 (± 0.07)	6.81 (± 0.06)	-	6.9 (± 0.1)	6.7 (± 0.1)

Table 5.4 list the values of T_{SU} for the samples for the measurements in Figures 5.8 to 5.11, respectively. T_{SU} is observed to have around the same values for all samples.

Figure 5.13 shows the variation of T_{SU} as a function of the magnetic field. T_{SU} for the bulk Pb (7.2 K) is marked as a reference in the figure, providing a baseline for comparison. In all samples analyzed, a slight decrease in T$_{SU}$ is observed as the magnetic field strength increases, with the minimum value recorded at 0.1 T. Specifically, for the QD1 sample, the values predominantly remain near the reference line.

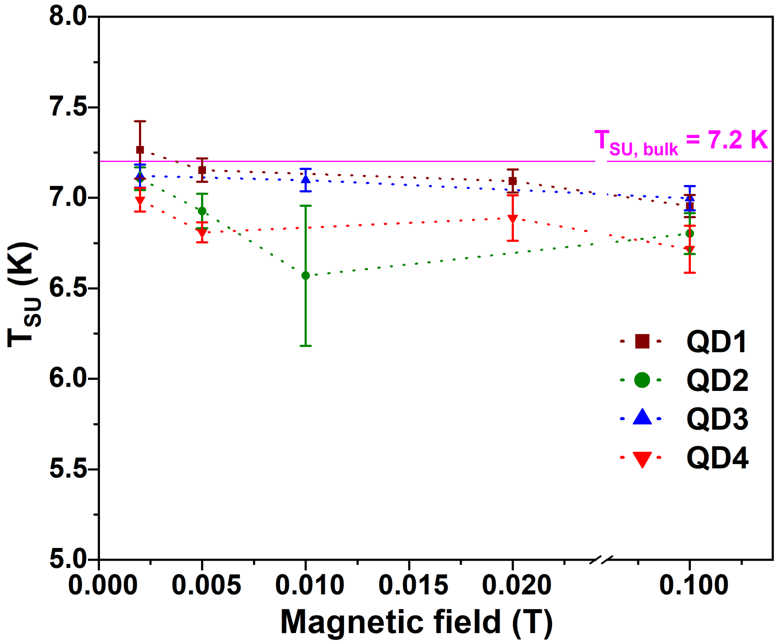

Figure 5.13: Superconducting transition temperature (T$_{SU}$) as a function of magnetic field for samples. The horizontal line in pink at T = 7.2 K is the T$_{SU}$ for the bulk Pb. The dotted lines serve as a guide to the eye.

Table 5.5: Critical exponent (β_1) for the samples. Missing values are due to lack of measurements at these fields.

$H_{ext,//}$ =	**0.002 T**	**0.005 T**	**0.01 T**	**0.02 T**	**0.1 T**
Sample	**Critical exponent (β_1)**				
QD1	0.53 (± 0.01)	0.53 (± 0.01)	-	0.61 (± 0.01)	0.67 (± 0.01)
QD2	0.49 (± 0.02)	0.61 (± 0.01)	0.66 (± 0.02)	-	0.82 (± 0.02)
QD3	0.55 (± 0.02)	-	0.66 (± 0.02)	-	0.81 (± 0.01)
QD4	0.80 (± 0.06)	0.96 (± 0.05)	-	0.87 (± 0.04)	0.9 (± 0.1)

Table 5.5 lists the values of the critical exponent (β_1). Figure 5.14 shows the variation of the critical exponent (β_1) as a function of the thickness of the EuS layer in the presence of 0.002 T and 0.1 T. β_1 is observed to be higher than the bulk value for EuS

for all samples. Furthermore, β_1 is observed to move towards the reference line with an increase in thickness of the EuS layer.

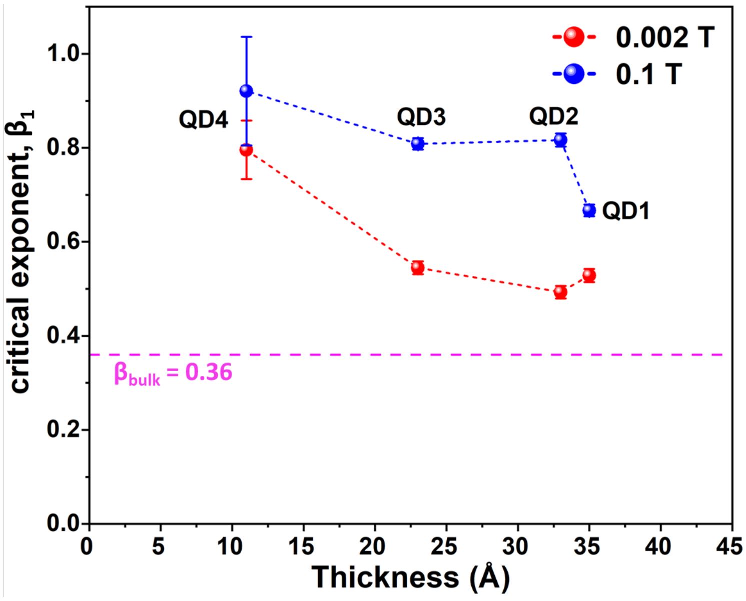

Figure 5.14: Critical exponent (β_1) as a function of the thickness of EuS layer for samples in presence of 0.002 T and 0.1 T. The horizontal line in pink at $\beta_1 = 0.36$ is for the bulk EuS [123]. The dotted lines serve as a guide to the eye.

Figure 5.15 shows the variation of T_C as a function of the thickness of the EuS layer for the samples in the presence of 0.002 T and 0.1 T. T_C is observed to increase with increasing EuS thickness for the same field.

Below T_C for EuS, an alignment of Eu magnetic moments begins, and saturation magnetization is achieved as the temperature drops to 0 K. A trend toward a reduced T_C is observed in the samples as the thickness of the EuS layer decreases [Table 5.3]. With the decrease in EuS thickness, the atomic surface-to-volume ratio increases for thinner films, resulting in low number of Eu^{2+} ions for the exchange interactions [124, 125, 126]. Thus, the Curie transition tends to occur at lower temperatures. Above T_C for EuS, the magnetic signal dissipates as increasing thermal fluctuations destroy the magnetic order. In addition, the Curie transition is smeared and shows a slight increase in T_C with an increase in the applied in-plane magnetic field for the same sample [Figure 5.12]. The external magnetic field suppresses the effects of thermal energy on moments near T_C, and the moments have the energetic advantage to remain aligned up along the field [127]. Thus, T_C appears to increase due to the effects of the external magnetic

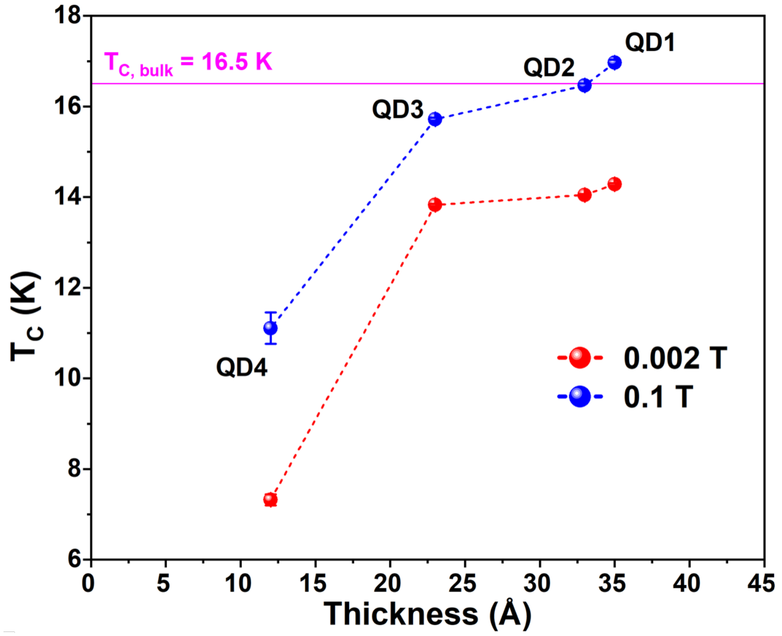

Figure 5.15: Curie temperature (T_C) as a function of the thickness of EuS layer for samples in presence of 0.002 T and 0.1 T. The horizontal line in pink at T = 16.5 K is the T_C for the bulk EuS. The dotted lines serve as a guide to the eye.

field. The critical exponent (β_1) was found to be higher for these samples than the bulk value of EuS [Table 5.5]. This discrepancy is probably due to the surface anisotropy effect for thin EuS films also studied previously by Dauth *et al.* [128]. Moreover, these effects may explain the slight increase in β_1 value with an increase in EuS thickness. Additionally, the increase in β_1 value with increase in the applied magnetic field is due to the magnetic field effects, discussed previously for T_C.

Below 8 K, the Pb layer exhibits superconductivity, and the splitting observed near 7 K in the magnetization versus temperature curves [Figs. 5.8 to 5.11] is due to the expulsion of the magnetic field by Pb in superconducting state. If the sample is field-cooled, then either magnetic flux penetrates or full destruction of superconductivity occurs. Moreover, the magnetic response of the sample below 8 K is a combined response from diamagnetic Pb and ferromagnetic EuS layers in the sample. For bulk Pb below T_{SU}, the superconducting behavior is type I and the critical magnetic field is around 0.08 T. Although the sample was field-cooled (FC) to destroy the superconducting in Pb, the magnetic field strength of even 0.1 T was not enough, as indicated by the small dip in the FC curve for samples at higher fields. As reported in the literature, the critical magnetic field increases when the thickness of the lead layer goes below the coherence length of the lead (ξ_{Pb}), i.e. around 800 Å [43]. In the present study, the thickness of the thin Pb films is around 400 Å or less, which is below the coherence length of Pb (in bulk). Therefore, Pb thin films were still superconducting after FC in 0.1 T. The superconducting transition (T_{SU}) in Pb is found to be consistent and occurs around 7 K in all samples [Table 5.4].

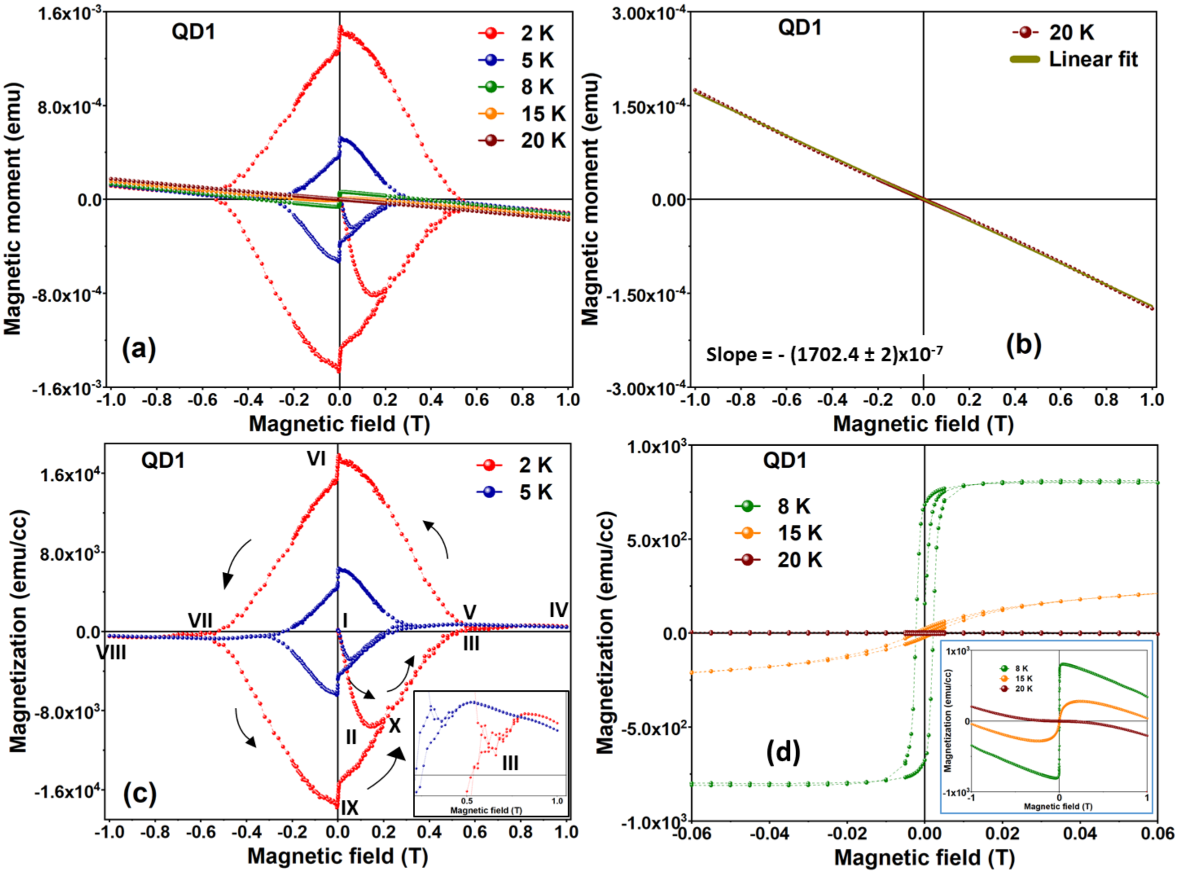

Figure 5.16: Magnetic hysteresis loops recorded for the QD1 sample at 5 different temperatures. (a) Raw data. (b) Raw data for 20 K and its linear fit. (c) Normalized data at 2 K and 5 K. Inset shows the zoomed region on the curves in the range from 0.2 to 1 T. (d) Normalized data for temperatures 8 K, 15 K, and 20 K. Inset shows the data for full range of magnetic field. The dotted lines serve as a guide to the eye.

Moreover, hysteresis loops for the samples in the magnetic field range up to ± 1 T were recorded. The normalization process and slope correction of the data are discussed in the SQUID magnetometry section of Chapter 2 (3.2.4). Figure 5.16 shows the hysteresis loops for the QD1 sample. Figure 5.16 (a) shows the raw data recorded at temperatures of 2 K, 5 K, 8 K, 15 K and 20 K. All the data curves follow the negative slope at both ends of the magnetic-field range. Figure 5.16 (b) shows the raw data recorded at 20 K, along with a linear fit. At this temperature, the sample does not show hysteresis. The average slope of the fit to the data is - $(1702.4 \pm 1.9)\times10^{-7}$ emu T^{-1}. The verage slope of the fit to the data is determined using the process discussed in Section 3.2.4 (Chapter 3). This data set was used for the slope correction of the remaining data sets.

Figure 5.16 (c) shows the normalized magnetization data at 2 K and 5 K. These curves show a complex magnetic response as the magnetic field is cycled, marked by numbers (in Roman). The magnetic response is linear, with a negative slope from points I through II. After saturation at point II for the 2 K data, the magnitude of the magnetization begins to decrease as $H_{ext,//}$ increases further. This trend continues until point III, where the curve begins to deviate and crosses the line M = 0 near 0.52 (± 0.02) T, then the slope decreases significantly and then becomes slightly negative [shown in the inset image of Figure 5.16 (c)] at point IV as the applied field increases to $H_{ext,//}$ = 1 T. When the field decreases from 1 T back toward zero, the magnetization follows the same curve from points IV to V, but around 0.58 (± 0.02) T the magnetization starts to increase towards positive value, peaking at point VI. After reaching point VI, a drop in magnetization is observed within a range of ± 0.005 T as the field crosses from positive to negative values. At point VII, magnetization crosses the M = 0 line, and then the slope changes, exhibiting the opposite behavior of the signal at positive fields near point III. As the field intensity goes from -1 to 0 T, magnetization plunges further to negative values, hitting a minimum at point IX. A rise in magnetization is observed when the field changes sign from negative to positive. Subsequently, as the field value increases from 0 T, magnetization traces back along the original curve near point X. Data at 2 K and 5 K exhibit analogous behavior, though features are noted at distinct points and occur at lower magnetic fields for 5 K data.

Figure 5.16 (d) shows the normalized data for 8 K, 15 K, and 20 K. Post-normalization, the slopes of the curves shift to a positive value in the high-field regions. At 8 K, the curve exhibits a hysteresis loop and saturates at M = (797 ± 106) emu/cc around 0.01 T. At 15 K, the hysteresis loop is still present but narrower than the 8 K data. At 20 K, no hysteresis loop is detected. The inset of Figure 5.16 (d) presents data over the entire magnetic field range, illustrating a slope change in the curves at high fields, eventually leading to a negative value for slopes.

Figure 5.17 presents the hysteresis loops for the QD2 sample. Panel (b) includes raw data at 20 K with a linear fit, indicating no hysteresis at this temperature similar to QD1. The average slope of the fit is - $(1813 \pm 2)\times10^{-7}$ emu T^{-1} and was used for slope correction in other data sets.

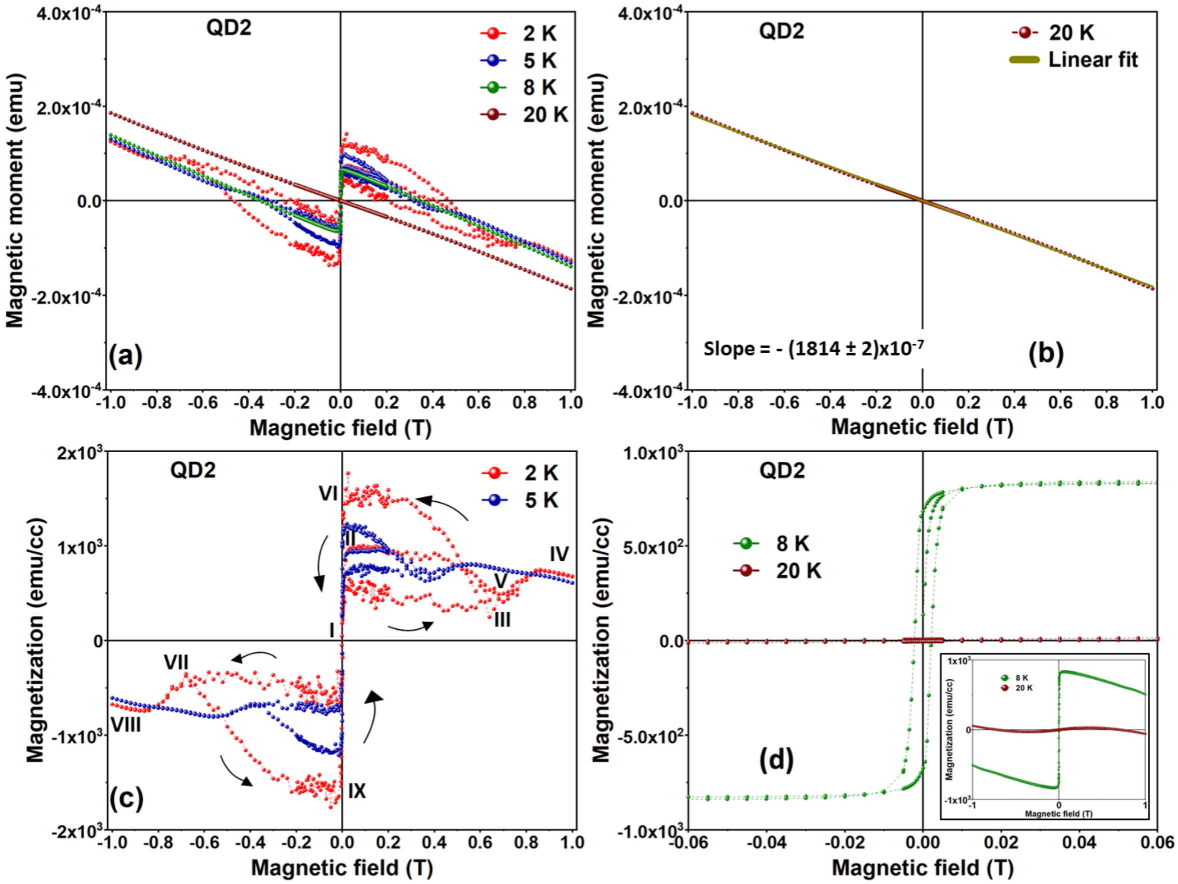

Figure 5.17: Magnetic hysteresis loops recorded for the QD2 sample at 4 different temperatures. (a) Raw data. (b) Raw data for 20 K and its linear fit. (c) Normalized data at 2 K and 5 K. (d) Normalized data for temperatures 8 K and 20 K. The dotted lines serve as a guide to the eye.

Figure 5.17 (c) shows the normalized magnetization data at 2 K and 5 K. In contrast to the sample QD1, the magnetic response is linear with a positive slope when the field increases from 0 T. After saturation at point II for the 2 K data, the magnitude of the magnetization begins to decrease as $H_{ext,//}$ increases further. Similar artefacts are observed in the magnetic response as for the QD1 sample near points III and VIII. However, in contrast to the sample QD1, the magnetization suddenly drops to negative when the field crosses from positive to negative values. Figure 5.17 (d) presents the normalized data for 8 K and 20 K. At 8 K, the curve shows a hysteresis loop, saturating at M = (817 ± 76) emu/cc near 0.02 T.

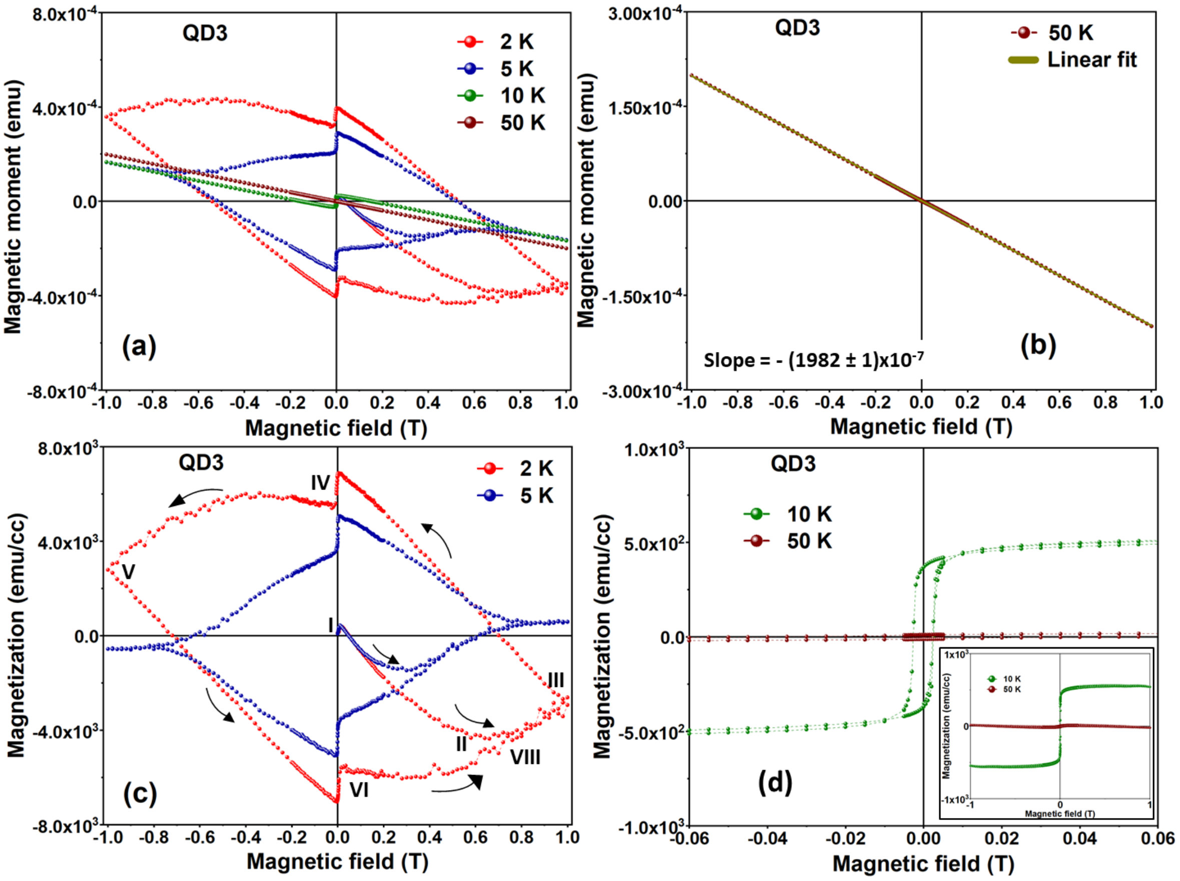

Figure 5.18: Magnetic hysteresis loops recorded for the QD3 sample at 4 different temperatures. (a) Raw data. (b) Raw data for 50 K and its linear fit. (c) Normalized data at 2 K and 5 K. (d) Normalized data for temperatures 10 K and 50 K. The dotted lines serve as a guide to the eye.

Figure 5.18 shows the hysteresis loops for the QD3 sample. Subfigure (b) shows raw data at 50 K with a linear fit revealing no hysteresis. The average slope of the fit is -(1982 ± 1)$\times10^{-7}$ emu T^{-1}, applied to adjust other dataset slopes. Figure 5.18 (c) shows the normalized magnetization data at 2 K and 5 K. In contrast to QD1 and similarly to the sample QD2, the magnetic response at 2 K and 5 K is linear with a positive slope from point I to II and then it changes back to a negative slope around 0.01 T. After saturation at point II for the 2 K data, the magnitude of the magnetization begins to decrease as $H_{ext,//}$ increases further. However, ± 1 T field was not enough to see the full curve for magnetization at 2 K. But for data at 5 K, the behavior is similar to that at 5 K for the QD1 sample [Figure 5.16 (c)], except for the magnetic response near point I.

Figure 5.18 (d) presents the normalized measurements at 10 K and 50 K. At 10 K, a noticeable hysteresis loop is observed with saturation at M = (459 ± 41) emu/cc around 0.02 T. In contrast, at 50 K, no hysteresis is detected and the normalized magnetic response is approximately M = 0 emu/cc.

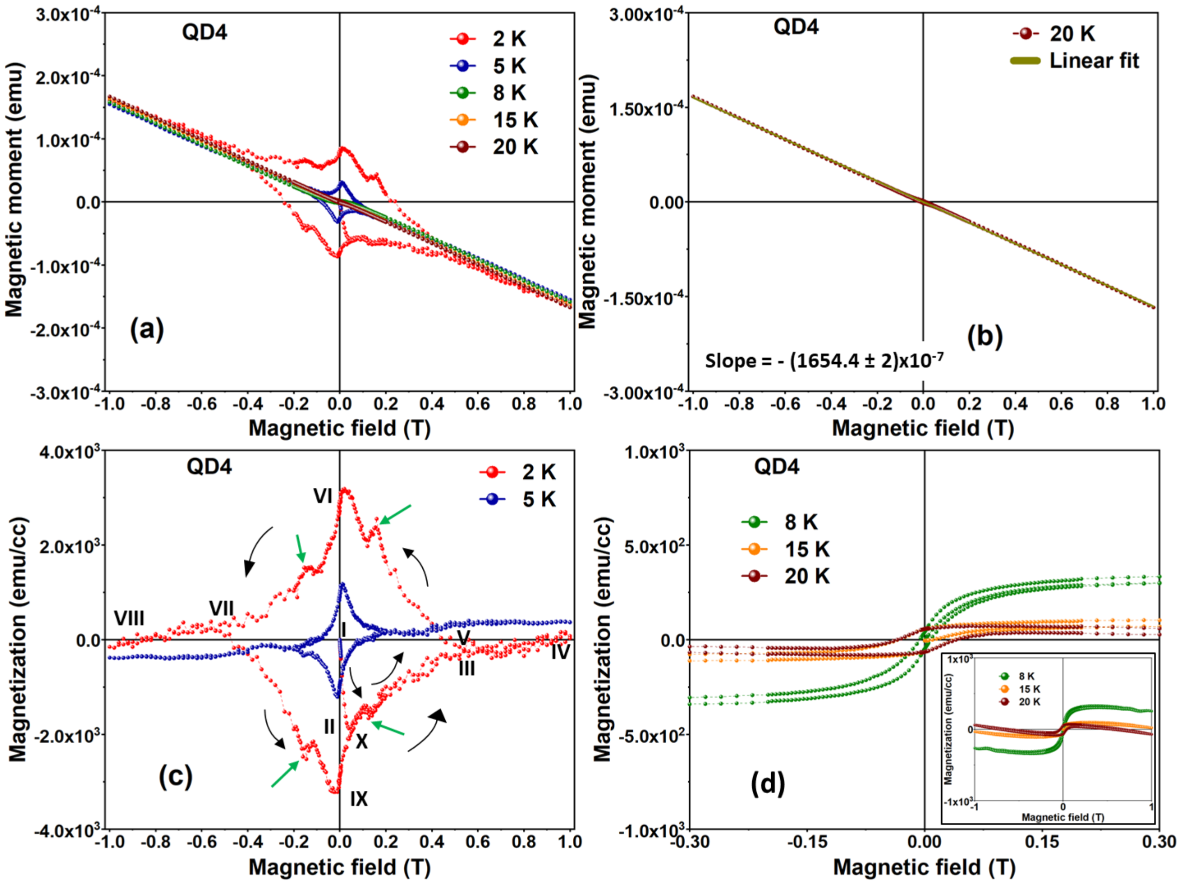

Figure 5.19: Magnetic hysteresis loops recorded for the QD4 sample at 5 different temperatures. (a) Raw data. (b) Raw data for 20 K and its linear fit. (c) Normalized data at 2 K and 5 K. (d) Normalized data for temperatures 8 K, 15 K, and 20 K. The dotted lines serve as a guide to the eye.

Figure 5.19 presents the hysteresis loops of the QD4 sample. Figure 5.19 (b) displays data for 20 K with linear fit, showing no hysteresis. The average slope of the fit is - (1654

± 2)×10^{-7} emu T^{-1}, employed to adjust the slopes of other data sets. Figure 5.19 (c) shows the normalized magnetization data at 2 K and 5 K. The magnetization curves at 2 K and 5 K shows a similar behavior to the curves for the sample QD1, except that the features are observed at lower values of magnetic field and magnetization. Furthermore, kinks [marked by green arrows in Figure 5.19 (c)] were observed in the 2 K magnetization curve at approximately ± 0.15 T. Figure 5.19 (d) shows the normalized data for 8 K, 15 K, and 20 K. At 8 K, the curve exhibits a hysteresis loop and saturates at M = (330 ± 62) emu/cc around 0.24 T. In contrast to the samples QD1 and QD2, the normalized magnetic response for 20 K shows a hysteresis loop and does not lie close to the line corresponding to M = 0 emu/cc.

Figure 5.20 presents the hysteresis loops of the InAs substrate. In Figure 5.20 (a), raw data at temperatures of 5 K and 300 K are depicted, both showing a negative slope. Figure 5.20 (b) displays the slope-corrected data for both temperatures. The slope of the data at 300 K, - (1614.2 ± 0.9)×10^{-7} emu T^{-1}, is used to correct the slopes of both data sets. The data at 5 K and 300 K show an unexpected magnetic response. At 5 K within the ± 1 T magnetic field range, the magnetization curve exhibits a decrease in magnitude before changing sign, as indicated by black stars in the inset of Figure 5.20 (b). Following the change in sign, magnetization increases towards a region denoted by orange stars (around ± 2 T), then deviates again, and the magnitude rises in the opposite direction until another deviation marked by blue stars occurs, ultimately saturating at both ends of the field range.

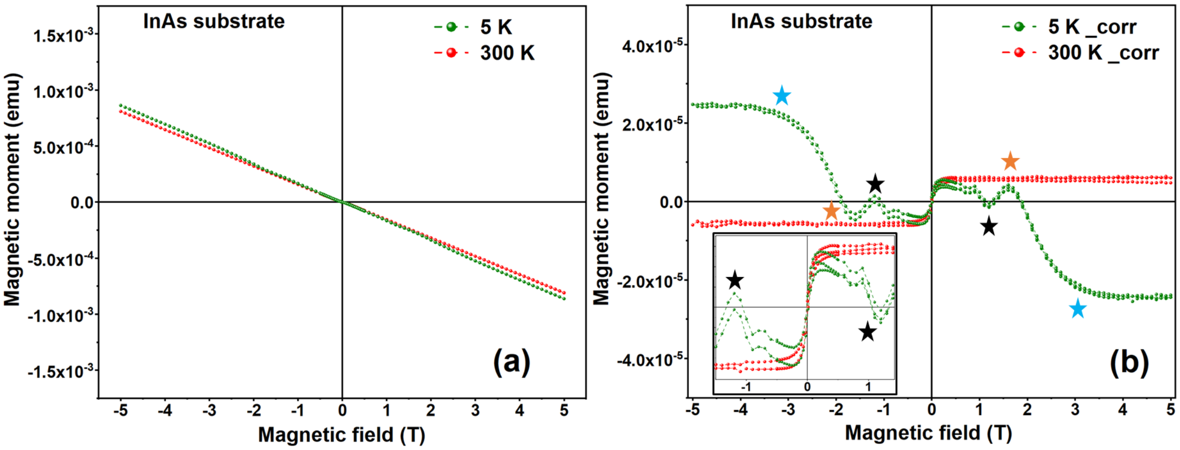

Figure 5.20: Magnetic hysteresis loops recorded for the 20 mm^2 piece of InAs substrate. (a) Raw data for temperatures 5 K and 300 K. (b) Slope corrected data for temperatures 5 K and 300 K. The dotted lines serve as a guide to the eye.

Tables 5.6 list the upper critical field (H_{C2}) values for the samples. The approach to determine H_{C2} is explained in the chapter on methods (Section 3.2.4). H_{C2} was found to be the lowest in the case of the QD4 sample at 2 K and 5 K. Meanwhile, H_{C2} for QD1 and QD2 is approximately the same under both temperature conditions examined. However, the QD3 sample exhibits the highest H_{C2} at 5 K. The artefacts observed in the magnetization curves, such as slope change around ± 1 T, for the samples can be attributed to the unusual magnetic response of the InAs substrate, as illustrated in the inset of Figure 5.20 (b). The reason behind the substrate's deviation from the anticipated diamagnetic behavior remains unclear. However, the unusual magnetic response of InAs at 5 K differs from the standard ferromagnetic or paramagnetic behavior.

Table 5.6: The upper critical magnetic field (H_{C2}) for Pb layer in the samples.

Upper critical magnetic field (H_{C2}, T)		
	Temperature	
Sample	**2 K**	**5 K**
QD1	0.58 (± 0.02)	0.32 (± 0.02)
QD2	0.67 (± 0.01)	0.35 (± 0.01)
QD3	-	0.84 (± 0.02)
QD4	0.54 (± 0.01)	0.19 (± 0.02)

The initial steep increase in the magnitude of magnetization observed in hysteresis curves with a negative slope for the samples QD1 and QD4 at low fields is attributed to the diamagnetic response of superconducting Pb. As the magnetic field increases, the response reaches a near-saturation level and then decreases smoothly, indicating the suppression of superconductivity. This superconducting behavior of Pb is classified as type II rather than type I because of the gradual decline in magnetization, characteristic of type II superconductors ([129]). When magnetic fields exceed the upper critical field (H_{c2}), the curves change to reflect the ferromagnetic response of the EuS layer. This behavior is evident in the 2 K and 5 K data plots in higher fields, as shown in Figs. 5.16 to 5.19. The shape of the M versus H curves observed in the data for 2 K and 5 K results from the combined magnetic response of ferromagnetic EuS and superconducting Pb. Moreover, above 8 K ($\geq T_{SU}$), the observed magnetic response is due to the ferromagnetic contribution from EuS. Above T_C, thermal energy disrupts the magnetic alignment in EuS, consequently, EuS is in the paramagnetic state. Therefore, at 20 K and 50 K, the sample exhibits a linear magnetic response.

5.4.3 Information on elemental magnetism and structure

Figs. 5.21 (a) and (b) show the normalized XANES and XMCD signal versus energy, respectively. The normalization process for XANES and XMCD data is shared in the chapter on methods (Section 3.2.5). An intense peak around 6977 eV is observed in the XANES results for all samples, as shown in Figure 5.21 (a). However, a peak around 6985 eV was observed only for the QD2 and QD3 samples. In addition, an additional peak around 7000 eV was observed for QD4. Figure 5.21 (b) shows the variation of the XMCD signal as a function of energy at 3 K (in 3 T). A peak around 6975 eV is observed for all the samples.

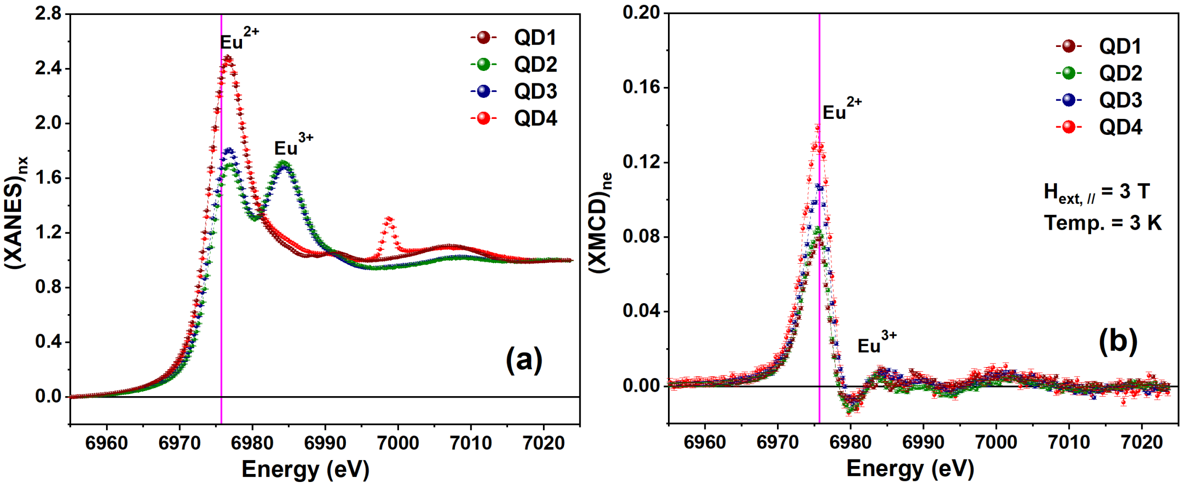

Figure 5.21: X-ray absorption spectra for the samples (shown in separate colors) recorded at 3 K in the presence of 3 T near Eu L_3-edge. (a) Normalized XANES spectra. (b) Normalized XMCD signal.

Table 5.7 lists the values of XMCD corresponding to the peak in Figure 5.21 (b) for the samples. These XMCD values were used to normalize the XMCD versus temperature [Figure 5.22] and XMCD versus field [Figure 5.23] plots.

The normalized XMCD signal at a fixed energy of X-rays, corresponding to the intense peak in XMCD versus energy results (marked by pink line in Figure 5.21) at 6975.72 eV, was measured as a function of temperature and external magnetic field. Figs. 5.22 (a) and (b) show the normalized XMCD signal as a function of temperature in magnetic fields of 0.3 T (0.1 T for QD3) and 3 T, respectively. The XMCD signal for the samples shows an increase as the temperature decreases, as shown in Figure 5.22

Table 5.7: XMCD values for the samples. These values are read from the peak in XMCD signal for each sample at 6975.72 eV, shown with a pink vertical line in Figure 5.21 (b).

XMCD at 3 K (3 T)	
Sample	**Values**
QD1	0.079 (± 0.001)
QD2	0.083 (± 0.001)
QD3	0.106 (± 0.001)
QD4	0.126 (± 0.002)

(a). An exception is observed in QD1, where the XMCD signal shows small variation with changes in temperature. In addition, a sharp drop in the XMCD signal is observed near 16 K for the QD3 sample and 10 K for the QD2 and QD4 samples.

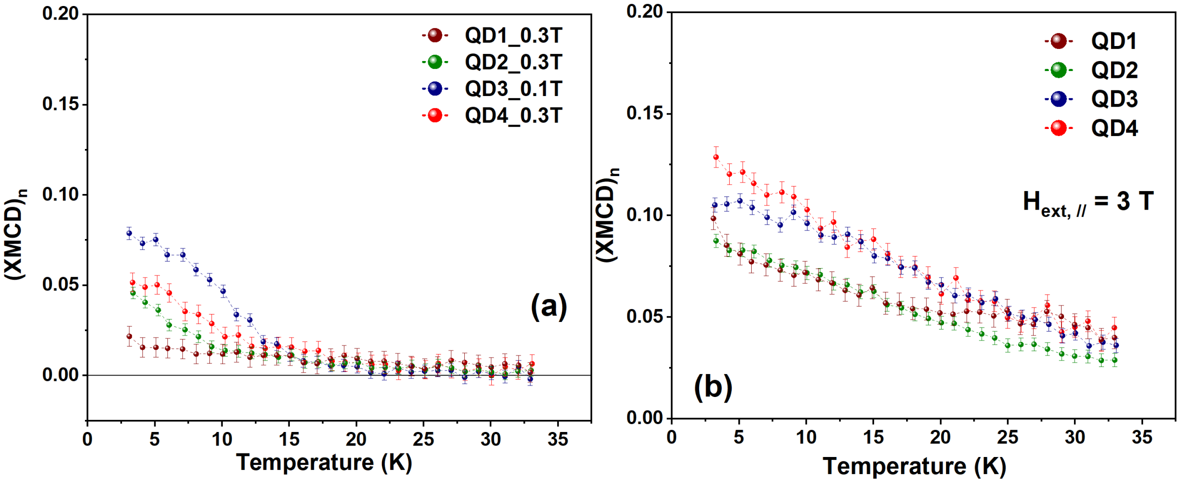

Figure 5.22: Normalized XMCD signal as a function of temperature measured in the presence of (a) 0.3 T (b) 3 T magnetic fields. The dotted lines serve as a guide to the eye.

XMCD signal in 3 T, as shown in Figure 5.22 (b), exhibits an increase as the temperature decreases. However, the slope of the increase in the XMCD signal with temperature for all samples is nearly linear, which is in contrast to the sharp increase observed for QD2 and QD3 in low fields [Figure 5.22 (a)].

Figure 5.23 shows the results for normalized XMCD versus magnetic field scans that were recorded at 3 K, below both T_{SU} and T_C. QD3 reaches saturation at lower magnetic fields (around ± 1.5 T). Subsequently, QD2 and QD4 reach a saturation point approximately at ± 4 T. However, the sample QD1 demonstrates an unexpected linear response that continues without saturation, even when subjected to higher magnetic fields.

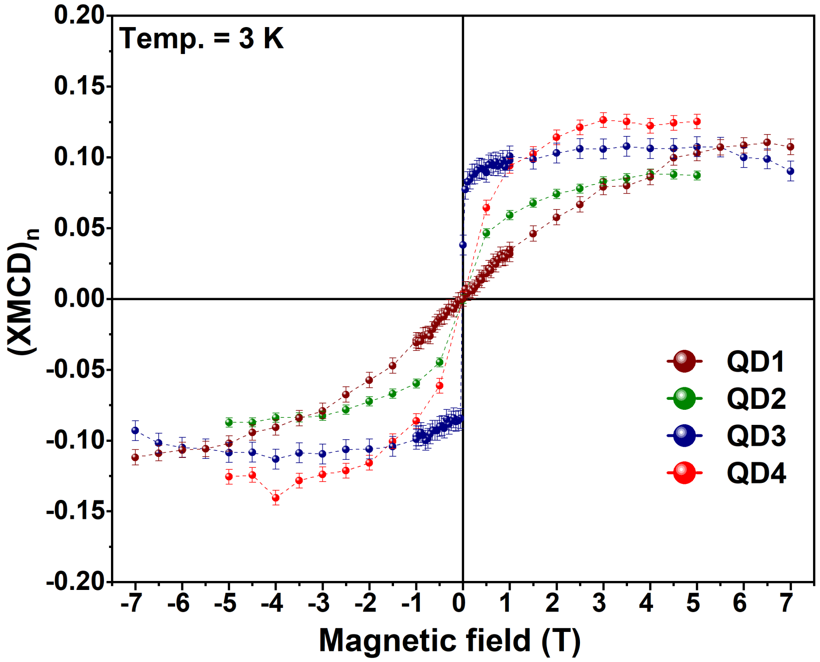

Figure 5.23: Normalized XMCD signal as a function of magnetic field for the samples at 3 K. The dotted lines serve as a guide to the eye.

Figure 5.24 shows the normalized XMCD versus energy results for the QD4 sample that were measured at three temperatures and two magnetic fields to study the variation of signal. The XMCD signal exhibits a peak approximately at 6975 eV for all curves. The XMCD signal is highest for the data recorded at a temperature of 3 K under an applied magnetic field of 3 T. This is succeeded by the data acquired at 8 K in a magnetic field of 3 T. Subsequently, the observations at 3 K in a reduced field of 0.3 T exhibit a lower signal, with the smallest signal being recorded at 30 K (in 3 T).

The intense peak consistently observed around 6977 eV in the normalized XANES results for the samples, shown in Figure 5.21 (a), is the characteristic peak of the Eu^{2+} valence state of the Eu ion [130]. However, the peak observed around 6985 eV for the QD2 and QD3 samples is attributed to the Eu^{3+} valence state peak [130], indicating a deviation from the EuS stoichiometry. The peak of the Eu^{2+} valence state remains dominant in the QD1 and QD4 samples, suggesting that the EuS layer in these samples is mostly in the Eu^{2+} state. The EuS layer grown below 670 K has been reported to cause defects, including the trivalent state of Eu [131]. In this study, although all EuS layers were grown below this temperature, only QD2 and QD3 samples displayed mixed valence states. Therefore, the cause of mixed valence states of Eu in QD2 and QD3 samples is still uncertain.

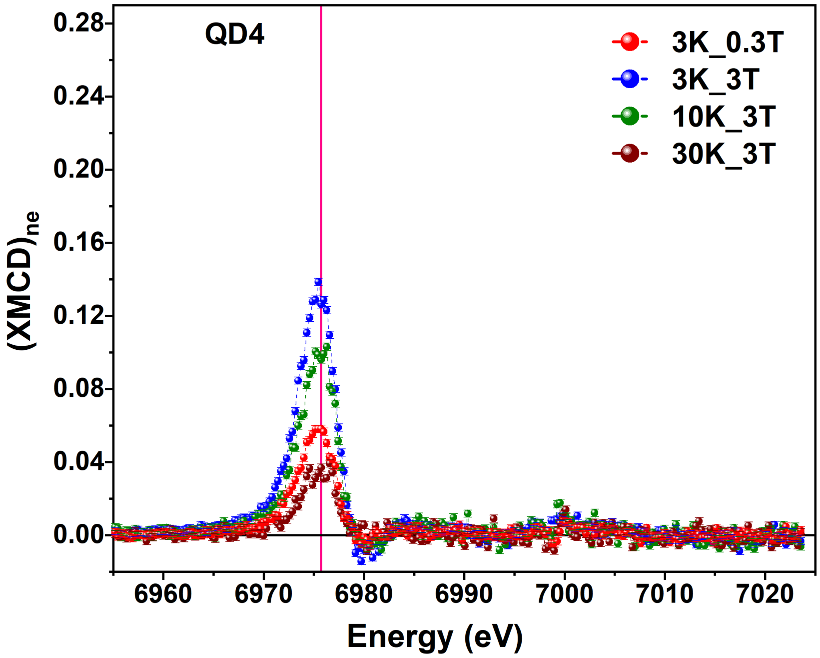

Figure 5.24: Normalized XMCD signal as a function of energy for the sample QD4 at different magnetic fields and temperatures.

In Figure 5.21 (b), the XMCD spectra reveal the contribution of each of the valence states of Eu to the ferromagnetism observed in the samples. The valence state Eu^{2+} contributes predominantly to ferromagnetism in all samples. The XMCD signal from the Eu^{3+} oxidation state is negligible compared to the Eu^{2+} state, indicating that these ions do not contribute to the ferromagnetism observed in the samples. It is not feasible to quantify the XMCD signal at the Eu L$_3$-edge due to mixing of the dipole ($2p \rightarrow 5d$) and quadrupole ($2p \rightarrow 4f$) transitions and the absence of sum rules [130]. Moreover, XMCD data as a function of energy is normalized using the XANES signal, and hence it should not be compared across samples. Similarly, the data for the XMCD versus temperature and XMCD versus H curves should not be compared across samples as these are normalized by the highest signal in the XMCD versus energy results for each sample. However, for each sample, comparison can be made between different points on the same XMCD curve.

The XMCD signal versus temperature (Figure 5.22) and field (Figure 5.23) shows a dependence consistent with ferromagnetic behavior and a transition temperature near 14 K for all samples, except QD1. For sample QD1, the signal increases approximately linearly with decreasing temperature at both 0.3 and 3 T, and no transition or saturation is observed at high field, consistent with paramagnetic behavior. Table 2.2 lists some of the possible compounds and the valence states of Eu. Considering the possibility that EuS might have transformed into stable compounds like Eu_2O_3 or Eu_2S_3 upon air exposure, the XANES analysis should reveal the presence of Eu^{3+} ions. But, QD1 has a single Eu^{2+} valence state [Figure 5.21 (a)]. Therefore, the reason behind this behavior of the QD1 sample from the anticipated ferromagnetic behavior remains unclear.

The decrease in XMCD signal for the sample QD4 [Figure 5.24] with temperature is consistent with ferromagnetic behavior, as the thermal fluctuations destroy the magnetic order. Comparison of the XMCD signals at 3 T and 0.3 T measured at 3 K reveals that a stronger external magnetic field aligns more Eu^{2+} moments within the EuS layer.

5.4.4 Structure and magnetism with depth

The recorded data from PNR and XRR, with their respective fits, for each sample are shared in the following subsections. The details of the analysis of the reflectometry data are shared in the chapter on data analysis [Section 4.1.5]. A modified structural and magnetic interface model approach [Section 4.1.5] was followed to fit the data for the samples, where the SLD and MSLD of the parts of the Pb layers near the interface with the EuS layer on both sides are allowed to vary independently.

Figure 5.25 illustrates a guide for naming parameters that defines the MSLD profile of a sample at a given temperature. Magnetic roughness towards the surface and substrate is designated as mrha and mrhb, respectively. The MSLD of a layer is expressed as rhoM. Correspondingly, the sample layers are arranged and enumerated from 1 to 3, based on their stacking order. The parameters concerning the magnetic roughness (mrha and mrhb) and MSLD of the EuS and both interfacial layers describe the MSLD profile of the sample. It is important to note that the parameters 1mrha and 2mrhb define the same part of the MSLD profile, also true for 2mrha and 3mrhb. However, Refl1D software only takes one of the parameters into account, that is, 1mrha and 2mrha in the present case. A total of 7 parameters (excluding 2mrhb and 3mrhb) were chosen to derive cross-correlations and evaluate uncertainties in their values.

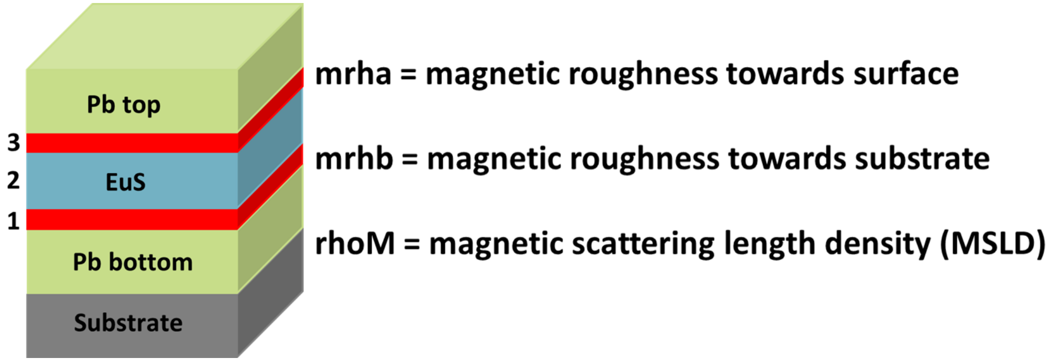

Figure 5.25: Schematic of a sample. 1-3 are the number assigned to the magnetic layers in the sample. 1 is for the interface layer at interface between EuS and bottom Pb layer. 2 is for the EuS layer and 3 is for the interface layer between EuS and the top Pb layer.

The reference values of the SLDs for the Pb, EuS, and InAs materials are listed in Table 5.8. These values are calculated using equations 3.6, 3.29 and 3.36. The computation utilizes data for neutron [132], and X-ray [133] scattering lengths.

Table 5.8: Reference values of SLDs for Pb, EuS and InAs. The MSLD values for Pb and EuS are given assuming Pb in pure Meissner state in presence of 0.1 T and EuS in saturation state, respectively.

	NSLD	**XSLD**	**MSLD**
Material	$\times 10^{-6}$ $\mathbf{Å}^{-2}$	$\times 10^{-6}$ $\mathbf{Å}^{-2}$	$\times 10^{-6}$ $\mathbf{Å}^{-2}$
Pb	3.09	72.22	-0.23
EuS	1.90	38.28	3.48
InAs	1.93	41.43	-

Sample QD1

Table 5.9 list the PNR measurements performed on the QD1 sample at ILL on the D17 instrument [80]. A total of three PNR measurements were performed for the sample to monitor the variations in the magnetic signal as a function of temperature. Figure 5.26 (a) shows the fitted PNR data for the QD1 sample. The simulated reflectivity of the selected model aligns well with the experimental data. The PNR data show a split between the reflectivities for spin-up (R^{+}) and spin-down (R^{-}) neutron measurements, except for the data at 50 K.

Table 5.9: PNR measurements for the QD1 sample.

PNR Measurements	
Temperature (K)	Magnetic field (T)
2	0.1
8	0.1
50	0.1

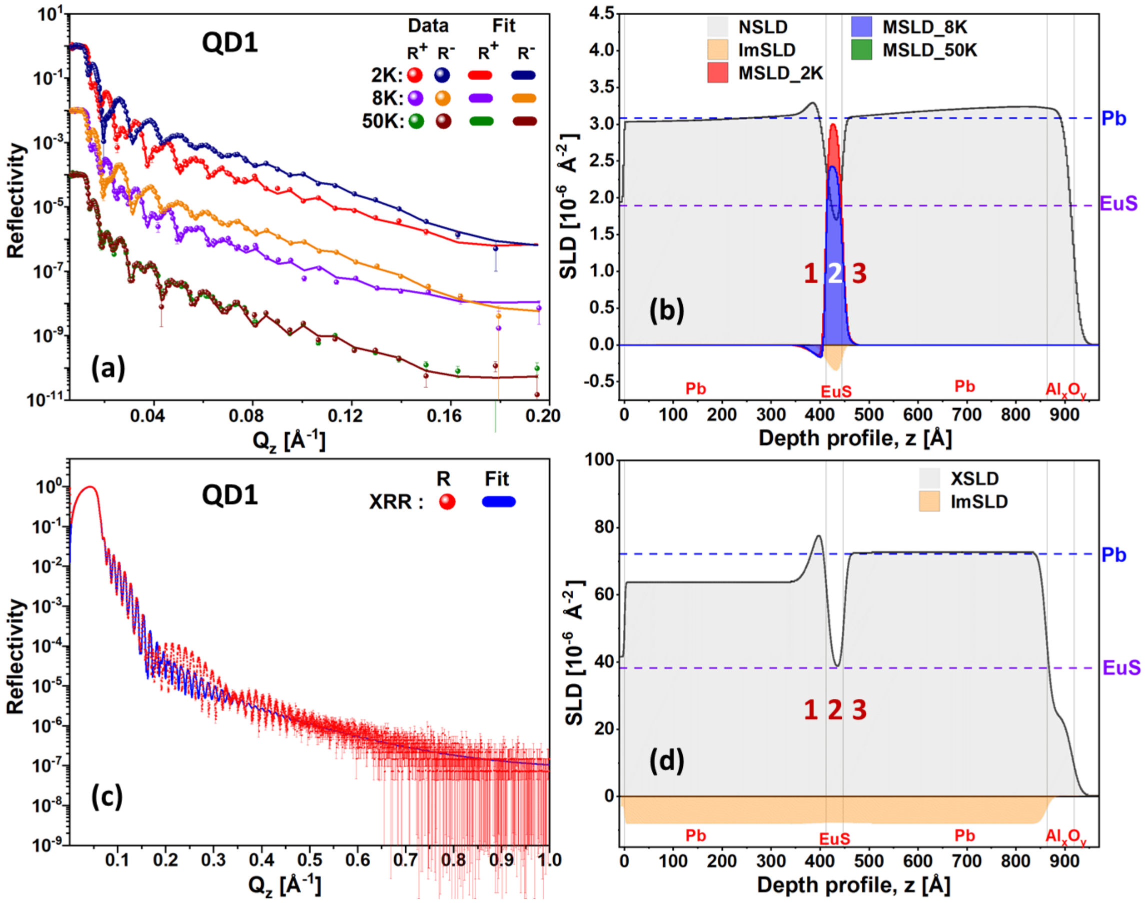

Figure 5.26: Fitted reflectometry data for the QD1 sample. (a) PNR data recorded at 2 K, 8 K and 50 K in the presence of 0.1 T with their respective fits. The datasets are shifted by 10^2 units along the y-axis to enhance clarity. R^+ and R^- stand for the reflectivity for spin up and spin down neutron measurements, respectively. (b) NSLD and MSLD versus depth profiles (c) Fitted XRR data. (d) XSLD versus depth profile. Absorption scattering length density (ImSLD) profiles for neutrons and X-rays are shown in orange color along with NSLD and XSLD profiles, respectively.

NSLD and MSLD profiles versus depth are shown in Figure 5.26 (b). The horizontal dotted lines correspond to the reference NSLD values for Pb (blue) and EuS (violet). The different layers in the sample are identified and named at the bottom of the SLD profiles. The NSLD of the bottom Pb layer is close to the reference NSLD (Table 5.8), except a gradient is observed near the interface with the EuS layer. This region of the bottom Pb layer near EuS is marked as the interface layer “1”. The NSLD of the interface layer “1” is higher than that of the bottom Pb. The NSLD of the EuS layer is slightly lower than the reference value for EuS (Table 5.8). For the upper Pb layer, a gradient is observed as well, and the NSLD increases slowly throughout the layer. The NSLD of the top Pb layer is higher than the reference value and the NSLD of the bottom Pb layer. The NSLD contrast between the top Pb layer and the capping layer is negligible; therefore, it is hard to comment on the NSLD of the capping layer. A negative MSLD at 2 K and 8 K is observed in the interface layer “1”, while the MSLD in the EuS layer is positive for both temperature. A negative MSLD means that the magnetic moments are aligned antiparallel to the moments in EuS layer. However, MSLD drops exponentially towards the interface layer “3”. The estimated values of the parameters are listed in Table 5.10. NSLD of the top Pb layer is around 6 % higher than the value in the reference. The NSLD of the EuS layer is approximately 10 % lower than the value in the reference for EuS.

Figures. 5.26 (c) and (d) show the fitted XRR data and the corresponding XSLD profile of the sample. The trend in the XSLD profile of the layers is observed to be similar to that in the NSLD profile. In the flat region of the sample SLD profiles, the NSLD and XSLD for the layer are estimated and shown in Table 5.10. NSLD of the top Pb layer is around 3 % higher than the value in the reference (Table 5.8). The NSLD of the EuS layer is approximately 10 % lower than the reference value for EuS.

Figure 5.27 (a) shows the comparison between the XRR data fitted with and without taking structural parameters, such as thickness and roughness, from the PNR fits. The XRR data (in red) and its fit (in blue) are the same as shown in Figure 5.26 (c). In cofitted XRR data, only the XSLDs of the layers were fitted while the thickness and roughness values were fixed at values obtained from the PNR fit results. However, for the XRR fit alone, all parameters were fitted, including thickness and roughness. Figure 5.27 (b) shows the XSLD profiles for both XRR fits.

Table 5.10: A list of the parameters and their estimated values from the fit to the reflectometry data for the sample QD1. The brackets contain the lower and upper bound values of the parameter.

Sample QD1			
Layer	**Thickness**	**NSLD**	**XSLD**
	(Å)	**($\times 10^{-6}$ Å^{-2})**	**($\times 10^{-6}$ Å^{-2})**
Cap	48.6 [47.7, 49.9]	3.19 [3.18, 3.20]	24.1 [23.8, 24.4]
Pb top	400.4 [399.2, 401.3]	3.259 [3.256, 3.263]	72.6 [72.5, 72.7]
Interface "3"	21.4 [20.42, 22.30]	2.93 [2.91, 2.94]	72.4 [70.8, 76.2]
EuS "2"	34.6 [34.5, 34.7]	1.70 [1.69, 1.71]	38.9 [37.6, 42.3]
Interface "1"	26.2 [25.3, 27.1]	3.28 [3.27, 3.30]	77.5 [75.8, 80.3]
Pb bottom	386.1 [385.1, 386.9]	3.02 [3.01, 3.02]	63.6 [62.4, 65.8]

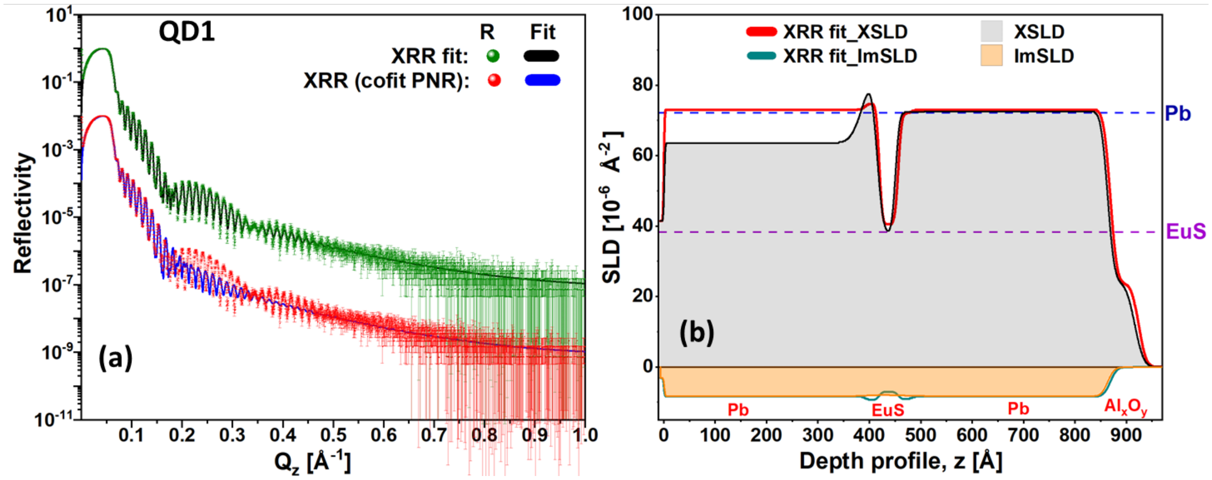

Figure 5.27: (a) Fitted XRR data and cofitted XRR data with structural parameters from PNR fits for the QD1 sample (b) A comparison of the XSLD profile for the fits. The reference XSLD for Pb (blue) and EuS (violet) are marked on the plots.

The estimated values of the thicknesses and XSLDs are compared in Tables 5.11 and 5.12. A difference in the thicknesses of the layers is observed for the PNR and XRR fits. However, there is only 1 % difference or less in the thickness of the entire stack of layers.

Figure 5.28 shows the SA as a function of Q_z, with fits for the data at 2 K, 8 K and 50 K recorded in the presence of 0.1 T. The selected model for the fits describes the

Table 5.11: A comparison of the estimated values of thickness from the two XRR fits for the sample QD1.

Sample QD1		
	Thickness (Å)	
Layer	**XRR (cofit PNR)**	**XRR fit**
Cap	48.6 [47.7, 49.9]	55.31 [55.26, 55.39]
Pb top	400.4 [399.2, 401.3]	386.3 [386.2, 388.0]
Interface “3”	21.4 [20.4, 22.3]	27.0 [26.2, 27.1]
EuS (“2”)	34.6 [34.5, 34.7]	36.7 [36.5, 36.8]
Interface “1”	26.2 [25.3, 27.1]	31.1 [29.4, 31.2]
Pb bottom	386.1 [385.1, 386.9]	388.8 [388.7, 390.4]

Table 5.12: A comparison of the estimated values of XSLD from the two XRR fits for the sample QD1.

Sample QD1		
	XSLD ($\times 10^{-6}$ Å^{-2})	
Layer	**XRR (cofit PNR)**	**XRR fit**
Cap	24.1 [23.8, 24.4]	23.69 [23.64, 23.70]
Pb top	72.6 [72.5, 72.7]	73.01 [73.00, 73.04]
Interface “3”	72.4 [70.8, 76.2]	72.0 [71.8, 72.5]
EuS (“2”)	38.9 [37.6, 42.3]	40.50 [39.96, 40.50]
Interface “1”	77.5 [75.8, 80.3]	74.8 [74.7, 75.0]
Pb bottom	63.6 [62.4, 65.8]	73.00 [72.98, 73.01]

features of the SA data well. The SA data points at 50 K exhibit a random distribution close to the zero line, with substantial error bars evident in the Q_z interval from 0.15 to 0.2 Å^{-1}. The SA value at 50 K is approximated as zero. Both the 2 K and 8 K datasets exhibit a non-zero SA signal, with the 2 K data showing a higher SA signal than the 8 K data. This difference is observed in the Q_z range of 0.01 to 0.05 Å^{-1} in Figure 5.28.

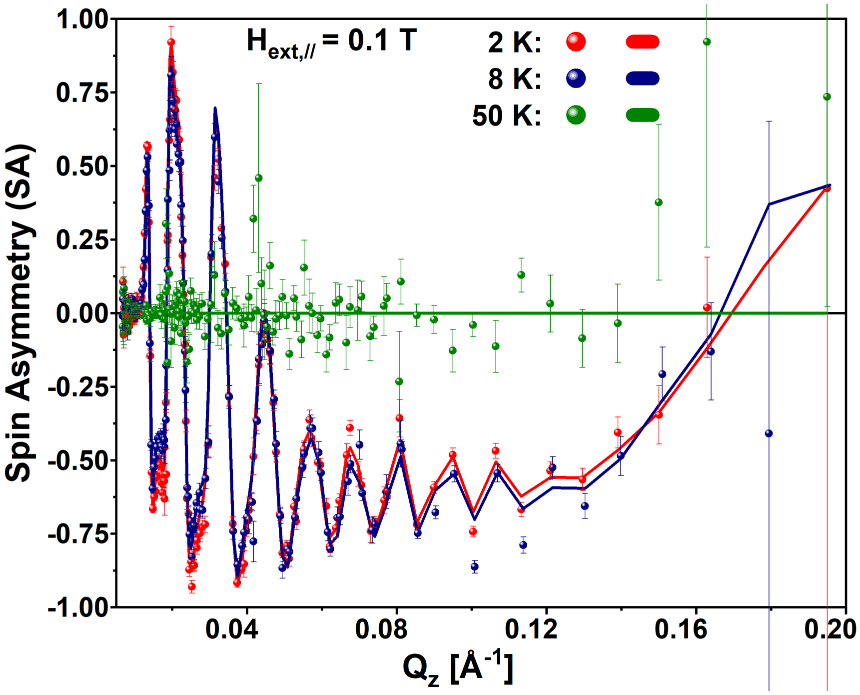

Figure 5.28: Spin asymmetry (SA) as a function of momentum transfer (Q_z) in presence of in-plane magnetic field of 0.1 T for QD1 is shown along with the respective fits.

Figure 5.29 shows a magnified view of the NSLD and MSLD profile near the EuS interface with both layers of Pb. The vertical green dotted lines [Figure 5.29] are a guide to the eye to see to what depth the magnetic signal diffused into adjacent interface layers surrounding EuS.

The results of the uncertainty analysis on a set of parameters that defines the MSLD profile at 2 K are shared in Figs. 5.30 and 5.31. A guide for interpreting these analyses is shared in the chapter on data analysis (Section 4.2.4). For a converged fit, the green line on the posterior distribution for each parameter should follow the shape of the distribution.

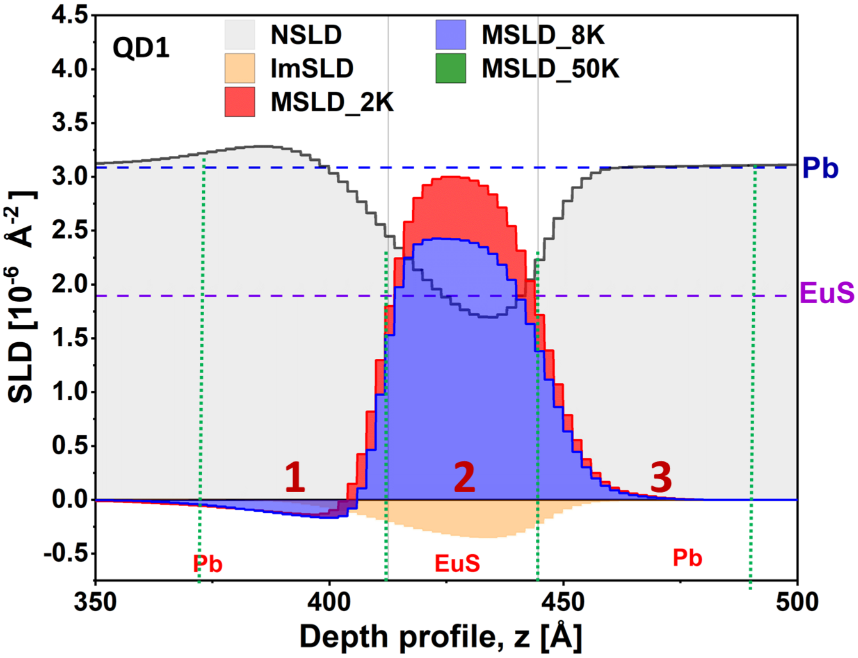

Figure 5.29: A magnified version of the NSLD and MSLD profiles of the sample QD1 near the EuS interface with both Pb layers. The vertical green dotted lines pass through the midpoints of the roughness profiles at interfaces and act as guide to estimate the thicknesses.

Figure 5.30 shows a chart of posterior distributions for the 7 parameters. A skewed distribution is observed for the parameter 3mrha_2K which is the magnetic roughness of the interface layer 3 towards the surface, shown with a red box in Figure 5.30. The distribution appears to reach its highest point near 0 and cannot become negative due to the physical constraints on the roughness parameter. Furthermore, the green line on the posterior distribution for each parameter does not closely follow the shape of the distribution, which means that the fit has not converged. Therefore, the analysis was repeated setting the value of the parameter 3mrha_ 2K at a roughness value of 7 Å, a value that lies within the distribution for this parameter. It was found that this adjustment did not alter the peak values in the posterior distributions of the other parameters. Moreover, constraining this parameter caused the green line to match the distribution more closely, as illustrated in Figure 5.31.

The posterior probability distribution for all the parameters in Figure 5.31 resembles the shape of a Gaussian distribution, inferring that the mean value of the parameters lies within the boundaries shown with the distribution. The mean values and their 68

% confidence intervals are listed in Table 5.13. Although the values of the parameters listed in Table 5.13 do not represent the actual values, they serve to define a specific shape of the MSLD profile of a sample under any given temperature and magnetic field conditions. Consequently, to obtain the precise values, one should refer directly to the MSLD profile itself. The actual estimated values are enumerated at the end of this section in Table 5.15.

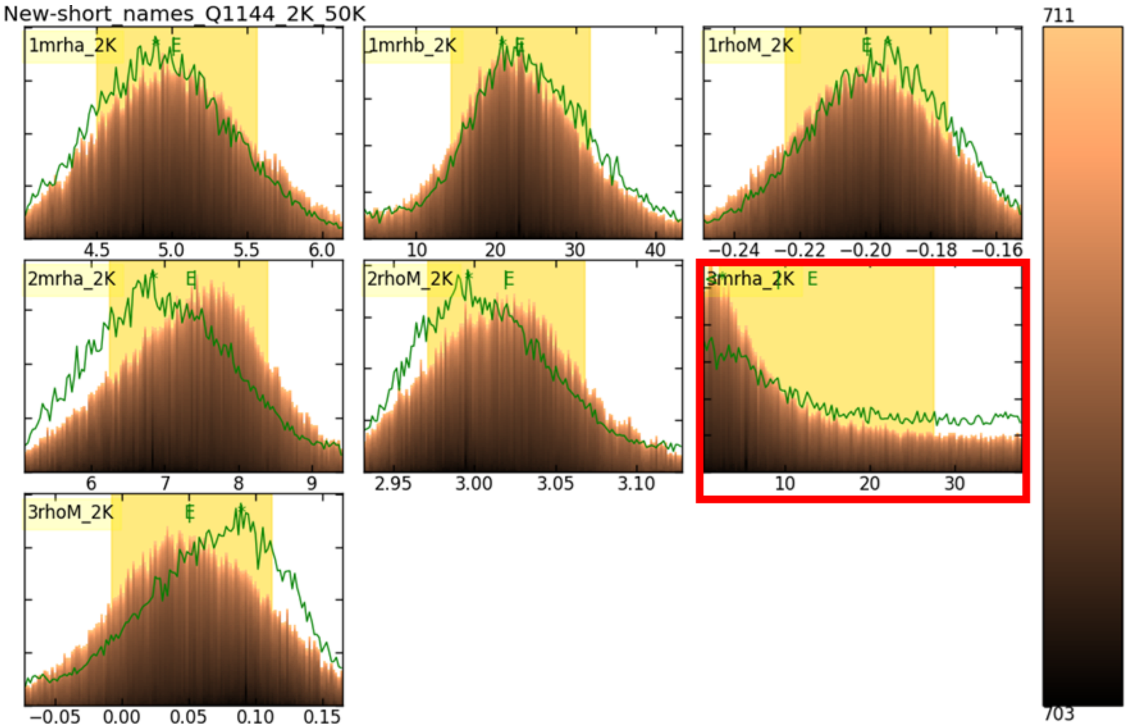

Figure 5.30: A chart of posterior distribution functions of the parameters for the sample QD1. The parameter's name is written on the top left side of the box that contain the distribution.

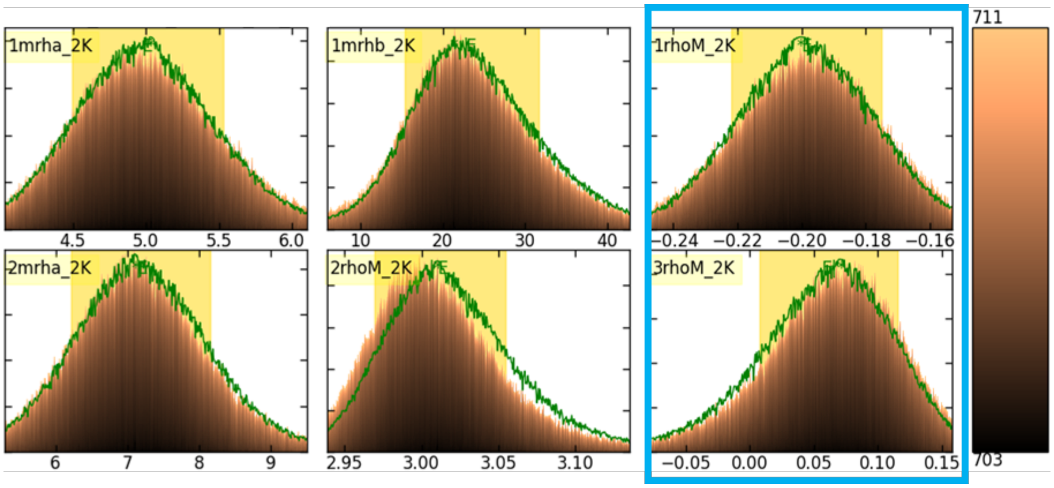

Figure 5.31: A chart of posterior distribution functions of the parameters for the sample QD1. The parameter's name is written on the top left side of the box that contain the distribution. The blue box highlights the distribution for the parameters 1rhoM_2K and 3rhoM_2K.

Table 5.13: List of parameters with mean values and 68 % confidence intervals for the QD1 sample (2 K) obtained from uncertainty analysis shown in Figure 5.31. Here, mrh (roughness) is in Å and rhoM is in $Å^{-2}$ units with a factor of 10^{-6}.

Parameter	**Mean**	**68% Interval**
1mrha_2K	5.0	[4.5, 5.5]
1mrhb_2K	24	[16, 32]
1rhoM_2K	- 0.20	[- 0.22, - 0.18]
2mrha_2K	7	[6, 8]
2rhoM_2K	3.02	[2.97, 3.05]
3rhoM_2K	0.06	[0.01, 0.12]

Figure 5.32 shows the correlations between the pair of 7 parameters. The row and column highlighted with the red box represent the cross-correlations of parameter 3mrha_2K with other parameters, corresponding to the uncertainty analysis shown in Figure 5.30. The distribution of these correlations does not peak inside the box, but spreads horizontally. However, the cross-correlations between other pair of parameters are well defined and peaks inside the boxes. By setting the value of parameter 3mrha_2K to 7 Å and repeating the correlation analysis, it becomes evident that this adjustment

does not influence the pattern of correlations between the remaining parameters, as illustrated in Figs. 5.32 and 5.33.

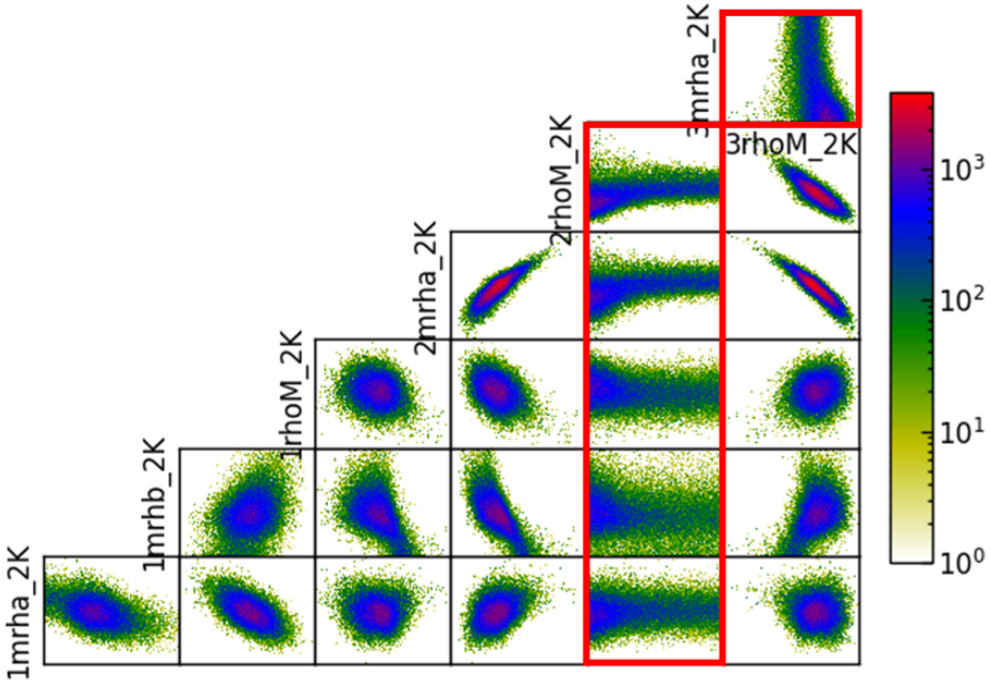

Figure 5.32: A chart of cross-correlations between a set of parameters for the sample QD1. The parameters corresponds to the model selected to fit the PNR data recorded at 2 K in presence of 0.1 T.

Each correlation plot between a pair of parameters is numbered 1 to 15 in Figure 5.33. It is observed that the distributions in all the correlation plots peak within the box. The red boxes (4, 5, 6, 7, 10, 13, 14, and 15) enclosing the correlation plots in Figure 5.33 show weak or no correlations. In contrast, the plots outlined in the cyan boxes (1, 3, 8, 9, 11, and 12) depict negative correlations among the parameters, whereas the light orange box (2) highlights a positive correlation.

The cross correlations between MSLDs are shown separately in Figure 5.34. Figure 5.34 (a) illustrates a weak correlation between the MSLD of layer 1 and layer 2. Similarly, Figure 5.34 (b) depicts a weak positive correlation between the MSLD of layer 1 and layer 3. In contrast, Figure 5.34 (c) exhibits a negative correlation between the MSLD of layer 2 and layer 3. Meanwhile, Figure 5.34 (d) demonstrates a positive correlation between the magnetic roughness toward the surface and the MSLD of layer 2. Finally, Figure 5.34 (e) presents a negative correlation between the magnetic roughness toward the surface of layer 2 and the MSLD of layer 3.

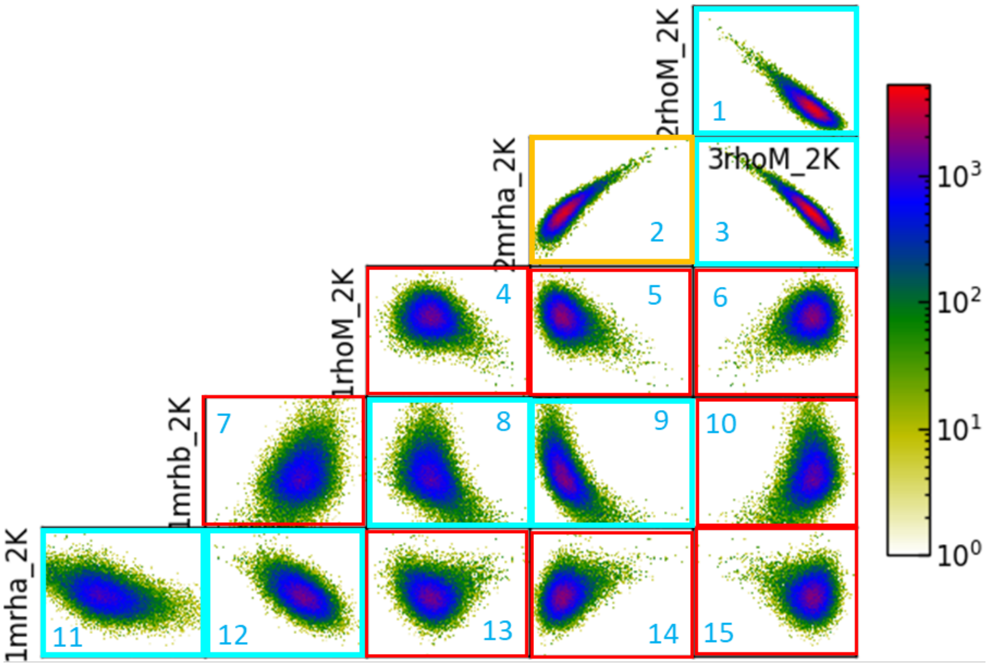

Figure 5.33: A chart of cross-correlations plots between a set of parameters for the sample QD1. The parameters corresponds to the model selected to fit the PNR data recorded at 2 K.

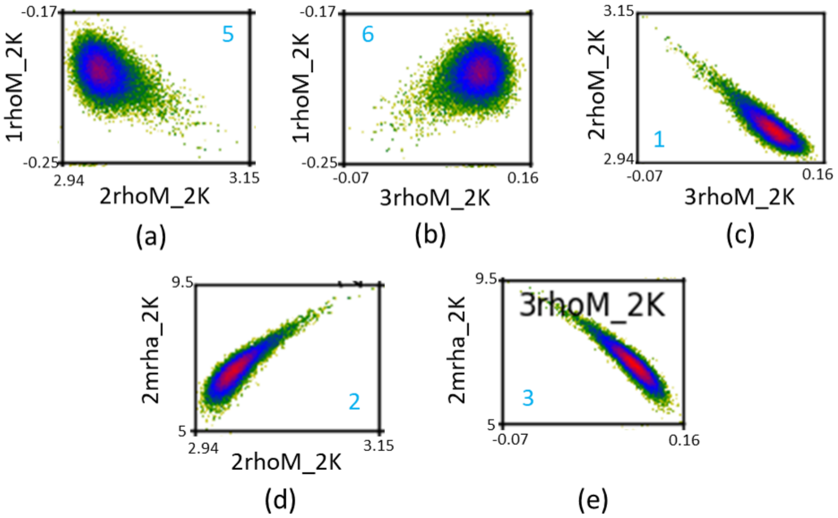

Figure 5.34: Correlation plot for the data at 2 K for the sample QD1 between parameter (a) MSLD of layer 1 and 2 (b) MSLD of layer 1 and 3 (c) MSLD of layer 2 and 3 (d) mrha and MSLD of layer 2 (e) mrha of layer 2 and MSLD of layer 3.

The results of the uncertainty analysis on a set of parameters that defines the MSLD profile at 8 K are shared in Figure 5.35. Similarly to the uncertainty analysis findings for the parameter 3mrha_2K [Figure 5.30], the parameter 3mrha_8K also exhibits a skewed distribution, shown in Figure 5.35. A similar approach was taken by fixing the value of this parameter to a value in the posterior distribution, that is, 7 Å, which made the green line follow the shape of the distribution more closely [Figure 5.37], and it was observed that this had no impact on the other distributions and cross-correlations. The uncertainty and correlation analysis for the parameters, including 3mrha_8K, are shared in Figs. 5.35 & 5.36.

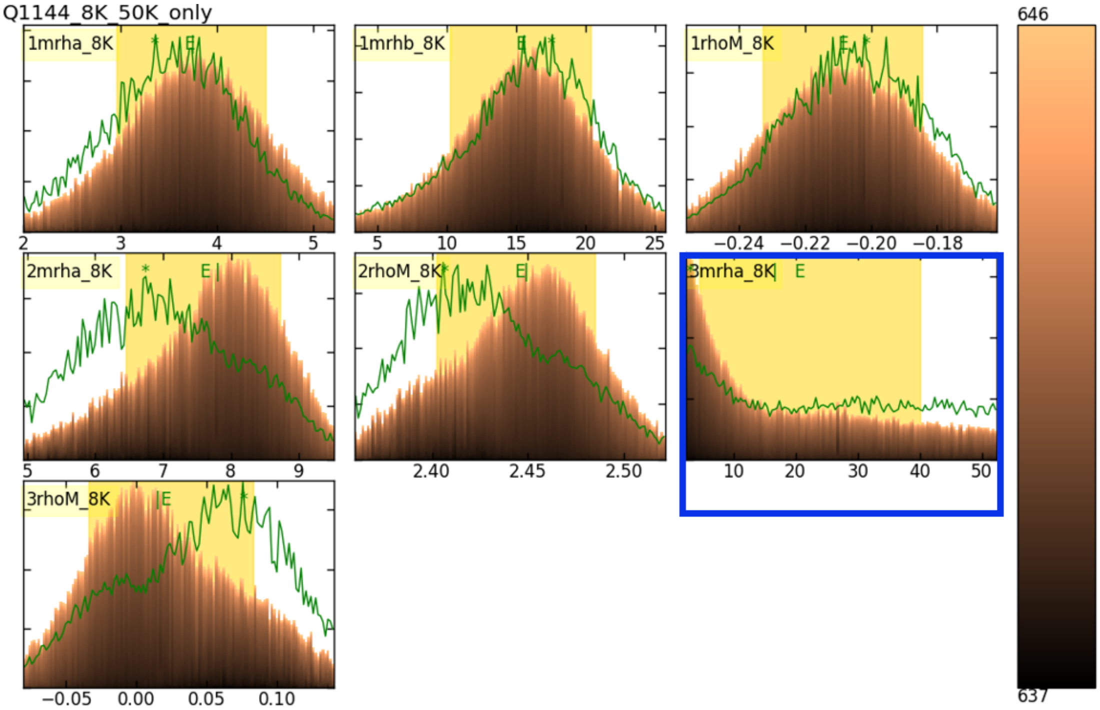

Figure 5.35: A chart of posterior distribution functions of the parameters for the sample QD1. The parameter's name is written on the top left side of the box that contain the distribution.

Figure 5.37 shows a chart of posterior distributions for the 6 parameters. The posterior probability distribution for all the parameters in Figure 5.37 resembles the shape of a Gaussian distribution, inferring that the mean value of the parameters lies within the boundaries shown with the distribution. The mean values and confidence intervals of 68 % are listed in Table 5.14. The actual estimated values of MSLDs at 8

K are listed at the end of this section in Table 5.15.

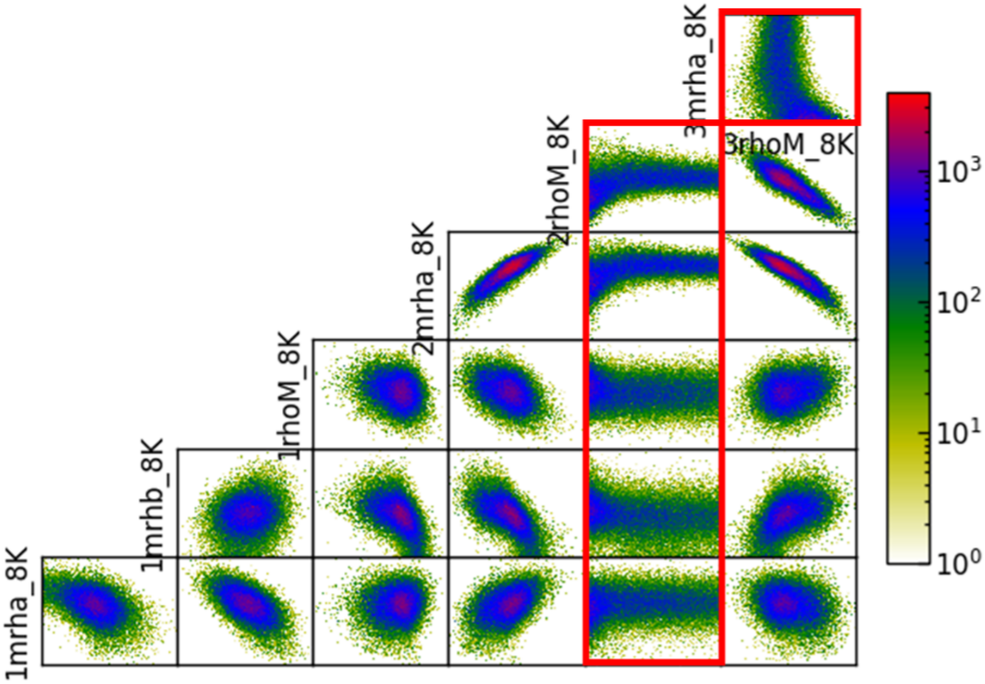

Figure 5.36: A chart of cross-correlations between a set of parameters for the sample QD1. The parameters corresponds to the model selected to fit the PNR data recorded at 8 K in presence of 0.1 T.

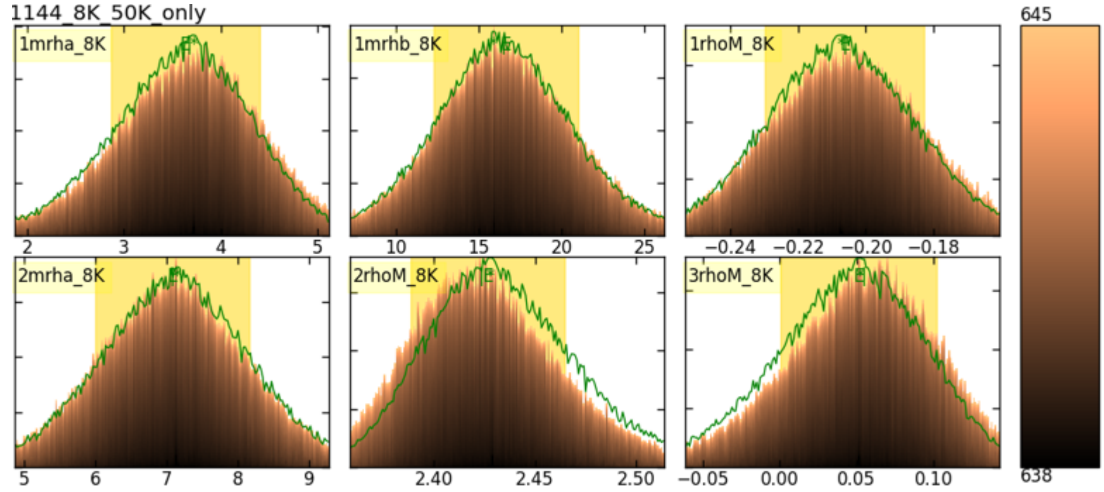

Figure 5.37: A chart of posterior distribution functions of the parameters for the sample QD1. The parameter's name is written on the top left side of the box that contain the distribution.

Table 5.14: List of parameters with mean values and 68 % confidence intervals for the QD1 sample (8 K). Here, mrh (roughness) is in Å and rhoM is in Å^{-2} units with a factor of 10^{-6}.

Parameter	**Mean**	**68% Interval**
1mrha_8K	3.6	[2.9, 4.4]
1mrhb_8K	17	[12, 21]
1rhoM_8K	- 0.21	[- 0.23, - 0.18]
2mrha_8K	7	[6, 8]
2rhoM_8K	2.43	[2.39, 2.46]
3rhoM_8K	0.05	[0.00, 0.10]

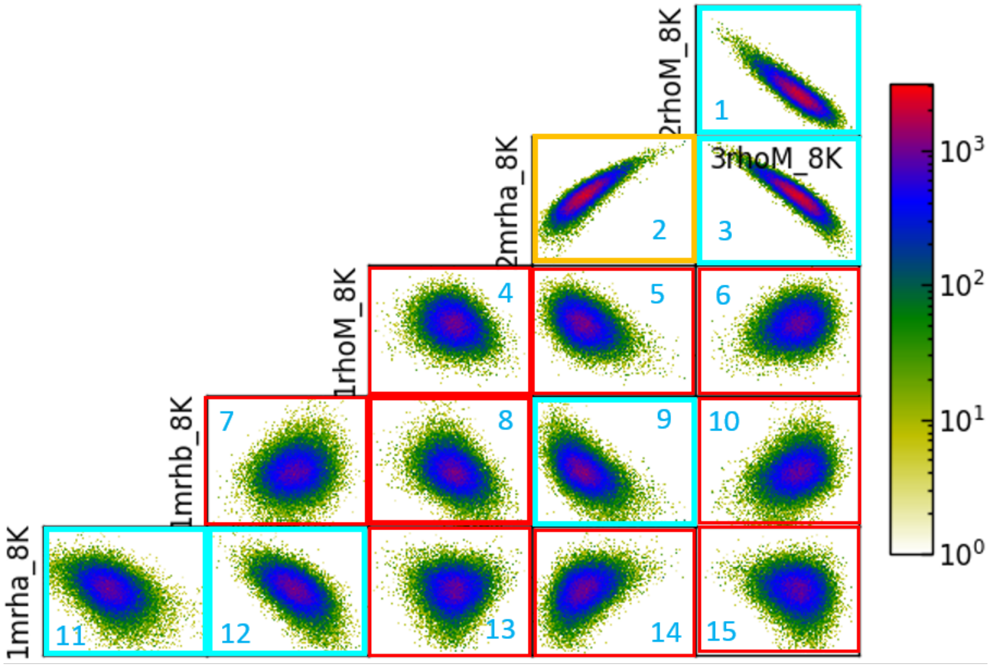

Figure 5.38: A chart of cross-correlations between a set of parameters for the sample QD1. The parameters corresponds to the model selected to fit the PNR data recorded at 8 K in presence of 0.1 T.

In Figure 5.38, it is evident that the distributions in all the correlation plots peak within the boxes for the parameters. The red boxes surrounding the correlation plots (4, 5, 6, 7, 8, 10, 13, 14 and 15) in Figure 5.38 indicate weak or absent correlations. In contrast, the plots outlined in the cyan boxes (1, 3, 9, 11 and 12) display negative correlations among the parameters, whereas the light orange box (2) highlights a positive correlation.

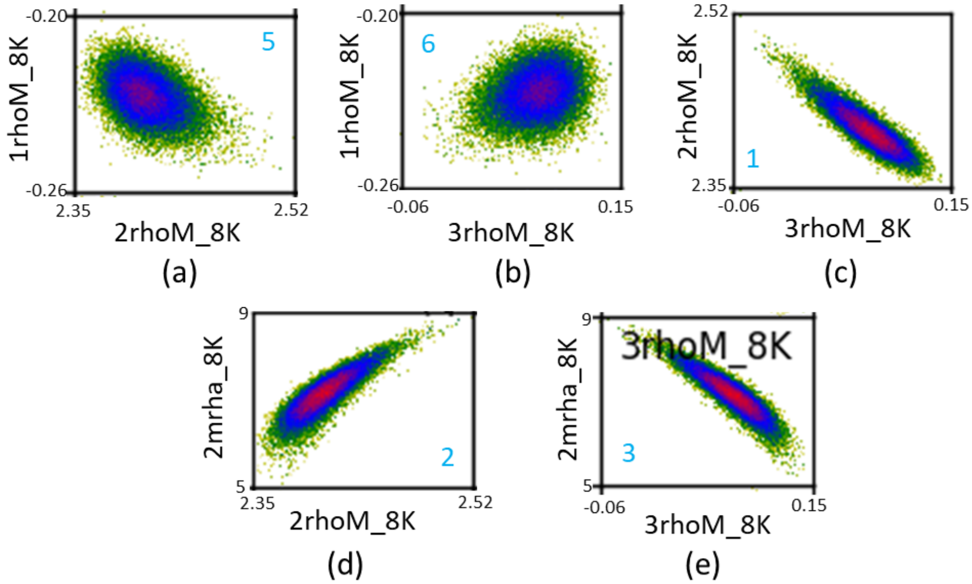

Figure 5.39: Correlation plot for the data at 8 K for the sample QD1 between (a) MSLD of layer 1 and 2 (b) MSLD of layer 1 and 3 (c) MSLD of layer 2 and 3 (d) Magnetic roughness towards surface and MSLD of layer 2 (e) Magnetic roughness towards surface of layer 2 and MSLD of layer 3.

The cross correlations between MSLDs are shown separately in Figure 5.39. Figure 5.39 (a) illustrates a weak negative correlation between the MSLD of layer 1 and layer 2. Similarly, Figure 5.39 (b) depicts a weak positive correlation between the MSLD of layer 1 and layer 3. In contrast, Figure 5.39 (c) exhibits a negative correlation between the MSLD of layer 2 and layer 3. Meanwhile, Figure 5.39 (d) demonstrates a positive correlation between the magnetic roughness toward the surface and the MSLD of layer 2. Finally, Figure 5.39 (e) presents a negative correlation between the magnetic roughness toward the surface of layer 2 and the MSLD of layer 3.

Table 5.15 lists the MSLD values for the EuS and interface layers at 2 K and 8 K for the QD1 sample. MSLD values are obtained from the peak of the MSLD profile in the EuS region and the dips observed in the interface layers. The error estimation is performed by adjusting the lower and upper limits of the parameters of Tables 5.13 and 5.14, then noting the peak and dip values in the MSLD profile. In summary, a negative MSLD is observed at the lower interface ("1") for both 2 K and 8 K. The magnetic

Table 5.15: MSLDs for the sample QD1 at 2 K and 8 K.

Sample QD1		
Layer	**MSLD (2 K)**	**MSLD (8 K)**
	($\times 10^{-6}$ Å^{-2})	**($\times 10^{-6}$ Å^{-2})**
Interface "3"	-	-
EuS ("2")	3.02 [2.97, 3.05]	2.43 [2.39, 2.46]
Interface "1"	- 0.17 [- 0.15, - 0.19]	- 0.20 [- 0.17, - 0.23]

parameters that define the MSLD profiles at 2 K and 8 K show similar uncertainty distributions and cross-correlations, except that the boundary values are different for each distribution.

Sample QD2

Table 5.16 list the PNR measurements performed on the QD2 sample at ILL on the D17 instrument [80]. A total of three PNR measurements were performed for the sample to monitor the variations in the magnetic signal as a function of temperature. Figure 5.40 (a) shows the fitted PNR data for the QD2 sample.

Table 5.16: PNR measurements for the QD2 sample performed at ILL [D17 instrument [80]]

PNR Measurements	
Temperature (K)	**Magnetic field (T)**
2	0.1
8	0.1
50	0.1

NSLD and MSLD depth profiles versus depth profiles are shown in Figure 5.40 (b). The trend in the NSLD profile for this sample is similar to that of the QD1 sample, except that the interface layers "1" and "3" both show a higher NSLD than the adjacent Pb layers. Moreover, similar to QD1, a negative MSLD is observed at both 2 K and 8 K in the interface layers. However, the magnitude of MSLD at 2 K is higher in the interface layer "3" than in the interface layer "1". Furthermore, MSLD at 8 K in the interface layer "1" is roughly approaching 0.

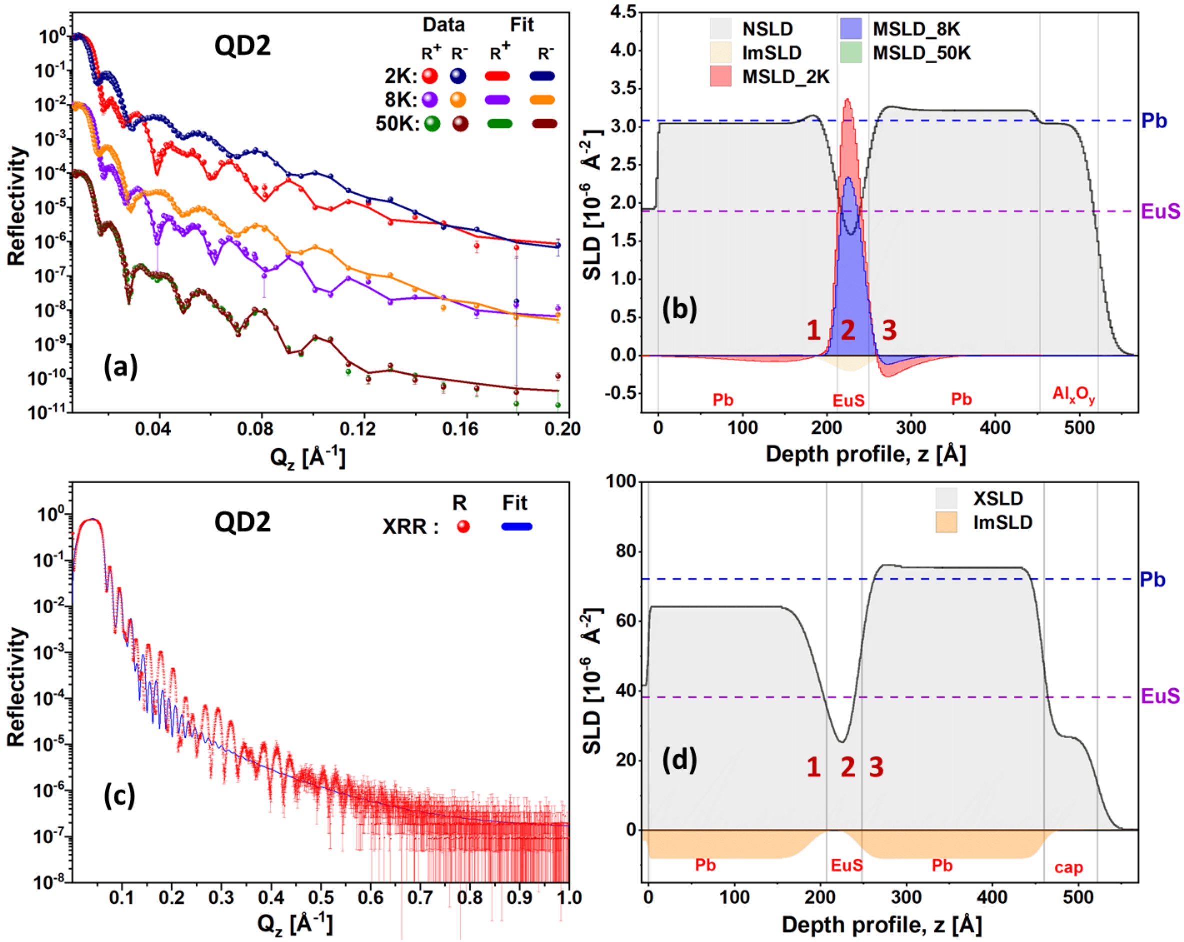

Figure 5.40: Fitted reflectometry data for QD1 sample. (a) PNR data recorded at 2 K, 8 K and 50 K in the presence of 0.1 T with their respective fits. The datasets are shifted by 10^2 units along the y-axis to enhance clarity. (b) NSLD and MSLD versus depth profiles (c) Fitted XRR data (d) XSLD versus depth profile. Absorption scattering length density (ImSLD) profiles for neutrons and X-rays are shown in orange color along with NSLD and XSLD profiles, respectively.

Figs. 5.40 (c) and (d) show the fitted XRR data and the corresponding XSLD profile of the sample. The trend in the XSLD profile of the layers is observed to be similar to that in the NSLD profile, except that no hump in XSLD was observed at the lower EuS/Pb interface. In the flat region of the sample SLD profiles, the NSLD and XSLD for the layer are estimated and shown in Table 5.17. NSLD of the top Pb layer is around 4 % higher than the value in the reference (Table 5.8). The NSLD of the EuS layer is approximately 17 % lower than the reference value for EuS.

Table 5.17: A list of the parameters and their estimated values from the fit to the reflectometry data for the sample QD2.

Sample QD2			
Layer	**Thickness**	**NSLD**	**XSLD**
	(Å)	**($\times 10^{-6}$ Å^{-2})**	**($\times 10^{-6}$ Å^{-2})**
Cap	72.0 [71.4, 72.7]	3.04 [3.03, 3.04]	26.7 [26.3, 27.3]
Pb top	204.3 [203.6, 205.0]	3.21 [3.20, 3.21]	75.3 [75.2, 75.5]
Interface "3"	2.1 [1.6, 2.6]	3.26 [3.22, 3.29]	76 [53, 84]
EuS ("2")	31.5 [31.4, 31.6]	1.58 [1.56, 1.59]	25 [23, 30]
Interface "1"	26.3 [25.9, 26.9]	3.14 [3.10, 3.17]	49 [48, 51]
Pb bottom	186.9 [186.4, 187.4]	3.04 [3.03, 3.04]	64 [62, 66]

Figure 5.41 (a) shows the comparison between the XRR data fitted with and without taking structural parameters from the PNR fits. The XRR data (in red) and its fit (in blue) are the same as shown in Figure 5.40 (c). The estimated values of the thicknesses and XSLDs are compared in Tables 5.18 and 5.19. Similarly to the QD1 sample, a difference in the thicknesses of the layers is observed for the PNR and XRR fits for the QD2 sample. However, the difference in the thickness of the entire layer stack is less than 1 %.

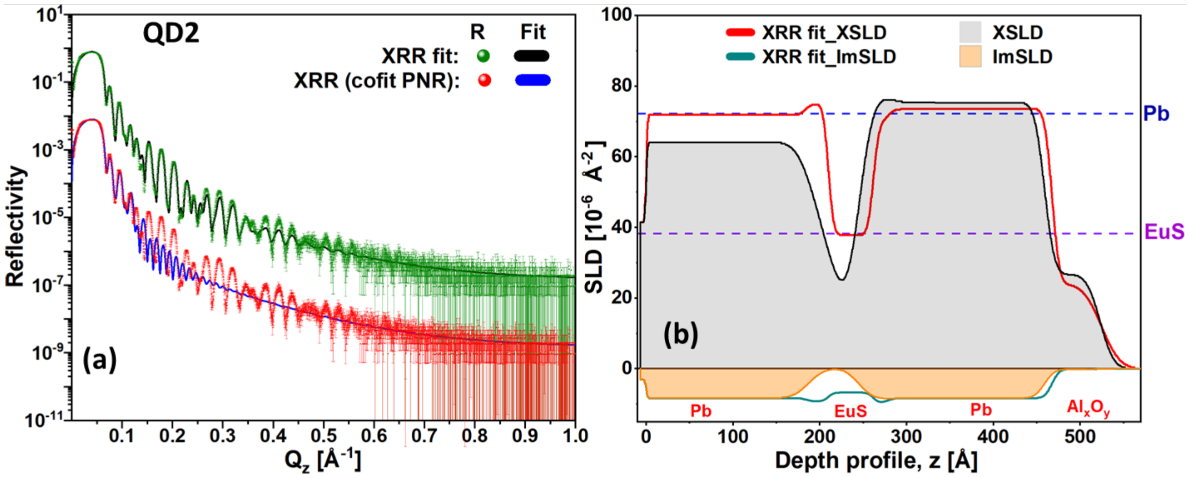

Figure 5.41: (a) Fitted XRR data and cofitted XRR data with structural parameters from PNR fits for the QD2 sample (b) A comparison of the XSLD profile for the fits. The reference XSLD for Pb (blue) and EuS (violet) are marked on the plots.

Table 5.18: A comparison of the estimated values of thickness from the two XRR fits for the sample QD2.

Sample QD2		
	Thickness (Å)	
Layer	**XRR (cofit PNR)**	**XRR fit**
Cap	72.0 [71.4, 72.7]	59.4 [58.9, 60.0]
Pb top	204.3 [203.6, 205.0]	191 [190, 192]
Interface “3”	2.1 [1.6, 2.6]	16.1 [15.8, 16.6]
EuS (“2”)	31.5 [31.4, 31.6]	52.3 [52.0, 53.0]
Interface “1”	26.3 [25.9, 26.9]	26 [25, 27]
Pb bottom	186.9 [186.4, 187.4]	181.7 [180.9, 182.6]

Table 5.19: A comparison of the estimated values of XSLD from the two XRR fits for the sample QD2.

Sample QD2		
	XSLD ($\times 10^{-6}$ Å^{-2})	
Layer	**XRR (cofit PNR)**	**XRR fit**
Cap	26.7 [26.3, 27.3]	24.2 [23.8, 24.4]
Pb top	75.3 [75.2, 75.5]	74.7 [74.5, 74.8]
Interface “3”	76 [53, 84]	72 [70, 73]
EuS (“2”)	25 [22, 30]	31.8 [31.6, 32.6]
Interface “1”	49 [48, 51]	71 [70, 72]
Pb bottom	64 [62, 66]	72 [71, 73]

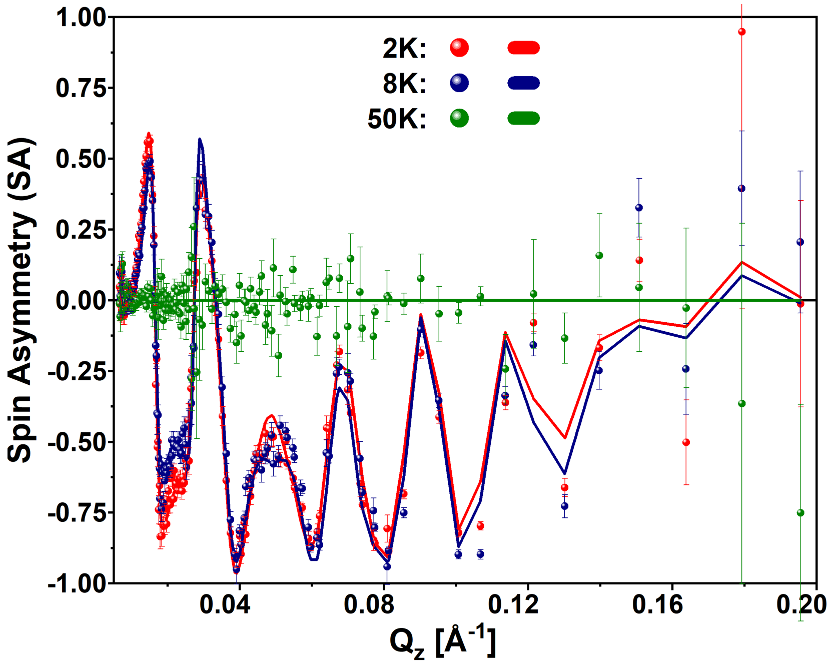

Figure 5.42: SA as a function of Q_z in presence of in-plane magnetic field of 0.1 T for the sample QD2 is shown along with the respective fits.

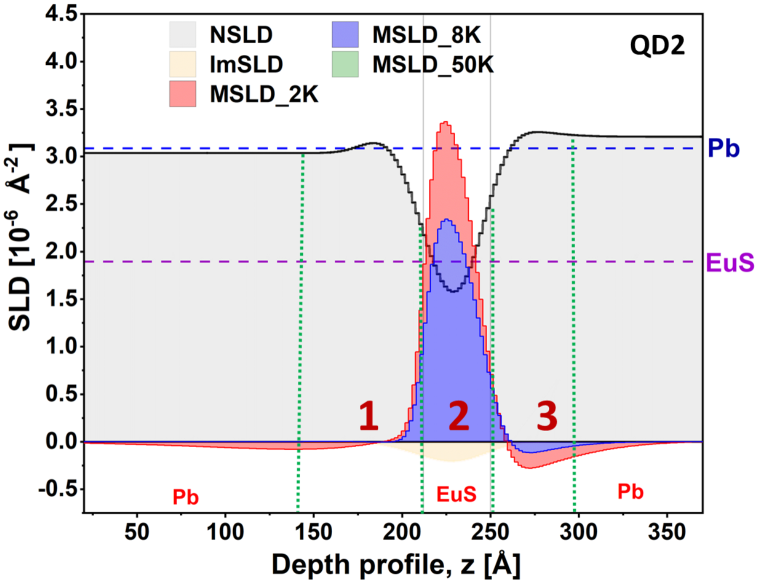

Figure 5.43: A magnified version of the NSLD and MSLD profiles of the sample QD2. The vertical green dotted lines pass through the midpoints of the roughness profiles at interfaces and act as guide to estimate the thicknesses.

Figure 5.42 illustrates the SA plotted against Q_z for the QD2 sample. The behavior of SA for the QD2 sample is similar to that observed for the QD1 sample [Figure 5.28].

Figure 5.43 illustrates an enlarged view of the NSLD and MSLD profiles close to the EuS layer interface with both Pb layers. The PNR data analysis revealed that the EuS layer has a positive MSLD, whereas the interface layers 1 and 3 have negative MSLD values. These MSLD values for each individual layer are detailed in Table 5.17.

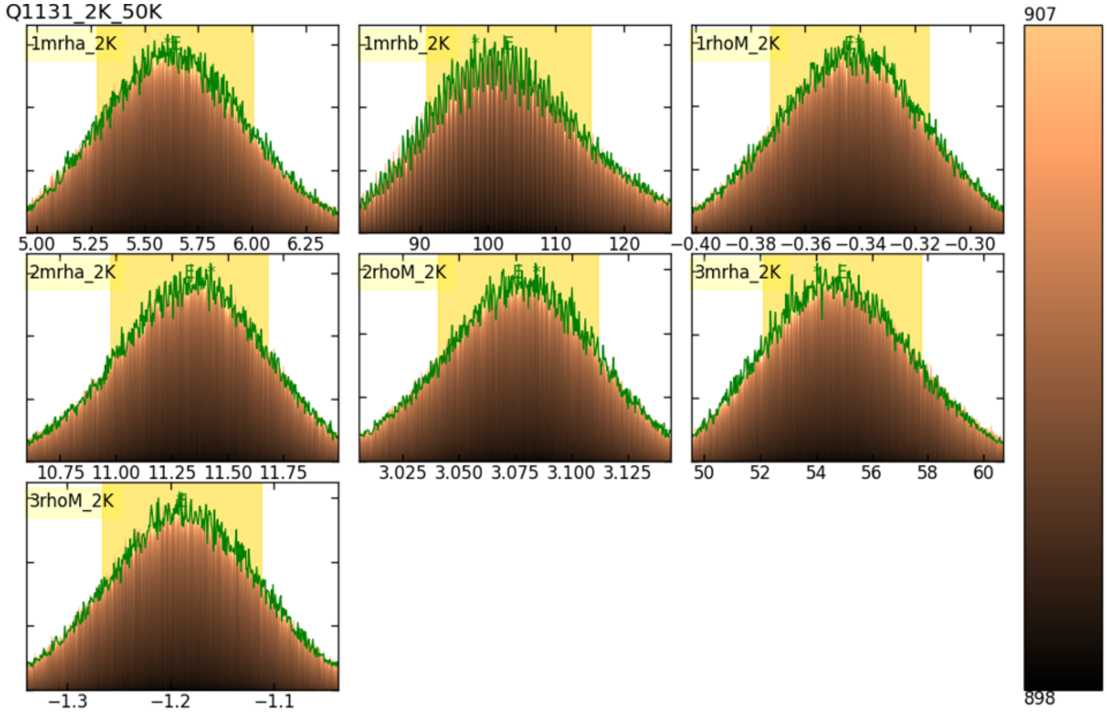

Figure 5.44: A chart of posterior distribution functions of the parameters for the sample QD2 (2 K). The parameter's name is written on the top left side of the box that contain the distribution.

A similar approach to the QD1 sample was followed for uncertainty and correlation analysis for this sample. The parameter that showed a skewed posterior distribution was fixed and the analysis was repeated again. The results of the uncertainty analysis on a set of parameters that defines the MSLD profile at 2 K are shared in Figure 5.44. The posterior probability distribution for all the parameters in Figure 5.44 resembles the shape of a Gaussian distribution, inferring that the mean value of the parameters lies within the boundaries shown with the distribution. The mean values of the parameters and their confidence intervals are listed in Table 5.20. The actual estimated values of

MSLD at 2 K and 8 K are listed at the end of this section in Table 5.22.

Table 5.20: Summary of parameters with mean values and 68 % confidence intervals obtained from uncertainty analysis shown in Figure 5.44. Here, mrh (roughness) is in Å and rhoM is in $Å^{-2}$ units with a factor of 10^{-6}.

Parameter	**Mean**	**68% Interval**
1mrha_2K	5.6	[5.3, 6.0]
1mrhb_2K	103	[91, 115]
1rhoM_2K	- 0.34	[- 0.37, - 0.32]
2mrha_2K	11.3	[11.0, 11.7]
2rhoM_2K	3.08	[3.04, 3.11]
3mrha_2K	55	[52, 58]
3rhoM_2K	- 1.19	[- 1.27, - 1.11]

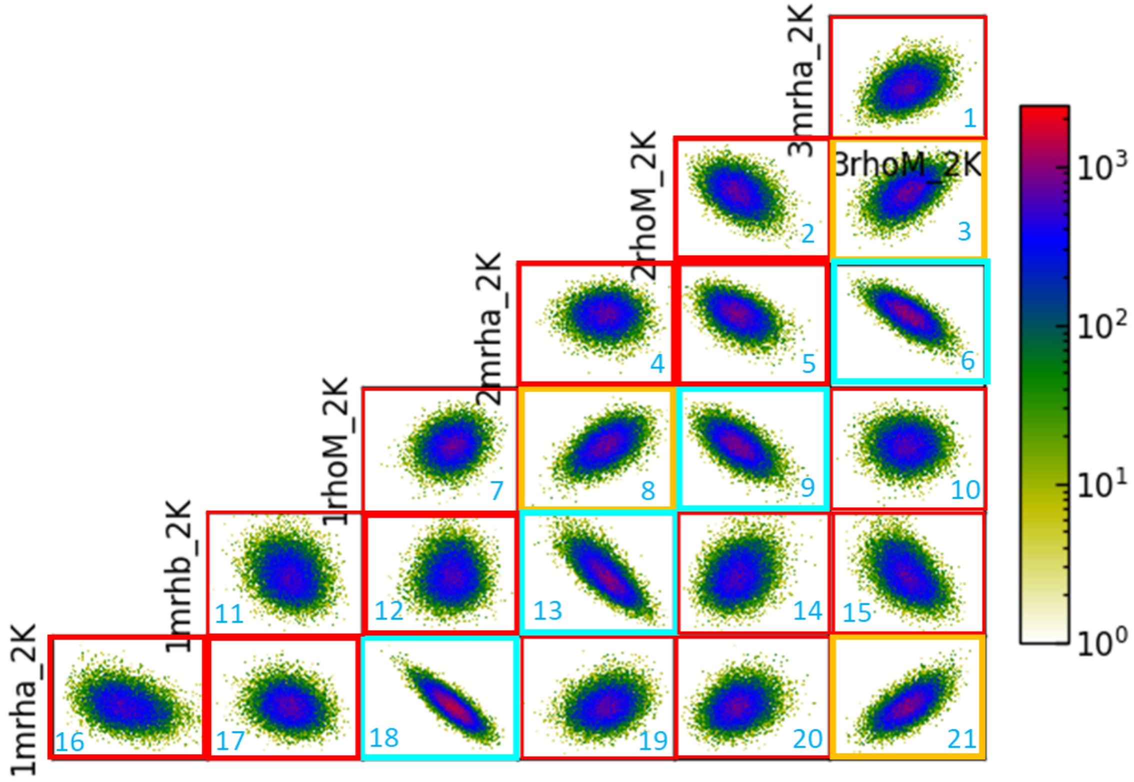

Figure 5.45: A chart of cross-correlations plots between a set of parameters for the sample QD2, corresponding to the model selected to fit the PNR data recorded at 2 K.

Figure 5.45 shows the correlations between the pair of 7 parameters. Similarly to QD1 cross-correlations at 2 K, the distributions in all the correlation plots peak within the box. The cross correlations between MSLDs are shown separately in Figure 5.46. In Figure 5.46 (a), a weak positive correlation is observed between the MSLD values of layer 1 and layer 2. Furthermore, Figure 5.46 (b) shows a weak correlation involving the MSLD of layer 1 and layer 3. Figure 5.46 (c) reveals a weak positive correlation of the MSLD of layer 2 and layer 3. Figure 5.46 (d) shows a negative correlation between magnetic roughnesses toward the surface for layer 1 and layer 2.

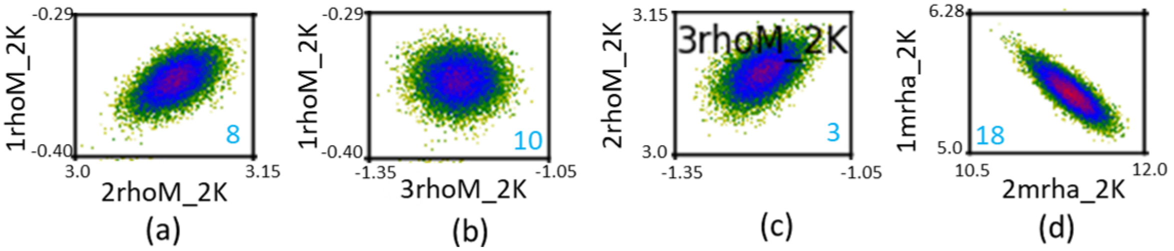

Figure 5.46: Correlation plot for the data at 2 K for the sample QD2 between (a) MSLD of layer 1 and 2 (b) MSLD of layer 1 and 3 (c) MSLD of layer 2 and 3.

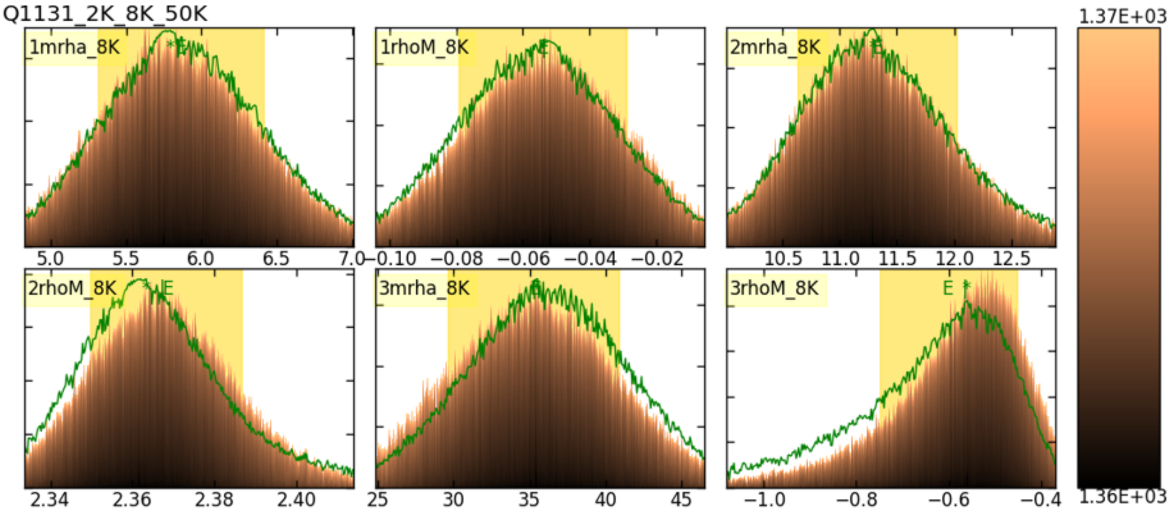

Figure 5.47: A chart of posterior distribution functions of the parameters for the sample QD2 (8 K). The parameter's name is written on the top left side of the box that contain the distribution.

The results of the uncertainty analysis on a set of parameters that defines the MSLD profile at 8 K are shared in Figure 5.47. The parameter 1mrhb_8K exhibited a skewed distribution and therefore its value was fixed following a similar approach to the sample QD1 (Subsection 5.4.4). The results of the uncertainty and correlation analysis for all parameters are shared in Appendices A [8]. Similarly to QD1, fixing the value of parameter 1mrhb_8K to 8 Å had no impact on the other posterior distributions and cross correlations. The uncertainty analysis for the parameters, excluding 1mrhb_8K, is shared in Figure 5.47. The estimated mean values of the parameters and confidence intervals are listed in Table 5.21.

Table 5.21: List of parameters with mean values and 68 % confidence intervals for the data at 8 K for the sample QD2.

Parameter	**Mean**	**68% Interval**
1mrha_8K	5.9	[5.3, 6.4]
1rhoM_8K	- 0.06	[- 0.08, - 0.03]
2mrha_8K	11.3	[10.6, 12.1]
2rhoM_8K	2.37	[2.35, 2.39]
3mrha_8K	35	[29, 41]
3rhoM_8K	- 0.6	[- 0.8, - 0.5]

Figure 5.48 shows a cross-correlation chart for the six parameters. In Figure 5.48, similar to the sample QD1 and data at 2 K for QD2, the distributions in all the correlation plots peak within the boxes.

Figure 5.49 (a) illustrates a weak correlation between the MSLD of layer 1 and layer 2. Similarly, Figure 5.49 (b) depicts a weak correlation between the MSLD of layer 1 and layer 3. Figure 5.49 (c) exhibits a weak positive correlation between the MSLD of layer 2 and layer 3. Meanwhile, Figure 5.49 (d) demonstrates a positive correlation between the magnetic roughness toward the surface and the MSLD of layer 3. Finally, Figure 5.49 (e) presents a negative correlation between the magnetic roughness toward the surface of layer 2 and the MSLD of layer 3.

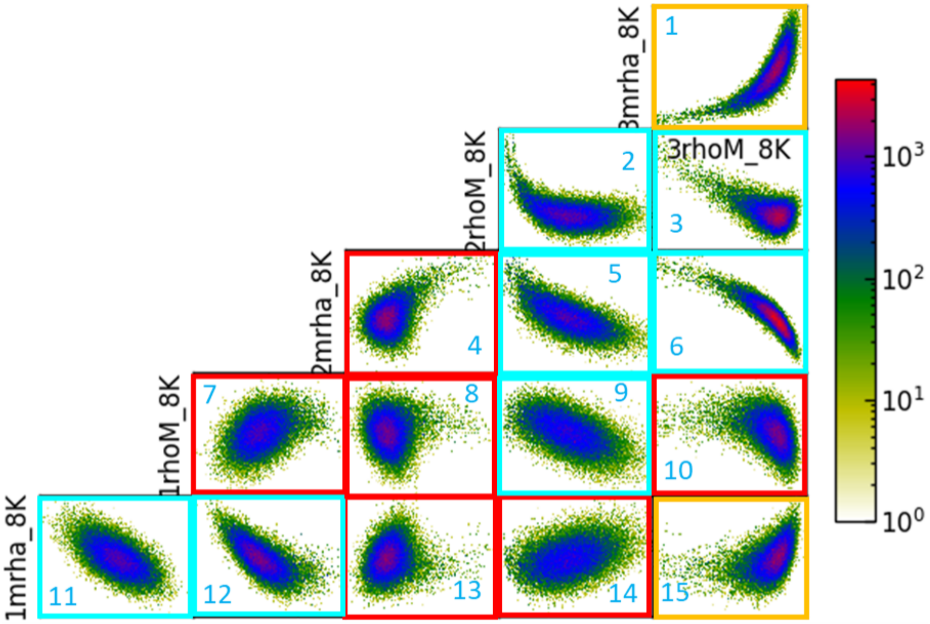

Figure 5.48: A chart of cross-correlations plots between a set of parameters for the sample QD2. The parameters corresponds to the model selected to fit the PNR data recorded at 8 K. A numbers is designated to each correlation plot for reference.

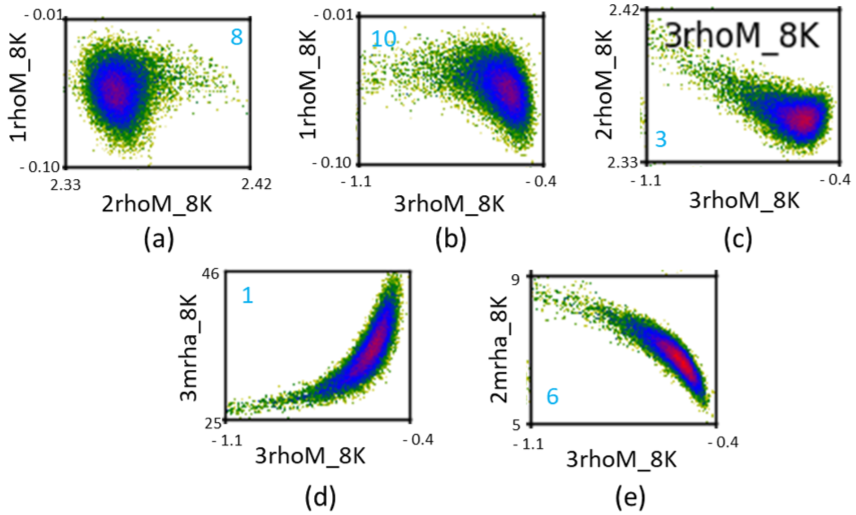

Figure 5.49: Correlation plot for the data at 8 K for the sample QD2 between (a) MSLD of layer 1 and 2 (b) MSLD of layer 1 and 3 (c) MSLD of layer 2 and 3 (d) Magnetic roughness towards surface and MSLD of layer 3 (e) Magnetic roughness towards surface of layer 2 and MSLD of layer 3.

Table 5.22 lists the MSLD values for the EuS and interface layers at 2 K and 8 K for the QD2 sample. MSLD values are obtained from the peak of the MSLD profile in the EuS region and the dips observed in the interface layers. The error estimation is performed by adjusting the lower and upper limits of the parameters of Tables 5.20 and 5.21, then noting the peak and dip values in the MSLD profile.

Table 5.22: MSLDs for the sample QD2 at 2 K and 8 K.

Sample QD2		
Layer	**MSLD (2 K)**	**MSLD (8 K)**
	($\times 10^{-6}$ Å^{-2})	**($\times 10^{-6}$ Å^{-2})**
Interface “3”	- 0.28 [- 0.20, - 0.36]	- 0.12 [- 0.08, - 0.16]
EuS (“2”)	3.37 [3.33, 3.41]	2.34 [2.32, 2.36]
Interface “1”	- 0.21 [- 0.18, - 0.24]	0

In summary, at 2 K, a negative MSLD is observed in interface layers “1” and “3”, while at 8 K, it is seen only in layer “3”. Similarly to the QD1 sample, the magnetic parameters at these temperatures exhibit similar uncertainty and cross-correlation patterns, with different boundary values for the posterior distribution.

Sample QD3

Two sample pieces, each measuring 400 mm^2, were cut from the same wafer. PNR measurements for piece 1 were performed on the POLREF instrument at ISIS [134], while the measurements for piece 2 were performed on the D17 instrument at ILL [80]. The ISIS measurements on the first piece occurred approximately one year prior to those at ILL for the second piece. Table 5.23 lists the recorded PNR measurements for the QD3 sample pieces. A total of five PNR measurements for each piece were performed to monitor the variations in the magnetic signals. Initially, the fitted results from POLREF data are presented, followed by the analysis of D17 instrument data in a later subsection.

Figure 5.50 shows the fitted PNR data, recorded at POLREF instrument, for the QD3 sample. The PNR data show a split between the reflectivities for spin-up (R^+) and spin-down (R^-) neutron measurements, except for the data at 50 K.

Table 5.23: PNR measurements for the two pieces of the sample QD3.

PNR measurements: QD3 sample			
Piece 1		**Piece 2**	
ISIS POLREF		**ILL D17**	
Temp. (K)	**$H_{ext,//}$ (T)**	**Temp. (K)**	**$H_{ext,//}$ (T)**
3.4	0.1	3.4	0.1
3.4 (FC)	0.1	3.4	0.5
6	0.1	3.4	3
8	0.1	8	3
50	0.1	50	3

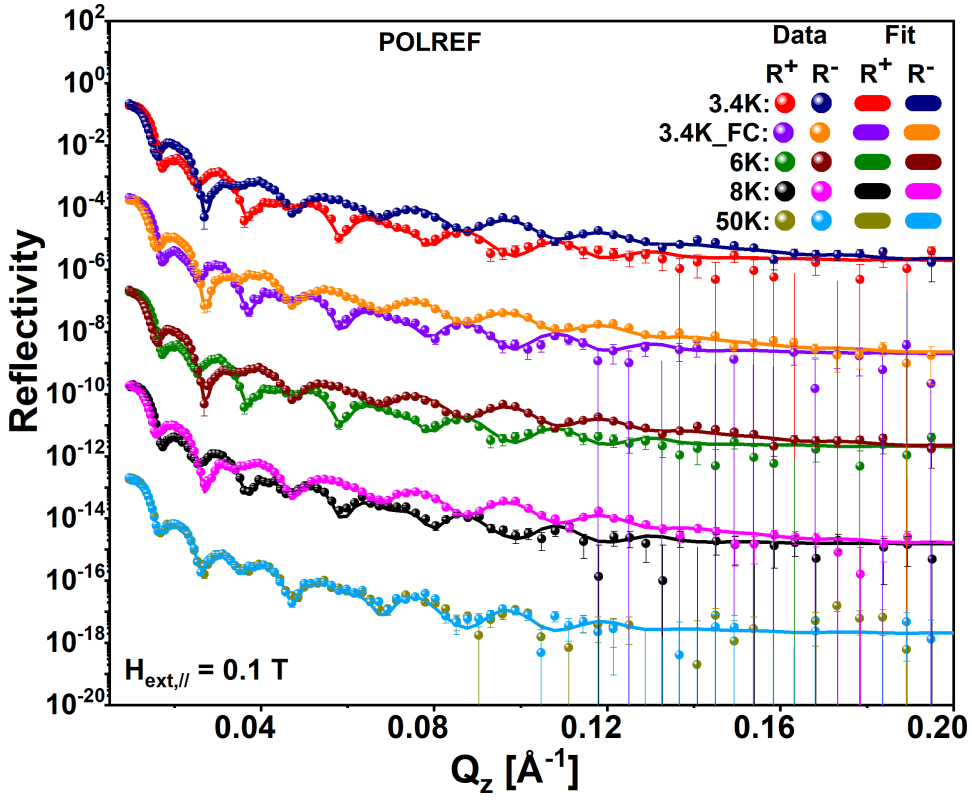

Figure 5.50: Fitted polarized neutron (PNR) data for the sample QD3 recorded for measurements as indicated in the plot. The datasets are shifted by 10^3 units along the y-axis to enhance clarity. The data were recorded at POLREF instrument.

NSLD and MSLD depth profiles versus depth profiles of the fits are shown in Figure

5.51. The trend in the NSLD profile for this sample is similar to that of the QD1 sample, except that the NSLDs of both Pb layers are close to the reference value for Pb (Table 5.8). Furthermore, similar to the QD1 and QD2 samples, a negative MSLD is observed at 3.4 K, 3.4 K (FC), 6 K, and 8 K in the interface layers. The estimated values of the structural parameters are listed in Table 5.24. NSLD of the bottom Pb layer is around 1 % higher than the reference value. The NSLD of the EuS layer is approximately 7 % lower than the reference value for EuS.

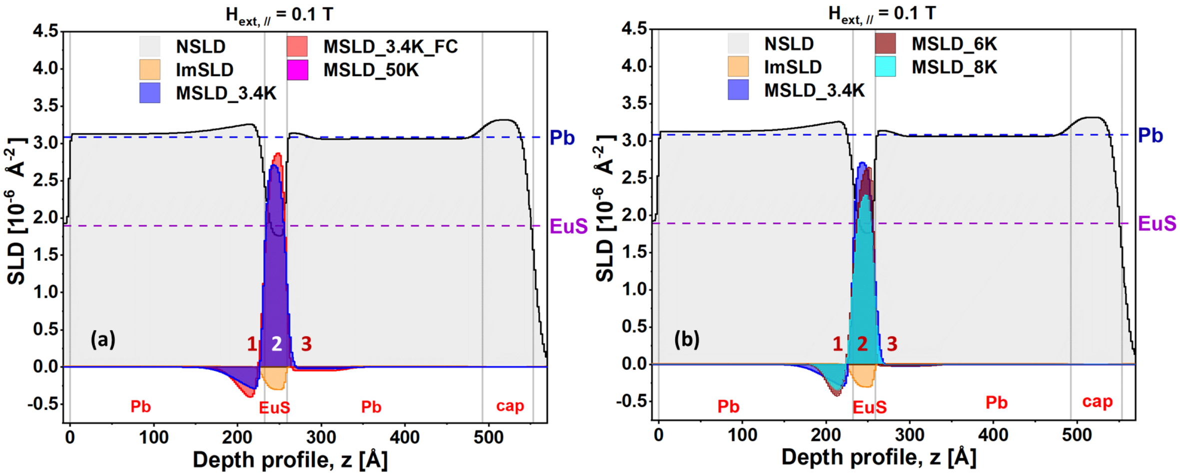

Figure 5.51: NSLD and ImSLD profiles for the sample QD3 are shown in both the plots. MSLD profiles for the the measurements at (a) 3.4 K, 3.4 K (FC), and 50 K (b) 3.4 K, 6 K, and 8 K.

Figure 5.52 (a) shows the comparison between the XRR data fitted with and without taking structural parameters from the PNR fits. XRR data, shown in red, along with their fit in blue, are fitted for the XSLD of layers, utilizing thickness and roughness parameters derived from PNR fits. Figure 5.52 (b) shows the XSLD profiles for both XRR fits. The trend in the XSLD profile of the layers for the XRR fit that is fitted with the PNR parameters is observed to be similar to that in the NSLD profile [shown in Figure 5.51], except that the XSLD of the lower Pb layer is observed to be higher than the XSLD of the top Pb layer. Furthermore, the XSLD profile for the XRR fit only depicts the similar XSLD for both Pb layers. The estimated values of the thicknesses and XSLDs for both fits are compared in Tables 5.25 and 5.26.

Table 5.24: A list of the parameters and their estimated values from the fit to the POLREF reflectometry data recorded for the sample QD3.

Sample QD3 (first piece)		
Layer	**Thickness**	**NSLD**
	(Å)	**($\times 10^{-6}$ Å^{-2})**
Cap	61 [59, 62]	3.31 [3.30, 3.32]
Pb top	167 [159, 176]	3.06 [3.06, 3.07]
Interface “3”	67 [58, 74]	3.14 [3.13, 3.15]
EuS (“2”)	26.4 [26.2, 26.5]	1.76 [1.74, 1.80]
Interface “1”	32 [30, 33]	3.26 [3.23, 3.30]
Pb bottom	201 [200, 203]	3.13 [3.12, 3.14]

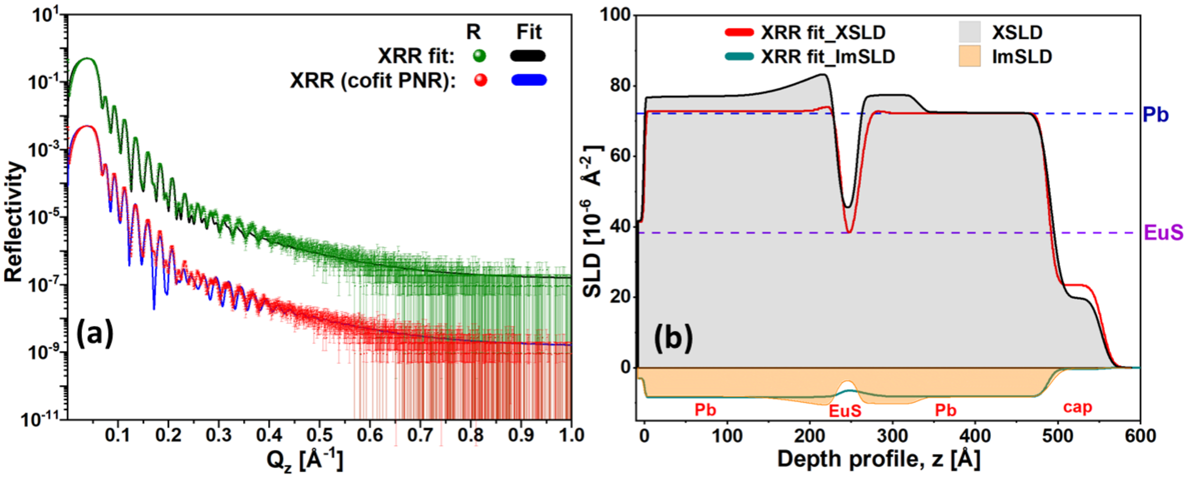

Figure 5.52: (a) Fitted XRR data and cofitted XRR data with structural parameters from PNR fits for the QD3 sample (b) A comparison of the XSLD profiles.

Similarly to the QD1 and QD2 samples, a difference in the thicknesses of the layers is observed for the PNR and XRR fits for the QD3 sample. However, the difference in the thickness of the entire layer stack is less than 1 %.

Figure 5.53 shows the SA as a function of Q_z, with respective fits. Similarly to QD1 and QD2 data at 50 K (in 0.1 T), SA data points at 50 K for the sample QD3 [shown in Figure 5.53 (b)] exhibit a random distribution close to the zero line and approximated as zero. The rest of the datasets exhibit a non-zero SA signal.

Table 5.25: A comparison of the estimated values of thickness from the two XRR fits for the sample QD3.

Sample QD3 (first piece)		
	Thickness (Å)	
Layer	**XRR (cofit PNR)**	**XRR fit**
Cap	61 [59, 62]	66.1 (65.7, 66.6)
Pb top	167 [159, 176]	222.8 (222.7, 223.1)
Interface “3”	67 [58, 74]	4.5 (4.1, 4.9)
EuS (“2”)	26.4 [26.2, 26.5]	23.8 (23.4, 24.2)
Interface “1”	32 [30, 33]	8 (5, 9)
Pb bottom	201 [200, 203]	229 (228, 231)

Table 5.26: A comparison of the estimated values of XSLD from the two XRR fits for the sample QD3.

Sample QD3 (first piece)		
	XSLD ($\times 10^{-6}$ Å^{-2})	
Layer	**XRR (cofit PNR)**	**XRR fit**
Cap	19.9 [19.2, 20.3]	23.45 [23.40, 23.50]
Pb top	72.3 [72.1, 72.5]	72.24 [72.16, 72.25]
Interface “3”	77 [76, 78]	77.43 [77.40, 77.46]
EuS (“2”)	45.4 [44.5, 46.3]	34.8 [34.2, 35.4]
Interface “1”	83 [81, 84]	78.1 [77.9, 78.2]
Pb bottom	77 [76, 79]	72.78 [72.77, 72.79]

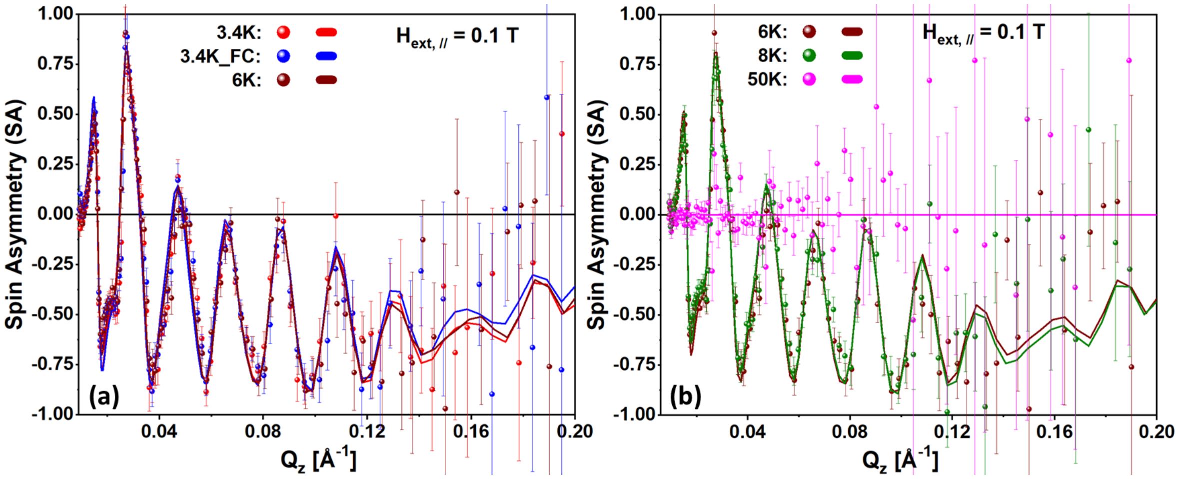

Figure 5.53: SA as a function of Q_z for the sample QD3 is shown along with the respective fits.

Figure 5.54 illustrates an enlarged view of the NSLD and MSLD profiles close to the EuS layer interface with both Pb layers. The PNR data analysis revealed that the EuS layer has a positive MSLD, whereas the interface layers 1 and 3 have negative MSLD values. These MSLD values for each individual layer are listed in Table 5.24.

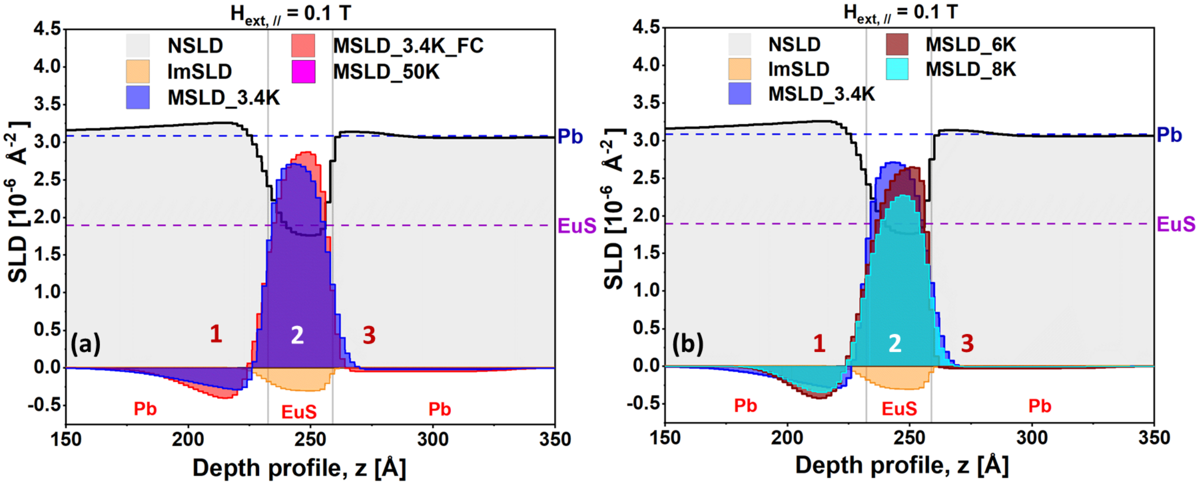

Figure 5.54: A magnified version of the NSLD and MSLD profiles of the QD3 sample near the EuS interface with both Pb layers.

A similar approach to the QD1 and QD2 samples was followed for the uncertainty and correlation analysis for this sample. The plots for all the uncertainty and correlation analyses are shared in Appendices A [8]. In correlation plots, red boxes denote weak or no correlations, cyan boxes indicate negative correlations, and a light orange box marks a positive correlation between parameter pairs. The actual estimated values of MSLDs at 3.4 K, 3.4 K (FC), 6 K, and 8 K are listed at the end of this section in Table 5.31.

The results of the uncertainty and correlation analysis for the parameters that define the MSLD profile at 3.4 K are shared in Figure 5.55. The analysis was repeated by fixing the value of the parameter 3mrha_3.4K is 8.87 Å. Figure 5.55 (a) shows well-defined posterior probability distributions for the parameters, except for the parameter 3mrha_3.4K. The mean values of the parameters and confidence intervals are listed in Table 5.27. Figure 5.55 (b) shows the correlations between the pair of six parameters. The distributions in all the correlation plots peak within the box. The MSLDs of the interface layer "1" and EuS show weak correlations with the MSLD of the interface layer "3" (correlations 1 and 6). However, MSLD in the interface layer "1" shows a weak negative correlation with the MSLD of EuS (correlation 5). A weak negative correlation (12) is observed between the parameters 1mrha_3.4K and 1rhoM_3.4K. Furthermore, a weak positive correlation (14) is observed between the parameters 1mrha_3.4K and 2rhoM_3.4K.

Table 5.27: Summary of parameters with mean values and 68 % confidence intervals for 3.4 K for sample QD3.

Parameter	**Mean**	**68% Interval**
1mrha_3.4K	4	[2, 6]
1mrhb_3.4K	25	[18, 32]
1rhoM_3.4K	- 0.37	[- 0.42, - 0.32]
2mrha_3.4K	4	[3, 6]
2rhoM_3.4K	2.69	[2.64, 2.76]
3rhoM_3.4K	- 0.02	[- 0.03, - 0.00]

The results of the uncertainty and correlation analysis for the parameters that define the MSLD profile at 3.4 K (FC) are shared in Figure 5.56. The analysis was repeated by fixing the value of the parameter 3mrha_3.4K_FC is 8.87 Å. Figure 5.56 (a) shows well-defined posterior probability distributions for the parameters. The mean values of the parameters and confidence intervals are listed in Table 5.28. Figure 5.56 (b) shows the correlations between the pair of six parameters. The correlation plots 1, 5, 6, 12 and 14 are similar as for correlation plots for 3.4 K data [Figure 5.55 (b)].

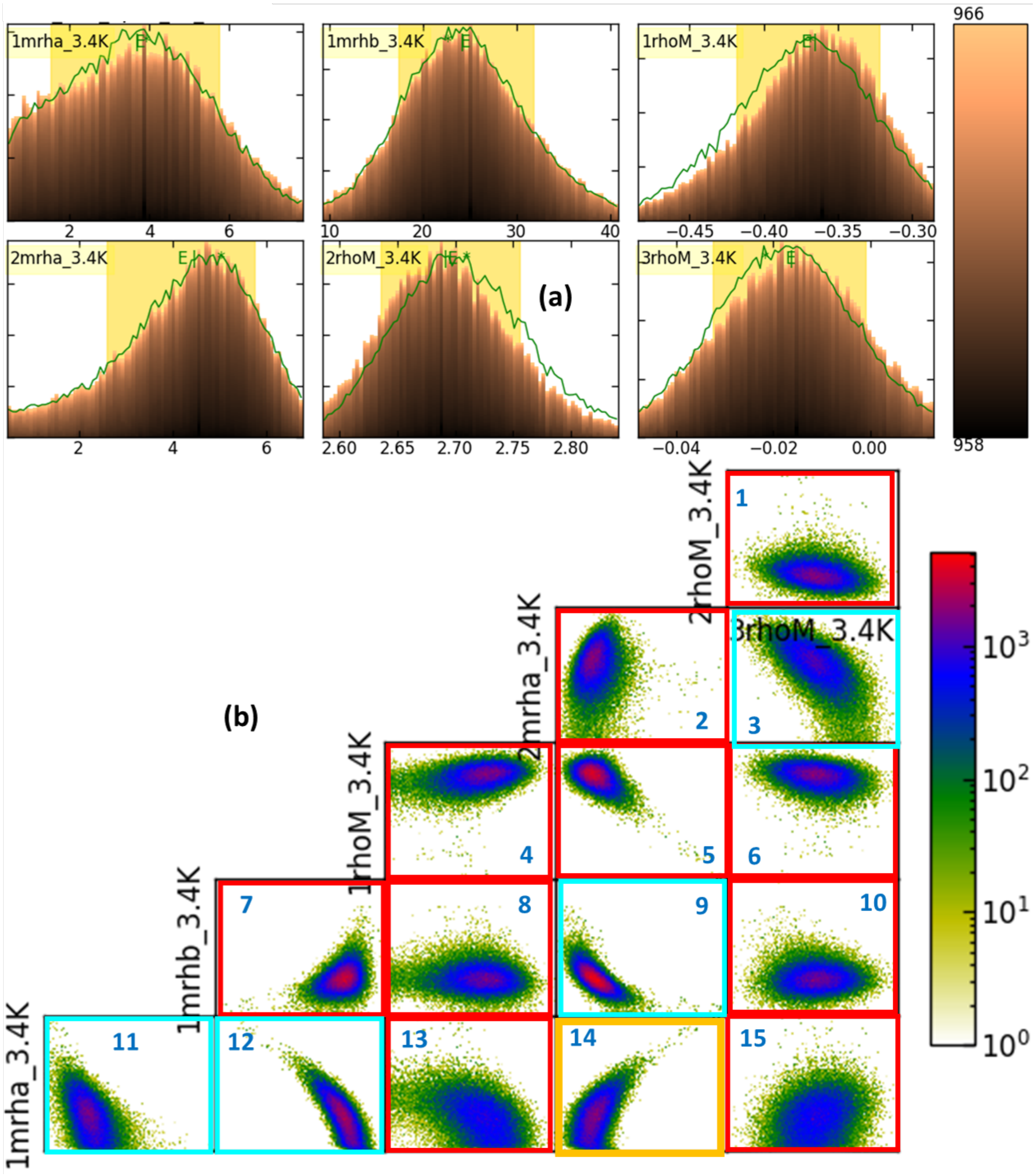

Figure 5.55: A chart of (a) posterior distribution functions of the parameters and (b) cross-correlations for the sample QD3 (3.4 K).

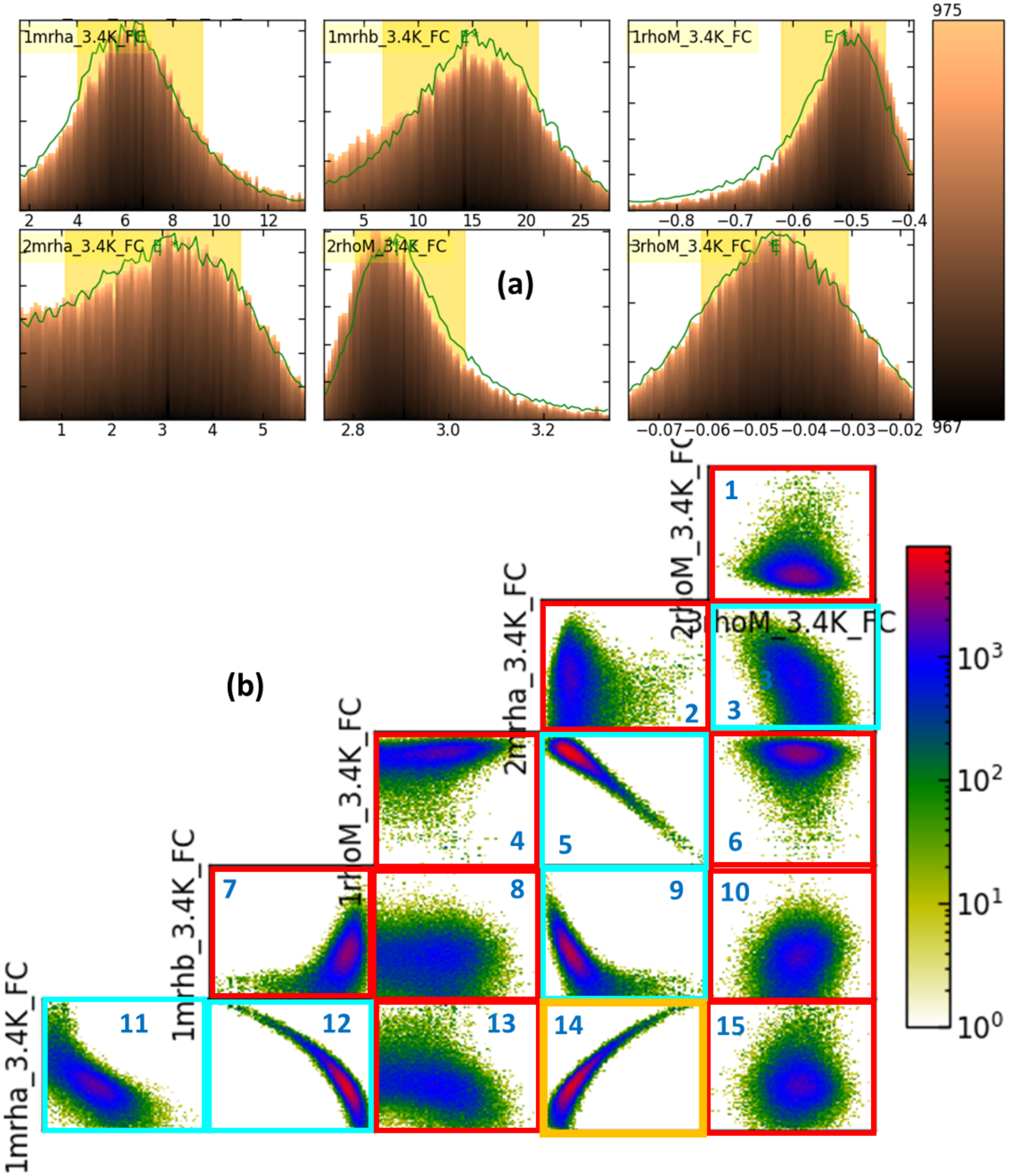

Figure 5.56: A chart of (a) posterior distribution functions of the parameters and (b) cross-correlations for the sample QD3 (3.4 K, FC).

Table 5.28: Summary of parameters with mean values and 68 % confidence intervals for the FC data at 3.4 K for the sample QD3.

Parameter	**Mean**	**68% Interval**
1mrha_3.4K_FC	7	[4, 9]
1mrhb_3.4K_FC	14	[7, 21]
1rhoM_3.4K_FC	- 0.54	[- 0.62, - 0.44]
2mrha_3.4K_FC	3	[1, 5]
2rhoM_3.4K_FC	2.9	[2.8, 3.0]
3rhoM_3.4K_FC	- 0.05	[- 0.06, - 0.03]

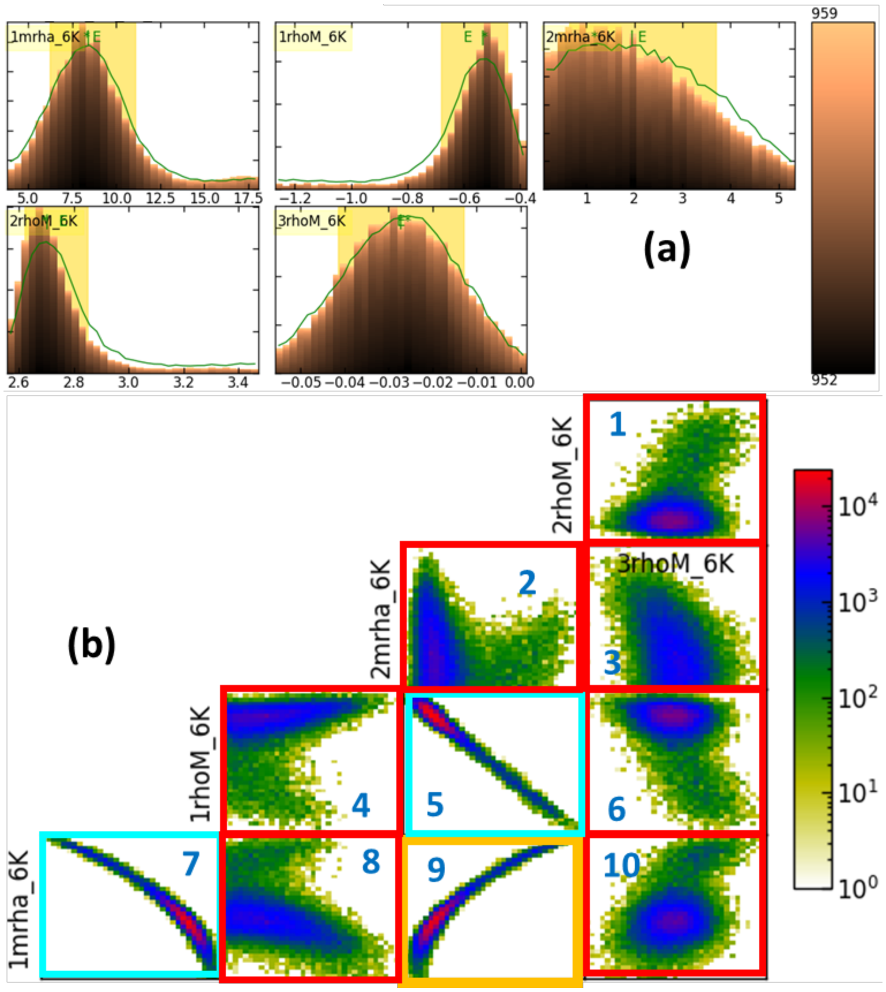

Figure 5.57: A chart of (a) posterior distribution functions of the parameters and (b) cross-correlations for the sample QD3 (6 K).

The results of the uncertainty and correlation analysis for the parameters that define the MSLD profile at 6 K are shared in Figure 5.57. The analysis was repeated by fixing the value of the parameters 1mrhb_6K and 3mrha_6K to 8 Å and 8.87 Å, respectively. Figure 5.57 (a) shows well-defined posterior probability distributions for the parameters. The mean values of the parameters and confidence intervals are listed in Table 5.29. Figure 5.57 (b) shows the correlations between the pair of six parameters. The correlation plots 1, 5, 6, 12 and 14 are similar as for correlation plots for 3.4 K and 3.4 K FC data [Plot (b) of Figure 5.55 and Figure 5.56]. However, the correlations 5, 12 and 14 for parameters at 6 K are stronger than the similar correlations for 3.4 K and 3.4 K FC data.

Table 5.29: Summary of parameters with mean values and 68 % confidence intervals for the data at 6 K for the sample QD3.

Parameter	**Mean**	**68% Interval**
1mrha_6K	9	[6, 11]
1rhoM_6K	- 0.6	[- 0.7, - 0.4]
2mrha_6K	2	[1, 4]
2rhoM_6K	2.8	[2.6, 2.9]
3rhoM_6K	- 0.03	[- 0.04, - 0.01]

The results of the uncertainty and correlation analysis for the parameters that define the MSLD profile at 8 K are shared in Figure 5.58. The analysis was repeated by fixing the value of the parameters 1mrhb_8K and 3mrha_8K to 9.56 Å and 8.87 Å, respectively. Figure 5.58 (a) shows well-defined posterior probability distributions for the parameters. The mean val‘ues of the parameters and confidence intervals are listed in Table 5.30. Figure 5.58 (b) shows the correlations between the pair of five parameters. The correlation plots (1, 5 and 6) for the MSLDs of the interface layer “1”, EuS and interface layer “3” show similar correlations as for other datasets. However, correlations 7 and 9 are less strong than 6 K [Figure 5.57 (b)], but similar to the correlations at 3.4 K [Figure 5.55 (b)] and 3.4 K FC [Figure 5.56 (b)].

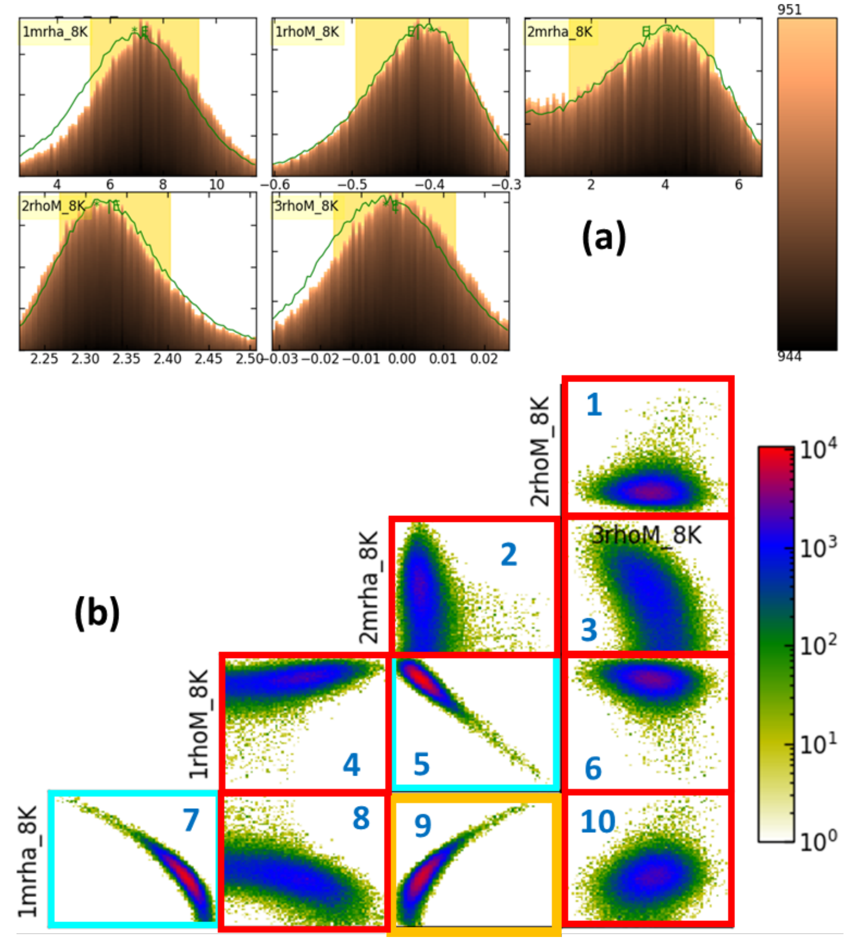

Figure 5.58: A chart of (a) posterior distribution functions of the parameters and (b) cross-correlations for the sample QD3 (8 K).

Table 5.30: Summary of parameters with mean values and 68 % confidence intervals for the data at 8 K for the sample QD3.

Parameter	**Mean**	**68% Interval**
1mrha_8K	7	[5, 9]
1rhoM_8K	- 0.42	[- 0.49, - 0.35]
2mrha_8K	4	[2, 5]
2rhoM_8K	2.34	[2.27, 2.40]
3rhoM_8K	- 0.00	[- 0.02, 0.01]

The following results are for the second piece of the QD3 sample. Figure 5.59

Table 5.31: MSLDs for the sample QD3 (first piece).

Sample QD3 (first piece)		
Layer	**MSLD (3.4 K)**	**MSLD (3.4 K FC)**
	($\times$10^{-6} Å^{-2})	**($\times$10^{-6} Å^{-2})**
Interface “3”	- 0.02 [- 0.00, - 0.04]	- 0.05 [- 0.03, - 0.07]
EuS (“2”)	2.71 [2.65, 2.77]	2.9 [2.8, 3.0]
Interface “1”	- 0.29 [- 0.24, - 0.34]	- 0.40 [- 0.31, - 0.49]

Table 5.32: MSLDs for the sample QD3 (first piece).

Sample QD3 (first piece)		
Layer	**MSLD (6 K)**	**MSLD (8 K)**
	($\times$10^{-6} Å^{-2})	**($\times$10^{-6} Å^{-2})**
Interface “3”	- 0.03 [- 0.01, - 0.05]	- 0.01 [0.01, - 0.03]
EuS (“2”)	2.7 [2.5, 2.8]	2.27 [2.20, 2.34]
Interface “1”	- 0.4 [- 0.3, - 0.6]	- 0.35 [- 0.28, - 0.42]

presents the fitted results of the PNR measurements performed on the D17 instrument. A higher magnetic field was selected for measurements to achieve a higher MSLD contrast across the layers. The simulated reflectivity of the selected model aligns well with the experimental data.

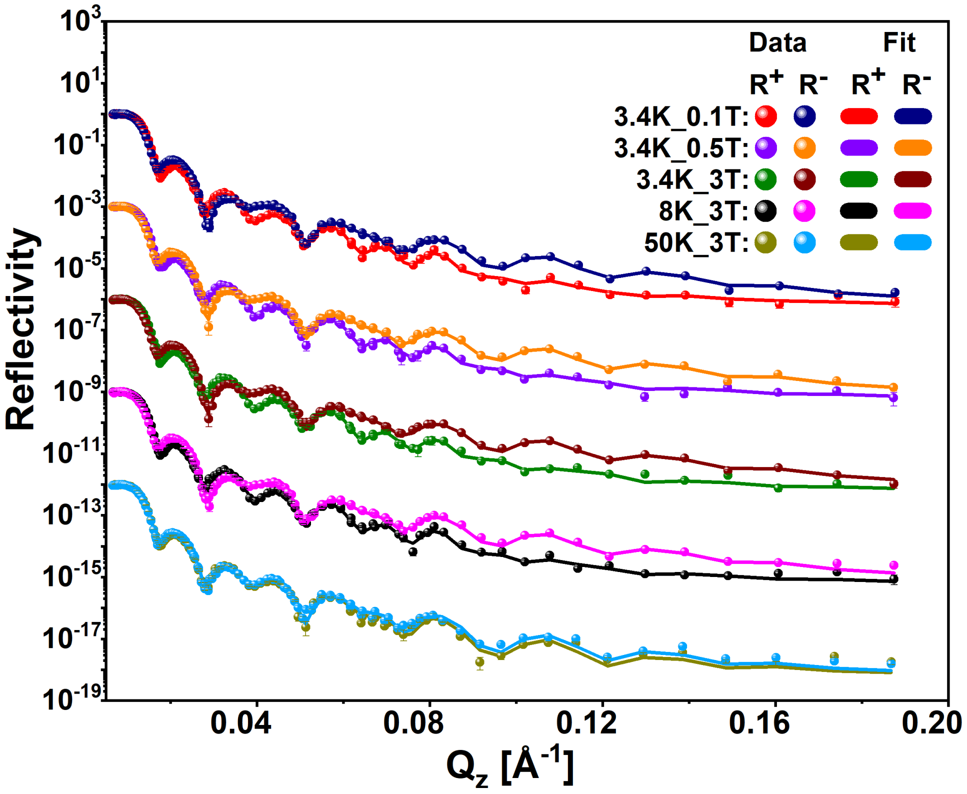

Figure 5.59: Fitted polarized neutron (PNR) data for the sample QD3 recorded for measurements as indicated in the plot. The datasets are shifted by 10^3 units along the y-axis to enhance clarity. The data were recorded at D17 instrument.

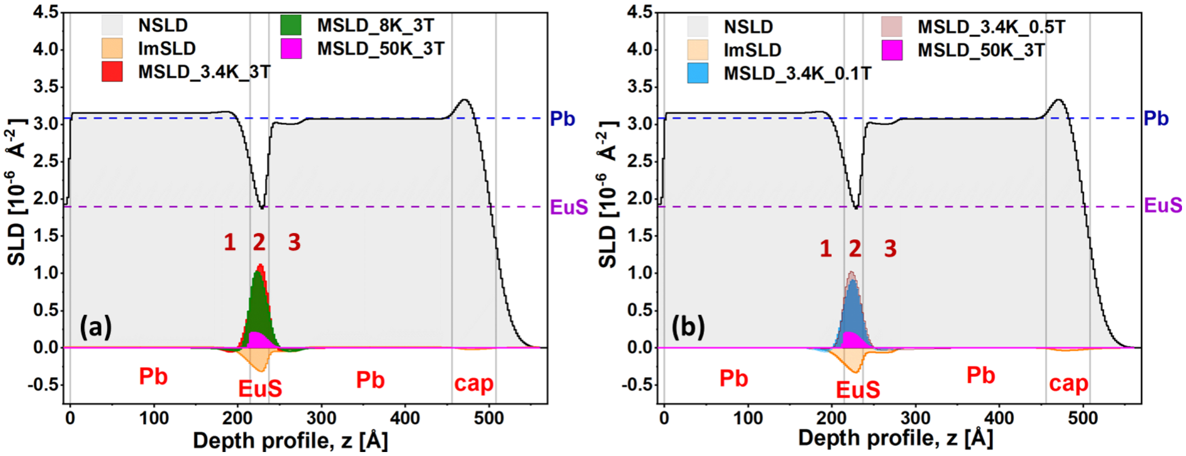

Figure 5.60: NSLD and ImSLD profiles for the sample QD3 are shown in both the plots. MSLD profiles for the the measurements as indicated in the plots.

NSLD and MSLD versus depth profiles are shown in Figure 5.60. The interface layers “1” and “3” both show a lower NSLD than the adjacent Pb layers. Moreover, a negative MSLD is observed in both interface layers, but the magnitude is very small compared to the samples QD1, QD2, and the first piece of QD3. Furthermore, at 3.4 K, the variation in MSLD within the EuS layer across different fields is small. In addition, a positive MSLD is observed in the EuS layer at 50 K (in 3 T). Table 5.33 list the parameters and their estimated values from the PNR fits. The NSLD for the lower Pb layer is around 2 % higher than the reference NSLD for Pb (Table 5.8). The NSLD of the EuS layer is approximately 1 % lower than the reference value of NSLD for EuS.

Table 5.33: A list of the parameters and their estimated values from the fit to the D17 instrument data for the sample QD3.

Sample QD3 (second piece)		
Layer	**Thickness**	**NSLD**
	(Å)	**($\times 10^{-6}$ Å^{-2})**
Cap	38.5 [38.1, 38.9]	3.64 [3.63, 3.66]
Pb top	187.2 [186.3, 188.0]	3.08 [3.07, 3.08]
Interface (3)	41.6 [41.0, 42.3]	3.03 [3.02, 3.03]
EuS (2)	21.9 [21.8, 22.0]	1.87 [1.86, 1.89]
interface (1)	13.4 [13.2, 13.6]	3.17 [3.15, 3.19]
Pb bottom	201.1 [200.8, 201.3]	3.15 [3.15, 3.16]

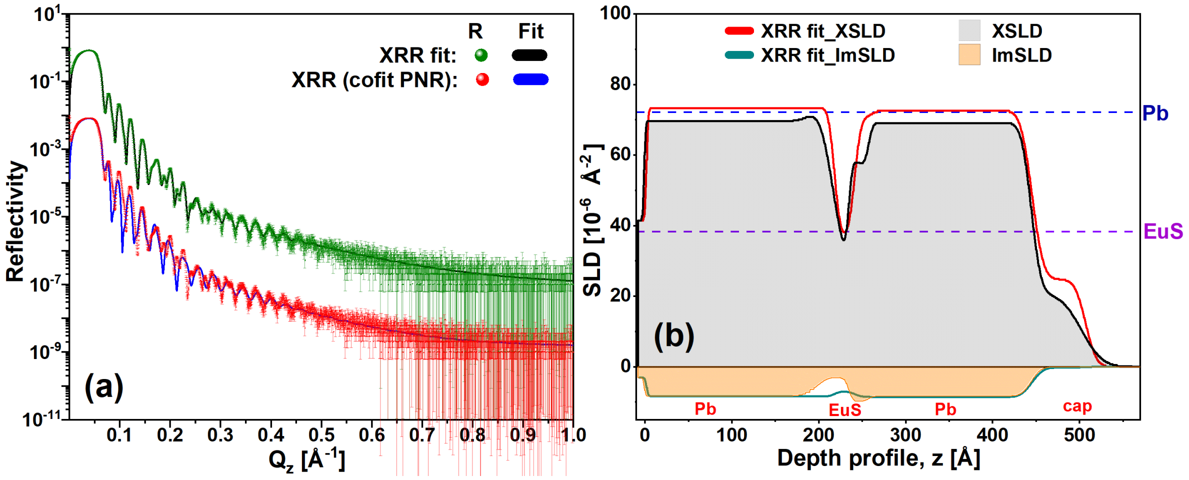

Figure 5.61: (a) Fitted XRR data and cofitted XRR data with structural parameters from PNR fits for the QD3 sample (b) A comparison of the XSLD profiles.

Figure 5.61 (a) shows the comparison between the XRR data fitted with and without taking structural parameters from the PNR fits. Figure 5.60 (b) shows the XSLD profiles for both XRR fits. The trend in the XSLD profile of the layers for the XRR fit that is fitted with the PNR parameters is observed to be similar to that in the NSLD profile [shown in Figure 5.60]. The estimated values of the thicknesses and XSLDs for both fits are compared in Tables 5.34 and 5.35. Similarly to the QD1 and QD2 samples, a difference in the thicknesses of the layers is observed for the PNR and XRR fits for the second piece of the QD3 sample. The difference in the thickness of the entire layer stack is less than 1 %.

Table 5.34: A comparison of the estimated values of thickness from the two XRR fits for the sample QD3.

Sample QD3 (second piece)		
	Thickness (Å)	
Layer	**XRR (cofit PNR)**	**XRR fit**
Cap	38.5 [38.1, 38.9]	61.38 [61.36, 61.42]
Pb top	187.2 [186.3, 188.0]	182.50 [182.44, 182.55]
Interface “3”	41.6 [41.0, 42.3]	21.98 [21.91, 22.05]
EuS (“2”)	21.9 [21.8, 22.0]	23.1 [22.9, 23.2]
Interface “1”	13.4 [13.2, 13.6]	17.5 [16.5, 18.4]
Pb bottom	201.1 [200.8, 201.3]	199.2 [198.6, 199.9]

Table 5.35: A comparison of the estimated values of XSLD from the two XRR fits for the sample QD3.

Sample QD3 (second piece)		
	XSLD ($\times 10^{-6}$ Å^{-2})	
Layer	**XRR (cofit PNR)**	**XRR fit**
Cap	20.8 [20.2, 21.7]	25.1 [24.9, 25.2]
Pb top	69.1 [69.0, 69.6]	72.35 [72.33, 72.36]
Interface “3”	57 [55, 60]	71.6 [71.5, 71.7]
EuS (“2”)	36 [33, 38]	36.6 [36.4, 36.8]
Interface “1”	71 [67, 73]	73.3 [73.2, 73.4]
Pb bottom	70 [68, 71]	73.3 [73.1, 73.4]

Figure 5.62 illustrates the SA plotted against Q_z for the measurements with their respective fits. All the datasets demonstrate a non-zero SA.

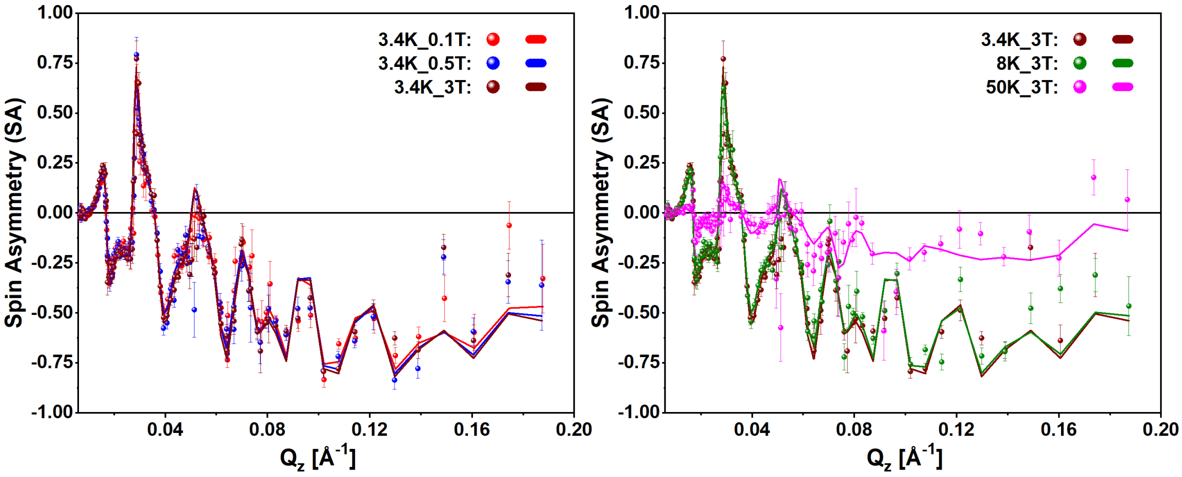

Figure 5.62: SA as a function of Q_z for second piece of the sample QD3 is shown along with the respective fits for measurements as indicated in the plots. The SA data for 3.4 K (in 3 T) and its fit is shown in both plots for comparison.

Due to the low MSLD contrast and values in the interface layers for other temperature and fields, uncertainty and correlation analyses were only tried for data at 3.4 K (in 3 T) to examine analysis and fit sensitivity to interface MSLDs. A similar approach to the QD1 and QD2 samples was followed for the uncertainty and correlation analysis for this sample. The results of the uncertainty analysis for the parameters that define the MSLD profile at 3.4 K (in 3 T) are shown in Figure 5.63. In contrasts to other samples, the posterior distributions in plot (a) are not well defined, and the green lines do not follow the shape of the distributions. Figure 5.63 (b) shows the posterior distributions for parameters after fixing the value of parameter 3mrha_3K_3T to 3.87 Å. Nevertheless, the distributions exhibit skewness, and the green line considerably deviates from their shape. The plots for the correlation analysis are shared in Appendices [8].

Table 5.36 lists the mean values and confidence intervals obtained from the uncertainty analysis performed for the parameters. At 3 K (3 T), the MSLD contrast for this sample is low, resulting in greater errors in the mean parameter values compared to earlier samples, making MSLD estimation at interfaces challenging.

Table 5.37 lists the MSLDs in the EuS layer under different temperature and magnetic field conditions.

Tables 5.38 and 5.39 compare the thicknesses and NSLDs of the two pieces of the

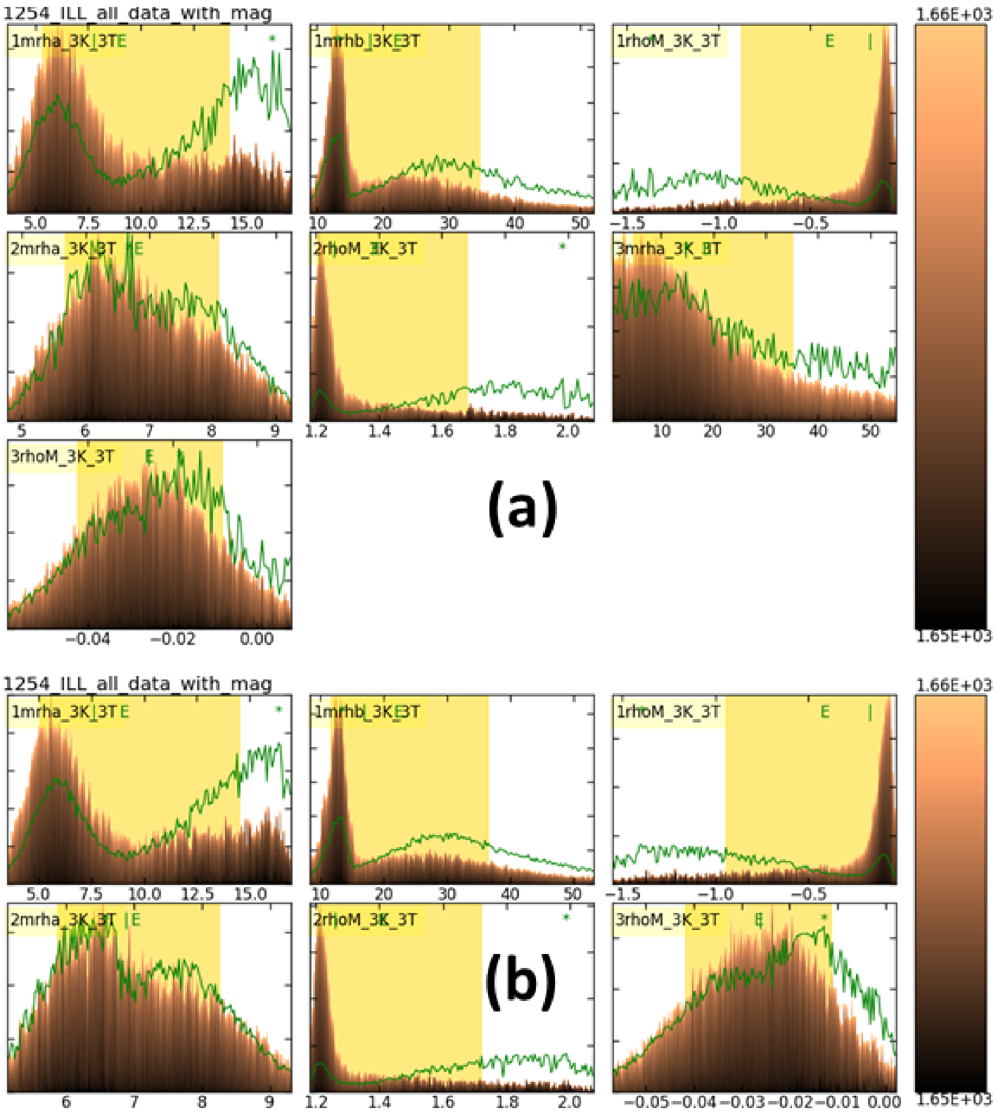

Figure 5.63: A chart of the posterior distribution functions of the parameters for second piece of the sample QD3. (a) Distributions for all parameters. (b) Distributions for parameters after fixing the value of parameter 3mrha_3K_3T to 3.87 Å.

Table 5.36: Summary of parameters with mean values and 68% confidence intervals at 3 K in a 3 T field fecond piece of the sample QD3.

Parameter	**Mean**	**68% Interval**
1mrha_3K_3T	9	[5, 14]
1mrhb_3K_3T	22	[12, 36]
1rhoM_3K_3T	- 0.4	[- 1.0, - 0.1]
2mrha_3K_3T	7	[6, 8]
2rhoM_3K_3T	1.4	[1.2, 1.7]
3rhoM_3K_3T	- 0.03	[- 0.04, - 0.01]

Table 5.37: MSLDs for the sample QD3 (second piece). Temp stands for temperature and field is the external in-plane magnetic field.

Sample QD3 (second piece)	
MSLD of EuS layer	
Temp in field	**MSLD ($\times 10^{-6}$ Å^{-2})**
3.4 K in 0.1 T	0.9 [0.8, 1.0]
3.4 K in 0.5 T	1.03 [0.99, 1.07]
3.4 K in 3 T	1.1 [0.9, 1.3]
8 K in 3 T	1.03 [0.98, 1.08]
50 K in 3 T	0.21 [0.19, 0.23]

QD3 sample. The difference in the thickness of the entire stack of layers for both pieces is around 49 Å.

Table 5.38: A comparison of the estimated thickness values for two pieces of the sample QD3. The information for the first piece can be found in Tables 5.24.

Sample QD3		
	Thickness (Å)	
Layer	**First**	**Second**
Cap	61 [59, 62]	38.5 [38.1, 38.9]
Pb top	167 [159, 176]	187.2 [186.3, 188.0]
Interface “3”	67 [58, 74]	41.6 [41.0, 42.3]
EuS (“2”)	26.4 [26.2, 26.5]	21.89 [21.80, 21.98]
Interface “1”	32 [30, 33]	13.4 [13.2, 13.6]
Pb bottom	201 [200, 203]	201.1 [200.8, 201.3]

Table 5.39: A comparison of the estimated NSLD values for two pieces of the sample QD3. The information for the first piece can be found in Tables 5.24.

Sample QD3		
	NSLD ($\times 10^{-6}$ Å^{-2})	
Layer	**First**	**Second**
Cap	3.31 [3.30, 3.32]	3.64 [3.63, 3.66]
Pb top	3.06 [3.06, 3.07]	3.08 [3.07, 3.08]
Interface “3”	3.10 [3.09, 3.11]	3.00 [3.00, 3.01]
EuS (“2”)	1.83 [1.81, 1.86]	1.55 [1.54, 1.56]
Interface “1”	3.35 [3.32, 3.39]	3.70 [3.68, 3.72]
Pb bottom	3.13 [3.12, 3.14]	3.15 [3.15, 3.16]

In summary, a negative MSLD is observed in the interface layers “1” and “3” for the first piece of the sample QD3, except for 50 K (0.1 T). The NSLD and XLSD at both interfaces of EuS with Pb layers are modified and different from the adjacent Pb layers. Despite having similar EuS thicknesses, the second piece of the QD3 sample (Table 5.37) shows reduced MSLD contrast relative to the first piece (Table 5.31), with an MSLD of 0.91×10^{-6} Å^{-2} as opposed to 2.71×10^{-6} Å^{-2} at 2 K (0.1 T). The MSLD in the interface layers for the second piece is negligible compared to the first piece.

Sample QD4

Similarly to the QD3 sample, there were two 400 mm^2 pieces of the QD4 sample that were cut from the same wafer. PNR measurements for piece 1 were performed on the POLREF instrument at ISIS [134], while the measurements for piece 2 were performed on the D17 instrument at ILL [80]. The ISIS measurements on the first piece occurred approximately one year prior to those at ILL for the second piece. Table 5.40 lists the recorded PNR measurements for the QD4 sample pieces.

Table 5.40: PNR measurements for two different pieces of the sample QD4.

PNR measurements: the QD4 sample			
Piece 1		**Piece 2**	
ISIS POLREF		**ILL D17**	
Temp. (K)	**$H_{ext,//}$ (T)**	**Temp. (K)**	**$H_{ext,//}$ (T)**
3.4	0.1	2	0.1
3.4 (FC)	0.1	2	0.8
6	0.1	8	0.1
8	0.1	100	0.1
30	0.1	-	-

The fitted results from PNR and XRR for the first piece of sample QD4 are shown in Figure 5.64. PNR data were recorded at POLREF instrument. Plot (b) presents the NSLD versus depth profile. The NSLDs of the top Pb layer lie close to the reference value for Pb (Table 5.8). However, the lower Pb layer shows an NSLD higher than that of the reference value. MSLD profiles suggest that the magnetism is mainly confined to the EuS layer. Negative MSLD in interfaces has not been detected for this sample. Plot (c) depicts the fitted XRR data, and plot (d) shows the XSLD depth profile. The XSLDs of both Pb layers are close to the reference value. The estimated values of the thicknesses and SLDs of the layers are listed in Table 5.41.

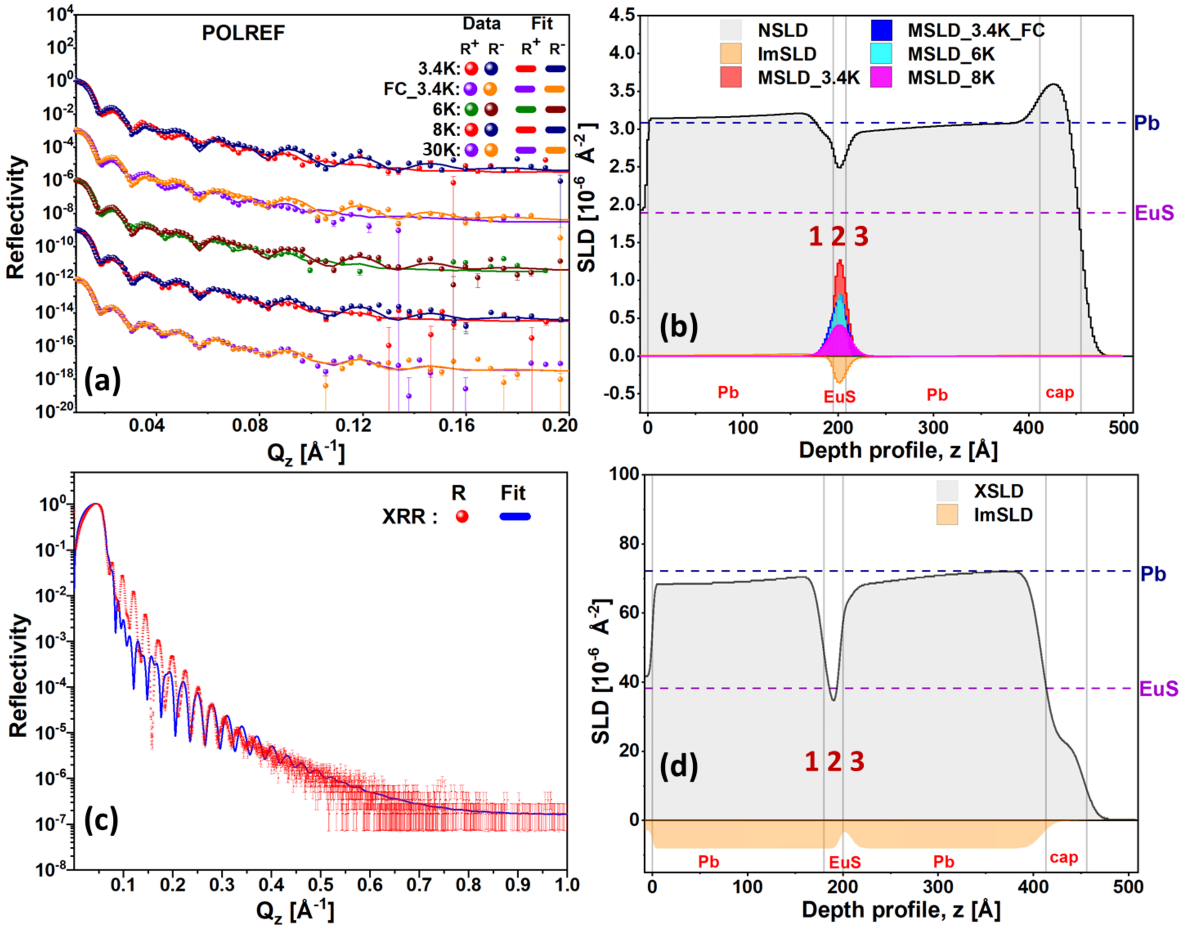

Figure 5.64: Fitted reflectometry data for the sample QD4. (a) Fitted PNR data. The datasets are shifted by 10^3 units along the y-axis to enhance clarity. The data were recorded at POLREF instrument. (b) NSLD and MSLD versus depth profiles (c) Fitted XRR data (d) XSLD versus depth profile.

Figure 5.65 shows the SA plotted against Q_z with the respective fits for the first piece of the QD4 sample. The SA points at 30 K randomly scatter around the zero line and are roughly equal to zero. In contrast to 30 K data, the other datasets demonstrate a non-zero SA.

Table 5.41: A list of the parameters and their estimated values from the fit to the POLREF instrument data for the sample QD4.

Sample QD4 (First piece)			
Layer	**Thickness**	**NSLD**	**XSLD**
	(Å)	**($\times 10^{-6}$ Å^{-2})**	**($\times 10^{-6}$ Å^{-2})**
Cap	31.8 [31.4, 32.3]	3.6 [3.5, 4.0]	23 [22, 25]
Pb top	174.6 [174.0, 175.3]	3.10 [3.10, 3.11]	72 [72, 76]
Interface (3)	33.2 [32.5, 33.8]	3.16 [3.15, 3.17]	64 [61, 69]
EuS (2)	13.7 [13.5, 13.9]	2.5 [2.4, 2.6]	35 [31, 40]
interface (1)	21.2 [20.8, 21.6]	2.8 [2.6, 2.9]	70 [66, 72]
Pb bottom	178.6 [178.1, 179.0]	3.11 [3.11, 3.12]	68 [66, 71]

Table 5.42: MSLDs for the sample QD4 (first piece). Temp stands for temperature and field is the external in-plane magnetic field.

Sample QD4 (first piece)	
MSLD of EuS layer	
Temp in field	**MSLD ($\times 10^{-6}$ Å^{-2})**
3.4 K in 0.1 T	1.3 [1.2, 1.4]
3.4 K in 0.1 T (FC)	0.74 [0.67, 0.82]
6 K in 0.1 T	0.81 [0.72, 0.88]
8 K in 0.1 T	0.4 [0.3, 0.5]
30 K in 0.1 T	0

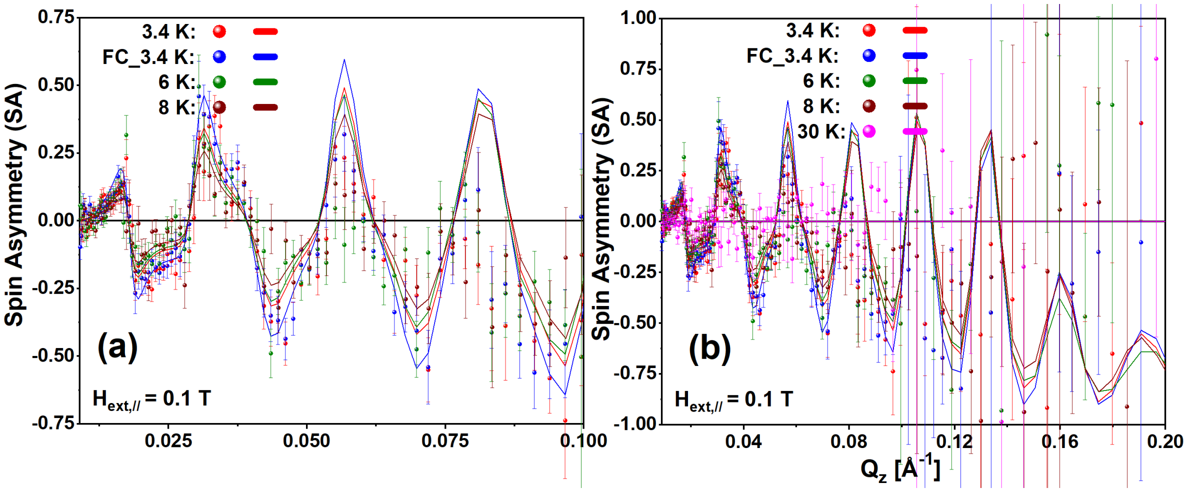

Figure 5.65: SA as a function of Q_z for the sample QD4 (first piece) is shown. (a) A enlarged view of the SA data (b) Full range SA data.

The fitted results from PNR and XRR for the second piece of the sample QD4 are shown in Figure 5.66. Plot (b) presents the NSLD versus depth profile. The NSLDs of the top and bottom Pb layers align closely with the reference value for the Pb. However, the upper interface layer (“3”) shows an NSLD higher than that of the adjacent Pb layer. MSLD profile in the middle shows a small difference between the curves for 2 K in 0.1 T and 0.8 T. Moreover, MSLD profiles imply that magnetism is restricted to the EuS layer. No negative MSLD has been observed at the interfaces of this sample. Plot (c) depicts the fitted XRR data, and plot (d) shows the XSLD depth profile. The XSLD of both Pb layers are close to the reference value. The estimated values of thickness and SLD are listed in Table 5.43. The NSLD and XSLD of the EuS layer exceed the values in the reference (Table 5.8).

Table 5.44 lists the values of MSLD for the EuS layer. It is observed that the difference between the MSLD at 2 K in 0.1 T and 0.8 T is around 0.05×10^{-6} Å^{-2}.

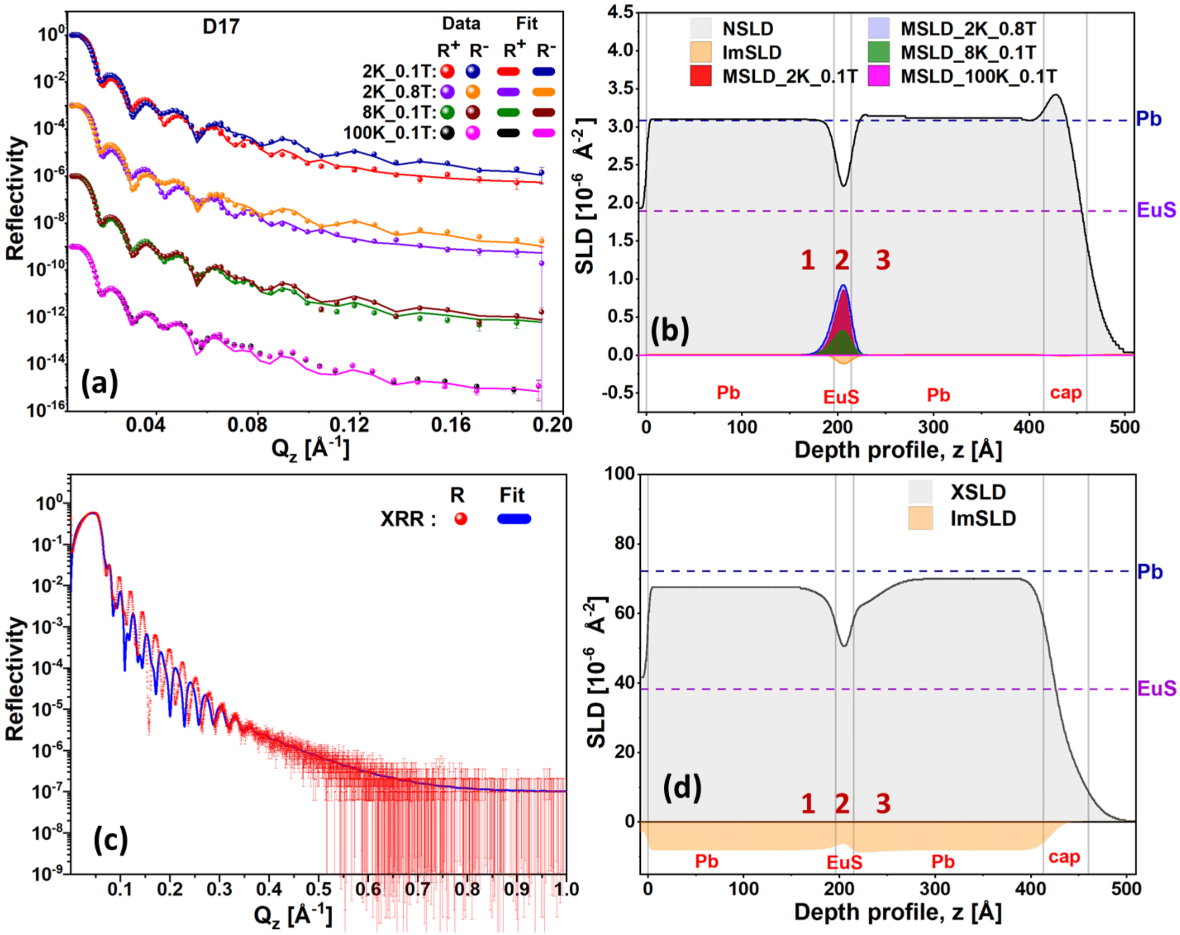

Figure 5.66: Fitted reflectometry data for the sample QD4. (a) Fitted PNR data. The datasets are shifted by 10^3 units along the y-axis to enhance clarity. The data were recorded at D17 instrument. (b) NSLD and MSLD versus depth profiles (c) Fitted XRR data (d) XSLD versus depth profile.

Figure 5.67 shows the SA plotted against Q_z with the respective fits. The points for SA at 100 K scatter randomly around the zero line, displaying notable error bars, particularly within the Q_z range of 0.15 to 0.20 Å^{-1}. At 100 K, the SA value is roughly equal to zero. A small difference between the curves for 2 K in 0.1 T and 0.8 T is observed. This difference is observable in the Q_z interval from 0.01 to 0.04 Å^{-1} as shown in Figure 5.67.

Table 5.43: A list of the structural parameters and their estimated values from the fit to the D17 instrument data for the sample QD4.

Sample QD4 (second piece)			
Layer	**Thickness**	**NSLD**	**XSLD**
	(Å)	**($\times$10^{-6} Å^{-2})**	**($\times$10^{-6} Å^{-2})**
Cap	27 [25, 29]	3.4 [3.3, 3.6]	32 [29, 34]
Pb top	181 [178, 189]	3.11 [3.10, 3.12]	69.9 [69.7, 70.4]
Interface (3)	28 [20, 30]	3.16 [3.12, 3.17]	46 [41, 51]
EuS (2)	14.2 [13.6, 14.7]	2.10 [2.06, 2.15]	51 [41, 52]
interface (1)	8 [1, 12]	3.08 [3.04, 3.22]	66 [61, 67]
Pb bottom	190 [187, 197]	3.11 [3.10, 3.12]	68 [65, 70]

Table 5.44: MSLDs for the sample QD4 (second piece). Temp stands for temperature and field is the external in-plane magnetic field.

Sample QD4 (second piece)	
MSLD of EuS layer	
Temp in field	**MSLD ($\times$10^{-6} Å^{-2})**
2 K in 0.1 T	0.82 [0.81, 0.85]
2 K in 0.8 T	0.87 [0.79, 0.91]
8 K in 0.1 T	0.29 [0.27, 0.33]
100 K in 0.1 T	0

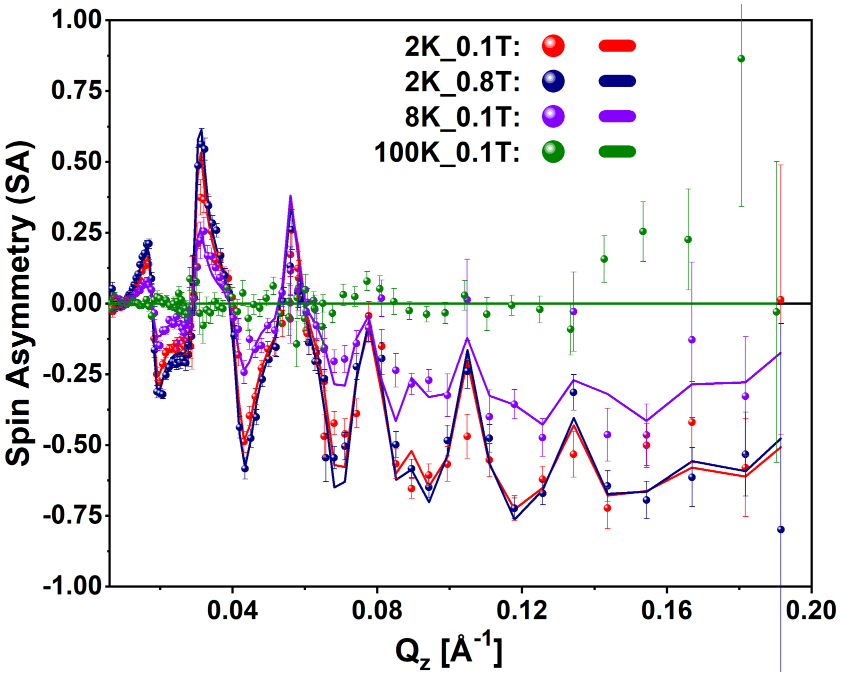

Figure 5.67: SA as a function of Q_z for the sample QD4 (second piece) is shown along with the respective fits.

Tables 5.45 and 5.46 compare the thicknesses and NSLDs of the two pieces of the QD4 sample. The difference in the thickness of the entire stack of layers for both pieces is around 5 Å.

Table 5.45: A comparison of the estimated thickness values for two pieces of the sample QD4. The information for the first piece can be found in Tables 5.41.

Sample QD4		
	Thickness (Å)	
Layer	**First**	**Second**
Cap	31.8 [31.4, 32.3]	27 [26, 29]
Pb top	174.6 [174.0, 175.3]	181 [179, 190]
Interface “3”	33.2 [32.5, 33.8]	28 [20, 30]
EuS (“2”)	13.7 [13.5, 13.9]	14.2 [13.6, 14.7]
Interface “1”	21.2 [20.8, 21.6]	8 [1, 12]
Pb bottom	178.6 [178.1, 179.0]	190 [187, 197]

Table 5.46: A comparison of the estimated NSLD values for two pieces of the sample QD4. The information for the first piece can be found in Tables 5.41.

Sample QD4		
	NSLD ($\times 10^{-6}$ Å^{-2})	
Layer	**First**	**Second**
Cap	3.6 [3.5, 4.0]	3.4 [3.3, 3.6]
Pb top	3.10 [3.10, 3.10]	3.11 [3.10, 3.12]
Interface “3”	3.16 [3.15, 3.17]	3.16 [3.12, 3.17]
EuS (“2”)	2.5 [2.4, 2.6]	2.10 [2.06, 2.15]
Interface “1”	2.8 [2.6, 2.9]	3.08 [3.04, 3.22]
Pb bottom	3.11 [3.11, 3.12]	3.11 [3.10, 3.12]

In summary, the NSLD and XSLD at the EuS and Pb interfaces are altered compared to the neighboring Pb layers. The model fits indicate the absence of MSLD in the interface regions in both pieces of the QD4 sample. The second piece of QD4, as listed in Table 5.44, exhibits lower MSLD values in the EuS layer compared to the first piece, with a value of 0.82×10^{-6} Å^{-2} at 2 K (in 0.1 T) versus 1.27×10^{-6} Å^{-2} at 3.4 K (in 0.1 T) for the first piece.

Reference samples

Reference samples of Pb (QD5) and EuS (QEu2) were studied by PNR and XRR techniques to have a reference for the SLD profiles. The samples were grown on an InAs (111 B) substrate and a capping layer was deposited to protect the sample surface. PNR measurements were recorded at the temperatures - 2 K, 8 K, and 50 K. The simple model, with detailed description about the process in the chapter on data analysis 4, was used to fit the reflectometry data for both samples, the original layers are marked in the SLD profile for each sample.

Figure 5.68 (a) shows the fitted reflectometry data for the reference sample of Pb (QD5). No splitting in the PNR curves was observed across all temperatures. Plot (b) presents the NSLD profile with depth, with the NSLD of the Pb layer aligning closely with reference values for the Pb. Plot (c) depicts the fitted XRR data, and plot (d) shows the XSLD depth profile. The XSLD for the Pb layer closely matches the reference value for Pb. The estimated values of thickness and SLD are listed in Table 5.47.

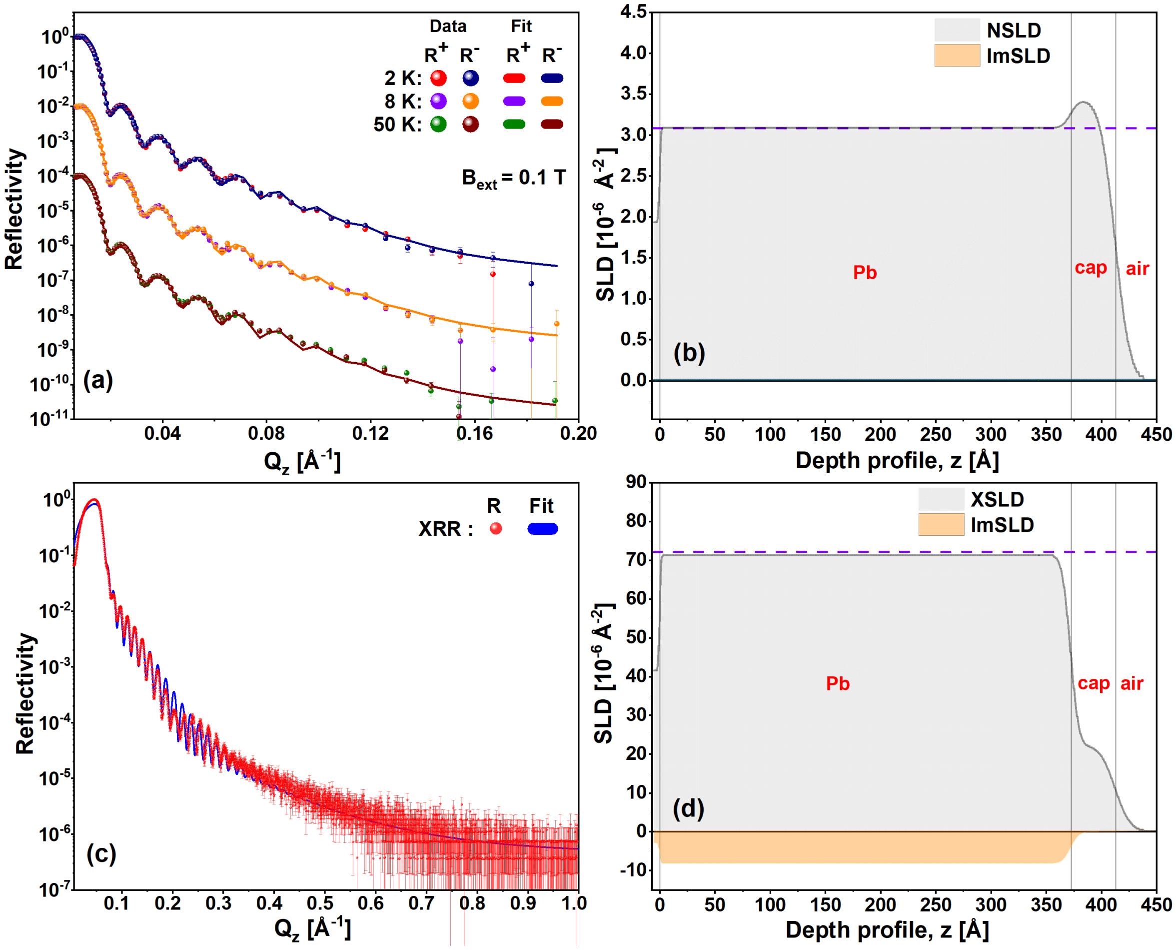

Figure 5.68: Fitted reflectometry data for Pb reference sample QD5. (a) Fitted PNR data. Data have been offset by 10^2 for clarity reasons. PNR data were recorded at D17 instrument. (b) NSLD profile versus depth (c) Fitted XRR data (d) XSLD profile versus depth.

Figure 5.69 shows SA as a function of Q_z for the QD5 sample. The data points in the lower q region are scattered randomly around the y = 0 line. Furthermore, the error bars are higher in the Q range from 0.15 to 0.20 $Å^{-1}$. Thus, the SA is estimated to be zero.

In Figure 5.70, the fitted PNR data is shown, with the assumption that Pb remains in an ideal Meissner state at a temperature of 2 K. At 2 K under a magnetic field of 0.1 T, the MSLD for the Pb layer is calculated using the equation 3.29, which results in approximately - 0.23 x 10^{-6} $Å^{-2}$. This value of MSLD is used to fit the PNR data and examine if the PNR fits are sensitive to it. Figure 5.70 (a) shows the split in the fits corresponding to R^+ and R^-. Furthermore, Figure 5.70 (b) includes the SA signal with their corresponding fits. In particular, it is found that the fit to the SA data at 2 K is significantly mismatched and deviates substantially.

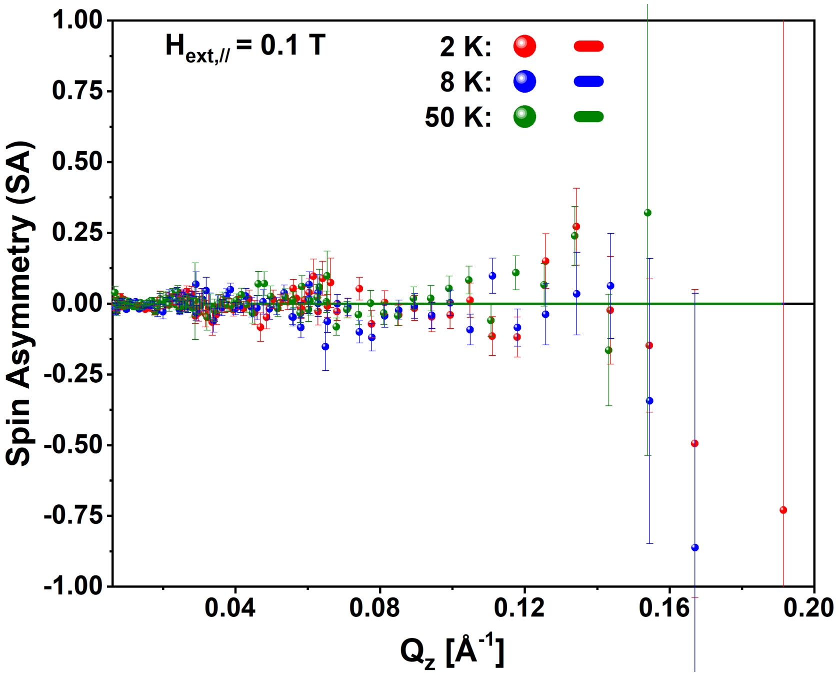

Figure 5.69: SA as a function of Q_z for Pb reference sample QD5 at 2 K, 8 K, and 50 K in presence of a magnetic field of 0.1 T.

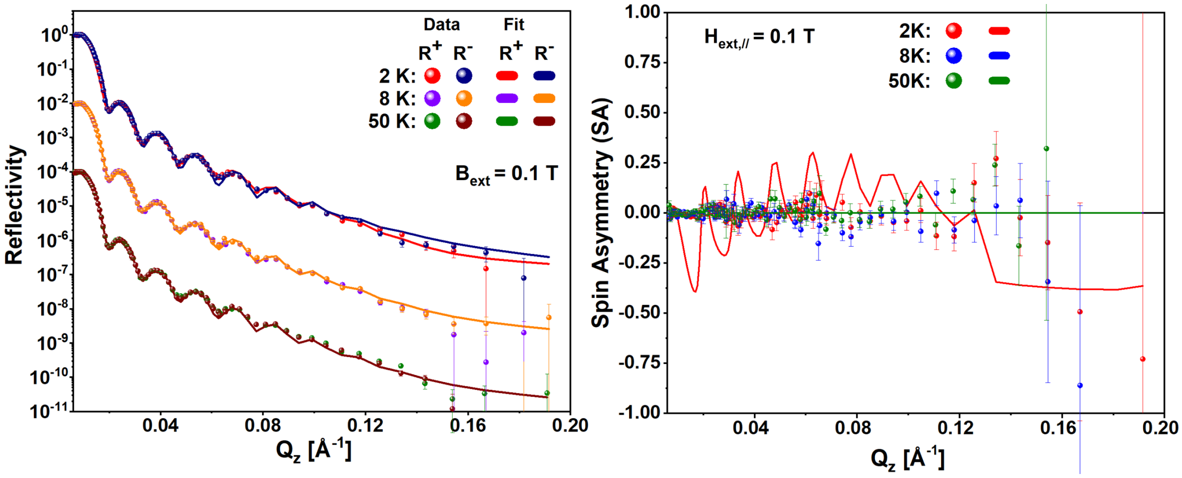

Figure 5.70: (a) Fitted PNR data for the sample QD5 assuming Pb being in a perfect Meissner state at 2 K. Datasets have been offset by 10^2 on y-axis for clarity reasons. (b) SA as a function of Q_z for the sample QD5.

The reflectometry data for the EuS reference sample (QEu2) is shown in Figure 5.71. Plot (a) shows the fitted PNR data for the measurements at 2 K (0.1 T), 8 K (0.1 T) and 50 K (3 T). Plot (b) shows the NSLD and MSLD versus depth profile of the sample. MSLD profile suggests that the magnetism is mainly confined to the EuS layer with a gradient towards the surface. The observation of the non-zero MSLD profile at 50 K (in 3 T) is discussed in more detail in the following chapter 6. Plots (c) and (d) show the fitted XRR data and XSLD versus depth profile, respectively. Analogous to its NSLD profile in plot (b), the XSLD for the EuS layer falls below the standard reference XSLD value. The estimated values of thickness and SLD are listed in Table 5.47.

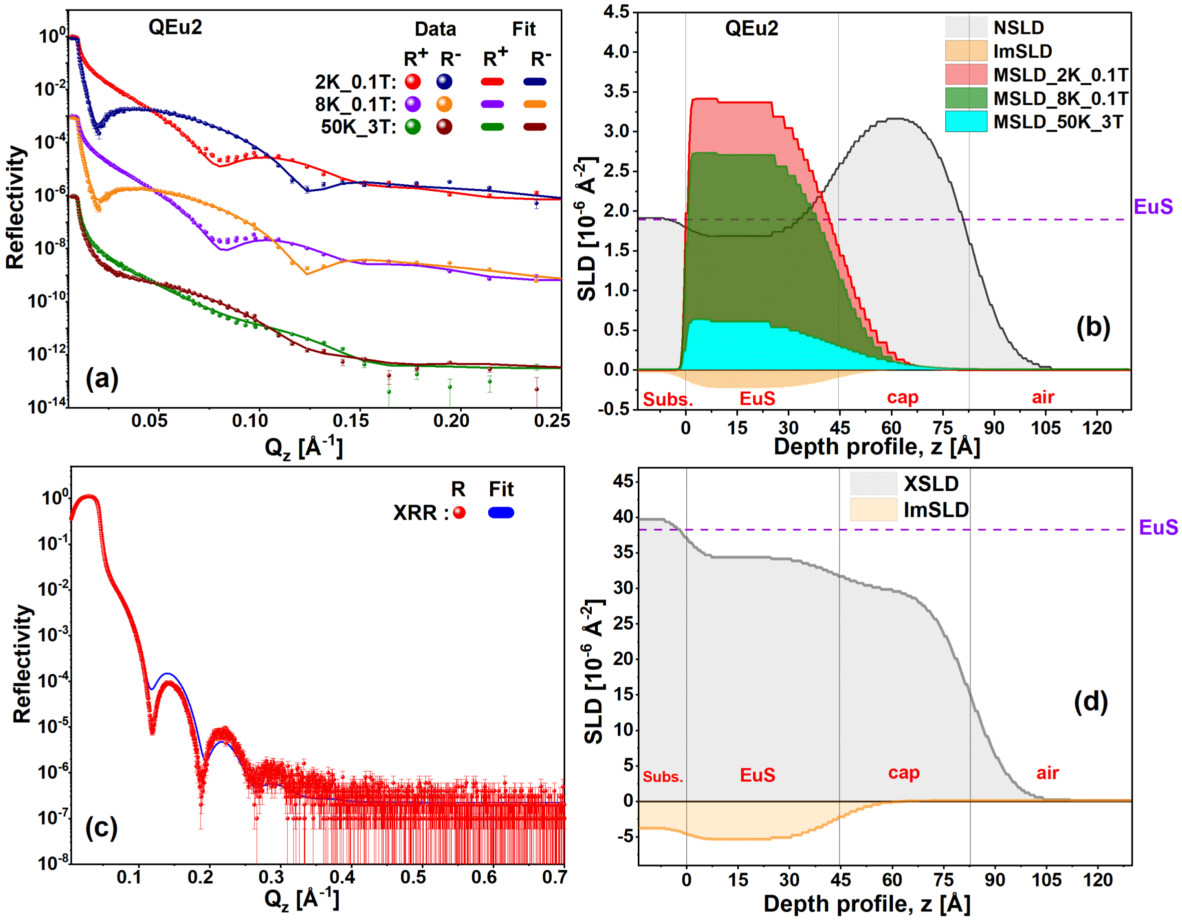

Figure 5.71: Fitted reflectometry data for the sample QEu2 (reference EuS). (a) Fitted PNR data. Data have been offset by 10^3 for clarity reasons. PNR data were recorded at D17 instrument. (b) NSLD profile with depth (c) Fitted XRR data (d) XSLD profile versus depth.

Table 5.47: List of parameters with their values and confidence intervals for the samples QD5 and QEu2.

Sample	**Thickness (Å)**	**NSLD ($\times 10^{-6}$ Å^{-2})**	**XSLD ($\times 10^{-6}$ Å^{-2})**
QD5 (Pb)	374 (372, 375)	3.08 [3.08, 3.10]	71.3 [71.1, 71.5]
QEu2 (EuS)	44.6 (44.2, 45.4)	1.68 [1.67, 1.69]	34.8 [33.6, 35.4]

Table 5.48: MSLD of EuS layer in the QEu2 sample. Temp stands for temperature and field is the external in-plane magnetic field.

QEu2 sample	
Temp in field	**MSLD ($\times 10^{-6}$ Å^{-2})**
2 K in 0.1 T	3.32 [3.23, 3.36]
8 K in 0.1 T	2.67 [2.63, 2.72]
50 K in 3 T	0.59 [0.56, 0.63]

The deposition of the reference layer of Pb on the InAs substrate leads to an NSLD that is close (less than 1%) to its reference value. Moreover, the XSLD for the Pb layer is around 2 % less than its value in the reference. However, the NSLD of the EuS reference layer in the QEu2 sample is approximately 11 % lower than the reference value of NSLD (Table 5.8). Similarly to NSLD, the XSLD of the EuS layer is approximately 9 % lower than the value in the reference.

5.5 General discussion

For samples QD1 and QD2, the NSLD of the Pb layer grown on the EuS layer is around 4 to 6 % higher than that of the Pb layer grown on InAs. However, for the QD3 and QD4 samples, the NSLDs of both Pb layers are close to each other within ± 2 %. Furthermore, the NSLDs and XSLDs of the interface layers are found to be different, upto ± 7 %, from those of the adjacent Pb layers in all samples. The detection of mixed valence states of Eu in QD2 and QD3, as validated by XANES data [Figure 5.21], might explain the elevated NSLD in the top Pb layer due to potential chamber contamination, leading to a compound such as PbS.

A discrepancy in the thickness measurements is noted between the PNR and XRR results, although the total stack thickness varies only by ± 1%. This may result from a lateral thickness gradient, as evidenced in two pieces of the same wafer for the samples

QD3 and QD4. The large footprint of the neutron beam averages over the whole sample, whereas the smaller footprint of the X-ray beam focuses on a local region. Consequently, lateral thickness variations might cause slight differences in thickness estimation between the methods. Furthermore, low SLD contrast complicates thickness estimates. In this study, the low NSLD contrast between the Pb and capping layers presents challenges in estimating thickness, but the higher XSLD contrast enhances the precision of XRR over PNR.

The QD5 sample, reference sample of Pb, did not show a magnetic signal at 2 K when subjected to a 0.1 T in-plane magnetic field, as illustrated in the spin asymmetry data [Figure 5.69]. Attempts to fit the data using an MSLD of -0.23×10^{-6} Å^{-2} [Figure 5.70], corresponding to the anticipated pure Meissner state of Pb in 0.1 T, show that Pb is not in the pure Meissner state. This observation aligns with the observed drop in the FC magnetization versus temperature curves at 0.1 T for the samples [Section 5.4.2]. Furthermore, the MSLD profile for the QEu2 sample [Figure 5.71] reveals that the magnetism is mainly confined to the EuS layer, without any negative MSLD at interfaces. This indicates that the observed negative MSLD in interface layers of other samples is not solely due to magnetism in EuS.

The fitted MSLD profiles suggest an extension of the magnetic signal into interface layers adjacent to the EuS layer for the samples QD1, QD2 and the first piece of QD3. The magnetic signal is more prominent in one interface layer than in the other and the magnetic signal gradually dies out in the Pb layers. The present study also finds that in the QEu2 sample [Figure 5.71], magnetism is mainly restricted to the EuS layer, with no leakage of magnetic signals detected at the interfaces. In the QD1 sample, the magnetic signal is more pronounced in the interface layer “1” than in “3”. The interface layer “1” exhibits a negative MSLD value of around - 0.2×10^{-6} Å^{-2} [Table 5.15], while it is approximately zero for the layer “3”. At 2 K and 8 K, the MSLDs in layer “1” are nearly equivalent (Δ MSLD $\approx 0.03\times10^{-6}$ Å^{-2}).

In contrast, for the QD2 sample [Table 5.22], both interface layers show negative MSLD values (around - 0.28×10^{-6} Å^{-2} at 2 K), except at 8 K where only the interface layer “3” exhibits a negative MSLD. At 2 K, the MSLD values in both interface layers are close (Δ MSLD $\approx 0.07\times10^{-6}$ Å^{-2}). Moreover, MSLD at 2 K in interface layer “1” exceeds that at 8 K (Δ MSLD $\approx 0.16\times10^{-6}$ Å^{-2}). For the first piece of the QD3 sample [Table 5.31], the interface layer “1” exhibits a higher magnitude of negative MSLD values compared to the interface layer “3”. Although the MSLD in the interface layer “1” varies slightly between temperatures, the POLREF data error bars are larger, making it challenging to discern a trend in the magnetic signal. The observed negative MSLD in the interface layers across samples implies that the magnetic moments in interface layers are aligned in a direction opposite to the moments in the EuS layer.

For the second piece of QD3 and both pieces of the QD4 sample, the MSLD contrast was comparatively lower than that of other samples examined in this study. The second pieces of the QD3 and QD4 samples unexpectedly exhibited lower MSLD contrast than the first pieces, despite comparable EuS thicknesses. Consequently, the weak MSLD contrast prevents any definitive conclusions regarding the interfacial magnetism. A plausible explanation for the reduced MSLD signal in the second pieces of both samples, relative to their first pieces, is the aging effect of the EuS layer. These measurements on the D17 instrument were recorded nearly a year later after the measurements at POLREF instrument. EuS, being metastable and prone to oxidation by air or moisture to its trivalent state, can degrade over time. Although the samples are capped with aluminum oxide, oxidation can creep in from the edges of the sample, affecting the magnetic signal of the EuS layer. For the QD4 sample, the MSLD contrast is likely lower than in other samples, probably due to the thinner EuS layer. As discussed earlier for the SQUID results [Section 5.4.2], thinner films have a higher atomic surface-to-volume ratio, which weakens the exchange interactions among magnetic Eu^{2+} ions. Furthermore, the SA curves for the second piece of sample QD4 [Figure 5.67] illustrate an example of the PNR sensitivity for an MSLD variation of approximately 0.1×10^{-6} $Å^{-2}$.

The paramagnetic behavior in the XMCD results for the QD1 sample [Figures 5.22 and 5.23], along with the reduced MSLD signals in the second pieces of the QD3 and QD4 samples, suggests the aging effects of EuS. However, it is important to note that oxidation alone is insufficient to account for these observations. This is because the XANES results indicate that QD1 and QD4 exhibit only single valence states, as shown in Figure 5.21. Thus, additional research is required to examine the aging effects in EuS.

A skewed distribution for specific parameters was observed in the uncertainty analysis results for the samples QD1, QD2, and QD3. This issue was addressed by fixing the parameter’s value. This occurrence may be due to the insensitivity of the model fits to these parameters. Constraining the value of the parameter imposes limits on correlated parameters, which enhance the robustness and reliability of the fit. Analysis of the correlation plots for the samples reveals some explicable correlations since all magnetic parameters collectively define the MSLD profile under any specific temperature and magnetic field conditions.

1. The correlation between magnetic roughness and MSLD of the same layer. Both parameters can influence the MSLD profile and its value for a thin magnetic layer such as the interface and EuS layers in this study. If the magnetic roughness changes, then this change can be compensated for by changing the MSLD to have the same shape of the MSLD profile. But there is a limit to these changes, and outside this limit the change in one parameter can not be compensated by the other. This limit is defined by the red region on a correlation plot. As these parameters specify the MSLD for the layer, this correlation is anticipated.

2. The correlation between the magnetic roughness of the bottom layer towards the surface and the MSLD of the layer on top. This correlation is also expected, as roughness can change the MSLD of the thin magnetic layer on top and eventually the MSLD contrast between layers.

However, the correlations between the magnetism in the EuS layer and the interfaces are of interest. A weak or no correlation is observed for MSLD in the interface layer "1" (1rhoM) with MSLD in the EuS layer (2rhoM) and interface layer "3" (3rhoM) for the samples QD1 [Figs. 5.34 and 5.39] and QD2 [Figs. 5.46 and 5.49]. This implies that the model fits are sensitive to the magnetism in the interface layer "1" and this magnetic signal is independent of the magnetism in both the EuS and the interface layer "3". Therefore, it can be uniquely estimated by fits.

Similarly to the samples QD1 and QD2, a weak or no correlation is observed for MSLD in the interface layer "1" (1rhoM) with MSLD in the interface layer "3" (3rhoM) for the QD3 sample. However, a negative correlation between MSLD in the interface layer "1" (1rhoM) and MSLD in the EuS layer (2rhoM) is observed for the sample QD3 correlation plots [Figs. 5.55 to 5.58] for all temperatures. But it is important to note that the whole distribution lies and peaks inside the box. The dimensions of these boxes are the same as the values on the x axis of the uncertainty plots for these parameters. The uncertainty plots are well defined and converging to a value with a certain error. Thus, it means that, though the parameters are correlated within a small region, they are still converging to a non-zero value of the magnetism in the interfacial layers. These values are significantly different from zero as confirmed by the uncertainty analysis for the parameters [Tables 5.13, 5.14, 5.20, 5.21, 5.27, 5.28, 5.29 and 5.30]. The thorough examination of parameter uncertainties and correlations for the observed MSLDs in the interface layers surrounding EuS reveals a robust and non-zero magnetic signal.

The induction of the magnetic signal in SU, below T_{SU}, antiparallel to the FM moments at the SU/FM interfaces was theoretically predicted by Bergeret *et al.* [117]. Furthermore, another study by Bergeret *et al.* [135] links the arrangement of moments to the quality of the SU/FM interface, which is antiparallel for rough interfaces. Additionally, the magnetic effects are predicted to be correlated with superconductivity rather than being a leakage of the magnetic signal. The antiparallel arrangement of moments is associated with the Cooper pairs in SU overlapping with the FM layer at the interface, resulting in one electron spin in FM leading to the antiparallel alignment of the second electron spin in SU. However, in contrast to theoretical predictions, a negative MSLD is observed at 8 K, slightly above T_{SU} for Pb layers in the samples. Consequently, the correlation with superconductivity is not entirely applicable in the current situation. Stahn *et al.* [27] also reported the observation of antiparallel arrangement of moment in SU in SU/FM multilayers and hints toward strong SU fluctuations above T_{SU}. The other possible explanation might be the diffusion of Eu ions in the interface layers. However, the origin of this magnetic signal is still debatable and requires further investigation.

5.6 Conclusions and summary

The behavior of ferromagnetism in EuS layers with thickness, temperature, and magnetic field is observed as expected by the theory. PNR and SQUID magnetometry both indicate that the thin Pb layers in the samples exhibited type II superconductivity instead of the anticipated type I behavior. PNR confirms the extension of the magnetic order in the interface layers close to EuS, which is more pronounced at one interface. The moments are aligned anti-parallel to the moments in the EuS layer. The magnitude of MSLD in the interface layers depends on the MSLD in the EuS layer. As the MSLD within the EuS layer approaches approximately 1×10^{-6} Å^{-2} or below, the magnetic signal present in the interface layers becomes considerably weak. Consequently, the PNR fitting procedure loses its sensitivity to these signals, making them difficult to detect or analyze. Furthermore, EuS thickness should be greater than or equal to 20 Å to be used to study MPEs in heterostructures, as further down the MSLD contrast is too low to observe and quantify the MPEs.

In summary, an investigation of the magnetic proximity effects was conducted at the EuS/Pb interfaces in heterostructures with different thicknesses of the EuS and Pb layers but with the same structure. The ferromagnetism in EuS behaved as expected by the theory. The induction of an antiparallel arrangement of moments is observed and quantified in the interface layers for the samples. Further investigation is necessary to identify the origin of the magnetic signal within interface layers.

Chapter 6

Magnetism in EuS

6.1 Motivation

After its discovery in 1962, the magnetic properties of EuS have been a subject of interest for researchers. The candidacy of this material has been tested for its applications in various fields of science and technology, i.e., as a spin filter for spintronic devices [124, 136, 137, 138, 139, 140, 141], to introduce magnetic proximity effects in non-magnetic materials in heterostructures [103, 142]. However, the low Curie temperature of EuS ($T_C \approx 16.5$ K) hinders its practical applications, and many efforts have been made in the past to increase the T_C of EuS [143, 144, 145]. Studies on multilayer structures with Co/EuS and Ni/EuS indicated that T_C of EuS could be increased to room temperature (RT) in proximity to the Co or Ni layer [130, 146]. The high T_C ferromagnets, such as Ni and Co, polarize the spins in the EuS thin layer antiferromagnetically and increase the T_C of the EuS layer.

Furthermore, Katmis *et al.* [31] observed an interfacial magnetism in Bi_2Se_3 of around 240 emu/cc at 5 K in 1 T near the EuS/Bi_2Se_3 interface in heterostructure and remained up to room temperature but with a reduced magnitude. They reported that a thin EuS film (approximately 50 Å) alone did not exhibit a magnetic signal at 50 K or higher under the same magnetic field strength. The observation of a magnetic signal at the interface well above T_C of EuS was linked to the breaking of the time-reversal symmetry locally on the surface of Bi_2Se_3 (topological insulator, TI). Then, a theoretical study by Kim *et al.* [147] on EuS/Bi_2Se_3 heterostructure demonstrated that the topological surface states of Bi_2Se_3 hybridize with the EuS states to enhance magnetic ordering and are crucial for unusual behavior at the interface. However, a study by Krieger *et al.* [148] reported that the origin of the magnetic signal at EuS/Bi_2Se_3 interface is independent of the topological properties of Bi_2Se_3. Furthermore, conflicting results emerged from a study by Figueroa *et al.* [149], in which no magnetic signal was detected in the TI at the interface of the EuS/TI bilayers at RT in the presence of 2 T with the measurements of the X-ray magnetic circular dichroism (XMCD). Moreover, no evidence of increased Eu magnetic moments in the EuS layer or a rise in T_C was found. Meanwhile, theoretical studies by Meyerheim *et al.* [150] and Fedorov *et al.* [49] attempted to explain the observed magnetic signal in the EuS/Bi_2Se_3 system by attributing it to sulfur atoms being magnetic at the interface, a result of dangling bonds and hybridization of interfacial states. This study also refuted the claims that interfacial magnetism is present in Bi_2Se_3, but points to an increase in T_C of EuS. The origin of the magnetic signal at high temperatures in these heterostructures is still debatable.

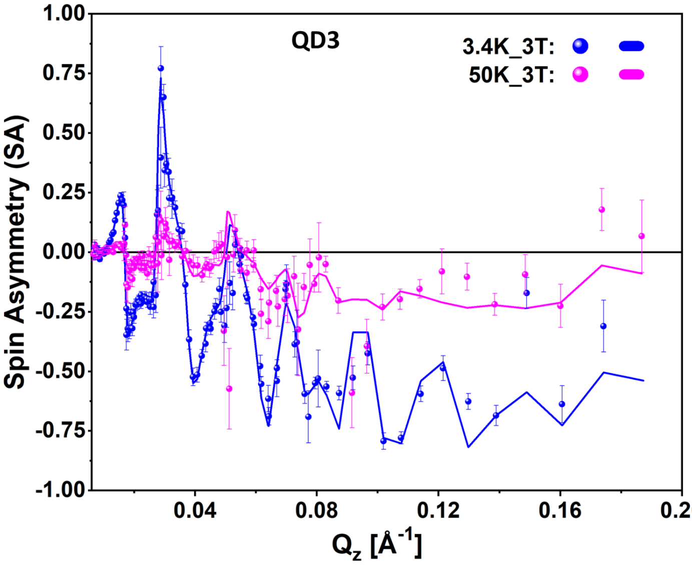

Figure 6.1: Spin asymmetry (SA) as a function of momentum transfer (Q_z) for the sample QD3 at 50 K in presence of 3 T in-plane magnetic field ($H_{ext,//}$).

In this work, while examining the magnetic proximity effects in heterostructures with EuS and Pb layers (Chapter 5), a magnetic moment of 0.42 μ_B per Eu ion was detected at 50 K (in 3 T) for the sample QD3. Figure 6.1 shows the SA signal as a function of Q_z for the QD3 sample for 3 K and 50 K in the presence of 3 T with their respective fits. This signal was not confined to the interface but was uniformly present within the EuS layer [Figure 5.60]. Observing a magnetic signal in the EuS layer above T_C, despite the absence of a topological insulator or any high T_C ferromagnet, raises a question about the origin of this signal and shows the need for an understanding of the magnetism at high temperatures in EuS thin films alone. To date, there appear to be no definite conclusions on the source of the magnetic signal above T_C in heterostructures involving EuS. Consequently, an investigation of the magnetic properties of the EuS thin films was conducted. Furthermore, it will provide insights on the presence of magnetic signal in

FM/TI heterostructures.

6.2 Aim

The objective of this investigation was to study and quantify the magnetic signal in the thin films of EuS above and below T_C. Furthermore, the aim was to study the variation of the magnetic signal as a function of temperature and applied magnetic fields. The understanding of magnetism in EuS thin films alone is crucial because it may have direct implications for studies investigating interfacial magnetism or optimizing EuS-based heterostructures designed for applications in spintronics and quantum computing.

6.3 Approach

Figure 6.2 shows the schematic of four EuS samples of different thicknesses from 15 to 100 Å that were fabricated for the study. The choice of these thicknesses is influenced by the thicknesses of EuS layers used in the study of MPEs in heterostructures (Chapter 5). The films were grown on InAs (111 B) substrates by e-beam deposition and capped with Al_xO_y. The details of the fabrication method are given in the chapter 2.

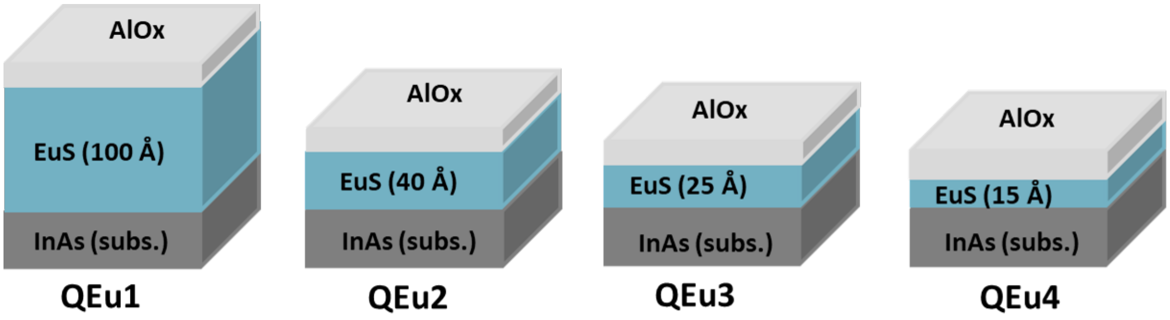

Figure 6.2: The schematic of four EuS samples with intended thicknesses is shown. Here QEu is the name for EuS sample.

The samples were studied with polarized neutron reflectometry (PNR) and X-ray reflectometry (XRR) to obtain depth-resolved magnetization and structural profiles of the samples. This information will help in assessing whether the signal above T_C is confined to the interface or uniformly distributed throughout the layer. The results are complemented by SQUID magnetometry to obtain information on the T_C of thin films of EuS and its variation with temperature and applied magnetic fields. PNR was preferred over SQUID magnetometry for the quantification of the magnetic signal from EuS thin films because volumetric magnetic characterization by SQUID is sensitive to other contributions as well such as diamagnetic contributions from the substrate and capping layers, which hinders a precise determination of the EuS moment. Moreover, X-ray diffraction (XRD) technique was used to acquire information on the crystalline structure of thin films.

6.4 Results and discussion

6.4.1 Characterization of crystalline structure

Figure 6.3 shows the XRD results for the four samples on both logarithmic and linear scales. The reference lines corresponding to the EuS (violet dashed line) and InAs (green solid lines) peaks are marked in the plots. Measurements were performed in θ - 2θ scanning mode, allowing us to examine lattice planes parallel to the sample surface. Reference peaks were indexed by comparing them with crystallographic powder data for InAs [119] and EuS [121]. Intense peaks are observed around 25.46°, 52.29°, and 82.72°. XRD peaks around 25.46°, 52.29°, and 82.72° are identified as substrate peaks corresponding to reflection planes InAs(111), InAs(222), and InAs(333), respectively. However, the InAs peaks are slightly shifted to the lower 2θ angles compared to the expected values.

There are no strong and distinct peaks in the XRD results that could be attributed to the EuS. EuS peaks for planes (111), (222), and (333) are expected to occur at angles of 25.88°, 53.22°, and 84.43°, respectively. However, for the QEu1 sample (in red), a less pronounced peak appears near 53.48°, highlighted with a black dotted circle in Figure 6.3 (a). In addition, all samples show the broadening of the intense InAs peak at 25.46°, highlighted with black arrows in Figure 6.3 (a). The broadening of the InAs peak at 82.72° is also observed, except for the QEu4 sample (in pink), which only exhibits broadening at the peak located at 25.46°. The estimated value of the unit cell parameter "a" for the FCC lattice of EuS from the observed peak at 53.48°, using the equation 3.39, is (5.93 ± 0.06) Å.

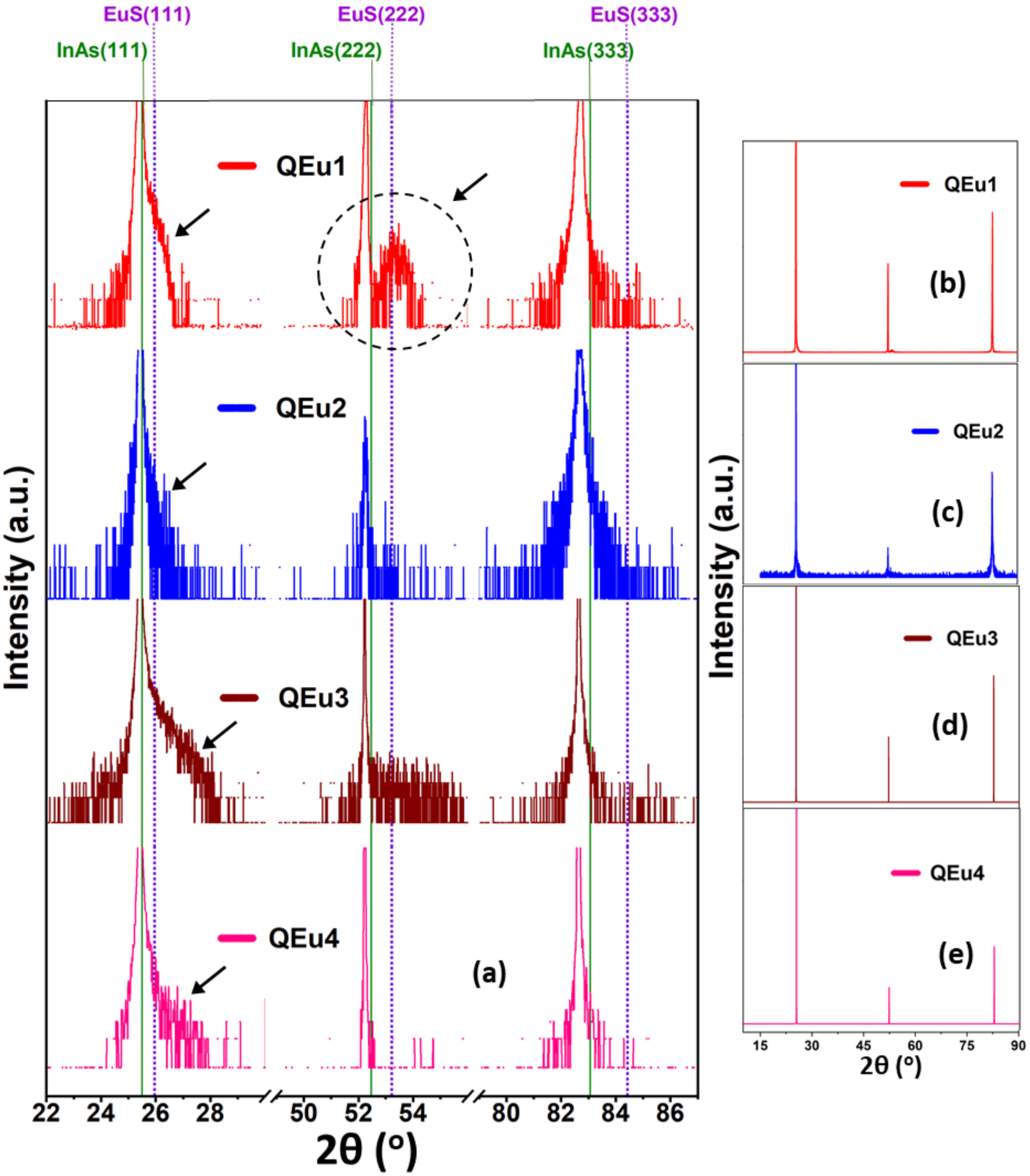

Figure 6.3: XRD results along with the dotted reference lines at peaks of InAs (green) and EuS (violet). (a) XRD results are shown on logarithmic scale and zoomed to show the peaks corresponding to EuS. The results are offset along the y-axis for better visibility. (b)-(e) The inset images shows the full XRD pattern on linear scale.

The main peaks observed in the XRD results [Figure 6.3] correspond to the crystalline planes of the InAs substrate. Minor deviations in peak positions may arise due to the InAs reflection planes not being perfectly parallel with the sample surface during the XRD measurements relative to the surface. This misalignment can make the interplanar distance appear larger, resulting in a shift of 2θ to lower values. XRD data do not show prominent and clear peaks that could be linked to EuS, except a single peak observed for the QEu1 sample near 53.48°. The unit cell parameter "a" determined for the cubic lattice of EuS closely matches the value reported in the literature for EuS [48]. However, the shoulder on the substrate peaks indicates the presence of a EuS(111) peak close by. The EuS layer in the samples, being very thin, contributes only a small volume to the observable XRD peaks that may result in a broadening of peaks and being obscured due to stronger XRD signals from the substrate. Additionally, the capping layer's amorphous structure may result in broad and diffuse characteristic peaks due to its absence of long-range atomic order [87].

6.4.2 Volume magnetometry

Figure 6.4 (a)-(d) shows the magnetization (M) as a function of temperature for the samples. The measurements were recorded while the samples were field cooled in the presence of an in-plane magnetic field ($H_{ext,//}$) as indicated in the plots. The Curie transition (T_C) is expected to occur around 16.5 K for EuS (in bulk). For comparison across samples, the magnetic response on the y axis is normalized to the volume of the EuS layer in each sample. To determine the volume, the thickness of the EuS layer is obtained from the PNR results. The detailed normalization process and the estimation of the Curie transition temperatures are discussed in Chapter 3 (Section 3.2.4). T_C is determined from the M versus temperature curves for each sample and is listed in Table 6.2.

Figure 6.4 (a) presents magnetization versus temperature data for the sample QEu1. As the field increases from 0.1 T to 0.3 T, magnetization rises at low temperatures. However, little change occurs when the field is further increased to 0.5 T (or 3 T) compared to the initial increase from 0.1 T to 0.3 T. A notable reduction in magnetization is seen between 14 K and 22 K for all fields, except 3 T, which shows a more gradual decline. Table 6.1 lists the values and errors in the volume of the EuS layer in the samples that were used for the normalization.

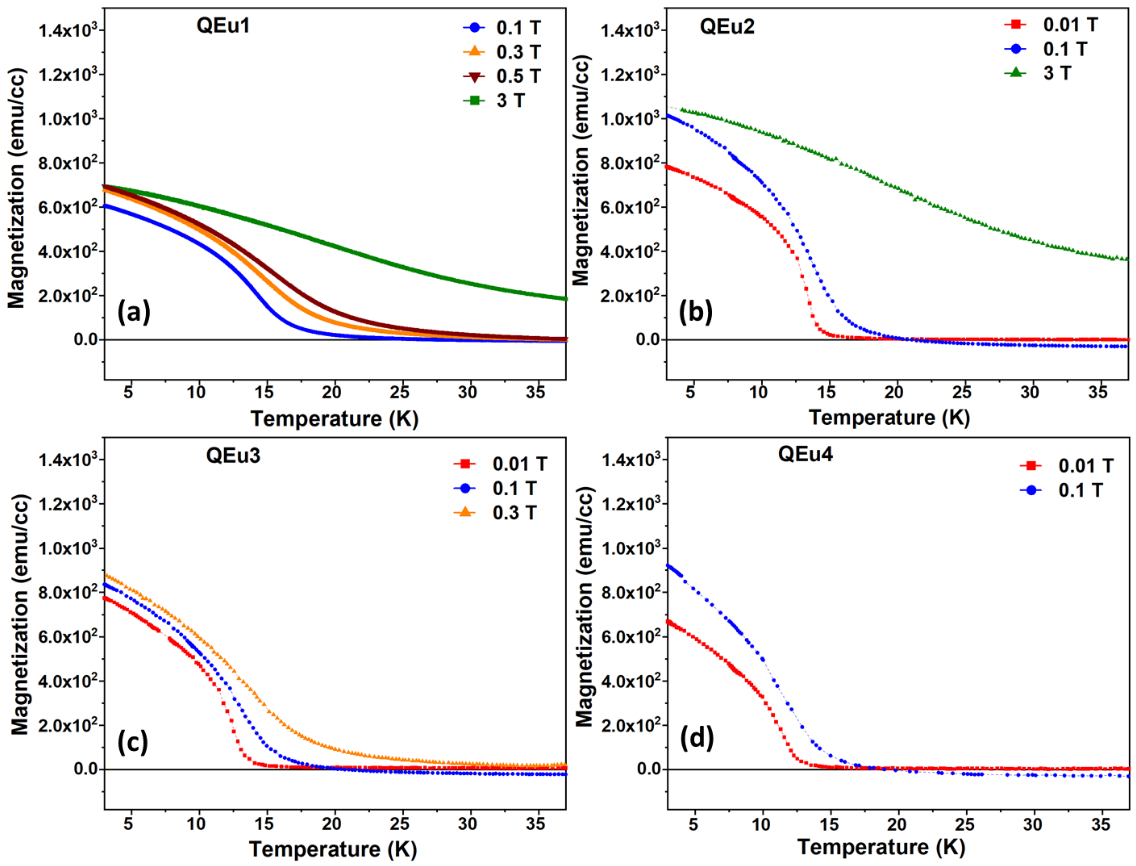

Figure 6.4: Magnetization (M) as a function of temperature in the presence of applied in-plane magnetic field as indicated in the plots. (a) QEu1 (b) QEu2 (c) QEu3 (d) QEu4. The dotted lines serve as a guide to the eye.

Table 6.1: Volume of EuS layer in the samples used for the normalization of the SQUID magnetometry data. The values for the thickness of EuS layer are taken from Tables. 6.5, 6.10, 6.15 and 6.20

Sample	**Volume (cc)**	**Error**
QEu1	2.1×10^{-7}	0.3×10^{-7}
QEu2	9×10^{-8}	1×10^{-8}
QEu3	4.7×10^{-8}	0.8×10^{-8}
QEu4	2.3×10^{-8}	0.4×10^{-8}

Similarly to the QEu1 sample, the remaining samples show a rise in magnetization at low temperatures with an increased magnetic field, as depicted in Figs. 6.4 (b) to (d). Table 6.2 summarizes the T$_C$ values obtained from measurements in Figure 6.4. The method for determining T$_C$ is detailed in Section 3.2.4. The QEu4 sample shows the lowest T$_C$ in 0.1 T, followed by the QEu3 sample. In contrast, T$_C$ for QEu1 and QEu2 are nearly identical.

Table 6.2: Curie transition temperature (T$_C$) for the samples. Missing values are due to lack of measurements at these fields.

H$_{ext,//}$ =	**0.01 T**	**0.1 T**	**0.3 T**
Sample	**Curie transition temperature (T_C, K)**		
QEu1	-	14.88 (± 0.04)	16.80 (± 0.06)
QEu2	13.52 (± 0.01)	14.9 (± 0.1)	-
QEu3	12.73 (± 0.06)	14.55 (± 0.09)	16.1 (± 0.1)
QEu4	11.98 (± 0.07)	13.0 (± 0.3)	-

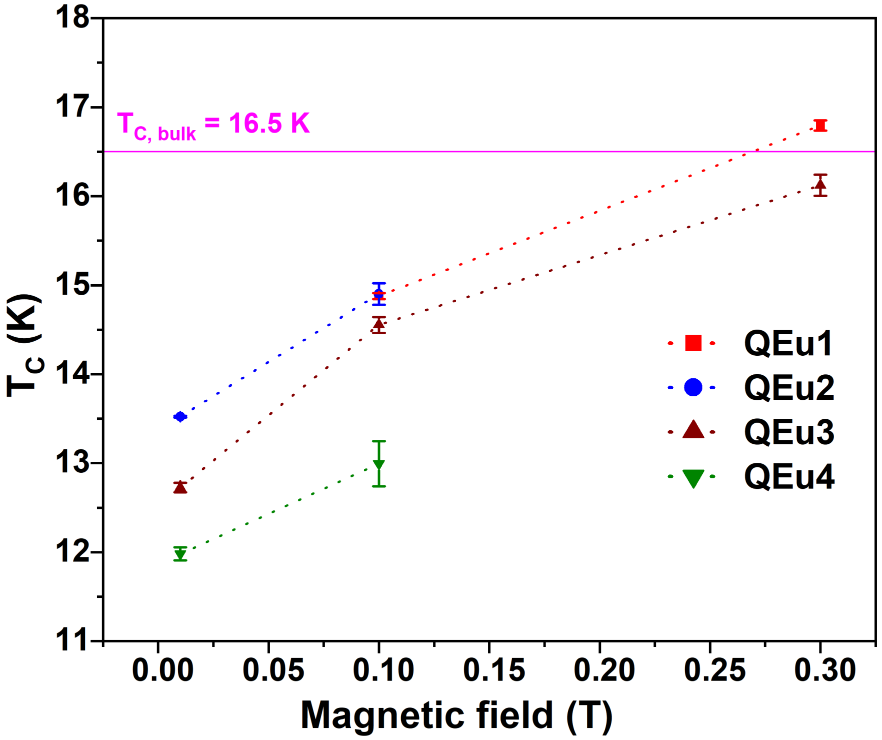

Figure 6.5: The variation of Curie temperature (T$_C$) with external magnetic field. The dotted lines serve as a guide to the eye.

Figure 6.5 presents the T$_C$ dependence on the magnetic field for the samples. Bulk

EuS T_C (16.5 K) serves as a reference on all plots. An increase in T_C with the magnetic field is noted for all samples. For the sample QEu1, T_C in 0.1 T slightly exceeds that of the bulk EuS.

Figure 6.6 shows the variation of T_C as a function of the thickness of the EuS layer for the samples in the presence of 0.1 T. In conditions of a constant magnetic field, increasing the EuS thickness results in a higher critical temperature, T_C.

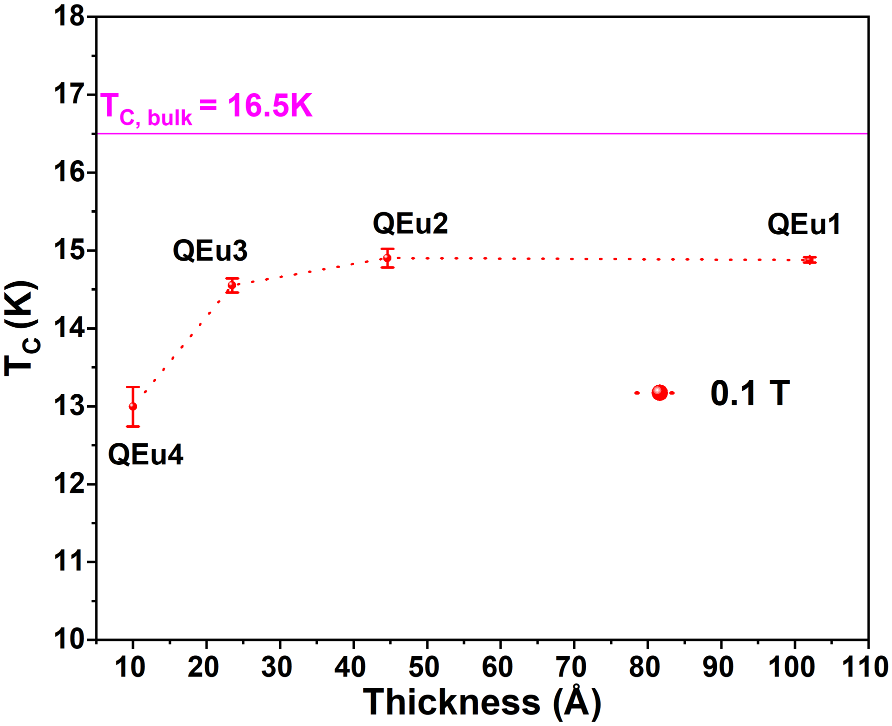

Figure 6.6: The variation in the Curie transition temperature with the thickness of the EuS layer in the presence of 0.1 T. The dotted lines serve as a guide to the eye.

When below T_C, the material behaves ferromagnetically, indicating that the magnetic moments align, creating a net magnetic moment in the EuS layer. Above T_C, the magnetization decreases because thermal energy overcomes magnetic exchange interactions, leading to the destruction of the magnetic order. A decrease in T_C of the samples is observed as the thickness of the EuS layer is reduced, while maintaining a constant magnetic field (Table 6.2). This drop in T_C with decreasing film thickness is consistent with the ferromagnetic behavior predicted by Schiller *et al.* [125] for Heisenberg ferromagnetic thin films and is experimentally reported in EuS thin films by Müller *et al.* [151]. This effect is due to the lower coordination number of magnetic ions at the interfaces, resulting from a higher surface-to-volume ratio, which hampers the establishment of long-range magnetic order. Therefore, Curie transitions occur at lower temperatures. Furthermore, the Curie transition becomes smeared and exhibits a slight T_C increase with a stronger in-plane magnetic field for the identical sample [Figure 6.5]. Figure 6.7 shows how elevating applied magnetic fields influences the Curie transition in FMs, with comparable effects observed in the samples under study. The external magnetic field diminishes the effects of thermal energy on magnetic moments near T_C, favoring their alignment with the field [127], thereby appearing to elevate T_C.

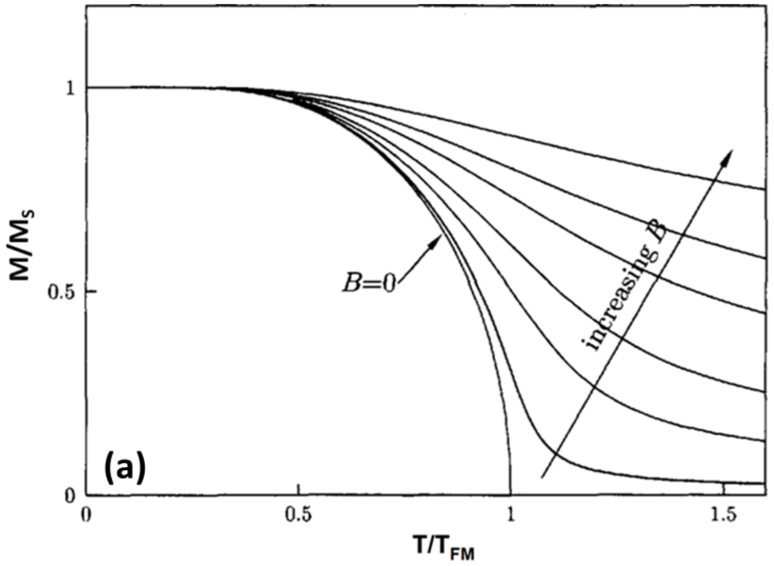

Figure 6.7: Normalized magnetization (M/M_S) as a function of temperature in the presence of different magnetic field strengths, for materials with J=1/2. This plot is taken from ref. [127].

The QEu2 sample exhibits the highest magnetization value below T_C in 0.1 T [Figure 6.4], followed by QEu4, QEu3 and finally QEu1. One of the possible reasons for this discrepancy could be deviation from stoichiometric growth of the EuS layer in the sample. The presence of mixed-valence states of Eu was observed for other samples in the present thesis [Figure 5.21]. Below T_C, the Eu^{2+} state contributes to ferromagnetism and the Eu^{3+} state to paramagnetism [152], therefore, the presence of the Eu^{3+} valence state could reduce the magnetic signal from the EuS layer. The other possibility for a reduced magnetic signal from QEu1 is the oxidation of the EuS layer that creeps from the edges in the sample, which changes the valence state from Eu^{2+} to Eu^{3+}.

Table 6.3 shows the critical exponent (β_1) values. For all samples, β_1 rises with

Table 6.3: Critical exponent (β_1) for the samples. Missing values are due to lack of measurements at these fields.

H$_{ext,//}$ =	**0.01 T**	**0.1 T**	**0.3 T**
Sample	**Critical exponent** (β_1)		
QEu1	-	0.52 (± 0.01)	0.64 (± 0.01)
QEu2	0.3 (± 0.1)	0.54 (± 0.03)	-
QEu3	0.41 (± 0.01)	0.63 (± 0.02)	0.76 (± 0.02)
QEu4	0.53 (± 0.02)	0.59 (± 0.05)	-

increasing magnetic field strength. Figure 6.8 presents β_1 as a function of EuS layer thickness in a 0.1 T field. The reference line in the figure marks the bulk EuS value (0.36) for comparison [123]. β_1 exceeds the bulk value for all samples and approaches the reference line as the EuS layer thickness increases.

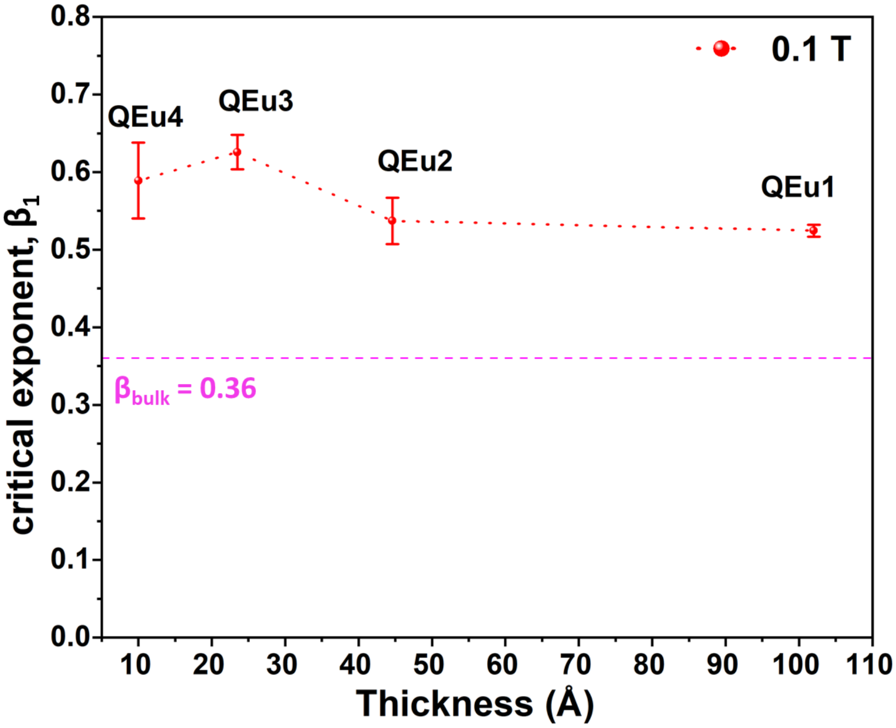

Figure 6.8: Critical exponent (β_1) as a function of the thickness of EuS layer for samples in presence of 0.1 T. The dotted lines serve as a guide to the eye.

The difference in the critical exponent (β_1) for these samples compared to the bulk

EuS value (Table 6.3) may result from surface anisotropy effects in thin EuS films, as previously examined by Dauth *et al.* [128]. Furthermore, these effects clarify the slight reduction in β_1 as the EuS thickness increases. The increase in β_1 with applied magnetic field can be attributed to magnetic field effects, as previously discussed for T_C.

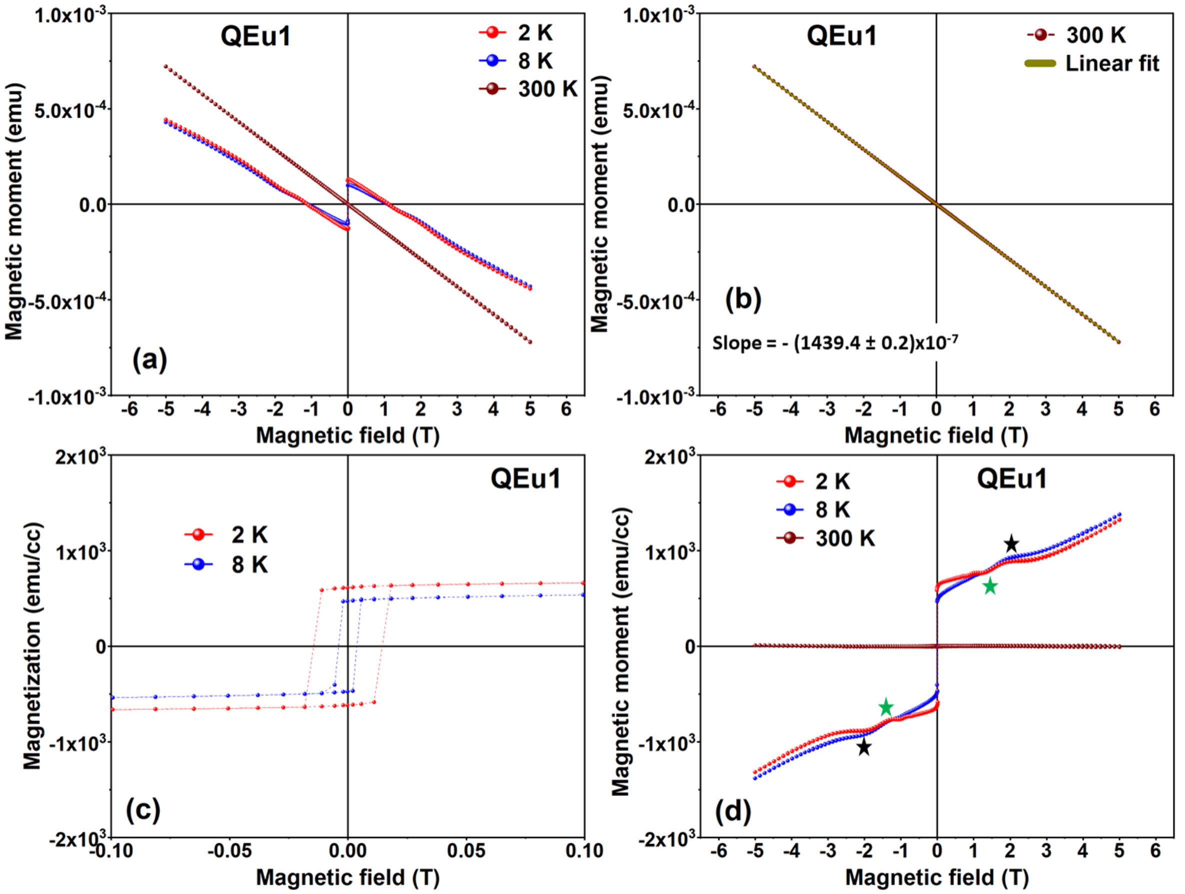

Figure 6.9: Magnetic hysteresis loops recorded for the QEu1 sample at temperatures indicated in the plots. (a) Raw data (b) Raw data for 300 K and its linear fit. (c) Normalized data at 2 K and 8 K (d) Normalized data. The dotted lines serve as a guide to the eye.

Hysteresis loops for the samples were recorded in magnetic fields up to ± 6 T. The SQUID magnetometry section in Chapter 2 (3.2.4) covers the normalization and slope correction processes. Figure 6.9 presents the hysteresis loops for the QEu1 sample. In Figure 6.9 (a), raw data at 2 K, 8 K, and 300 K are shown, with all data curves displaying a negative slope at the field range ends. Figure 6.9 (b) shows raw data at 300

K with a linear fit, indicating no hysteresis at this temperature. The average slope of the fit is - (1439.4 ± 0.2)$\times10^{-7}$ emu T^{-1} and was used for the slope correction of other data sets. Figure 6.9 (c) presents the normalized data for 2 K and 8 K, where, after normalization, the slopes of the curves become positive. Hysteresis loops are apparent in both temperatures, with the 8 K loop being narrower than the 2 K loop. Figure 6.9 (d) shows the normalized data across the full field range for 2 K, 8 K, and 300 K. At higher fields, both the 2 K and 8 K curves maintain a positive growth without reaching saturation. Some artefacts are observed in the magnetic response, such as the intersection of 2 K and 8 K curves at approximately ± 1.3 T, indicated by green stars in Figure 6.9 (d). Additionally, around 2 T, both curves exhibit a deviation (highlighted with black stars) before continuing their upward trend.

Figure 6.10 shows the hysteresis loops for the QEu2 sample. Figure 6.10 (a) shows the raw data recorded at temperatures of 4 K, 30 K, 50 K, and 300 K. Figure 6.10 (b) shows the raw data recorded at 300 K, along with a linear fit. The average slope of the fit to the data is - (1553.1 ± 0.4)$\times10^{-7}$ emu T^{-1}. This data set was used for the slope correction of the remaining data sets. Figure 6.10 (c) shows the normalized data for 4 K. At 4 K, the curves exhibit hysteresis loop. Figure 6.10 (d) shows the normalized data for the entire field range for 4 K, 30 K, 50 K, and 300 K. The normalized magnetic responses for 50 K and 300 K lie close to the line corresponding to M = 0 emu/cc. However, the slope of magnetization curve at 30 K is not zero and the curve continues to increase with increasing magnetic field. Moreover, similarly to the artefacts observed for the QEu1 sample, the magnetization curve at 4 K shows a slope change in the range from 1 T to 2 T and then saturates around ± 3 T.

Figure 6.11 presents the hysteresis loops for the QEu3 sample. The estimated average slope of this fit to 300 K data [Figure 6.11 (b)] is - (1502.5 ± 0.7)$\times10^{-7}$ emu T^{-1}, used to adjust the slopes across the dataset. In Figure 6.10 (d), the normalized magnetic responses for 200 K and 300 K lie close to the line corresponding to M = 0 emu/cc. Similarly to the QEu1 and QEu2 samples, artefacts are observed for sample QEu3. These artefacts include the negative slope of magnetization curve at 50 K and a slope change in the magnetization curve at 4 K in the range from 1 T to 2 T.

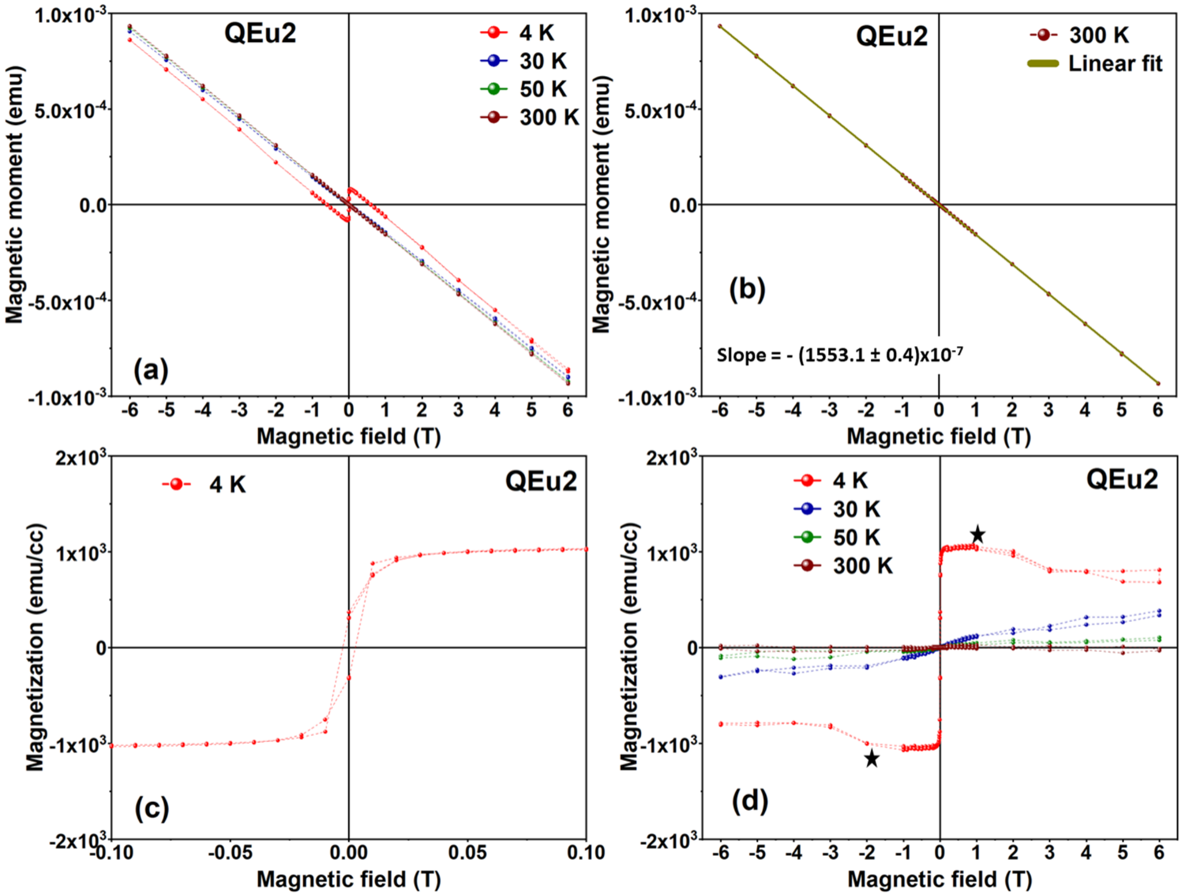

Figure 6.10: Magnetic hysteresis loops recorded for the QEu2 sample at temperatures indicated in the plots. (a) Raw data (b) Raw data for 300 K and its linear fit. (c) Normalized data at 4 K (d) Normalized data. The dotted lines serve as a guide to the eye.

Figure 6.12 shows the hysteresis loops for the QEu4 sample and the InAs substrate. The loops for the InAs substrate here are identical to those in the MPEs study [Figure 5.20]. In Figure 6.12 (a), the raw data for the QEu4 sample at 4 K and for the InAs substrate at 5 K and 300 K are shown. Figure 6.12 (b) presents raw data for the InAs substrate at 300 K and a linear fit with an average slope of - (1614.2 ± 0.9)$\times 10^{-7}$ emu T^{-1}, used for the slope correction of other data. Figure 6.12 (c) shows slope corrected data for the QEu4 sample at 4 K and the InAs substrate at 5 K and 300 K, with an unexpected magnetic response in the InAs substrate data at 5 K and 300 K. Black stars at ± 2 T denote deviation points at 4 K for QEu4 and 5 K for InAs. The 5 K InAs curve deviates and saturates at both magnetic field extremes, while the 4 K QEu4 curve deviates with increasing magnitude as the field increases. The green stars on the InAs curve at 5 K around ± 1.2 T denote a dip in the magnetic response. Figure 6.12 (d) displays 4 K data, normalized by the EuS layer volume, for the QEu4 sample.

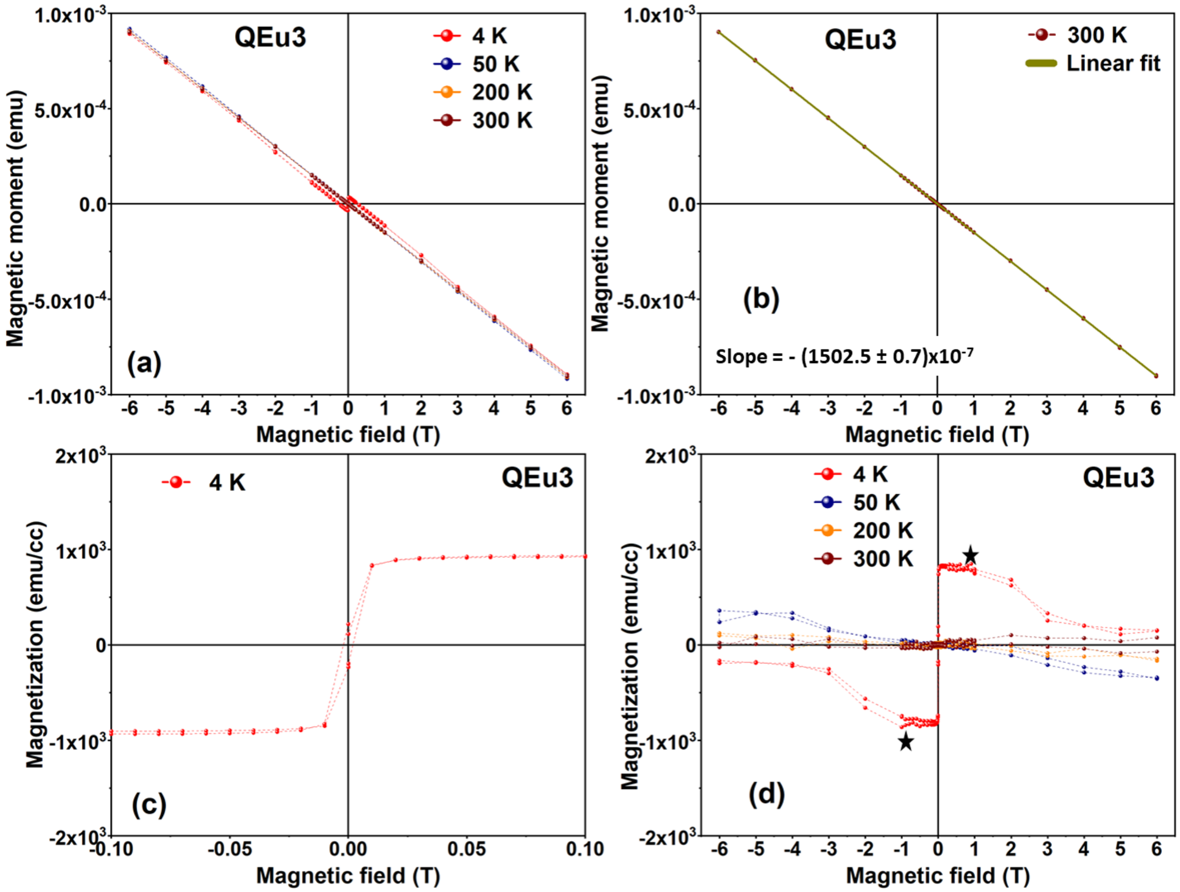

Figure 6.11: Magnetic hysteresis loops recorded for the QEu3 sample at temperatures indicated in the plots. (a) Raw data (b) Raw data for 300 K and its linear fit. (c) Normalized data at 4 K (d) Normalized data for temperatures 4 K, 50 K, 100 K, 200 K, and 300 K. The dotted lines serve as a guide to the eye.

The artefacts observed in the magnetization curves around ± 1.3 T and ± 2 T for all samples can be attributed to the unusual magnetic response of the InAs substrate, indicated by green and black stars in [Figure 6.12 (c)]. The reason behind the substrate's deviation from the anticipated diamagnetic behavior remains unclear. However, the unusual magnetic response of InAs at 5 K differs from the standard ferromagnetic or paramagnetic behavior.

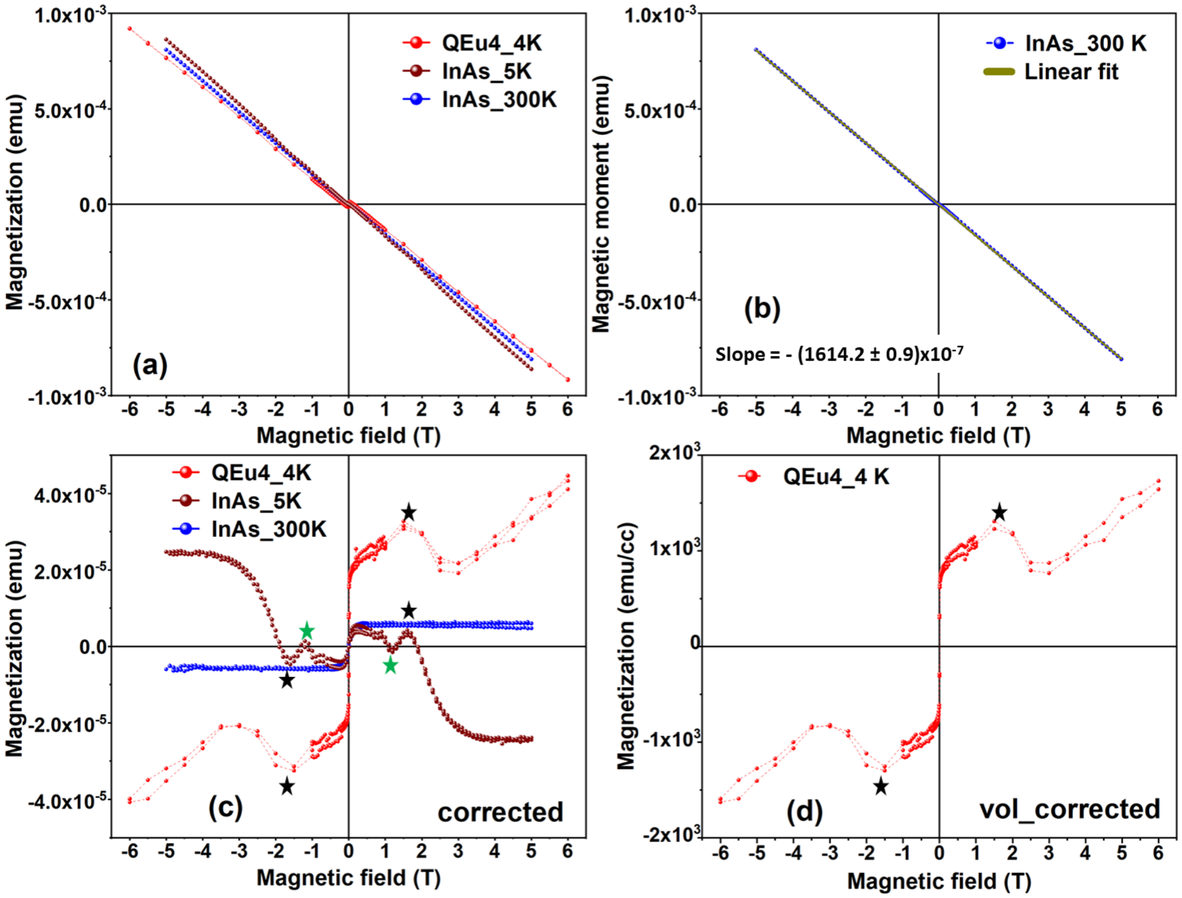

Figure 6.12: Magnetic hysteresis loops recorded for the QEu4 sample and InAs substrate. (a) Raw data for the QEu4 sample at 4 K and InAs substrate at 5 K and 300 K. (b) Raw data for InAs substrate at 300 K and its linear fit. (c) Slope corrected data for the QEu4 sample at 4 K and InAs substrate at 5 K and 300 K. (d) Normalized data for the QEu4 sample at 4 K. The dotted lines serve as a guide to the eye.

Moreover, it is observed that magnetization does not saturate in the case of the QEu1 and QEu4 samples even at high fields ± 6 T and the magnitude continues to increase at both ends of the field range in hysteresis loops [Figs. 6.9 and 6.12 (d)]. The non-saturation and linearly increased response with magnetic field resembles the paramagnetic behavior. This observation points to the mixed valence state of Eu in the samples. Additionally, as discussed earlier for the QEu4 sample, the non-saturation could result from a higher surface-to-volume ratio compared to other samples.

In contrast to the QEu1 and QEu4 samples, the magnetic response of QEu2 and QEu3 at both ends of the magnetic field range eventually saturates, but at a higher field for the QEu3 sample than for QEu2. In summary, all samples show hysteresis loops below T$_C$.

6.4.3 Structure and magnetism with depth

Data from specular PNR and XRR, along with the best-fit models for each sample, are presented in the following subsections. Furthermore, comparisons of spin asymmetry (SA) versus momentum transfer vector (Q$_z$) at different temperatures and magnetic field strengths are shown for each sample. Detailed data analysis can be found in the data analysis chapter (Section 4.1.5). The PNR data presented in this study were collected using the D17 instrument at ILL [80].

PNR data were collected at temperatures significantly below (2 K, 6 K, and 8 K) and above (50 K, 100 K, and 300 K) the T$_C$ of EuS under an in-plane magnetic field of 0.1 T, 3 T, and 6 T. This magnetic field was applied externally, parallel to the sample plane. Due to constraints in neutron beamtime, we had to limit the number of measurements per sample. Consequently, some PNR measurements were performed at only one incident angle instead of three to assess magnetic splitting. Thus, the data are presented over a limited Q-range (up to 0.1 $\mathring{A}^{-1}$), sufficient to determine whether the EuS layer is magnetic in the current samples.

The theoretical reference values of NSLD, MSLD and XSLD for the EuS layer are 1.90×10^{-6} $\mathring{A}^{-2}$, 3.48×10^{-6} $\mathring{A}^{-2}$ and 38.28×10^{-6} $\mathring{A}^{-2}$, respectively. These values are calculated using equations 3.6, 3.29 and 3.36. The computation utilizes EuS data for structural [48], neutron [132], and X-ray [133] scattering lengths.

Sample QEu1

Table 6.4 list the PNR measurements performed on the QEu1 sample. A total of eleven PNR measurements were performed for the sample to monitor the variations in the magnetic signal as a function of temperature and magnetic field. The fitted neutron (PNR) data for the sample QEu1 are shown in Figs.6.13 and 6.14. A simple model approach (Section 4.1.5) was followed to fit the data for this sample. The simulated reflectivity from the simple model aligns well with the experimental PNR data.

Table 6.4: PNR measurements for the sample QEu1.

PNR measurements: QEu1 sample	
Temperature (K)	**$H_{ext,//}$ (T)**
2	0.1
6	0.1
8	0.1
2	3
6	3
8	3
50	3
100	3
100	6
300	3
300	6

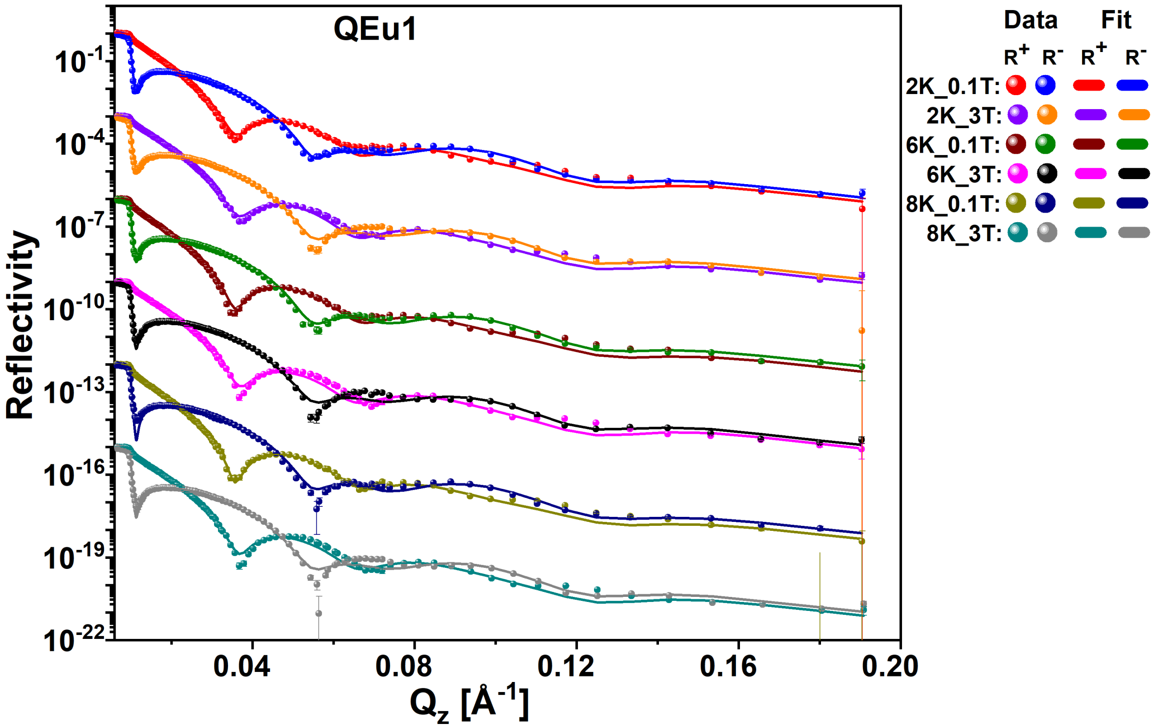

Figure 6.13: Specular polarized neutron reflectometry (PNR) data (dots) for spin-up (R^+) and spin-down (R^-) configuration with fits (line) are shown for the measurements as indicated in the plot. The curves are offset by 10^3 along y-axis for visibility.

NSLD and MSLD profiles versus depth for the sample QEu1 are shown in Figure 6.15. The horizontal dotted lines correspond to the reference NSLD value for EuS (1.90×10^{-6} Å^{-2}). The different layers in the sample are identified and named at the bottom of the SLD profiles. The NSLD profile for the sample shows that there is a gradient in the NSLD of the EuS layer toward the top. The estimated values of the parameters are listed in Table 6.5. The thickness of the EuS layer in the QEu1 sample is close to the intended thickness for this sample. The NSLD of the EuS layer is around 9 % lower than the theoretically calculated value of NSLD for EuS (1.90×10^{-6} Å^{-2}).

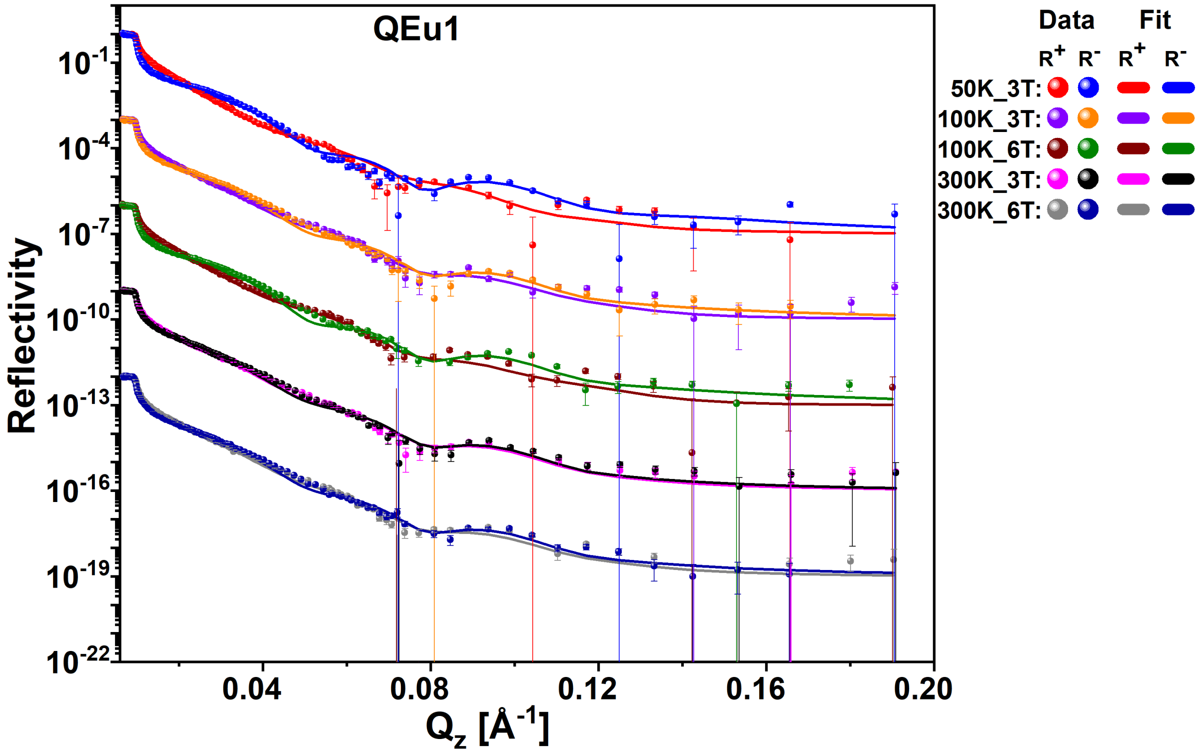

Figure 6.14: Specular polarized neutron reflectometry (PNR) data (dots) for spin-up (R^+) and spin-down (R^-) configuration with fits (lines) are shown for the measurements as indicated in the plot. The curves are offset by 10^3 along y-axis for visibility.

However, the MSLD profiles for all PNR measurements [Figure 6.15 (a) and (b)] are uniform throughout the EuS layer and decay according to the error function used to describe the magnetic roughness profiles. The estimated values of the MSLD in the EuS layer are listed in Table 6.6. Moreover, the MSLD for the PNR measurements recorded above T_C is non-zero in the EuS layer.

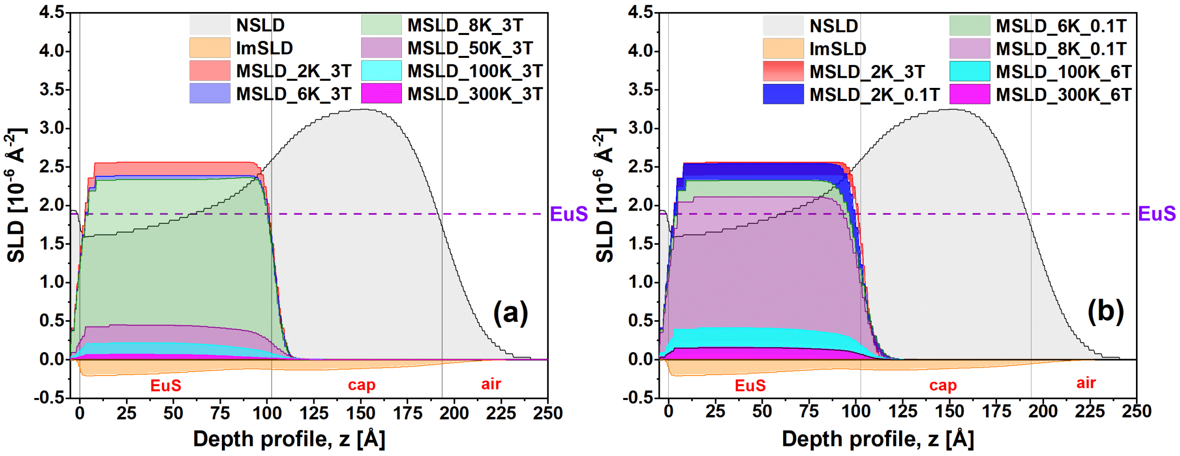

Figure 6.15: NSLD and MSLD profiles of the sample QEu1 with depth for the measurements as indicated in the plots. The absorption scattering length density (ImSLD) is shown with orange color in both plots. The reference NSLD for EuS (violet) are marked on the plots.

Table 6.5: A list of the parameters and their estimated values from the fit to the PNR data for the sample QEu1.

Sample QEu1		
Layer	**Thickness**	**NSLD**
	(Å)	**$(\times 10^{-6}$ Å$^{-2})$**
Cap	90.2 [89.1, 90.9]	3.42 [3.35, 3.51]
EuS	101.6 [100.9, 102.9]	1.72 [1.68, 1.77]

Figure 6.16 shows the SA as a function of Q_z, with fits for the measurements. The SA signal remains non-zero well above T_C of EuS in the sample, extending to temperatures as high as 300 K. The SA signal exhibits a rapid decrease from 8 K to 50 K [Figure 6.16 (a)], from 50 K to 300 K, the decrease is more gradual. This is not the case for temperatures below T_C, as the SA data for 2 K (in 0.1 T), 2 K (in 3 T), and 8 K (0.1 T) show a slight difference [Figure 6.16 (c)].

Table 6.6 presents MSLD values for the EuS layer in various temperatures and magnetic fields. The MSLD value nearly doubles with a magnetic field shift from 3 T to 6 T, as noted at 100 K and 300 K, similar to the behavior of the SA signal for these temperatures [Figure 6.16 (d)]. The MSLD discrepancy at 2 K and 6 K in 0.1 T exceeds that in 3 T; a similar trend is observed at 2 K and 8 K for both fields. The highest MSLD occurs at 2 K in 3 T, while the lowest is at 300 K in 3 T. At 2 K in 3 T, the maximum MSLD recorded is approximately 27 % lower than the theoretical MSLD of EuS, which is 3.48×10^{-6} Å^{-2}. Moreover, a MSLD difference of around 0.17×10^{-6} Å^{-2} between the values at 2 K in 0.1 T and 3 T is observed.

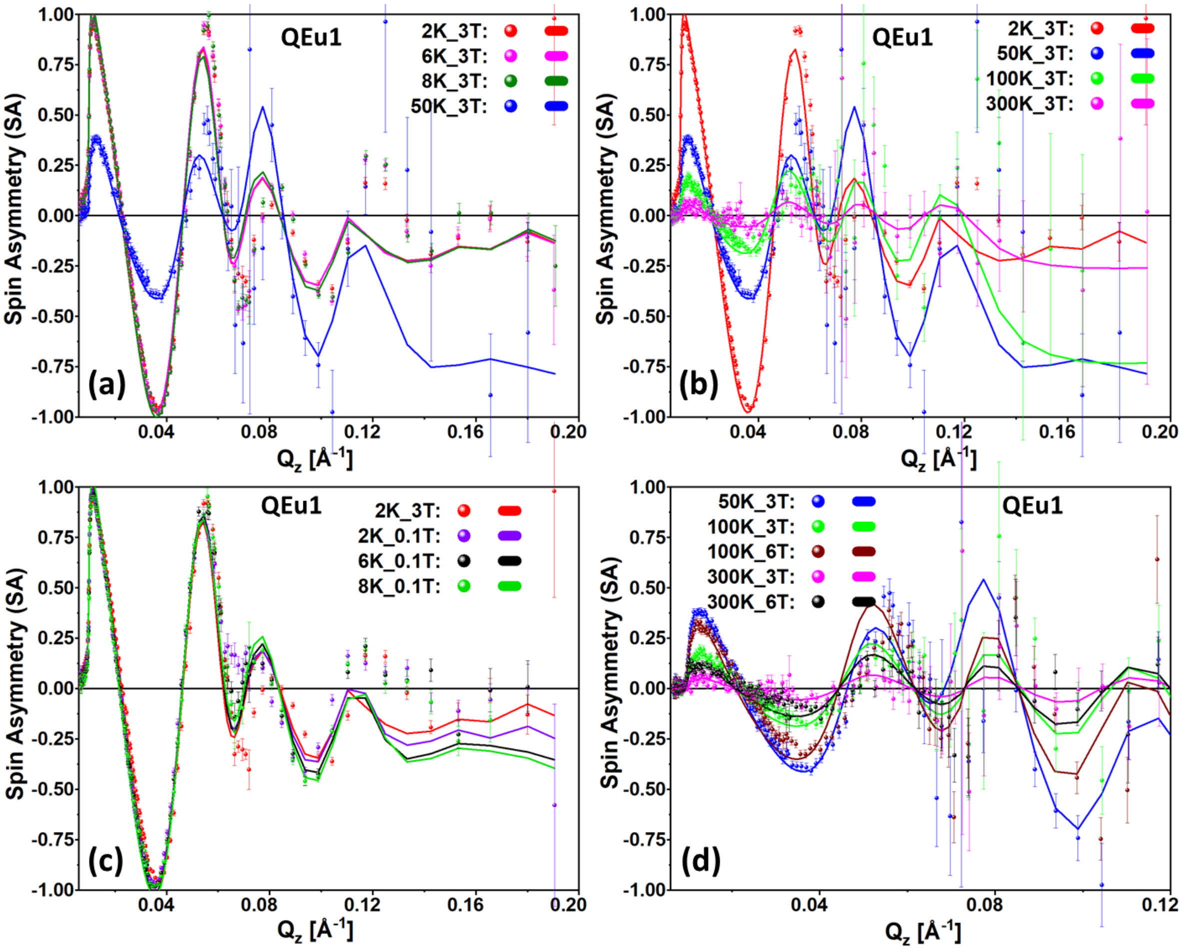

Figure 6.16: Spin asymmetry (SA) as a function of momentum transfer (Q_z) for the sample QEu1 is shown along with the respective fits for the measurements as indicated in the four plots.

A comparison of the MSLD values as a function of temperature under different magnetic fields for the QEu1 sample are shown in Figure 6.17.

Table 6.6: MSLD and magnetic moment per Eu ion (M_{Eu}) as a function of temperature and magnetic field for the sample QEu1. Temp. and $H_{ext,//}$ here stands for temperature and in-plane magnetic field, respectively.

Sample QEu1			
Temp. (K)	**$H_{ext,//}$ (T)**	**MSLD ($\times 10^{-6}$ Å^{-2})**	**M_{Eu} (μ_B/ion)**
2	0.1	2.38 [2.29, 2.43]	4.9 [4.6, 4.9]
6	0.1	2.0 [1.9, 2.2]	4.1 [3.9, 4.3]
8	0.1	1.80 [1.75, 1.90]	3.6 [3.5, 3.8]
2	3	2.55 [2.46, 2.60]	5.1 [4.9, 5.2]
6	3	2.50 [2.42, 2.57]	5.0 [4.9, 5.2]
8	3	2.4 [2.3, 2.5]	4.8 [4.6, 5.0]
50	3	0.44 [0.42, 0.50]	0.9 [0.8, 1.0]
100	3	0.18 [0.12, 0.22]	0.4 [0.2, 0.4]
100	6	0.35 [0.30, 0.43]	0.7 [0.6, 0.9]
300	3	0.06 [0.03, 0.09]	0.11 [0.05, 0.17]
300	6	0.12 [0.09, 0.16]	0.25 [0.18, 0.33]

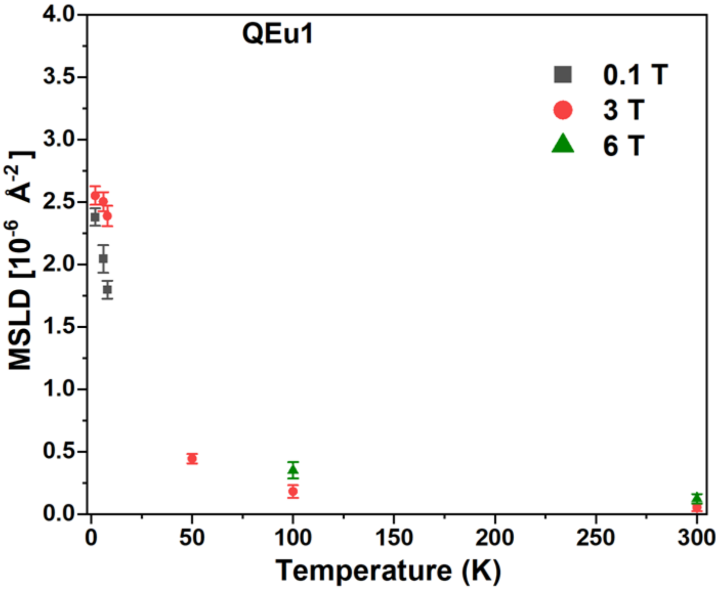

Figure 6.17: MSLD as a function of temperature for the sample QEu1 in the presence of 0.1 T, 3 T, and 6 T. The dotted lines serve as a guide to the eye.

Figure 6.18 (a) shows the comparison between the XRR data fitted with and without taking structural parameters, such as thickness and roughness, from the PNR fits. Figure 6.18 (b) shows the XSLD profiles for both XRR fits. The estimated values of thickness and XSLD are compared in Tables 6.7 and 6.8.

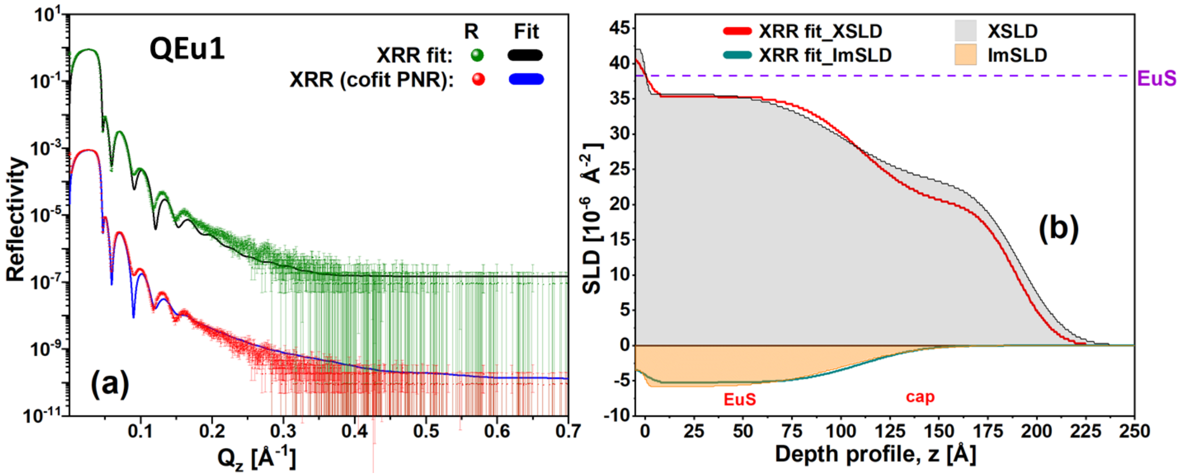

Figure 6.18: (a) Fitted XRR data and cofitted XRR data with structural parameters from PNR fits for the QEu1 sample (b) A comparison of the XSLD profile for the fits. The reference XSLD for EuS (violet) are marked on the plots.

Table 6.7: A comparison of the estimated values of thickness from the two XRR fits for the sample QEu1.

Sample QEu1		
	Thickness (Å)	
Layer	**XRR (cofit PNR)**	**XRR fit**
Cap	90.2 [89.0, 90.9]	79.3 [79.2, 79.6]
EuS	101.6 [100.9, 102.9]	110.3 [109.4, 110.4]

A difference in the thicknesses of the layers is observed for the PNR and XRR fits. However, the difference is less than 1 % in the thickness of the entire stack of layers. Moreover, the XSLD fitted values for the EuS layer from both fits are close to each other and around 7 % less than the reference XSLD value for EuS (38.28×10^{-6} Å^{-2}).

Table 6.8: A comparison of the estimated values of XSLD from the two XRR fits for the sample QEu1.

Sample QEu1		
	XSLD ($\times 10^{-6}$ Å^{-2})	
Layer	**XRR (cofit PNR)**	**XRR fit**
Cap	22.8 [22.8, 23.0]	20.0 [19.9, 20.1]
EuS	35.74 [35.71, 35.74]	35.32 [35.27, 35.33]

Sample QEu2

Table 6.9 list the PNR measurements performed on the QEu2 sample. A total of eight PNR measurements were performed. Figure 6.19 shows the fitted PNR data for the QEu2 sample. The simulated reflectivity of the selected model aligns well with the experimental data. PNR data for 100 K (in 3 T), 100 K (in 6 T), and 300 K (in 6 T) were recorded only for one incident angle of the neutron beam. To analyze the data for this sample, a simple model approach (Section 4.1.5) was adopted similar to that of the QEu1 sample.

Table 6.9: PNR measurements for the sample QEu2.

PNR measurements: QEu2 sample	
Temperature (K)	**$H_{ext,//}$ (T)**
2	0.1
6	0.1
8	0.1
2	3
50	3
100	3
100	6
300	6

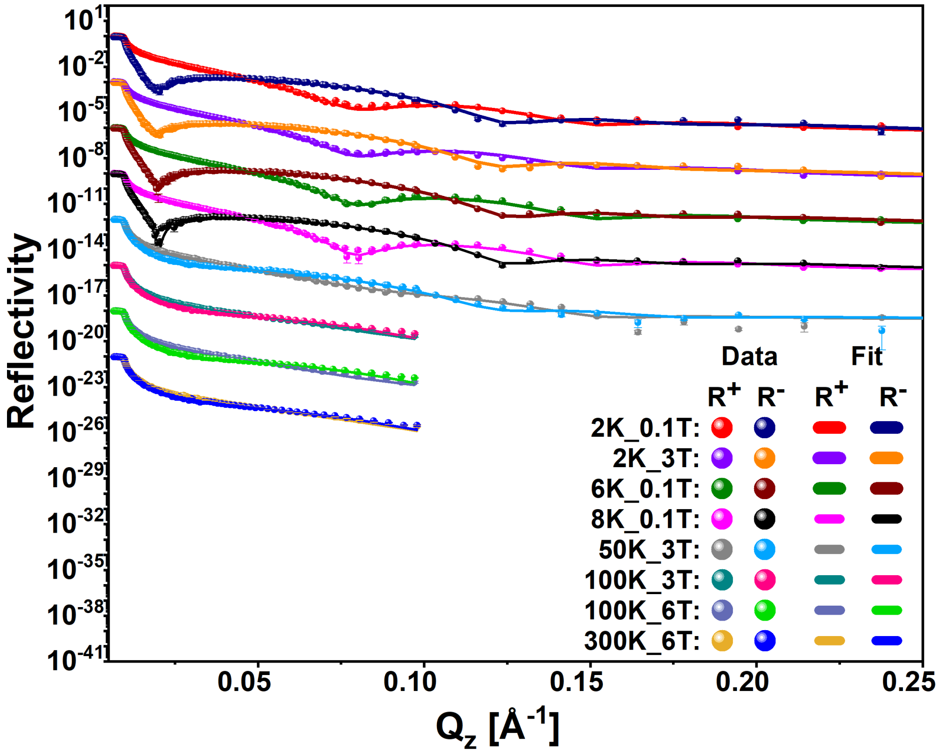

Figure 6.19: Specular polarized neutron reflectometry (PNR) data (dots) for spin-up (R^+) and spin-down (R^-) configuration with fits (line) for the sample QEu2 are shown for the measurements as indicated in the plot. The curves are offset by 10^3 along y-axis for visibility.

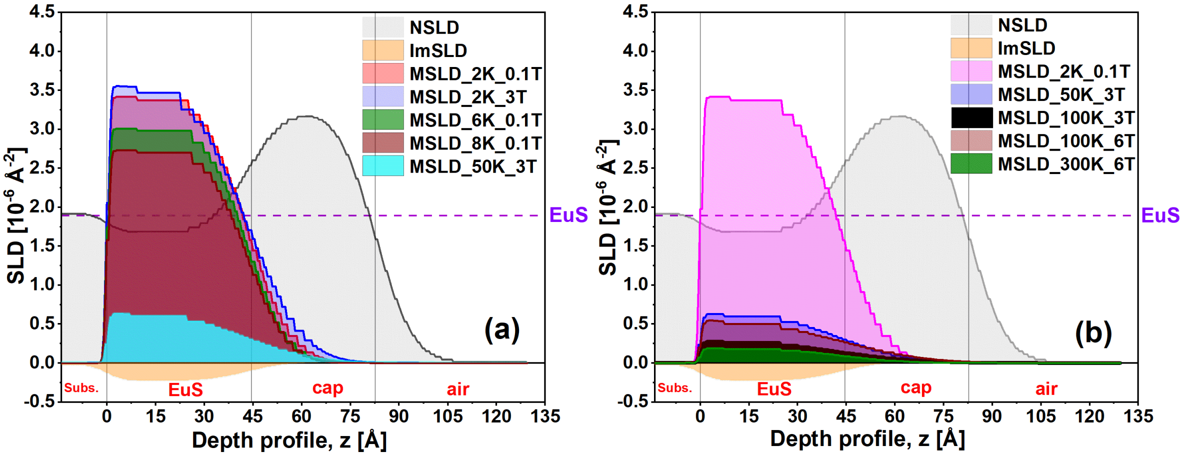

Figure 6.20: NSLD and MSLD versus depth profiles of the sample QEu2. The absorption scattering length density (ImSLD) is shown with orange color in both plots. The reference NSLD for EuS (violet) are marked on the plots.

The NSLD and MSLD profiles versus depth obtained from the model fits are shown in Figure 6.20. The NSLD profile for the sample indicates the uniformity in the NSLD throughout the EuS layer. The estimated values of the thickness and NSLD are listed in Table 6.10. The NSLD of the EuS layer is around 11 % lower than the theoretically calculated value for EuS, which is 1.90×10^{-6} Å^{-2}. Similarly to the QEu1 sample, the MSLD for the PNR measurements recorded above T_C is non-zero in the EuS layer. The estimated values of the MSLD in the EuS layer are listed in Table 6.11.

Table 6.10: A list of the parameters and their estimated values from the fit to the PNR data for the sample QEu2.

Sample QEu2		
Layer	**Thickness**	**NSLD**
	(Å)	**($\times10^{-6}$ Å^{-2})**
Cap	38.2 [37.1, 38.6]	3.20 [3.18, 3.26]
EuS	44.6 [44.2, 45.4]	1.68 [1.67, 1.69]

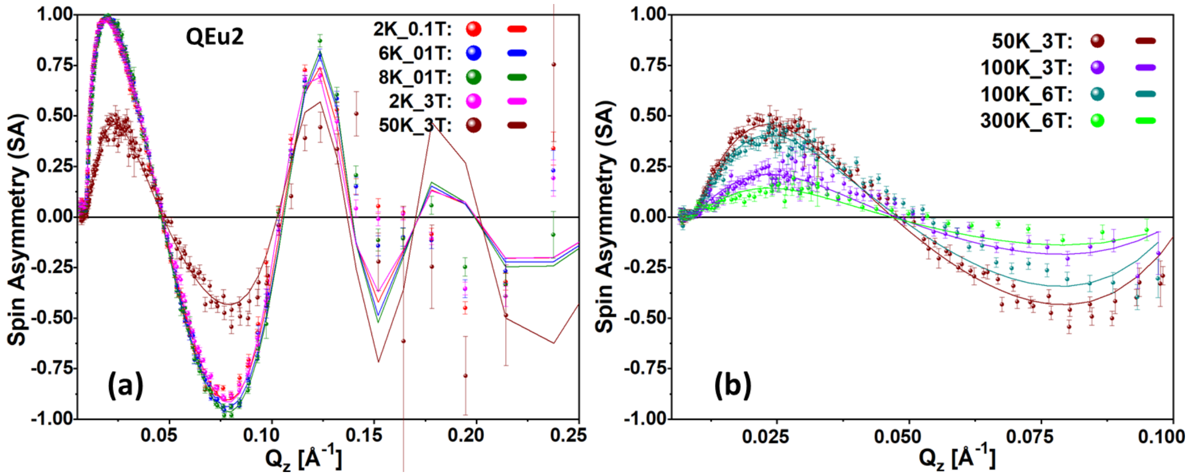

Figure 6.21: Spin asymmetry (SA) as a function of momentum transfer (Q_z) for the sample QEu2 is shown along with the respective fits for the measurements as indicated in the two plots. The SA curve for 50 K (in 3 T) is shown in both graphs to compare data from low and high temperatures.

Figure 6.21 shows the SA as a function of Q_z for the sample QEu2, with fit for the measurements. Similarly to the QEu1 sample, the SA signal remains non-zero well above T_C of EuS in the sample, extending to temperatures as high as 300 K. Furthermore, a trend similar to that observed in the QEu1 sample is observed for the measurements in 3 T and 6 T for the same temperature.

Table 6.11 presents the values for MSLD and the net magnetic moment per Eu ion for the QEu2 sample at various temperatures and magnetic fields. Similarly to the QEu1 sample (Table 6.6), the MSLD value nearly doubles with a magnetic field shift from 3 T to 6 T, as noted at 100 K. Similarly to the QEu1 sample, the highest MSLD value is observed at 2 K in 3 T. The highest MSLD observed at 2 K (in 3 T) is approximately 2 % less than the theoretical value of MSLD for EuS. Moreover, a MSLD difference of around 0.1×10^{-6} Å^{-2} between the values at 2 K in 0.1 T and 3 T is observed.

Table 6.11: Magnetic scattering length density (MSLD) and magnetic moment per Eu ion (M_{Eu}) as a function of temperature and magnetic field for the sample QEu2. Temp. and $H_{ext,//}$ here stands for temperature and in-plane magnetic field, respectively.

Sample QEu2			
Temp. (K)	**$H_{ext,//}$ (T)**	**MSLD ($\times10^{-6}$ Å^{-2})**	**M_{Eu} (μ_B/ion)**
2	0.1	3.32 [3.23, 3.35]	6.7 [6.5, 6.8]
6	0.1	2.94 [2.91, 2.98]	5.92 [5.85, 5.99]
8	0.1	2.68 [2.63, 2.72]	5.4 [5.3, 5.5]
2	3	3.42 [3.34, 3.43]	6.9 [6.7, 6.9]
50	3	0.63 [0.59, 0.67]	1.26 [1.20, 1.34]
100	3	0.28 [0.26, 0.33]	0.6 [0.5, 0.7]
100	6	0.56 [0.52, 0.62]	1.1 [1.1, 1.3]
300	6	0.19 [0.11, 0.22]	0.4 [0.2, 0.5]

The graphs of MSLD versus temperature under different magnetic fields are shown in Figure 6.22. Similarly to the QEu1 sample, PNR measurements conducted at 50 K, 100 K, and 300 K under magnetic fields of 3 T and 6 T indicate that magnetism persists in the sample.

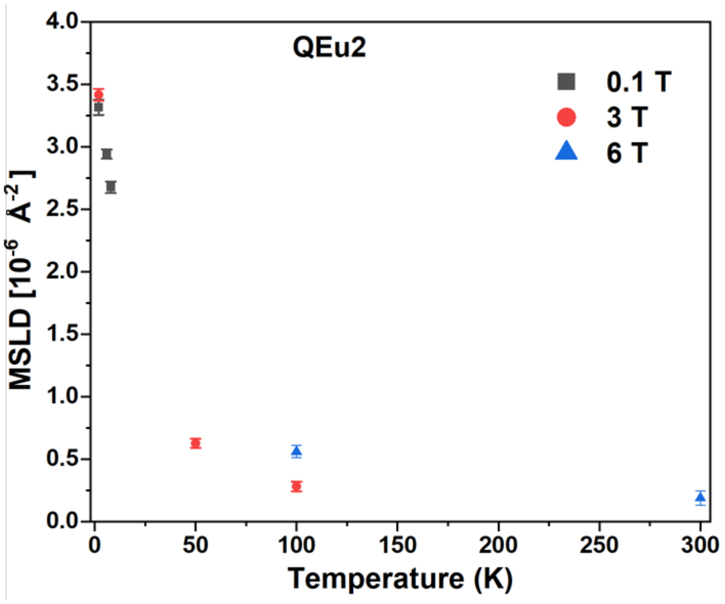

Figure 6.22: (a) MSLD as a function of temperature for the sample QEu2 in the presence of 0.1 T, 3 T, and 6 T. The dotted lines serve as a guide to the eye.

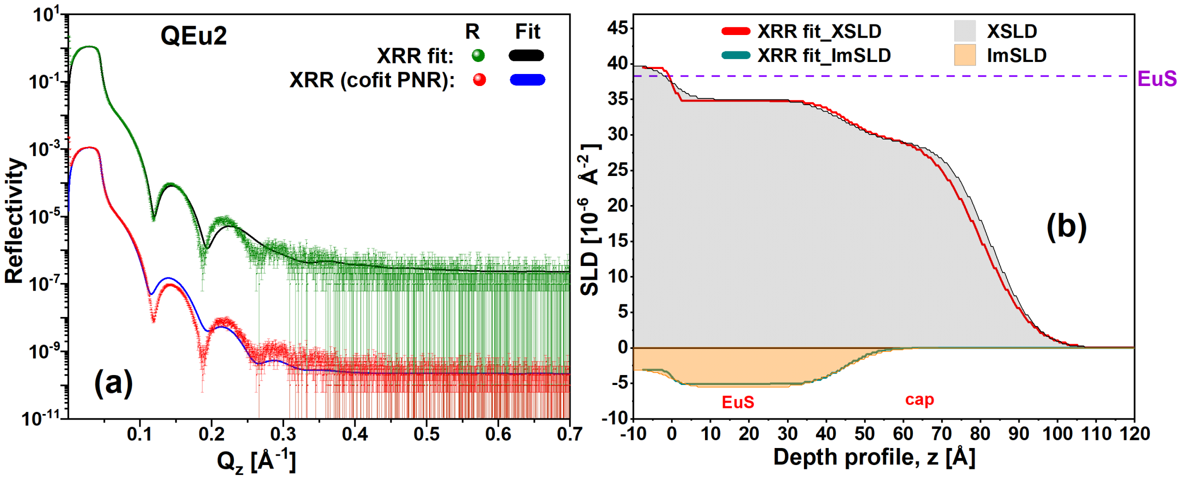

Figure 6.23: (a) Fitted XRR data and cofitted XRR data with structural parameters from PNR fits for the QEu2 sample (b) A comparison of the XSLD profile for the fits. The reference XSLD for EuS (violet) are marked on the plots.

Figure 6.23 (a) presents the comparison of XRR data, fitted with or without including structural parameters such as thickness and roughness of the PNR fits. Figure 6.23 (b) illustrates the corresponding XSLD profiles. Similar to the NSLD profile for the EuS layer, the XSLD profiles remain constant within the EuS region, suggesting a uniform electron density. The estimated thickness and XSLD values are listed in Tables 6.12 and 6.13.

Table 6.12: A comparison of the estimated values of thickness from the two XRR fits for the sample QEu2.

Sample QEu2		
	Thickness (Å)	
Layer	**XRR (cofit PNR)**	**XRR fit**
Cap	38.2 [37.1, 38.6]	35.3 [34.6, 35.5]
EuS	44.6 [44.2, 45.4]	45.2 [44.6, 46.5]

Table 6.13: A comparison of the estimated values of XSLD from the two XRR fits for the sample QEu2.

Sample QEu2		
	XSLD ($\times 10^{-6}$ Å^{-2})	
Layer	**XRR (cofit PNR)**	**XRR fit**
Cap	29.0 [28.8, 29.2]	29.6 [29.4, 29.8]
EuS	35.0 [34.9, 35.1]	34.8 [34.8, 35.0]

Analogous to QEu1, a variation in layer thickness is noted between the PNR and XRR fits, but it differs by about 3% for the total stack thickness. Furthermore, the XSLD fitted values for the EuS layer are similar in both fits, approximately 9% lower than the reference XSLD value for EuS (38.28×10^{-6} Å^{-2}).

Sample QEu3

Table 6.14 list the PNR measurements performed on the QEu3 sample. A total of four PNR measurements were performed. Figure 6.24 (a) presents the fitted results for the PNR data. PNR data for 50 K (in 3 T) and 100 K (in 3 T) were recorded only for the first incident angle of the neutron beam. To analyze the data for this sample, a simple model approach (Section 4.1.5) was adopted similar to that of the QEu1 and QEu2 samples.

The NSLD and MSLD profiles versus depth obtained from the model fits are shown in Figure 6.24 (b). The NSLD profile for the EuS layer shows gradients on both sides.

The estimated values of the thickness and NSLD are listed in Table 6.15. Moreover, similar to the QEu1 and QEu2 samples, the MSLD for the PNR measurements recorded above T_C is non-zero in the EuS layer. The estimated values of the MSLD in the EuS layer are listed in Table 6.16.

Table 6.14: PNR measurements for the sample QEu3.

PNR measurements: the QEu3 sample	
Temperature (K)	**$H_{ext,//}$ (T)**
2	0.1
2	3
50	3
100	3

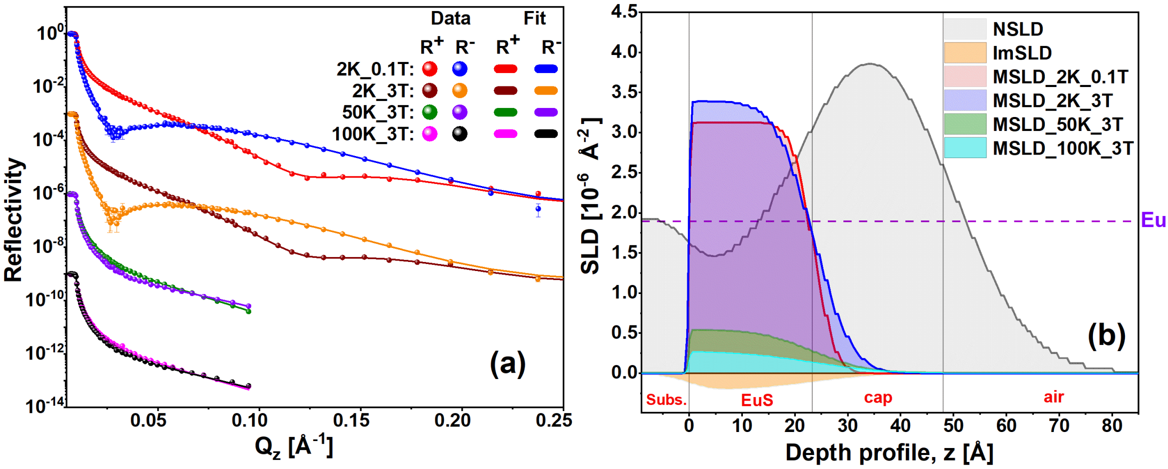

Figure 6.24: Fitted polarized neutron (PNR) data for the sample QEu3 recorded at 2 K (in 0.1 T), 2 K (in 3 T), 50 K (in 3 T), and 100 K (in 3 T). The datasets are shifted by 10^3 units along the y-axis to enhance clarity. R^+ and R^- stand for spin up and spin down reflectivity, respectively. (b) NSLD and MSLD profiles with depth. The reference NSLD for EuS (violet) are marked on the plots.

Similarly to the QEu1 and QEu2 samples, the NSLD of the EuS layer is around 22 % lower than the theoretically calculated value for EuS (1.90×10^{-6} Å^{-2}). The value of NSLD for the EuS layer in the QEu3 sample is read from the dip of the NSLD profile.

A comparison of the SA signal as a function of Q_z for the QEu3 sample is shown in

Table 6.15: A list of the parameters and their estimated values from the fit to PNR data for the sample QEu3.

Sample QEu3		
Layer	**Thickness**	**NSLD**
	(Å)	**($\times 10^{-6}$ Å^{-2})**
Cap	24.4 [24.2, 25.1]	3.8 [3.7, 3.9]
EuS	23.5 [23.1, 23.5]	1.47 [1.41, 1.54]

Figure 6.25. Similarly to the QEu1 and QEu2 sample, the SA signal at 50 K and 100 K (above T$_C$), in the presence of 3 T are non-zero.

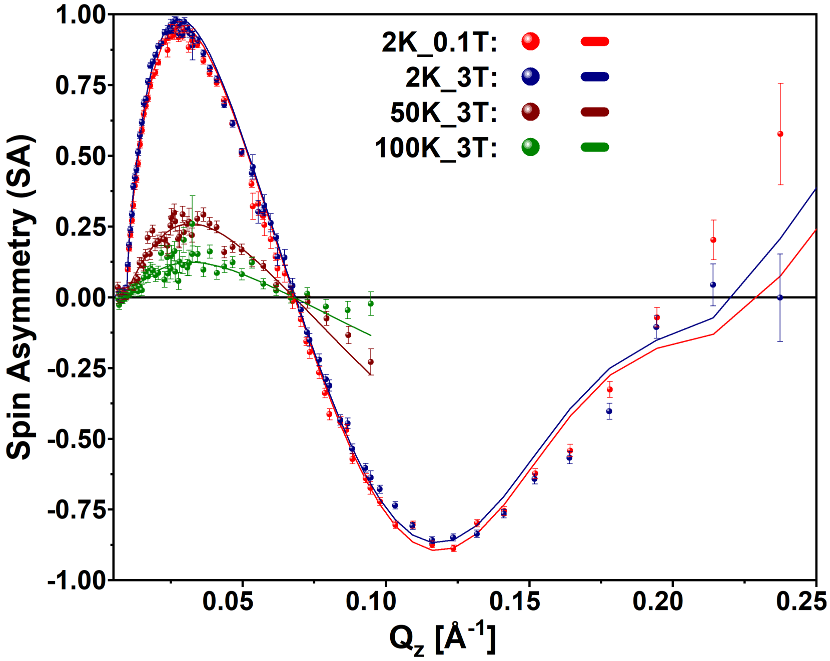

Figure 6.25: Spin asymmetry (SA) plotted as a function of momentum transfer (Q_z) for the sample QEu3 for the measurements as indicated in the plot.

Table 6.16 shows the MSLD values and the net magnetic moment per Eu ion for the QEu3 sample. Similarly to the QEu1 and QEu2 samples, the peak MSLD is observed at 2 K in 3 T. This maximum MSLD at 2 K (in 3 T) is about 3% lower than the theoretical value of MSLD for EuS. Furthermore, there is an MSLD discrepancy of approximately 0.29×10^{-6} Å^{-2} between the values at 2 K in 0.1 T and 3 T, which is greater than for the QEu1 and QEu2 samples. Similarly to the QEu1 and QEu2 samples, non-zero MSLD at 50 K and 100 K in 3 T indicate that magnetism persists in the sample. The graphs of MSLD versus temperature under different magnetic fields are shown in Figure 6.26

Table 6.16: MSLD and M_{Eu} as a function of temperature and magnetic field for the sample QEu3.

Sample QEu3			
Temp. (K)	**$H_{ext,//}$ (T)**	**MSLD ($\times10^{-6}$ Å^{-2})**	**M_{Eu} (μ_B/ion)**
2	0.1	3.08 [3.06, 3.16]	6.2 [6.2, 6.3]
2	3	3.37 [3.33, 3.40]	6.77 [6.69, 6.82]
50	3	0.53 [0.51, 0.56]	1.08 [1.02, 1.13]
100	3	0.27 [0.25, 0.30]	0.54 [0.50, 0.60]

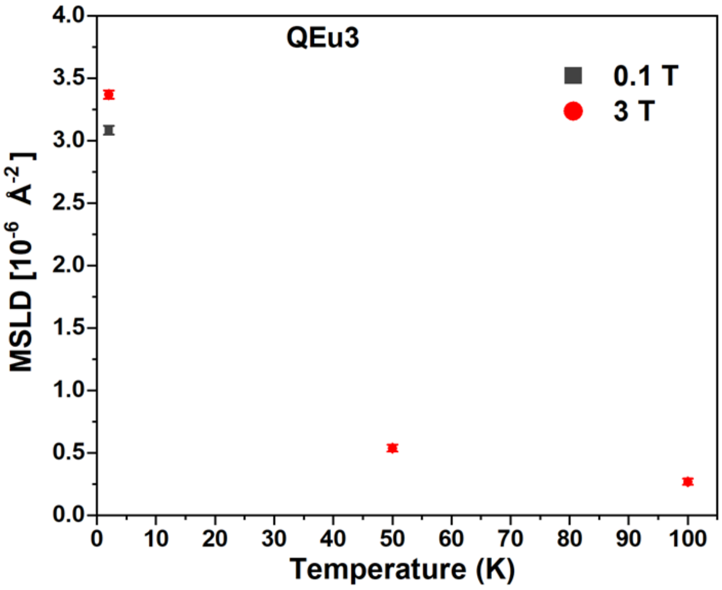

Figure 6.26: MSLD as a function of temperature for the sample QEu3 in the presence of 0.1 T and 3 T. The dotted lines serve as a guide to the eye.

Figure 6.27 shows the comparison between the fitted XRR data and XSLD profiles for the sample QEu3. The estimated values of thickness and XSLD are compared in Tables 6.17 and 6.18.

As with the QEu1 and QEu2 samples, the PNR and XRR fits exhibit a disparity in layer thicknesses. This variation amounts to approximately 10% for the total layer stack. Furthermore, the XSLD fitted values for the EuS layer from both fits are close, being roughly 5% below the reference XSLD value for EuS (38.28×10^{-6} Å^{-2}).

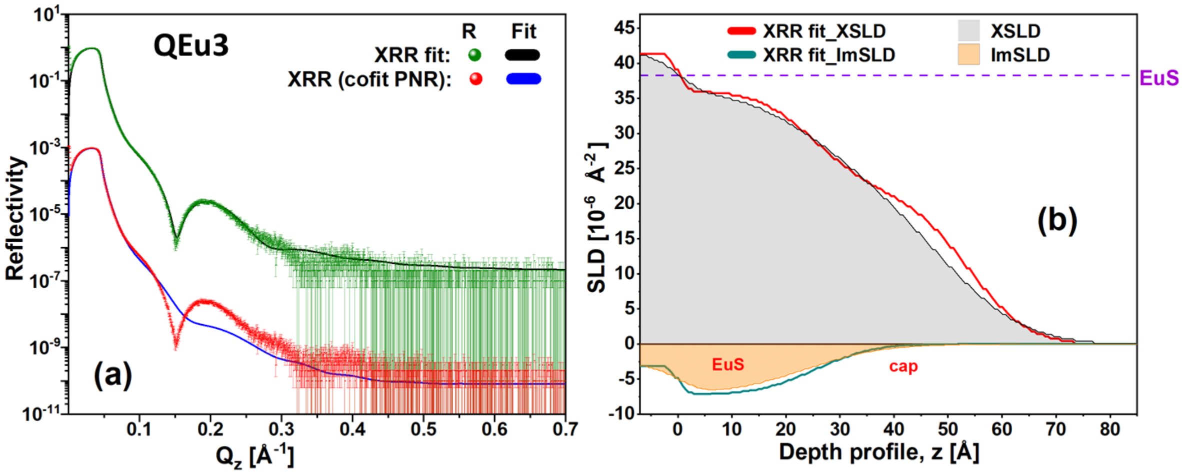

Figure 6.27: (a) Fitted XRR data and cofitted XRR data with structural parameters from PNR fits for the QEu3 sample. (b) A comparison of the XSLD profiles.

Table 6.17: A comparison of the estimated values of thickness from the two XRR fits for the sample QEu3.

Sample QEu3		
	Thickness (Å)	
Layer	**XRR (cofit PNR)**	**XRR fit**
Cap	24.4 [24.2, 25.1]	28.2 [27.9, 28.5]
EuS	23.5 [23.1, 23.5]	25.5 [25.0, 26.2]

Table 6.18: A comparison of the estimated values of XSLD from the two XRR fits for the sample QEu3.

Sample QEu3		
	XSLD ($\times10^{-6}$ Å^{-2})	
Layer	**XRR (cofit PNR)**	**XRR fit**
Cap	25.3 [25.0, 25.8]	21.6 [21.1, 22.4]
EuS	36.1 [35.8, 36.1]	36.1 [35.9, 36.3]

Sample QEu4

Table 6.19 list the PNR measurements performed on the QEu4 sample. A total of six PNR measurements were performed. Figure 6.28 presents the fitted results for the PNR data. PNR data for 50 K (in 3 T), 100 K (in 3 T), 100 K (in 6 T), and 300 K (in 6 T) were recorded only for the first incident angle of the neutron beam. During the reflectivity data analysis, it was found that adjusting the roughness profile of the layers alone could not fully account for the reflectivity curve features for this sample. Therefore, the interface between the EuS and the capping layer was structurally modified by taking a part of the capping layer and allowing the NSLD to vary independently. A detailed description of the method is provided in the chapter on data analysis (Section 4.1.5).

Table 6.19: PNR measurements for the sample QEu4.

PNR measurements: the QEu4 sample	
Temperature (K)	**$H_{ext,//}$ (T)**
2	0.1
2	3
50	3
100	3
100	6
300	6

The NSLD and MSLD versus depth profiles for the QEu4 sample are shown in Figure 6.29. The NSLD profile for the EuS layer shows gradients on both sides. The estimated values of the thickness and NSLD are listed in Table 6.20. Similarly to the other samples, the NSLD of the EuS layer is lower (around 12 %) than the reference value for EuS (1.90×10^{-6} Å^{-2}).

Similarly to the samples studied previously, the MSLD for the PNR measurements recorded above T_C is non-zero in the EuS layer. The estimated values of the MSLD in the EuS layer are listed in Table 6.21.

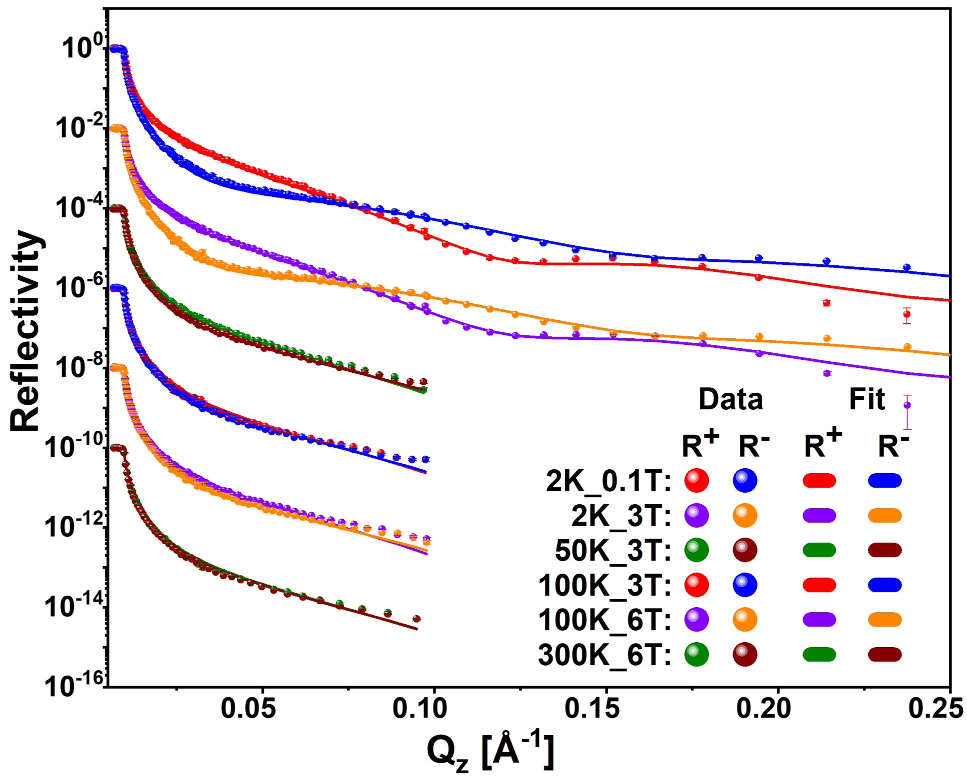

Figure 6.28: Fitted PNR data for the sample QEu4 recorded for the measurements as indicated in the plot. The datasets are shifted by 10^2 units along the y-axis to enhance clarity.

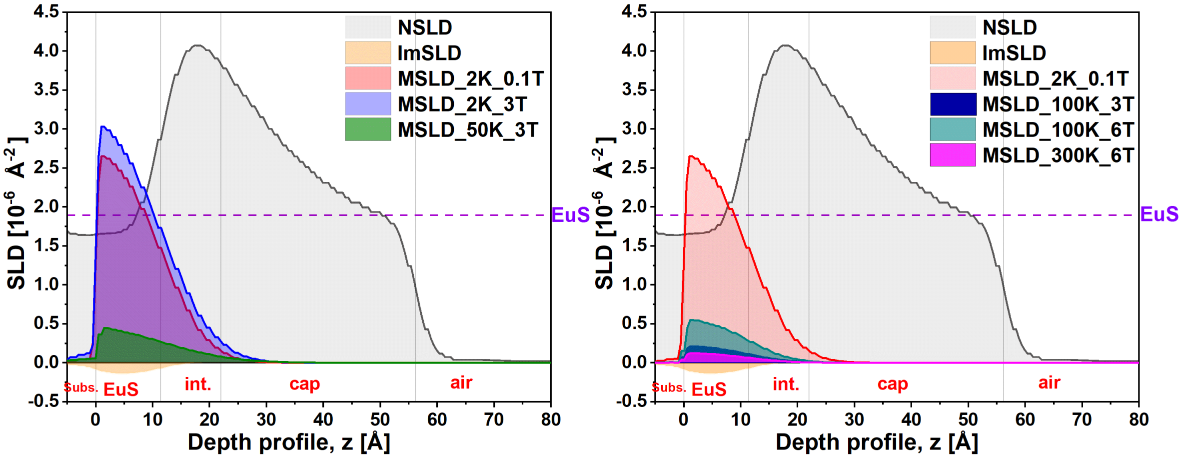

Figure 6.29: NSLD and MSLD profiles with depth for the sample QEu4 for measurements as indicated in the plots.

Table 6.20: A list of the parameters and their estimated values from the fit to PNR data for the sample QEu4.

Sample QEu4		
Layer	**Thickness**	**NSLD**
	(Å)	**($\times 10^{-6}$ Å^{-2})**
Cap	34.3 [33.7, 34.4]	2.0 [1.9, 2.1]
Interface layer	10.5 [10.1, 11.6]	4.1 [4.0, 4.2]
EuS	11.4 [10.7, 11.7]	1.7 [1.3, 1.8]

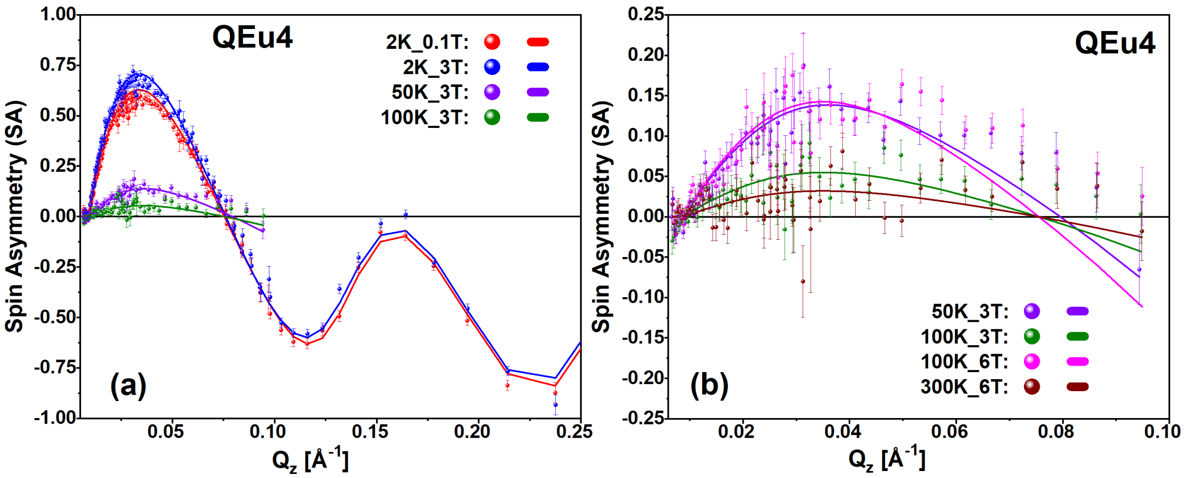

Figure 6.30: Spin asymmetry (SA) as a function of momentum transfer (Q_z) for the sample QEu4 is shown along with the respective fits for the measurements as indicated in the plots. Note that in graph (b), the y-axis scale is adjusted differently to improve the visibility of the variations observed in the SA curves.

Figure 6.30 shows the SA as a function of Q_z for the sample QEu4, with fit for measurements. A weaker SA signal is observed for this sample compared to other samples that were studied for this investigation. Similarly to the other samples, the SA signal remains non-zero well above T_C of EuS in the sample, extending to temperatures as high as 300 K. Furthermore, a trend similar to that observed in the QEu1 and QEu2 samples is observed for the measurements in 3 T and 6 T for the same temperature. The SA signals at temperatures above T_C are small but not negligible, as shown in Figure 6.30 (b). The difference between the SA signal at 2 K in 0.1 T and 3 T is higher compared to other samples.

Table 6.21 presents the MSLD and the net magnetic moment per Eu ion for the QEu4 sample at different temperatures and magnetic fields. The peak MSLD occurs at 2 K in 3 T, around 13% lower than the reference value for EuS (i.e. 3.48×10^{-6} Å^{-2}). Furthermore, the MSLD difference of approximately 0.38×10^{-6} Å^{-2} between 2 K in 0.1 T and 3 T is the largest among the samples analyzed.

Table 6.21: Magnetic scattering length density (MSLD) and net magnetic moment per Eu ion (M_{Eu}) as a function of temperature and magnetic field for the sample QEu4. Temp. and $H_{ext,//}$ here stands for temperature and in-plane magnetic field, respectively.

Sample QEu4			
Temp. (K)	**$H_{ext,//}$ (T)**	**MSLD ($\times10^{-6}$ Å^{-2})**	**M_{Eu} (μ_B/ion)**
2	0.1	2.7 [2.6, 2.9]	5.4 [5.2, 5.7]
2	3	3.0 [2.9, 3.3]	6.1 [5.9, 6.5]
50	3	0.5 [0.4, 0.6]	0.9 [0.8, 1.1]
100	3	0.2 [0.1, 0.3]	0.4 [0.2, 0.6]
100	6	0.6 [0.5, 0.7]	1.1 [1.0, 1.3]
300	6	0.1 [0.0, 0.3]	0.3 [0.1, 0.5]

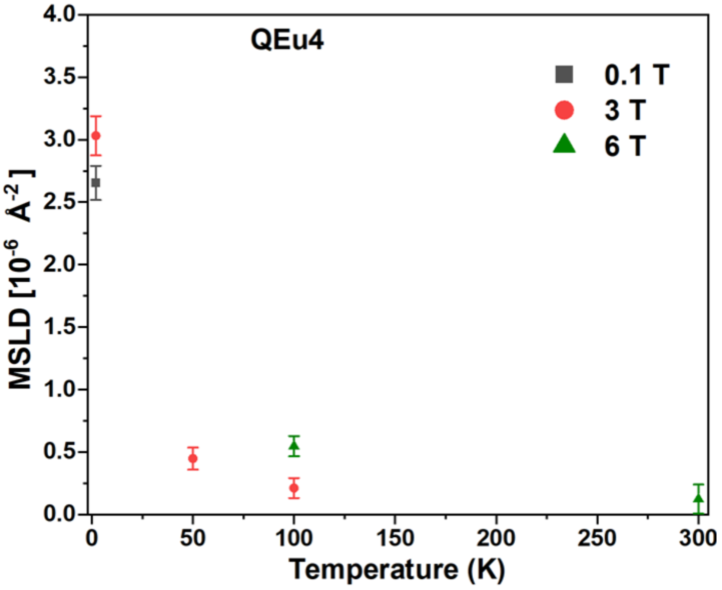

Figure 6.31: MSLD as a function of temperature for the sample QEu4 in the presence of 0.1 T, 3 T and 6 T. The dotted lines serve as a guide to the eye.

The graphs of MSLD versus temperature under different magnetic fields are shown in Figure 6.31. Similarly to the other studied samples, PNR measurements conducted at 50 K, 100 K, and 300 K under magnetic fields of 3 T and 6 T indicate that magnetism persists in the sample.

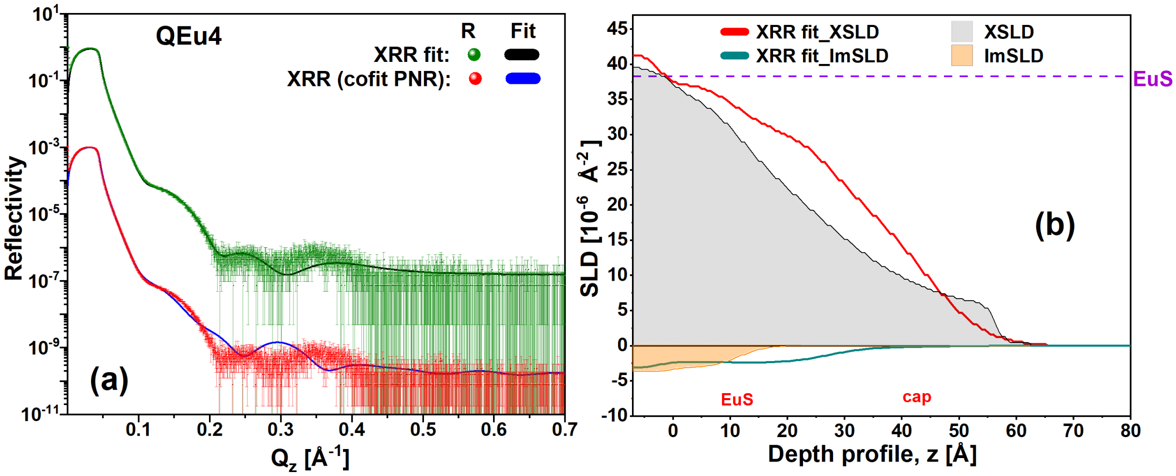

Figure 6.32: (a) Fitted XRR data and cofitted XRR data with structural parameters from PNR fits for the QEu4 sample. (b) A comparison of the XSLD profile for the fits. The reference XSLD for EuS (violet) are marked on the plots.

Figure 6.32 (a) illustrates the comparison between the XRR data fitted with and without incorporating structural parameters, such as thickness and roughness, derived from PNR fits. Tables 6.22 and 6.23 provide the estimated thickness and XSLD values.

Table 6.22: A comparison of the estimated values of thickness from the two XRR fits for the sample QEu4.

Sample QEu4		
	Thickness (Å)	
Layer	**XRR (cofit PNR)**	**XRR fit**
Cap	34.3 [33.7, 34.4]	16.6 [16.2, 17.1]
Interface layer	10.5 [10.1, 11.6]	16.0 [13.4, 16.6]
EuS	11.4 [10.7, 11.7]	13.5 [12.2, 13.5]

As with the samples studied previously, the PNR and XRR fits exhibit a disparity

Table 6.23: A comparison of the estimated values of XSLD from the two XRR fits for the sample QEu4.

Sample QEu4		
	XSLD ($\times 10^{-6}$ Å^{-2})	
Layer	**XRR (cofit PNR)**	**XRR fit**
Cap	5.1 [4.9, 5.3]	21.2 [20.8, 24.0]
Interface layer	36.7 [36.6, 37.7]	30.7 [28.9, 31.2]
EuS	39.8 [39.7, 40.3]	37.2 [36.1, 37.8]

in layer thicknesses. This variation amounts to approximately 22% for the total layer stack.

Figure 6.33 compares the observed MSLD values for the samples as a function of temperature in presence of 3 T. For temperatures below T$_C$, the MSLD values follow a descending order: QEu2, QEu3, QEu4, and QEu1.

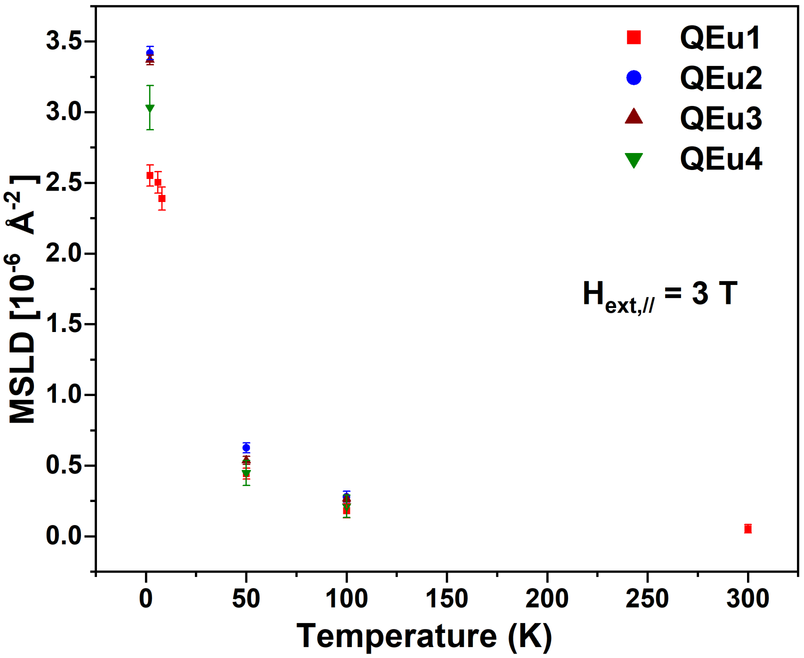

Figure 6.33: Comparison of the MSLD signal as function of temperature for the measurements below and above T$_C$ in the presence of 3 T.

6.5 General discussion

The NSLD and XSLD of the EuS layer is consistently found to be lower than the reference values. This could arise from stoichiometric deviations, strain effects, oxidation, layer inhomogeneity, etc. Since the lattice mismatch between InAs and EuS is less than 1 %, the strain effects are not likely to be the reason. The oxidation of EuS could lead to the formation of compounds listed in Table 2.2 with their NSLD values, but this should lead to an increase in the NSLD value. Moreover, the NSLD is proportional to the scattering units per unit volume (Equation 3.6). Thus, any non-uniform density from vacancies or incomplete layer growth decreases the average atomic density, can result in a reduced NSLD.

There is a noted inconsistency in thickness estimation between the PNR and XRR fits, probably due to the low XSLD contrast between EuS and the capping layer, which complicates the ability of the XRR technique to accurately estimate thickness. However, PNR benefits from both higher NSLD and additional MSLD contrasts between EuS and the capping layer, which improves its precision over XRR. In this thesis a comparable finding was reported in the MPEs study [Chapter 5].

PNR results for all the samples studied show non-zero MSLD values (and SA signal) for temperatures above T_C in the presence of 3 T and 6 T. The magnetic signal is homogeneous throughout the EuS thin film rather than being confined to the interface, as confirmed by the MSLD and NSLD profiles of the samples [Figs. 6.15, 6.20, 6.24, and 6.29]. This observation contradicts the claims of the potential interfacial origin of magnetism in EuS-based heterostructures [31]. Tables 6.24, 6.25, and 6.26 summarize the observed values of the net magnetic moment per Eu ion in the samples as a function of temperature and magnetic field. M_{Eu} above T_C is significant compared to M_{Eu} below T_C for the samples.

There is a small difference in M_{Eu} for 2 K in 0.1 T and 3 T indicating that a higher magnetic field strength is needed to saturate the magnetic moments in the EuS layer. Moreover, M_{Eu} decreases with increase in temperature for the same $H_{ext,//}$, which can be explained by the destruction of magnetic order by thermal fluctuations. Table 6.27 lists the difference in the values for the sample. This difference is plotted for all samples in Figure 6.34. Moreover, the difference is lowest for the QEu2 sample and highest for the QEu4 sample. This indicates that the moments in the QEu2 sample are closer to saturation than other samples in 0.1 T. Additionally, the non-saturation state at higher fields was also observed in the hysteresis loops for QEu1 [Figure 6.9], QEu3 [Figure

Table 6.24: Net magnetic moment per ion (M_{Eu}) as a function of temperature and magnetic field for the samples.

M_{Eu} (μ_B/ion)				
Layer	**2 K (0.1 T)**	**6 K (0.1 T)**	**8 K (0.1 T)**	**2 K (3 T)**
QEu1	4.8 [4.6, 4.9]	4.1 [3.9, 4.3]	3.6 [3.5, 3.8]	5.1 [4.9, 5.2]
QEu2	6.7 [6.5, 6.8]	5.9 [5.9, 6.0]	5.4 [5.3, 5.5]	6.9 [6.7, 6.9]
QEu3	6.2 [6.2, 6.4]	-	-	6.77 [6.69, 6.82]
QEu4	5.4 [5.2, 5.7]	-	-	6.1 [5.9, 6.6]

Table 6.25: Net magnetic moment per ion (M_{Eu}) as a function of temperature and magnetic field for the samples.

M_{Eu} (μ_B/ion)				
Layer	**6 K (3 T)**	**8 K (3 T)**	**50 K (3 T)**	**100 K (3 T)**
QEu1	5.0 [4.9, 5.2]	4.8 [4.6, 4.9]	0.89 [0.84, 0.99]	0.4 [0.2, 0.4]
QEu2	-	-	1.3 [1.2, 1.4]	0.6 [0.5, 0.7]
QEu3	-	-	1.08 [1.02, 1.13]	0.6 [0.5, 0.6]
QEu4	-	-	0.9 [0.8, 1.1]	0.4 [0.2, 0.6]

Table 6.26: Net magnetic moment per ion (M_{Eu}) as a function of temperature and magnetic field for the samples.

M_{Eu} (μ_B/ion)			
Layer	**100 K (6 T)**	**300 K (3 T)**	**300 K (6 T)**
QEu1	0.7 [0.6, 0.9]	0.11 [0.05, 0.17]	0.25 [0.18, 0.33]
QEu2	1.1 [1.1, 1.3]	-	0.4 [0.2, 0.5]
QEu3	-	-	-
QEu4	1.1 [1.0, 1.3]	-	0.3 [0.1, 0.5]

6.11] and QEu4 [Figure 6.12] samples.

Table 6.27: The difference in the net magnetic moment per ion (M_{Eu}) at 2 K in presence of 0.1 T and 3 T for the samples.

δM$_{Eu}$ (μ_B/ion)	
QEu1	0.4 (± 0.2)
QEu2	0.2 (± 0.1)
QEu3	0.6 (± 0.1)
QEu4	0.8 (± 0.4)

In the presence of an external magnetic field, the magnetization (M) can be calculated using the Curie-Brillouin law, as expressed mathematically in equation 6.1. Here, J denotes the total angular momentum, which comprises both spin and orbital components. Here, B_J is the Brillouin function (expressed in equation 6.3), H_{ext} is the external magnetic field, M is the magnetization, k_B is the Boltzmann constant, and g is the Landé factor.

$$\mathrm{M} = \mathrm{N} gJ\mu_B B_J(x) \tag{6.1}$$

$$x = \frac{gJ\mu_B \mathrm{H}_{ext}}{k_B \mathrm{T}} \tag{6.2}$$

$$B_J(x) = \frac{2J+1}{2J}\coth\left(\frac{(2J+1)}{2J}x\right) - \frac{1}{2J}\coth\left(\frac{x}{2J}\right) \tag{6.3}$$

At small x values, B_J can be expanded, leading to a reformulated equation 6.4, known as Curie law. Equation 6.4 relates paramagnetic susceptibility (χ) to both the effective number of Bohr magnetons (μ_{eff}) and temperature. Here, C is the Curie constant.

$$\chi = \frac{C}{\mathrm{T}} = \frac{\mathrm{M}}{\mathrm{H}_{ext}} \tag{6.4}$$

$$C = \frac{\mu_B^2}{3k_B} g^2 J(J+1)\mathrm{N} \tag{6.5}$$

$$\mu_{\text{eff}} = gJ(J+1)^{1/2} \tag{6.6}$$

$$\mathrm{M} \propto \frac{\mu_{\text{eff}} \cdot \mathrm{H}_{ext}}{T} \tag{6.7}$$

Equation 6.7 demonstrates that magnetization is directly proportional to both the magnetic field and μ_{eff}, and inversely proportional to temperature. Consequently, with constant μ_{eff}, magnetization increases with a rise in the magnetic field and decreases as temperature rises. The experimental values of μ_{eff} for the valence states of Eu^{2+} and Eu^{3+} are around 7.9 and 3.4 [153], respectively. This implies that for a constant magnetic field and temperature, the magnetic response of Eu^{2+} ions is higher than that of Eu^{3+} ions.

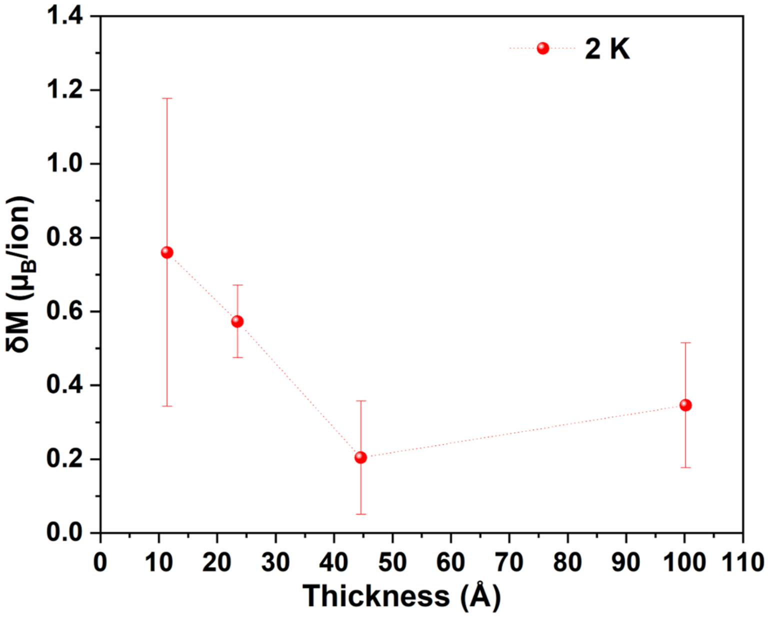

Figure 6.34: A difference in the net magnetic moment per ion (M_{Eu}) at 2 K in 0.1 T and 3 T plotted as a function of thickness of EuS layer for the samples. The dotted lines serve as a guide to the eye.

Figure 6.35 shows the net magnetic moment per Eu ion versus the thickness of the EuS layer at temperatures above T_C of EuS for the samples. Among the samples, QEu2 exhibits the strongest signal across all temperature and magnetic field conditions, followed by QEu3, with QEu1 and QEu4 displaying comparable magnitudes. Therefore, it suggests that M_{Eu} above T_C is not related to the thickness of the EuS layer.

The trend in the magnetic response below T_C from SQUID [Figure 6.4] and PNR measurements (Table 6.24) generally agrees, except for the QEu4 sample, potentially due to a higher relative error in volume estimation for QEu4 sample (Table 6.1). The low magnetic signal observed for the QEu1 sample at all temperatures above and below T_C could be attributed to a mixed valence state of Eu. As discussed earlier, Eu^{3+} ions have a lower magnetic response than Eu^{2+} ions.

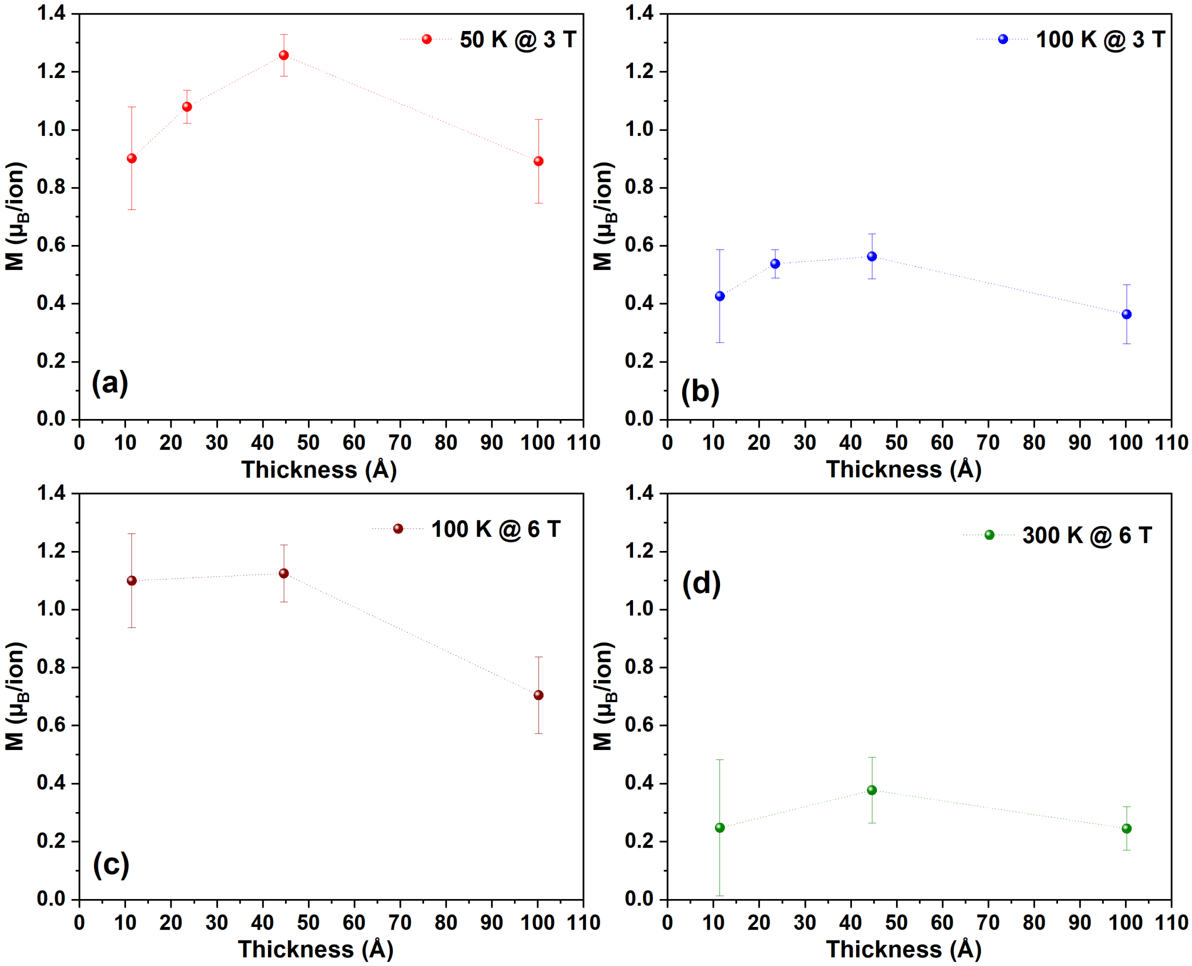

Figure 6.35: Net magnetic moment per ion (M_{Eu}) as a function of thickness of EuS layer for the samples at (a) 50 K (in 3 T) (b) 100 K (in 3 T) (c) 100 K (in 6 T) (d) 300 K (in 6 T). The dotted lines serve as a guide to the eye.

Moreover, it is observed across all samples that the magnetic signal above T_C is directly related to the magnetic field strength, since M_{Eu} (or MSLD) nearly doubles when the magnetic field increases from 3 T to 6 T at both 100 K and 300 K. This behavior can be explained using equation 6.7, which shows that with a constant μ_{eff} and temperature, magnetization is directly proportional to the magnetic field strength ($M \propto H_{ext}$). Furthermore, the non-zero MSLD observed at 50 K in 3 T for the QD3 sample [Figure 5.60] in the present thesis can also be explained by this observation.

Table 6.28 compares the theoretically calculated value of M_{Eu} for the bulk EuS and the observed values for thin EuS films in the samples. In the examined samples, the experimentally measured M_{Eu} for the thin EuS layers consistently exceeds theoretical predictions, with the QEu2 sample showing values approximately 10 times greater. This suggests a variation in the magnetic characteristics of thin EuS films relative to bulk EuS. The underlying causes of this discrepancy are not yet clear. This observation could impact the application of EuS as a spin filter in spintronics, given the assumption that EuS maintains bulk properties at thicknesses greater than 30 Å [124].

Table 6.28: A comparison of the theoretically calculated values for the magnetic moment per unit ion (M_{Eu}) using equation 6.1 and the observed values using PNR as a function of temperature (Temp.) and magnetic field ($H_{ext,//}$) for the samples.

M_{Eu} (μ_B/ion)			
Temp. (in $H_{ext,//}$)	**Theory**	**Experiment**	
50 K (3 T)	0.12	0.9 [0.8, 1.0]	QEu1
		1.26 [1.20, 1.34]	QEu2
		1.08 [1.02, 1.13]	QEu3
		0.9 [0.8, 1.1]	QEu4
100 K (3 T)	0.06	0.4 [0.2, 0.4]	QEu1
		0.6 [0.5, 0.7]	QEu2
		0.54 [0.50, 0.60]	QEu3
		0.4 [0.2, 0.6]	QEu4
300 K (3 T)	0.02	0.11 [0.05, 0.17]	QEu1
100 K (6 T)	0.12	0.7 [0.6, 0.9]	QEu1
		1.1 [1.1, 1.3]	QEu2
		1.1 [1.0, 1.3]	QEu4
300 K (6 T)	0.04	0.25 [0.18, 0.33]	QEu1
		0.4 [0.2, 0.5]	QEu2
		0.3 [0.1, 0.5]	QEu4

Furthermore, the observation of paramagnetic polarization in EuS above T_C may explain some of the features of other systems that seek weak interfacial magnetism in heterostructures at elevated temperatures. The high effective moment (μ_{eff}) of EuS makes these magnetic signals detectable under moderate magnetic fields. Assuming paramagnetic behavior ($M \propto H_{ext}$) and scaling the magnetic moments obtained at 50 K and 300 K (Tables 6.25 and 6.26) under a 3 T field by dividing by 3, the resultant moments align with those reported by Katmis *et al.* [31] for the EuS layer coupled with Bi_2Se_3 in a 1 T field. However, for the EuS/Bi_2Se_3 study, the magnetic signal above T_C was associated with the breaking of the time-reversal symmetry at the interface. In particular, for thin EuS layers, the volume-distributed magnetic moment may be hard to distinguish from interfacially concentrated moments. The enhancement of the moment is particularly pronounced at temperatures close to T_C, e.g. below 50 K. In addition, The literature includes studies on EuS thin films near Co [130] or Ni [146] under strong magnetic fields, noting similar magnetic signals as this thesis. Nonetheless, these studies reach differing conclusions by associating the signal with proximity effects. In the present thesis, the samples only had EuS layers without any topological insulator or ferromagnet in proximity, and yet similar moments are observed.

6.6 Conclusions and summary

SQUID measurements confirmed that the behavior of the ferromagnetism and T_C of the EuS thin films in the samples with thickness, temperature and magnetic field was similar to what was expected by theory. PNR results confirm that magnetism exists above T_C (up to 300 K) in thin EuS films alone in the presence of 3 T and 6 T magnetic fields, with a thickness as low as 11 Å. The MSLD profiles from PNR for the samples confirm that the magnetic signal is homogeneous throughout the film rather than confined to the interface. The strength of the observed magnetic signal above T_C in EuS thin films depends on the applied magnetic field and temperature. The behavior of the observed magnetism above T_C is likely to be paramagnetic.

In summary, an investigation of the behavior and quantification of the magnetic signal below and above T_C of EuS thin films with thicknesses ranging from 15 to 100 Å was conducted. PNR results confirmed that magnetism exists in EuS thin films alone above T_C and that the signal is uniformly present throughout the EuS layer. However, the observation of magnetic signals in the EuS layers alone in the present study may have implications for the fabrication of devices that utilize EuS material and operate at high temperatures (approaching RT) in the presence of high magnetic fields.

Chapter 7

Conclusions and outlook

The findings from the investigations on MPEs and magnetism in EuS thin films alone reveal several promising research directions to tackle identified challenges and explore more avenues.

There remains a pressing need to find effective ways to enhance MPEs at the interfaces in the heterostructures. This could involve optimizing material deposition techniques to fabricate cleaner interfaces that can enhance magnetic interactions at the interfaces [135]. Moreover, a type II superconducting behavior of lead was observed in the samples with non-consistent higher critical field values for the similar thickness of Pb thin films in samples. This issue can be resolved by either investigating the origin of this issue or replacing Pb with other superconducting materials where the superconducting behavior is consistent. Furthermore, another area for improvement is the change of substrate material for the fundamental study purposes to avoid interference with the measurement of the XMCD signal at the Pb edge for MPEs study. XMCD could provide more conclusive results on the presence of MPEs in Pb.

The observation of the magnetic signal above T_C in EuS thin films raises concerns about the suitability of EuS material for device applications, where unwanted signals above T_C could disrupt device functioning. Therefore, further investigation is needed to identify and understand the origin of this magnetic signal. One of the possible ways is to perform XAS measurements (XANES + XMCD) to examine the stoichiometry of EuS thin films and examining the magnetic signal from the valence states present. If the origin is related to the stoichiometry of EuS, then efforts can be made to modify the deposition parameters while growing, which could suppress this. Furthermore, the stoichiometric study of EuS thin films and the relationship of stichometry with deposition parameters can open up new avenues for optimizing the growth and enhancing EuS magnetic properties. However, a parallel study could be conducted to identify ways to amplify this magnetic signal and explore its practical applications, as it is dependent on both field and temperature, making it easier to toggle.

There were indications of aging effects in EuS samples that warrant further investigation, such as XMCD results for the QD1 sample in Chapter 5. Techniques such as XMCD, SQUID magnetometry, PNR, and XRD could be employed to monitor the variation in the magnetic and structural properties of EuS thin films over time. The insights from these measurements can help to assess the long-term reliability and degradation mechanisms of the EuS material. Furthermore, replacing the metastable EuS with a more stable FM that possesses a high magnetic moment per ion could address stability concerns. However, if EuS remains the material of choice for the studies, then it is imperative that the samples/devices must be kept in an inert environment to prevent loss of ferromagnetism in EuS thin films for practical applications. Moreover, it is advisable to maintain a minimum thickness of approximately 20 Å to achieve a high magnetic response.

Chapter 8

Appendix

8.1 Sample QD2 uncertainty and correlation plots

8.1.1 8 K ZFC

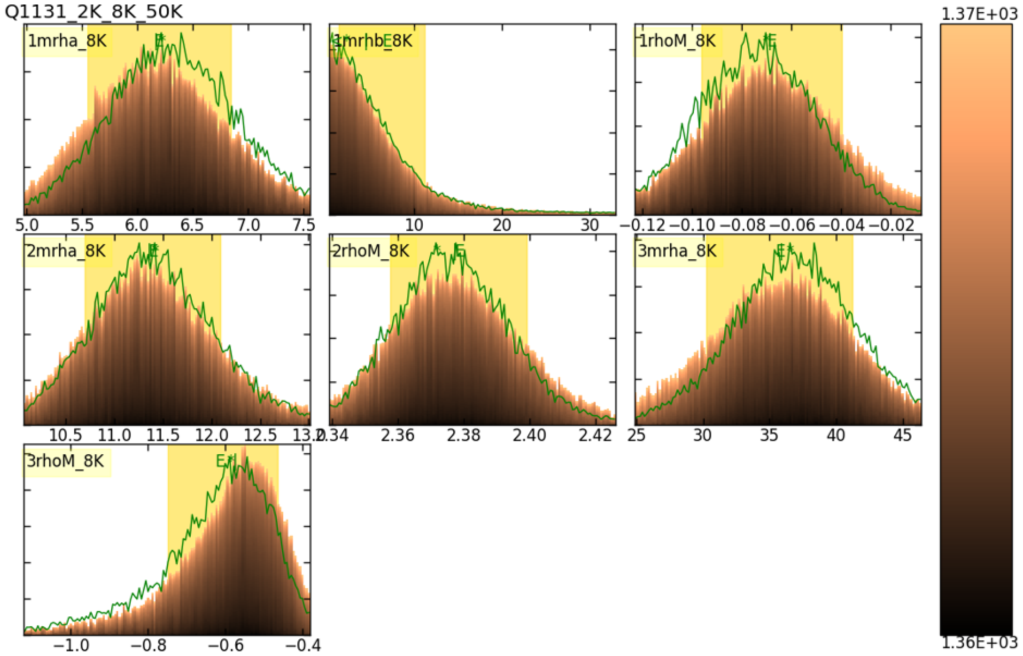

Figure 8.1: A chart of posterior distribution functions of the parameters for sample QD2 (8 K). The parameter's name is written on the top left side of the box that contain the distribution.

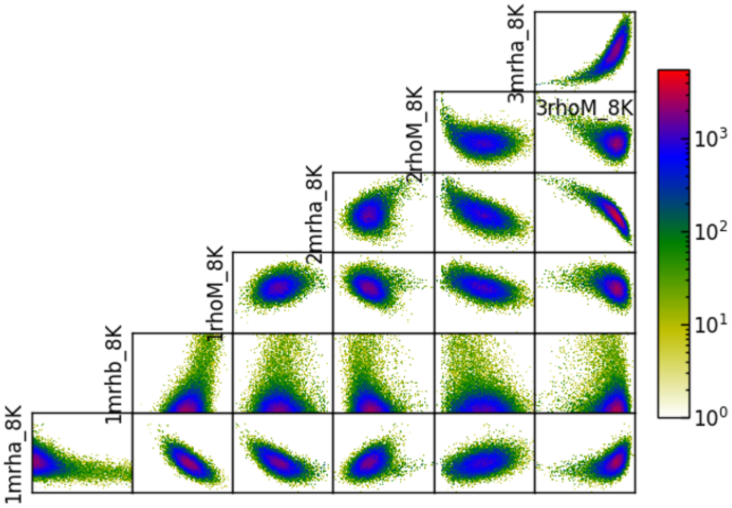

Figure 8.2: A chart of cross-correlations plots between a set of parameters for sample QD2. The parameters corresponds to the model selected to fit the PNR data recorded at 8 K.

8.2 Sample QD3 first piece: Analysis results for POLREF instrument data

8.2.1 3.4 K ZFC

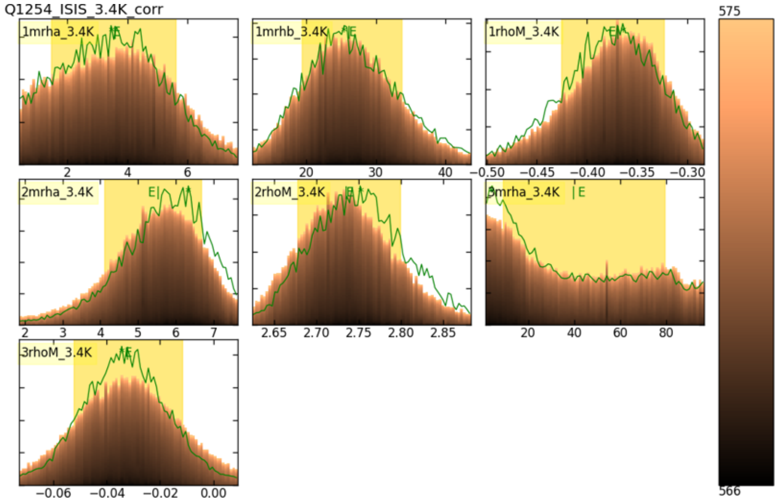

Figure 8.3: A chart of posterior distribution functions of the parameters for sample QD3. The parameter's name is written on the top left side of the box that contain the distribution.

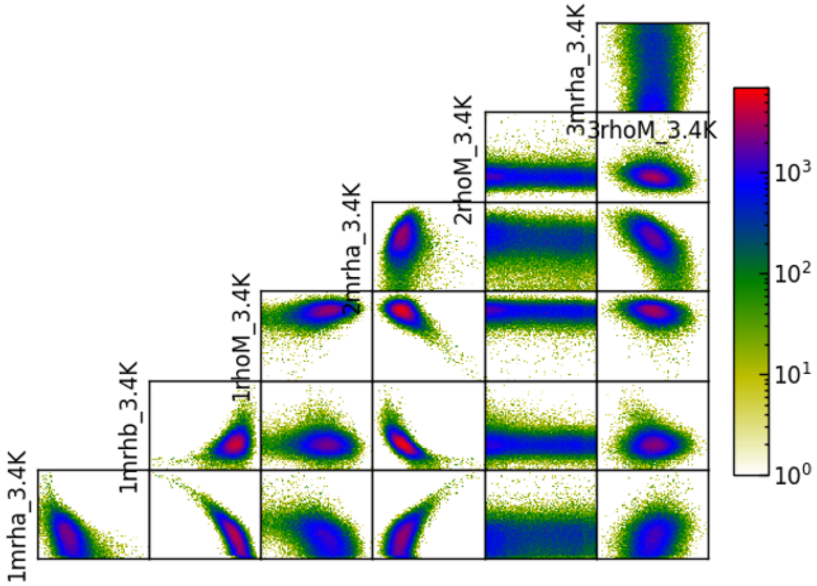

Figure 8.4: A chart of cross-correlations plots between a set of parameters for sample QD3. The parameters corresponds to the model selected to fit the PNR data recorded at 3.4 K (ZFC).

8.2.2 3.4 K FC

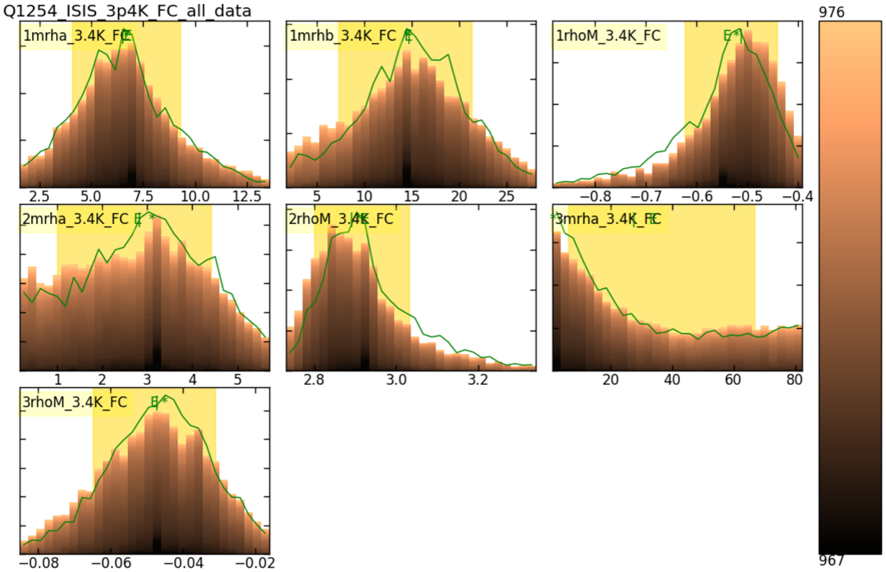

Figure 8.5: A chart of posterior distribution functions of the parameters for sample QD3. The parameter's name is written on the top left side of the box that contain the distribution.

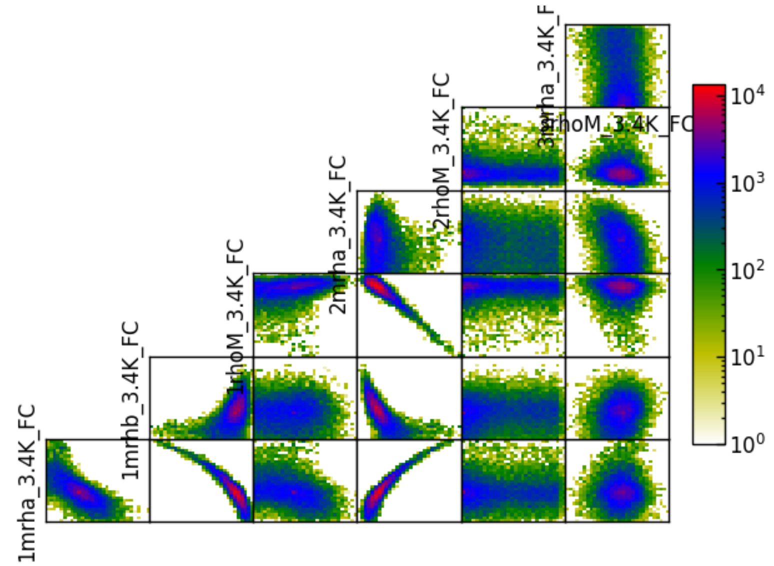

Figure 8.6: A chart of cross-correlations plots between a set of parameters for sample QD3. The parameters corresponds to the model selected to fit the PNR data recorded at 3.4 K (FC).

8.2.3 6 K ZFC

First step

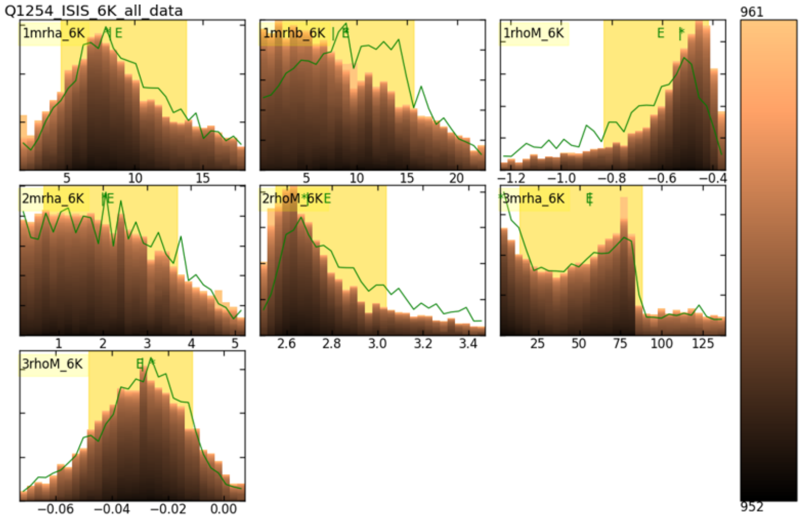

Figure 8.7: A chart of posterior distribution functions of the parameters for sample QD3 (6 K). The parameter's name is written on the top left side of the box that contain the distribution.

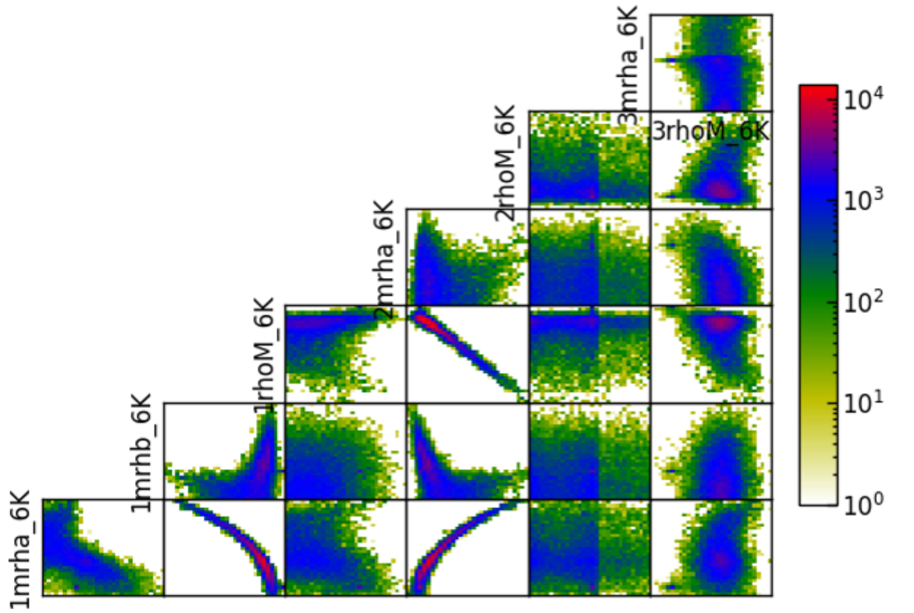

Figure 8.8: A chart of cross-correlations plots between a set of parameters for sample QD3. The parameters corresponds to the model selected to fit the PNR data recorded at 6 K.

Second step

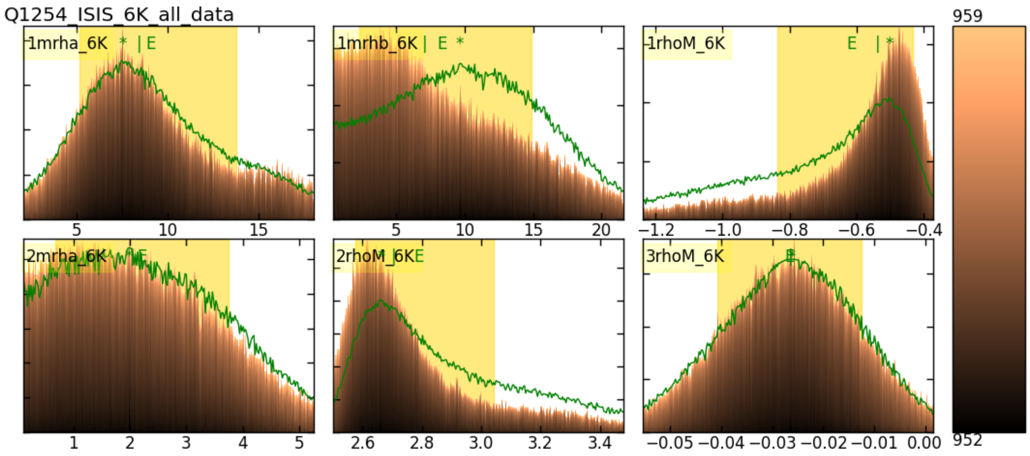

Figure 8.9: A chart of posterior distribution functions of the parameters for sample QD3 (6 K). The parameter's name is written on the top left side of the box that contain the distribution. The value of the parameter 3mrha_6K was fixed to 13.5 Å.

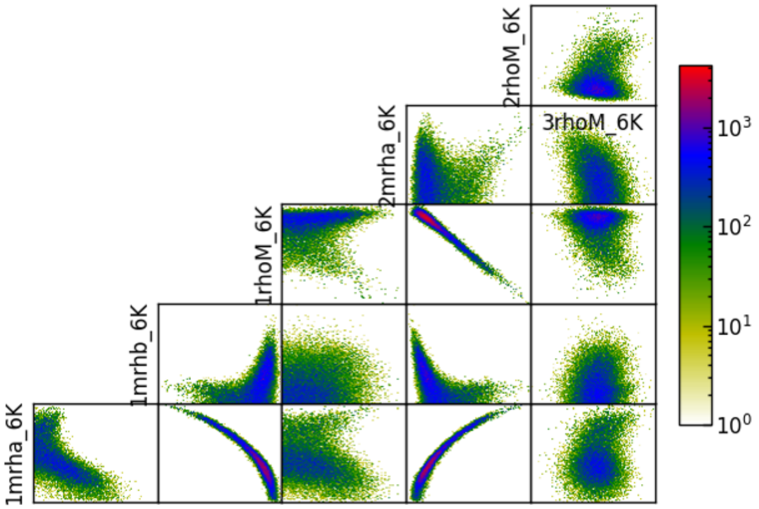

Figure 8.10: A chart of cross-correlations plots between a set of parameters for sample QD2. The parameters corresponds to the model selected to fit the PNR data recorded at 8 K. A numbers is designated to each correlation plot for reference.

8.2.4 8 K ZFC

First step

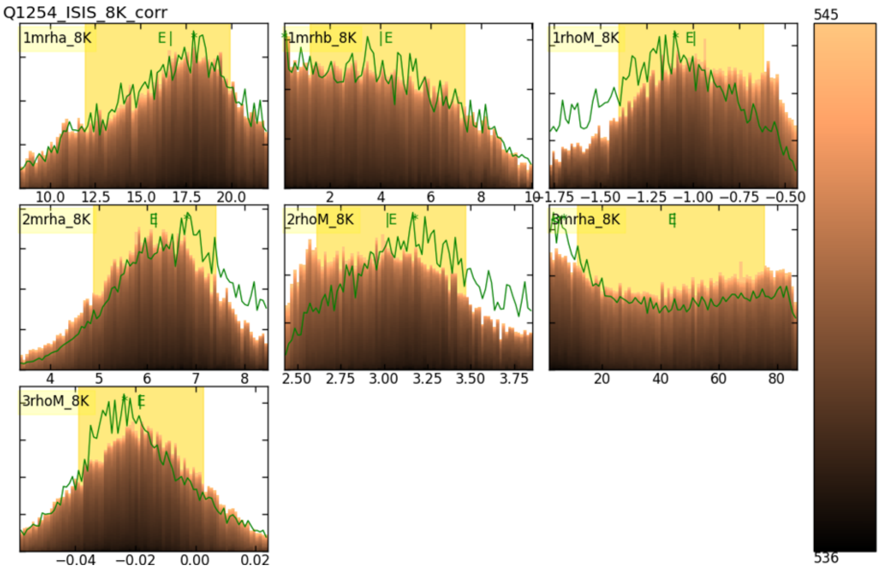

Figure 8.11: A chart of posterior distribution functions of the parameters for sample QD2 (8 K). The parameter's name is written on the top left side of the box that contain the distribution. The value of the parameter 1mrhb_8K was fixed to 13.5 Å.

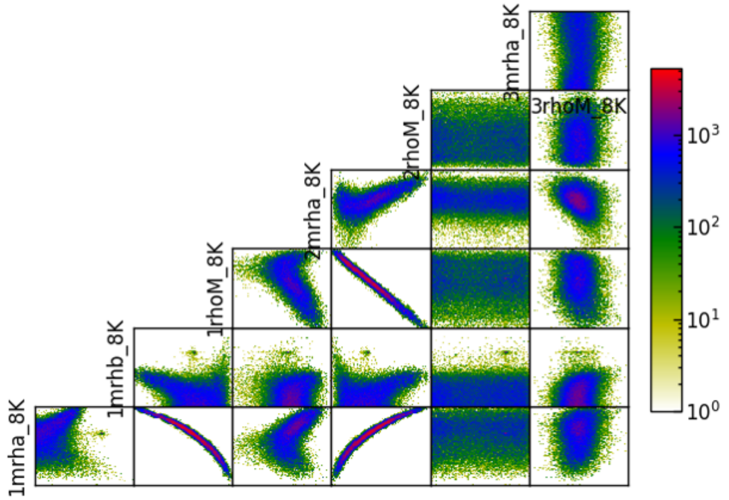

Figure 8.12: A chart of cross-correlations plots between a set of parameters for sample QD2. The parameters corresponds to the model selected to fit the PNR data recorded at 8 K. A numbers is designated to each correlation plot for reference.

Second step

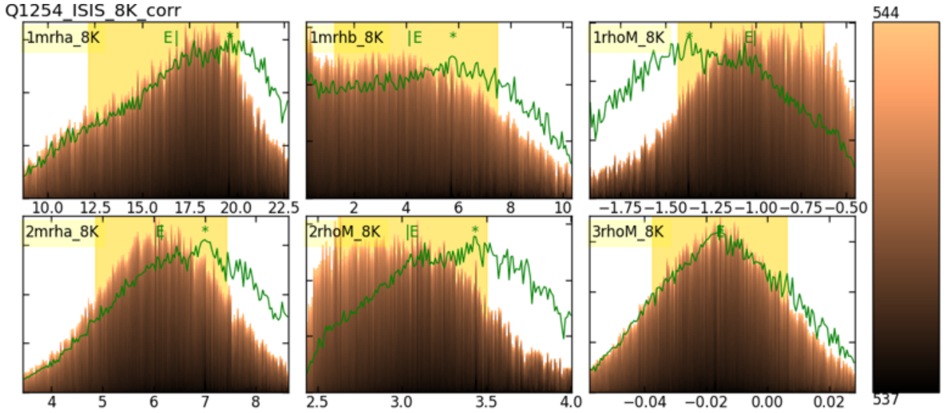

Figure 8.13: A chart of posterior distribution functions of the parameters for sample QD2 (8 K). The parameter's name is written on the top left side of the box that contain the distribution. The value of the parameter 1mrhb_8K was fixed to 13.5 Å.

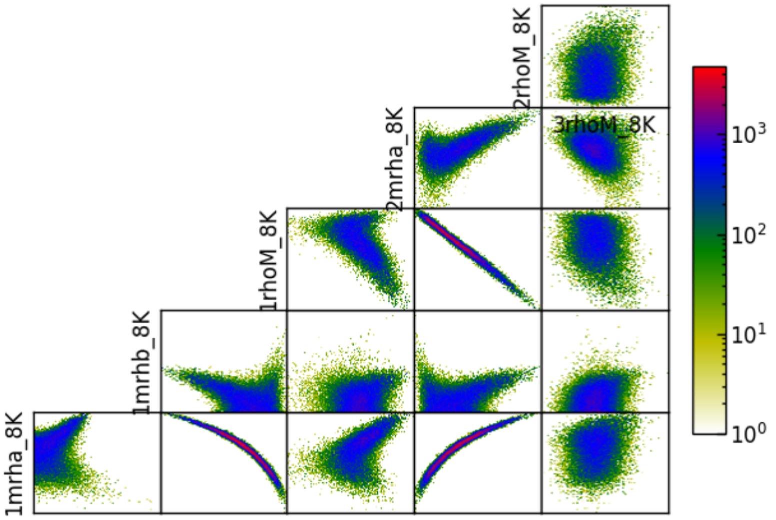

Figure 8.14: A chart of cross-correlations plots between a set of parameters for sample QD2. The parameters corresponds to the model selected to fit the PNR data recorded at 8 K. A numbers is designated to each correlation plot for reference.

8.3 Sample QD3 second piece: Analysis results for D17 instrument data

8.3.1 3.4 K (in 3 T)

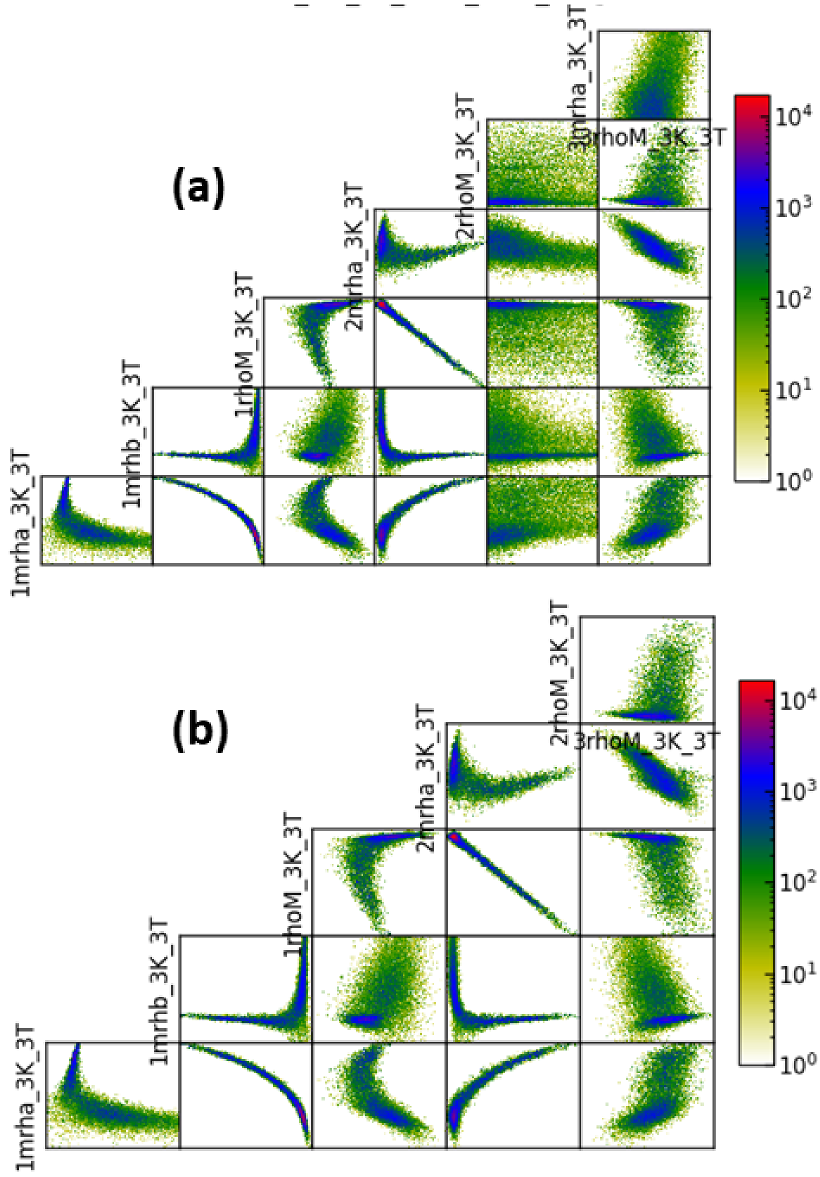

Figure 8.15: A chart of cross-correlations plots between a set of parameters for the second piece of sample QD3. The parameters corresponds to the model selected to fit the PNR data recorded at 3.4 K (in 3 T). (a) Cross-correlation for all the parameters (b) Cross correlation after fixing the value of parameter 3mrha_3K_3T to 3.87 Å.

Table 8.1: Summary of parameters with mean values and 68% confidence intervals for the data at 3 K in a 3 T field for sample QD3 (second piece).

Parameter	**Mean**	**68% Interval**
1mrha_3K_3T	9.1	[5.0, 14.5]
1mrhb_3K_3T	22.0	[11.7, 36.4]
1rhoM_3K_3T	-0.41	[-0.94, -0.07]
2mrha_3K_3T	7.0	[5.87, 8.26]
2rhoM_3K_3T	1.41	[1.21, 1.72]
3rhoM_3K_3T	-0.023	[-0.042, -0.011]

Bibliography

[1] J. I. Cirac and P. Zoller. Quantum Computations with Cold Trapped Ions. *Physical Review Letters*, 74(20):4091–4094, 5 1995.

[2] M. Saffman, T. G. Walker, and K. Mølmer. Quantum information with Rydberg atoms. *Reviews of Modern Physics*, 82(3):2313–2363, 8 2010.

[3] F. Arute, K. Arya, R. Babbush, D. Bacon, J. C. Bardin, R. Barends, R. Biswas, S. Boixo, F. G. S. L. Brandao, D. A. Buell, B. Burkett, Y. Chen, Z. Chen, B. Chiaro, R. Collins, W. Courtney, A. Dunsworth, E. Farhi, B. Foxen, A. Fowler, C. Gidney, M. Giustina, R. Graff, K. Guerin, S. Habegger, M. P. Harrigan, M. J. Hartmann, A. Ho, M. Hoffmann, T. Huang, T. S. Humble, S. V. Isakov, E. Jeffrey, Z. Jiang, D. Kafri, K. Kechedzhi, J. Kelly, P. V. Klimov, S. Knysh, A. Korotkov, F. Kostritsa, D. Landhuis, M. Lindmark, E. Lucero, D. Lyakh, S. Mandrà, J. R. McClean, M. McEwen, A. Megrant, X. Mi, K. Michielsen, M. Mohseni, J. Mutus, O. Naaman, M. Neeley, C. Neill, M. Y. Niu, E. Ostby, A. Petukhov, J. C. Platt, C. Quintana, E. G. Rieffel, P. Roushan, N. C. Rubin, D. Sank, K. J. Satzinger, V. Smelyanskiy, K. J. Sung, M. D. Trevithick, A. Vainsencher, B. Villalonga, T. White, Z. J. Yao, P. Yeh, A. Zalcman, H. Neven, and J. M. Martinis. Quantum supremacy using a programmable superconducting processor. *Nature*, 574(7779):505–510, 10 2019.

[4] L. S. Madsen, F. Laudenbach, M. F. Askarani, F. Rortais, T. Vincent, J.F. F. Bulmer, F. M. Miatto, L. Neuhaus, L. G. Helt, M. J. Collins, A. E. Lita, T. Gerrits, S.W. Nam, V. D. Vaidya, M. Menotti, I. Dhand, Z. Vernon, N. Quesada, and J. Lavoie. Quantum computational advantage with a programmable photonic processor. *Nature*, 606(7912):75–81, 6 2022.

[5] N. P. de Leon, K. M. Itoh, D. Kim, K. K. Mehta, T. E. Northup, H. Paik, B. S. Palmer, N. Samarth, S. Sangtawesin, and D. W. Steuerman. Materials challenges and opportunities for quantum computing hardware. *Science*, 372(6539), 4 2021.

[6] S. D. Sarma, M. Freedman, and C. Nayak. Topological quantum computation. *Physics Today*, 59(7):32–38, 7 2006.

[7] A.Yu. Kitaev. Fault-tolerant quantum computation by anyons. *Annals of Physics*, 303(1):2–30, 1 2003.

[8] E. Majorana. Teoria simmetrica dell'elettrone e del positrone. *Il Nuovo Cimento*, 14(4):171–184, 4 1937.

[9] R. Aguado and L. P. Kouwenhoven. Majorana qubits for topological quantum computing. *Physics Today*, 73(6):44–50, 6 2020.

[10] A. Y. Kitaev. Unpaired Majorana fermions in quantum wires. *Physics-Uspekhi*, 44(10S):131–136, 10 2001.

[11] M. Franz. Majorana's wires. *Nature Nanotechnology*, 8(3):149–152, 3 2013.

[12] F. Wilczek. Majorana returns. *Nature Physics*, 5(9):614–618, 2009.

[13] P. W. Brouwer. Enter the Majorana Fermion. *Science*, 336(6084):989–990, 5 2012.

[14] S. D. Sarma. In search of Majorana. *Nature Physics*, 19(2):165–170, 2 2023.

[15] C. Nayak, S. H. Simon, A. Stern, M. Freedman, and S. D. Sarma. Non-Abelian anyons and topological quantum computation. *Reviews of Modern Physics*, 80(3):1083–1159, 9 2008.

[16] S. D. Sarma, M. Freedman, and C. Nayak. Majorana zero modes and topological quantum computation. *npj Quantum Information*, 1(1), 12 2015.

[17] M. Franz. Race for Majorana fermions. *Physics*, 3, 3 2010.

[18] S. M. Frolov, M. J. Manfra, and J. D. Sau. Topological superconductivity in hybrid devices. *Nature Physics*, 16(7):718–724, 7 2020.

[19] S. Vaitiekėnas, Y. Liu, P. Krogstrup, and C. M. Marcus. Zero-bias peaks at zero magnetic field in ferromagnetic hybrid nanowires. *Nature Physics*, 17(1):43–47, 1 2021.

[20] J. D. Sau, R. M. Lutchyn, S. Tewari, and S. D. Sarma. Generic New Platform for Topological Quantum Computation Using Semiconductor Heterostructures. *Physical Review Letters*, 104(4):040502, 1 2010.

[21] C. X. Liu, S. Schuwalow, Y. Liu, K. Vilkelis, A. L. R. Manesco, P. Krogstrup, and M. Wimmer. Electronic properties of InAs/EuS/Al hybrid nanowires. *Physical Review B*, 104(1), 7 2021.

[22] A. F. Volkov, F. S. Bergeret, and K. B. Efetov. Odd Triplet Superconductivity in Superconductor-Ferromagnet Multilayered Structures. *Physical Review Letters*, 90(11):117006, 3 2003.

[23] Y. Kalcheim, O. Millo, A. Di Bernardo, A. Pal, and J. W. A. Robinson. Inverse proximity effect at superconductor-ferromagnet interfaces: Evidence for induced triplet pairing in the superconductor. *Physical Review B*, 92(6):060501, 8 2015.

[24] O. Maistrenko, C. Autieri, G. Livanas, P. Gentile, A. Romano, C. Noce, D. Manske, and M. Cuoco. Inverse proximity effects at spin-triplet superconductor-ferromagnet interface. *Physical Review Research*, 3(3):033008, 9 2021.

[25] R. Cai, Y. Yao, P. Lv, Y. Ma, W. Xing, B. Li, Y. Ji, H. Zhou, C. Shen, S. Jia, X. C. Xie, I. Žutić, Q. Sun, and W. Han. Evidence for anisotropic spin-triplet Andreev reflection at the 2D van der Waals ferromagnet/superconductor interface. *Nature Communications*, 12(1):6725, 11 2021.

[26] A. Paschoa, J. L. Gonzalez, V. P. Nascimento, and E. C. Passamani. The role of the stray field on superconducting properties of hybrid ferromagnetic/superconducting heterostructures. *Journal of Applied Physics*, 128(4), 7 2020.

[27] J. Stahn, J. Chakhalian, Ch Niedermayer, J. Hoppler, T. Gutberlet, J. Voigt, F. Treubel, H. U. Habermeier, G. Cristiani, B. Keimer, and C. Bernhard. Magnetic proximity effect in perovskite superconductor/ferromagnet multilayers. *Physical Review B - Condensed Matter and Materials Physics*, 71(14), 2005.

[28] J. Xia, V. Shelukhin, M. Karpovski, A. Kapitulnik, and A. Palevski. Inverse proximity effect in superconductor-ferromagnet bilayer structures. *Physical Review Letters*, 102(8), 2 2009.

[29] D. V. Seleznyov, V. O. Yagovtsev, N. G. Pugach, and L. Tao. Ferromagnetic insulator induced inverse proximity effect in superconducting DoS. *Journal of Magnetism and Magnetic Materials*, 595:171645, 4 2024.

[30] H. Kepa, P. Sankowski, P. Kacman, C. F. Majkrzak, A. Yu Sipatov, and T. M. Giebultowicz. Neutron scattering studies of the spin structure of magnetic semiconductor superlattices. In *AIP Conference Proceedings*, volume 772, pages 313–314, 6 2005.

[31] F. Katmis, V. Lauter, F. S. Nogueira, B. A. Assaf, M. E. Jamer, P. Wei, B. Satpati, J. W. Freeland, I. Eremin, D. Heiman, P. Jarillo-Herrero, and J. S. Moodera. A higherature ferromagnetic topological insulating phase by proximity coupling. *Nature*, 533(7604):513–516, 5 2016.

[32] M. Li, Q. Song, W. Zhao, J. A. Garlow, T. H. Liu, L. Wu, Y. Zhu, J. S. Moodera, M. H. W. Chan, G. Chen, and C. Z. Chang. Dirac-electron-mediated magnetic proximity effect in topological insulator/magnetic insulator heterostructures. *Physical Review B*, 96(20), 11 2017.

[33] R. O. M. Aboljadayel, C. J. Kinane, C. A. F. Vaz, D. M. Love, R. S. Weatherup, P. Braeuninger-Weimer, M. B. Martin, A. Ionescu, A. J. Caruana, T. R. Charlton, J. Llandro, P. M. S. Monteiro, C. H. W. Barnes, S. Hofmann, and S. Langridge. Determining the Proximity Effect-Induced Magnetic Moment in Graphene by Polarized Neutron Reflectivity and X-ray Magnetic Circular Dichroism. *ACS Applied Materials and Interfaces*, 15(18):22367–22376, 5 2023.

[34] N. Satchell, P. Quarterman, J. A. Borchers, G. Burnell, and N. O. Birge. Absence of magnetic interactions in Ni-Nb ferromagnet-superconductor bilayers. *Superconductor Science and Technology*, 36(5), 5 2023.

[35] G. Awana, R. Fujita, A. Frisk, P. Chen, Q. Yao, A. J. Caruana, C. J. Kinane, N. J. Steinke, S. Langridge, P. Olalde-Velasco, S. S. Dhesi, G. Van Der Laan, X. F. Kou, S. L. Zhang, T. Hesjedal, and D. Backes. Critical analysis of proximity-induced

magnetism in MnTe/Bi2Te3 heterostructures. *Physical Review Materials*, 6(5), 5 2022.

[36] Y. N. Khaydukov, B. Nagy, J. H. Kim, T. Keller, A. Rühm, Y. V. Nikitenko, K. N. Zhernenkov, J. Stahn, L. F. Kiss, A. Csik, L. Bottyán, and V. L. Aksenov. On the feasibility to study inverse proximity effect in a single S/F bilayer by Polarized Neutron Reflectometry. *JETP Letters*, 98(2):107–110, 9 2013.

[37] Y. Khaydukov, E. Kravtsov, R. Morari, D. Lenk, L. Mustafa, G. Kim, M. Trapp, V. Zhaketov, V. Proglyado, V. Zrdavkov, Y. Nikitenko, H-A. Krug von Nidda, T. Keller, R. Steitz, R. Tideks, A. Sidorenko, V. Ustinov, V. Aksenov, and B. Keimer. Neutron reflectometry studies of Gd/Nb and Cu30Ni70/Nb superlattices. *Journal of Physics: Conference Series*, 1389(1):012060, 11 2019.

[38] J. Bardeen, L. N. Cooper, and J. R. Schrieffer. Theory of Superconductivity. *Physical Review*, 108(5):1175–1204, 12 1957.

[39] W. B. Pearson and I. M. Templeton. Superconducting Transition of Lead. *Physical Review*, 109(4):1094–1094, 2 1958.

[40] G. Chanin and J. P. Torre. Critical-Field Curve of Superconducting Lead. *Physical Review B*, 5(11):4357–4364, 6 1972.

[41] M. Tinkham. *Introduction to Superconductivity (second ed.)*. McGraw-Hill, Inc, New York, second edition, 1996.

[42] S. Michotte, L. Piraux, S. Dubois, F. Pailloux, G. Stenuit, and J. Govaerts. Superconducting properties of lead nanowires arrays. *Physica C: Superconductivity*, 377(3):267–276, 9 2002.

[43] R. F. Gasparovic and W. L. McLean. Superconducting Penetration Depth of Lead. *Physical Review B*, 2(7):2519–2526, 10 1970.

[44] V. Mourik, K. Zuo, S. M. Frolov, S. R. Plissard, E. P. A. M. Bakkers, and L. P. Kouwenhoven. Signatures of Majorana Fermions in Hybrid Superconductor-Semiconductor Nanowire Devices. *Science*, 336(6084):1003–1007, 5 2012.

[45] O. Madelung. *Physics of III-V Compounds*. John Wiley & Sons, Inc., New York,, 1965.

[46] J. P. McCarthy. Preparation and properties of epitaxial InAs. *Solid-State Electronics*, 10(7):649–655, 7 1967.

[47] S. Massidda, A. Continenza, A. J. Freeman, T. M. de Pascale, F. Meloni, and M. Serra. Structural and electronic properties of narrow-band-gap semiconductors: InP, InAs, and InSb. *Physical Review B*, 41(17):12079–12085, 6 1990.

[48] W. Nowacki. Die Kristallstruktur von EuS. *Zeitschrift für Kristallographie - Crystalline Materials*, 99(1-6):339–341, 12 1938.

[49] A. V. Fedorov, G. Poelchen, S. V. Eremeev, S. Schulz, A. Generalov, C. Polley, C. Laubschat, K. Kliemt, N. Kaya, C. Krellner, E. V. Chulkov, K. Kummer, D. Yu. Usachov, A. Ernst, and D. V. Vyalikh. Insight into the Temperature Evolution of Electronic Structure and Mechanism of Exchange Interaction in EuS. *The Journal of Physical Chemistry Letters*, 12(34):8328–8334, 9 2021.

[50] D. D. Berkner. Magneto-optic study of the critical region of EuS. *Physics Letters A*, 54(5):396–398, 10 1975.

[51] S. V. Houten. Magnetic interaction in EuS, EuSe, and EuTe. *Physics Letters*, 2(5):215–216, 10 1962.

[52] O. W. Dietrich, A. J. Henderson, and H. Meyer. Spin-wave analysis of specific heat and magnetization in EuO and EuS. *Physical Review B*, 12(7):2844–2855, 10 1975.

[53] H. G. Bohn, W. Zinn, B. Dorner, and A. Kollmar. Neutron scattering study of spin waves and exchange interactions in ferromagnetic EuS. *Physical Review B*, 22(11):5447–5452, 12 1980.

[54] D. B. Newell, F. Cabiati, J. Fischer, K. Fujii, S. G. Karshenboim, H. S. Margolis, E. de Mirandés, P. J. Mohr, F. Nez, K. Pachucki, T. J. Quinn, B. N. Taylor, M. Wang, B. M. Wood, and Z. Zhang. The CODATA 2017 values of h, e, k, and N for the revision of the SI. *Metrologia*, 55(1):L13–L16, 4 2018.

[55] A. Goschew, J. Griesmar, and P. Fumagalli. Epitaxial growth of EuS on InAs(100) and InP(100). *Thin Solid Films*, 625:106–110, 3 2017.

[56] N. Bouad, L. Chapon, R. M. Marin-Ayral, F. Bouree-Vigneron, and J. C. Tedenac. Neutron powder diffraction study of strain and crystallite size in mechanically alloyed PbTe. *Journal of Solid State Chemistry*, 173(1):189–195, 6 2003.

[57] NIST Centre for Neutron Research Scattering Length Density }Calculator; https://www.ncnr.nist.gov/resources/n-lengths/list.html.

[58] X. Wan, J. Dong, and S. Y. Savrasov. Mechanism of magnetic exchange interactions in europium monochalcogenides. *Physical Review B*, 83(20):205201, 5 2011.

[59] G. Wu, Y. Wang, Q. Gong, L. Li, and X. Wu. An Intelligent Temperature Control Algorithm of Molecular Beam Epitaxy System Based on the Back-Propagation Neural Network. *IEEE Access*, 10:9848–9855, 2022.

[60] M. A. Herman and H. Sitter. *Molecular Beam Epitaxy*, volume 7. Springer Berlin Heidelberg, Berlin, Heidelberg, 1996.

[61] T. D. Vu, Z. Chen, X. Zeng, M. Jiang, S. Liu, Y. Gao, and Y. Long. Physical vapour deposition of vanadium dioxide for thermochromic smart window applications. *Journal of Materials Chemistry C*, 7(8):2121–2145, 2019.

[62] P. A. Savale. Physical Vapor Deposition (PVD) Methods for Synthesis of Thin Films: A Comparative Study. *Archives of Applied Science Research*, 8:1–8, 2016.

[63] https://en.wikipedia.org/wiki/Electron-beam_physical_vapor_deposition#cite_note-1.

[64] G. Joy. *Preparation of thin films*. Marcel Dekker, New York, 2 1992.

[65] H. Kronmuller and S. S. P. Parkin. *Handbook of magnetism and advanced magnetic materials*. John Wiley & Sons, 2007.

[66] A. Furrer, J. Mesot, and T. Strässle. *Neutron Scattering in Condensed Matter Physics*, volume 04. World Scientific, 5 2009.

[67] A. T. Boothroyd. *Principles of Neutron Scattering from Condensed Matter*. Oxford University Press, first edition, 2020.

[68] V. W. Cohen, N. R. Corngold, and N. F. Ramsey. Magnetic Moment of the Neutron. *Physical Review*, 104(2):283–291, 10 1956.

[69] J. Penfold and R. K. Thomas. The application of the specular reflection of neutrons to the study of surfaces and interfaces. *Journal of Physics: Condensed Matter*, 2(6):1369–1412, 2 1990.

[70] L. De Broglie. Recherches sur la théorie des Quanta. *Annales de Physique*, 10(3):22–128, 4 1925.

[71] C. F. Majkrzak, K. V. O'Donovan, and N. F. Berk. Polarized Neutron Reflectometry. In *Neutron Scattering from Magnetic Materials*, pages 397–471. Elsevier, 2006.

[72] V. F. Sears. Fundamental aspects of neutron optics. *Physics Reports*, 82(1):1–29, 2 1982.

[73] H. Kiessig. Untersuchungen zur Totalreflexion von Röntgenstrahlen. *Annalen der Physik*, 402(6):715–768, 1 1931.

[74] A. Fresnel. Mémoire sur la loi réflexion imprime a la lumiere polarisée. *Mém. de l'Acad*, 11:393–433, 1823.

[75] H. Zabel. X-ray and neutron reflectivity analysis of thin films and superlattices. *Applied Physics A Solids and Surfaces*, 58(3):159–168, 3 1994.

[76] L. Névot and P. Croce. Caractérisation des surfaces par réflexion rasante de rayons X. Application à l'étude du polissage de quelques verres silicates. *Revue de Physique Appliquée*, 15(3):761–779, 1980.

[77] L. G. Parratt. Surface Studies of Solids by Total Reflection of X-Rays. *Physical Review*, 95(2):359–369, 7 1954.

[78] F. Abelès. Recherches sur la propagation des ondes électromagnétiques sinusoïdales dans les milieux stratifiés. *Annales de Physique*, 12(5):596–640, 4 1950.

[79] M. Born, E. Wolf, A. B. Bhatia, P. C. Clemmow, D. Gabor, A. R. Stokes, A. M. Taylor, P. A. Wayman, and W. L. Wilcock. *Principles of Optics*. Cambridge University Press, 7 edition, 10 1999.

[80] D17 instrument, ILL. https://www.ill.eu/users/instruments/instruments-list/d17/description/instrument-layout.

[81] J. Daillant and A. Gibaud. *X-ray and Neutron Reflectivity: Principles and Applications*, volume 58. Springer Berlin Heidelberg, Berlin, Heidelberg, 1999.

[82] A. Gibaud, M. S. Chebil, and T. Beuvier. X-Ray Reflectivity. volume 51, pages 191–216. Springer, Berlin, 2013.

[83] Rigaku SmartLab diffractometer. https://rigaku.com/products/x-ray-diffraction-and-scattering/xrd/smartlab.

[84] B. D. Cullity and S. R. Stock. *Elements of X-ray Diffraction*. Pearson Education Limited, Edinburgh, 3 edition, 10 2013.

[85] Crystal Patterns Made Plane and Simple. NobelPrize.org. Nobel Prize Outreach AB 2024. Fri. 2 Aug 2024., 1915.

[86] M. Birkholz. *Thin Film Analysis by X-Ray Scattering*. Wiley, 1 edition, 2005.

[87] G. F. Harrington and J. Santiso. Back-to-Basics tutorial: X-ray diffraction of thin films. *Journal of Electroceramics*, 47(4):141–163, 12 2021.

[88] A. M. Miller, M. Lemon, M. A. Choffel, S. R. Rich, F. Harvel, and D. C. Johnson. Extracting information from X-ray diffraction patterns containing Laue oscillations. *Zeitschrift für Naturforschung B*, 77(4-5):313–322, 5 2022.

[89] P. D. Nellist. Scanning Transmission Electron Microscopy. In *Springer Handbook of Microscopy*, pages 49–99. Springer International Publishing, Cham, 2019.

[90] A. A. Sousa and R. D. Leapman. Development and application of STEM for the biological sciences. *Ultramicroscopy*, 123:38–49, 12 2012.

[91] D. B. Williams and C. B. Carter. The Transmission Electron Microscope. In *Transmission Electron Microscopy*, pages 3–17. Springer US, Boston, MA, 1996.

[92] M. T. Otten. High-Angle annular dark-field imaging on a tem/stem system. *Journal of Electron Microscopy Technique*, 17(2):221–230, 2 1991.

[93] K. Gramm, L. Lundgren, and O. Beckman. SQUID Magnetometer for Magnetization Measurements. *Physica Scripta*, 13(2):93–95, 2 1976.

[94] SQUID Magnetometer Quantum Design MPMS-3. https://www.qdusa.com/products/mpms3.html.

[95] M. Sawicki, W. Stefanowicz, and A. Ney. Sensitive SQUID magnetometry for studying nanomagnetism. *Semiconductor Science and Technology*, 26(6):064006, 6 2011.

[96] M. Buchner, K. Höfler, B. Henne, V. Ney, and A. Ney. Tutorial: Basic principles, limits of detection, and pitfalls of highly sensitive SQUID magnetometry for nanomagnetism and spintronics. *Journal of Applied Physics*, 124(16), 10 2018.

[97] G. V. der Laan and A. I. Figueroa. X-ray magnetic circular dichroism - A versatile tool to study magnetism. *Coordination Chemistry Reviews*, 277:95–129, 10 2014.

[98] J. Stöhr, H. A. Padmore, S. Anders, T. Stammler, and M. R. Scheinfein. Principles of x-ray magnetic dichroism spectromicroscopy. *Surface Review and Letters*, 5(6), 1998.

[99] J. Als-Nielsen. X-rays and matter - the basic interactions. *Comptes Rendus. Physique*, 9(5-6):479–486, 4 2008.

[100] G. S. Henderson, F. M. F. de Groot, and B. J. A. Moulton. X-ray Absorption Near-Edge Structure (XANES) Spectroscopy. *Reviews in Mineralogy and Geochemistry*, 78(1):75–138, 1 2014.

[101] S. Macke and E. Goering. Magnetic reflectometry of heterostructures. *Journal of Physics: Condensed Matter*, 26(36):363201, 9 2014.

[102] ID12 beamline setup, European synchrotron Radiation Facility (ESRF), https://www.esrf.fr/UsersAndScience/Experiments/EMD/ID12.

[103] Y. Liu, A. Luchini, S. Martí-Sánchez, C. Koch, S. Schuwalow, S. A. Khan, T. Stankevič, S. Francoual, J. R. L. Mardegan, J. A. Krieger, V. N. Strocov, J. Stahn, C. A. F. Vaz, M. Ramakrishnan, U. Staub, K. Lefmann, G. Aeppli, J. Arbiol, and P. Krogstrup. Coherent Epitaxial Semiconductor-Ferromagnetic Insulator InAs/EuS Interfaces: Band Alignment and Magnetic Structure. *ACS Applied Materials and Interfaces*, 12(7):8780–8787, 2 2020.

[104] A. Glavic and M. Björck. GenX 3: The latest generation of an established tool. *Journal of Applied Crystallography*, 55:1063–1071, 8 2022.

[105] M. Björck and G. Andersson. GenX : an extensible X-ray reflectivity refinement program utilizing differential evolution. *Journal of Applied Crystallography*, 40(6):1174–1178, 12 2007.

[106] A. Glavic. GenX's documentation: https://aglavic.github.io/genx/doc/.

[107] M. Björck. Fitting with differential evolution: An introduction and evaluation. *Journal of Applied Crystallography*, 44(6):1198–1204, 12 2011.

[108] P. Kienzle. Refl1D: Neutron and X-Ray Reflectivity Analysis Release 0.8.14. Technical report, 2021.

[109] Bumps documentation, https://bumps.readthedocs.io/en/latest/.

[110] M. Doucet, J. H. Cho, G. Alina, J. Bakker, W. Bouwman, P. Butler, K. Campbell, M. Gonzales, R. Heenan, A. Jackson, and P. Juhas. SasView Version 4.1. Zenodo and http://www. sasview. org. 2017 Aug., 2017.

[111] J. A. Vrugt, C. J. F. ter Braak, C. G. H. Diks, B. A. Robinson, J. M. Hyman, and D. Higdon. Accelerating Markov Chain Monte Carlo Simulation by Differential Evolution with Self-Adaptive Randomized Subspace Sampling. *International Journal of Nonlinear Sciences and Numerical Simulation*, 10(3), 1 2009.

[112] DREAM algorithm, https://bumps.readthedocs.io/en/latest/guide/optimizer.html#fit-de.

[113] L. Tierney. Markov Chains for Exploring Posterior Distributions. *The Annals of Statistics*, 22(4), 12 1994.

[114] R. J. Barlow. Practical statistics for particle physics. *CERN Yellow Rep. School Proc.*, 5:149–197, 2020.

[115] Y. Oreg, G. Refael, and F. V. Oppen. Helical liquids and Majorana bound states in quantum wires. *Physical Review Letters*, 105(17), 10 2010.

[116] R. M. Lutchyn, J. D. Sau, and S. D. Sarma. Majorana fermions and a topological phase transition in semiconductor-superconductor heterostructures. *Physical Review Letters*, 105(7), 8 2010.

[117] F. S. Bergeret, A. F. Volkov, and K. B. Efetov. Induced ferromagnetism due to superconductivity in superconductor- ferromagnet structures. *Physical Review B - Condensed Matter and Materials Physics*, 69(17), 5 2004.

[118] S. D. Escribano, A. Maiani, M. Leijnse, K. Flensberg, Y. Oreg, A. L. Yeyati, E. Prada, and R. S. Souto. Semiconductor-ferromagnet-superconductor planar heterostructures for 1D topological superconductivity. *npj Quantum Materials*, 7(1), 12 2022.

[119] Indium Arsenide (InAs), Crystallography Open Database (COD), COD:1011353.

[120] Lead (Pb), Crystallography Open Database (COD), COD:1531228.

[121] Europium Sulfide (EuS), Crystallography Open Database (COD), COD:1010444.

[122] P. Scherrer. Nachr Ges Wiss Goettingen. *Math. Phys.*, 2:98–100, 1918.

[123] J. Als-Nielsen, O. W. Dietrich, W. Kunnmann, and L. Passell. Critical Behavior of the Heisenberg Ferromagnets EuO and EuS. *Physical Review Letters*, 27(11):741–744, 9 1971.

[124] M. Müller, R. Schreiber, and C. M. Schneider. Magnetic properties of EuS spin filter tunnel contacts to silicon. *Journal of Applied Physics*, 109(7), 4 2011.

[125] R. Schiller and W. Nolting. Thickness dependent Curie temperatures of ferromagnetic Heisenberg films. *Solid State Communications*, 110(2):121–125, 3 1999.

[126] M. Müller, G. Miao, and J. S. Moodera. Thickness dependence of ferromagnetic- and metal-insulator transition in thin EuO films. *Journal of Applied Physics*, 105(7), 4 2009.

[127] S. J. Blundell. Order and magnetic structures. In *Magnetism in Condensed Matter*, chapter 5, pages 85–110. Oxford University Press, New York, 10 2001.

[128] B. Dauth, W. Dürr, and S. F. Alvarado. Magnetism at the surface of the Heisenberg ferromagnet EuS. *Surface Science*, 189-190:729–735, 10 1987.

[129] A. Sanchez and C. Navau. Critical-current density from magnetization loops of finite high-T c superconductors. *Supercond. Sci. Technol*, 14:444–447, 2001.

[130] S. D. Pappas, P. Poulopoulos, B. Lewitz, A. Straub, A. Goschew, V. Kapaklis, F. Wilhelm, A. Rogalev, and P. Fumagalli. Direct evidence for significant spin-polarization of EuS in Co/EuS multilayers at room temperature. *Scientific Reports*, 3, 2 2013.

[131] C. J. P. Smits. *EuS based thin film layered systems : magnetoresistance and coupling phenomena*. PhD thesis, Technische Universiteit Eindhoven, Eindhoven, 1 2006.

[132] V. F. Sears. Neutron scattering lengths and cross sections. *Neutron News*, 3(3):26–37, 1 1992.

[133] J. Kirz. *X-Ray Data Booklet*. Lawrence Berkeley Laboratory, University of California, Berkeley, CA (United States), 10 1985.

[134] POLREF instrument, ISIS, UK. https://www.isis.stfc.ac.uk/pages/polref.aspx.

[135] F. S. Bergeret, A. Levy Yeyati, and A. Martín-Rodero. Inverse proximity effect in superconductor-ferromagnet structures: From the ballistic to the diffusive limit. *Physical Review B - Condensed Matter and Materials Physics*, 72(6), 8 2005.

[136] J. S. Moodera, T. S. Santos, and T. Nagahama. The phenomena of spin-filter tunnelling, 4 2007.

[137] G. X. Miao and J. S. Moodera. Controlling magnetic switching properties of EuS for constructing double spin filter magnetic tunnel junctions. *Applied Physics Letters*, 94(18), 2009.

[138] P. LeClair, J. K. Ha, H. J. M. Swagten, J. T. Kohlhepp, C. H. van de Vin, and W. J. M. de Jonge. Large magnetoresistance using hybrid spin filter devices. *Applied Physics Letters*, 80(4):625–627, 1 2002.

[139] C. J. P. Smits, A. T. Filip, J. T. Kohlhepp, H. J. M. Swagten, B. Koopmans, and W. J. M. de Jonge. Magnetic and structural properties of EuS for magnetic tunnel junction barriers. *Journal of Applied Physics*, 95(11):7405–7407, 6 2004.

[140] P. Wachter. The optical electrical and magnetic properties of the europium chalcogenides and the rare earth pnictides. *C R C Critical Reviews in Solid State Sciences*, 3(2):189–241, 7 1972.

[141] A. Mauger and C. Godart. The magnetic, optical, and transport properties of representatives of a class of magnetic semiconductors: The europium chalcogenides. *Physics Reports*, 141(2-3):51–176, 8 1986.

[142] Y. Liu, S. Vaitiekėnas, S. Martí-Sánchez, C. Koch, S. Hart, Z. Cui, T. Kanne, S. A. Khan, R. Tanta, S. Upadhyay, M. E. Cachaza, C. M. Marcus, J. Arbiol, K. A. Moler, and P. Krogstrup. Semiconductor-Ferromagnetic Insulator-Superconductor Nanowires: Stray Field and Exchange Field. *Nano Letters*, 20(1):456–462, 1 2020.

[143] S. Demokritov, U. Rücker, and P. Grünberg. Enhancement of the Curie temperature of epitaxial EuS(100) films caused by growth dislocations. *Journal of Magnetism and Magnetic Materials*, 163(1-2):21–26, 10 1996.

[144] C. Müller, H. Lippitz, J. J. Paggel, and P. Fumagalli. Evidence of exchange-induced spin polarization in the semiconductor EuS at 300K. *Journal of Applied Physics*, 99(7), 4 2006.

[145] A. Goschew, M. Scott, and P. Fumagalli. Verification of antiferromagnetic exchange coupling at room temperature using polar magneto-optic Kerr effect in thin EuS/Co multilayers with perpendicular magnetic anisotropy. *Applied Physics Letters*, 109(6), 8 2016.

[146] P. Poulopoulos, A. Goschew, V. Kapaklis, M. Wolff, A. Delimitis, F. Wilhelm, A. Rogalev, S. D. Pappas, A. Straub, and P. Fumagalli. Induced spin-polarization of EuS at room temperature in Ni/EuS multilayers. *Applied Physics Letters*, 104(11), 3 2014.

[147] J. Kim, K. Kim, H. Wang, J. Sinova, and R. Wu. Understanding the Giant Enhancement of Exchange Interaction in Bi2Se3-EuS Heterostructures. *Physical Review Letters*, 119(2):027201, 7 2017.

[148] J. A. Krieger, Y. Ou, M. Caputo, A. Chikina, M. Döbeli, M. A. Husanu, I. Keren, T. Prokscha, A. Suter, Cui Zu Chang, J. S. Moodera, V. N. Strocov, and Z. Salman. Do topology and ferromagnetism cooperate at the EuS/Bi2Se3 interface? *Physical Review B*, 99(6), 2 2019.

[149] A. I. Figueroa, F. Bonell, M. G. Cuxart, M. Valvidares, P. Gargiani, G. Van Der Laan, A. Mugarza, and S. O. Valenzuela. Absence of Magnetic Proximity

Effect at the Interface of Bi2Se3 and (Bi,Sb)2Te3 with EuS. *Physical Review Letters*, 125(22), 11 2020.

[150] H. L. Meyerheim, A. Ernst, K. Mohseni, A. Polyakov, I. V. Maznichenko, P. A. Buczek, A. Coati, and S. S. P. Parkin. Structure and Magnetism of EuS on Bi2Se3(0001). *Physica Status Solidi (B) Basic Research*, 258(1), 1 2021.

[151] M. Müller, R. Schreiber, and C. M. Schneider. Controlling magnetic properties of EuS-based spin valve structures on Si(001). *IEEE Transactions on Magnetics*, 47(6 PART 1):1635–1638, 2011.

[152] B. J. Ruck, H. J. Trodahl, J. H. Richter, J. C. Cezar, F. Wilhelm, A. Rogalev, V. N. Antonov, B. D. Le, and C. Meyer. Magnetic state of EuN: X-ray magnetic circular dichroism at the Eu M 4,5 and L2,3 absorption edges. *Physical Review B - Condensed Matter and Materials Physics*, 83(17), 5 2011.

[153] C. Kittel. Diamagnetism and paramagnetism. In *Introduction to Solid State Physics*, chapter 11, pages 297–320. John Wiley & Sons, NewYork, 8th edition, 11 2004.